UNIVERSITI PUTRA MALAYSIA
BERILMU BERBAKTI

PROCEEDING OF 7TH INTERNATIONAL SYMPOSIUM ON ADVANCED MATERIALS AND NANOTECHNOLOGY

12 – 13 September **2023**

iSAMN 2023

THEME:
Nanotechnology Towards Green and Sustainable Future

Proceeding of 7th International Symposium on Advanced Materials and Nanotechnology

Publisher:

Institute of Nanoscience and Nanotechnology

Universiti Putra Malaysia

Vol. 1, 2023
eISSN : 2811-4655

Editor: Ts. Dr. Intan Helina Hasan

Publisher's address:

Institute of Nanoscience and Nanotechnology (ION2),
Universiti Putra Malaysia
43400 UPM Serdang, Selangor,
Malaysia

Table of Contents

Keynote Lectures

Conference papers

Nanotechnology: Engineering Materials and Processes for The Green Economy

Ruslinda **A. Rahim**

National Nanotechnology Centre
Ministry of Science, Technology and Innovation (MOSTI), Malaysia

Abstract

There is growing recognition that the transition to a more sustainable economic growth is vital. The existing approach on continuously increasing natural resource consumption with concomitant pollutants emission cannot guarantee an environmentally sustainable socioeconomic growth, especially when resources are becoming increasingly scarce. Pollution due to increased industrial output which is not environmentally friendly will have adverse impacts on human lives and livelihoods as well as the natural ecosystem. As societies around the world face serious challenges, we are actively searching for new technologies and innovation to offer direct or indirect solutions in almost every aspect of modern life, ranging from health to environment and energy. Nanotechnology is one of the most promising enabling technologies of the 21st century. This keynote will discuss the roles of nanotechnology and advanced materials in introducing solutions and opportunities to address various challenges, hence allowing transition to the green economy.

Manganese Oxide Nanorod-Supported Ni@Ir Core-Shell Nanoparticles Catalyzed Complete Dehydrogenation of Hydrazine-Borane

Mehmet **Zahmakiran**

Department of Biotechnology, Bartin University, Turkiye

Abstract

Hydrazine borane (HB; $N_2H_4BH_3$) has been considered to be one of the most promising solid chemical hydrogen storage materials owing to its high hydrogen capacity and stability under ambient conditions. Despite that, the high purity of hydrogen production from the complete dehydrogenation of HB stands as a major problem that needs to be solved for the convenient use of HB in on-demand hydrogen production systems. In this study, we describe the development of a new catalytic material comprised of bimetallic Ni@Ir core-shell nanoparticles (NPs) supported on OMS-2-type manganese oxide octahedral molecular sieve nanorods (Ni@Ir/OMS-2), which can reproducibly be prepared by following a synthesis protocol including (i) the oleylamine-mediated preparation of colloidal Ni@Ir NPs and (ii) wet impregnation of these ex situ synthesized Ni@Ir NPs onto the OMS-2 surface. The characterization of Ni@Ir/OMS-2 has been done by using various spectroscopic and visualization techniques, and their results have revealed the formation of well-dispersed Ni@Ir core-shell NPs on the surface of OMS-2. The catalytic employment of Ni@Ir/OMS-2 in the dehydrogenation of HB showed that Ni-0.22@Ir-0.78/OMS-2 exhibited high dehydrogenation selectivity (>99%) at complete conversion with a turnover frequency (TOF) value of 2590 h(-1) at 323 K, which is the highest activity value among all reported catalysts for the complete dehydrogenation of HB.

Facile, Cost-Effective and Environment-Friendly Approaches Towards Oriented Thin Film Fabrication for Flexible Organic Electronic Devices

Shyam S. **Pandey**

Graduate School of LSSE, Kyushu Institute of Technology

Abstract

To harness the full potential of solution processable conjugated polymers (CPs) as active device elements for flexible organic electronic devices, fabrication of their large-area thin films by low-cost and environmentally benign techniques is inevitable. Therefore, facile fabrication of large-area uniform films with controllable film morphology, thickness and minimal interference to underlying layers is inevitable. We have developed and improvised the floating film transfer method (FTM), which not only provides large area uniform thin films but also they are highly oriented. FTM-processed thin films are not only oriented but also provide edge-ON orientation, which is highly desired for planer devices like organic field effect transistors. It has been demonstrated that oriented thin films of the NR-P3HT prepared by FTM led to a remarkable enhancement in the field effect mobility (>10^2 times) as compared to their spin-coated film counterparts. Utilizing highly edge-on oriented thin film thin films of PBTTT-C14 processed by FTM, we have not only demonstrated a very high optical dichroism of >10 but also an OFET mobility of 1.24 cm^2/Vs, which is one of the highest reported mobility values for this class of CPs. Recently, we have demonstrated the control of the extent and direction of molecular orientation using DPP-TTT, which is rather difficult to orient owing to its molecular rigidity. Harnessing the synergy of orientation and molecular orientation under FTM using DPP-TTT, the very high field-effect mobility of 12.4 $cm^2V^{-1}s^{-1}$ was recently demonstrated, which is also of the highest values reported for solution-processable semiconducting polymers We have also recently improvised the solvent-less friction transfer (FT) method as solvent assisted friction transfer (SAFT) and demonstrated that CPs generally imparting face-ON orientation can be oriented in to Edge-ON manner. At the same time SAFT can be used to fabricate oriented thin films of flexible as well as rigid substrates.

Aptamer-Based Biosensor: From R&D to Commercialisation

Eda Yuhana **Ariffin**
Biogenes Technologies Sdn Bhd., Malaysia

Abstract

Aptamer-based biosensors have emerged as a promising technology at the intersection of molecular recognition and sensing application. In BIOGENES, aptamers are designed and validated using bio-computational technique, which is faster and cheaper than conventional lab-based method. Our platform technologies include APTCAD-aptamer design platform, APTFAB-aptamer and sensor fabrication platform and APTSENS-digital diagnostics platform. All three platforms connected via cloud to support journey from R&D to commercialisation. These platforms are practical for application ranging from human healthcare to animal health, agriculture, food safety and environmental monitoring.

Keywords: Aptamer; aptamer-based biosensor; sensing technology; Research & Development; commercialisation

Resistivity Analysis of Nickel Nanoparticles Additive-based Magnetorheological Grease

Norzilawati **Mohamad**[1*], Farhan **Ramli**[1], Saiful Amri **Mazlan**[2,3], Norfazliana **Abdullah**[1], Mohd Syahlan Mohd **Syukri**[1]

[1]Faculty of Engineering, Universiti Malaysia Sabah, Jalan UMS, 8400 Kota Kinabalu, Sabah, Malaysia
[2] Engineering Materials and Structures (eMast) iKohza, Malaysia-Japan International Institute of Technology (MJIIT), Universiti Teknologi Malaysia, 55410 Kuala Lumpur, Malaysia
[3] Department of Mechanical Engineering, College of Engineering, University of Business & Technology (UBT), P.O Box No 21448, Jeddah, Saudi Arabia

*Corresponding author's phone: +6088-320 348
E-mail: norzilawati@ums.edu.my

ABSTRACT

Magnetorheological grease (MRG) is classified as smart material due to the tunable rheological properties with the presence of external magnetic force. The improvement in the yield performance of MRG under an applied magnetic field is actively studied. However, there is a very limited study related to the conductivity properties that have been reported. Therefore, this paper is to investigate the effect of nickel nanoparticles base MRG (NMRG) on conductivity properties through resistivity analysis. In this study, the NMRG sample was fabricated between different sizes of magnetic particles and grease. Then, the resistivity analysis was conducted through a simple self-develop test rig setup. Further analysis of the chemical compound and hydrophobicity effect were examined. The results show that the resistivity values decrease with the additional percentage of nickel nanoparticles. The hydrophobicity effect also increases by 8.4% due to the disrupted highly dynamic hydrogen bonds formed between polar and non-polar molecules which is proven by FTIR. By having dual properties, the applications of MR materials can be broadened in many applications and industries.

Keywords—magnetorheological grease; nickel nanoparticles; additive; physical properties; resistivity properties

1.0 INTRODUCTION

Magnetorheological (MR) materials have attracted attention of the researchers in medical devices due to their tunable rheology properties and promising high performance. Extensive studies related to the prototype of rehabilitation devices integrated with MR fluids have been developed [1]. However, due to the drawback of the MR fluids, MR grease (MRG) is introduced as a replacement. MRG was invented by Rankin et. al. [2], in 1999 as a viscoplastic medium in MR fluid to solve the sedimentation problem.

Recently, MRG is actively studied by researchers focusing on the improvement of magnetic properties by the addition of solid and liquid additives. Kim et. al. [3] and Mohamad et. al. [4], investigated the effect of dilution oil on the MRG. The result reported that the initial viscosity decrease aligns with material performance. In another study, several magnetic nanoparticles have been studied by researchers. The viscosity trend of the MRG with nanoparticles showed decreasing trend at off-state conditions, while increasing when the external magnetic force was applied [5], [6]. The

performance of MRG with nanoparticles also improved by 86% [7]. Besides, the improvement in the response time of the MRG is reported [8].

While significant researchers focus on the improvement of magnetic properties, some researchers diverge their focus on developing MRG as materials consist of dual properties; magnetic and conductivity properties. Therefore, this paper the effect of nickel nanoparticles base MRG (NMRG) on conductivity properties through resistivity analysis. A series of NMRG samples are fabricated and analysed using a self-develop resistivity test rig. The results are discussed in the following section of the paper.

2.0 MATERIALS

Samples were fabricated utilizing three components; carbonyl iron particles (CIPs), grease and nickel nanoparticles by mechanical stirrer. The CIPs purchased from Sigma Aldrich were in spherical shape with an average diameter size of 5 µm. The lithium grease with NLGI 2 (UMW GRANTT International Sdn. Bhd.) was chosen as a suspension medium. The additive nickel nanoparticles with a diameter size of 100 nm were purchased from ACS Material LLC. The composition used for CIPs and nickel nanoparticles were 70 wt% and 1, 3 and 5 wt% respectively. All the components are mixed for 1 hour at 300 rpm under room conditions to obtain homogeneity or further characterization. Table 1 is the summary of the samples prepared.

TABLE 1: Sample Composition

Samples	CIPs (wt%)	Nickel (wt%)	Grease (wt%)
NMRG1	70	1	29
NMRG3	70	3	27
NMRG5	70	5	25
MRG0	70	0	30

3.0 EXPERIMENTAL

The physical characterization of the samples was analyzed through Fourier Transform Infrared Spectroscopy (FTIR) for the identification of compound class. The chemical compound class was analyzed in the wavelength between 500 – 4000 cm^{-1}. The wettability properties of samples were measured using Attension Theta Tensiometer equipment equipped with the software. The distilled water was selected as a liquid while NMRG samples as the solid surface during the test. A feasible study on the resistivity properties of NMRG was conducted using a simple self-develop test rig as shown in Figure 1. The 1 mL of NMRG was sandwiched with the 1 mm copper plate. The permanent magnet with 0.1 Tesla (T) was placed at the top and bottom layer by layer. The resistance value measured by a digital multimeter was recorded. The test was repeated several times for consistency.

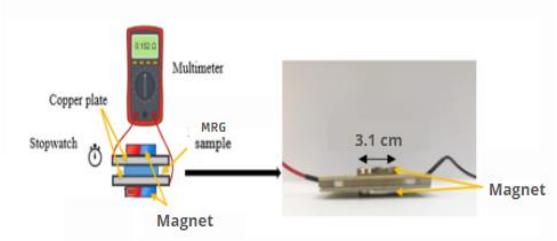

Fig. 1: Resistivity experimental setup

4.0 RESULTS AND DISCUSSION

Figure 2 shows the resistivity analysis of NMRG under the influence of magnetic fields. As a preliminary study, a simple self-developed test rig was set up to measure the resistance of the samples. The results exhibit that the resistance value of NMRG increases with increasing of nickel nanoparticles with a magnetic field strength of 0.2T. It is also worth noting that the resistivity values are saturated although by increasing the permanent magnet. It is expected that the presence of nickel nanoparticles with magnetic properties has developed a bridge to the unfilled void between CIPs in a greased medium. This is because metallic bonding inside the NMRG tends to attract the CIPs and the NMRG properties of conductivity will increase. In contrast, the resistivity

values increase due to the agglomeration of nickel nanoparticles to the CIPs which form colloids and become a resistance in the grease.

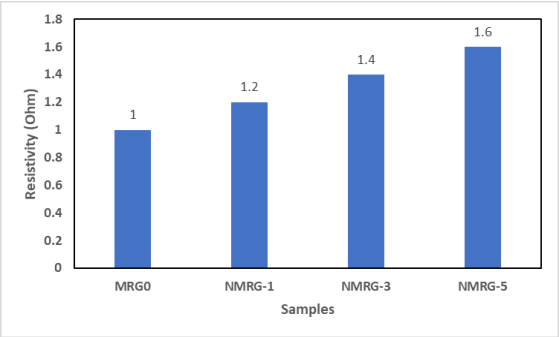

Fig. 2: Resistivity analysis of NMRG

The negative result in resistivity is correlated with the chemical compound and hydrophobicity effect. Figure 3 shows the FTIR result analysis for NMRG samples. In general, a similar absorbance frequency trend was observed for all samples. The medium sharp peak of C-H stretching was vibrated at the wavelength range between 3000 – 2800 cm^{-1} which represents the alkane compound class. A strong binding energy formed from the stable alkane group will lead to high resistance in the sample. A change in the absorbance is observed for the wavelength between 1550 – 1300 cm^{-1}. A strong absorbance peak was observed at frequency 1550 cm^{-1} which represents stretching nitro compound (N-O). Besides, a weak alcohol compound; O-H bending appeared at frequency range 1370 cm^{-1}. A medium-light of C-H was absorbed at 1450 cm^{-1} due to the presence of an alkane group. A weak vibration at the wavelength of 700 cm^{-1} depicted bending alkene (C=C). This proves that increasing the wt% of the nickel nanoparticles has weakened the alkene bond. Therefore, electron transfer is occurring at this frequency. In a nutshell, the electron transferring process inactively occurs in the NMRG due to most of the chemical groups appearing as stable bonds.

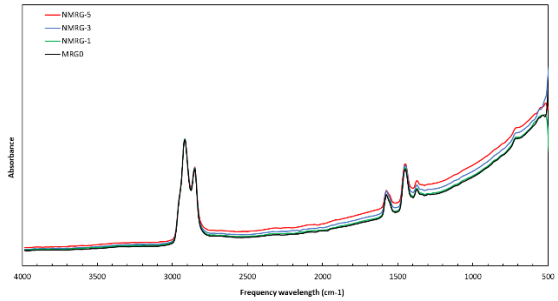

Fig. 3: FTIR analysis of NMRG samples

The wettability analysis of the samples was characterized using contact angle measurements. The summarized results were exhibited in Figure 4. It is acknowledged that initially, grease has intrinsic hydrophobic characteristics while metallic particles (CIPs and nickel) will be hydrophilic. Analysis shows that all samples have inherent hydrophobic properties which have a contact angle >90°. The increasing wetting behavior on the hydrophobicity was recorded by increasing nickel nanoparticles. The hydrophobicity effect of NMRG5 increased by 8.4% compared to the MRG0. This indicates that the chemical bond of the metallic composition between CIPs and nickel in NMRG has disrupted the highly dynamic hydrogen bonds formed between polar and non-polar molecules. This statement is also aligned by the FTIR result which shows that electron energy transfer happens at the unstable double bond of the alkene group. Thus, the microstructural changes which contributed to the alteration of the surface of the NMRG have increased the hydrophobicity effect.

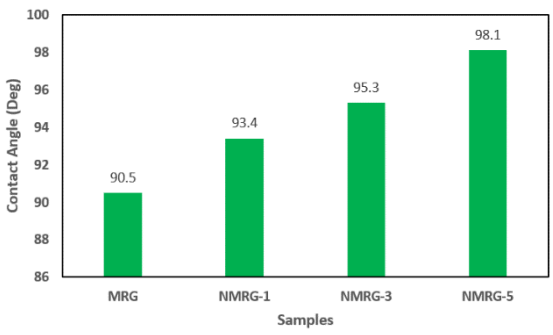

Fig. 4: Summary of NMRG wettability analysis

5.0 CONCLUSION

In conclusion, the effect of nickel nanoparticles based on NMRG on conductivity properties through resistivity analysis was investigated. The NMRG samples were mechanically fabricated with variations in wt% of nickel nanoparticles in the range of 1 – 5 wt%. The resistivity results show an increment pattern by the addition of nickel nanoparticles which aligned with the hydrophobicity result. The decreasing trend is supported by the FTIR results which show that the binding energy of the electron transfer is high by the formation of colloids in the NMRG. This phenomenon leads to the increase of resistance in the NMRG which results in decreasing conductivity properties. A continuation of this study will be focusing on the microstructural and rheology effect as well as the impact of nickel as a coating-based NMRG.

ACKNOWLEDGEMENTS

This study was fully funded by Universiti Malaysia Sabah.

REFERENCES

[1] M. F. Fardan, B. W. Lenggana, U. Ubaidillah, S.-B. Choi, D. D. Susilo, and S. Z. Khan, “Revolutionizing Prosthetic Design with Auxetic Metamaterials and Structures: A Review of Mechanical Properties and Limitations,” *Micromachines (Basel)*, vol. 14, no. 6, p. 1165, May 2023.

[2] P. J. Rankin, A. T. Horvath, and D. J. Klingenberg, “Magnetorheology in viscoplastic media,” *Rheol Acta*, vol. 38, no. 5, pp. 471–477, 1999.

[3] J. Kim, J. Ko, Y. Liu, I. Kim, and H. Choi, “Effect of medium oil on magnetorheology of soft magnetic carbonyl iron particles,” vol. 170, no. 2004, p. 5246, 2012.

[4] N. Mohamad, A. Yasser, A. Fatah, S. A. Mazlan, N. A. Nordin, and M. Nabil, “Dilution dependent of different types of redispersing oils on magnetorheological greases,” vol. 5, no. x, pp. 5–8, 2017.

[5] N. Mohamad, Ubaidillah, S. A. Mazlan, S.-B. Choi, and Naim Abdul Halim, “Improvement of magnetorheological greases with superparamagnetic nanoparticles,” in *MATEC Web of Conferences*, 2018.

[6] J. H. Park, M. H. Kwon, and O. O. Park, “Rheological properties and stability of magnetorheological fluids using viscoelastic medium and nanoadditives,” *Korean Journal of Chemical Engineering*, vol. 18, no. 5, pp. 580–585, 2001.

[7] S. M. A. Tarmizi *et al.*, “Incorporation of cobalt ferrite on the field dependent performances of magnetorheological grease,” *Journal of Materials Research and Technology*, vol. 9, no. 6, pp. 15566–15574, 2020.

[8] S. M. A. Tarmizi *et al.*, “Improvement of rheological and transient response of magnetorheological grease with amalgamation of cobalt ferrite,” *Journal of Materials Research and Technology*, vol. 23, pp. 1285–1295, Mar. 2023.

An Ohmic Contact Formations on TiO_2-Based Thick Film using Interdigitated Electrode Graphite on Different Substrate

Azlinda Abu **Bakar** [1,5,*], Mohd Nizar **Hamidon**[1,3], Mohd Hanif **Yaacob**[2], Suriati **Paiman**[4], Haslina **Jaafar**[3], Wan Nurshiela **Wan Jusoh**[5], Intan Helina **Hasan**[1], Farah Nabilah **Shafiee**[1], Suleiman **Babani**[1]

[1]Institute of Nanoscience and Nanotechnology, Universiti Putra Malaysia, 43400 UPM Serdang, Selangor, Malaysia
[2]Department of Computer and Communication Systems, Faculty of Engineering, Universiti Putra Malaysia, 43400 UPM Serdang, Selangor
[3]Department of Electrical and Electronic, Faculty of Engineering, Universiti Putra Malaysia, 43400 UPM Serdang, Selangor, Malaysia
[4]Department of Physics, Faculty of Science, Universiti Putra Malaysia, 43400 UPM Serdang, Selangor, Malaysia
[5]Section of Aerospace, Malaysians Institute of Aviation Technology, Universiti Kuala Lumpur, 43000 Dengkil, Selangor, Malaysia

*Corresponding author's phone: +603-8769 7533
E-mail: gs56982@student.upm.edu.my

ABSTRACT

This work investigated the Ohmic contact between thick film graphite as an electrode and a TiO_2-based sample. MWCNT and B_2O_3 materials were added using mixing and doping processes respectively. The mixing and doping used a fixed volume of 5 wt.% MWCNT and 5 wt.% B_2O_3, for paste preparations. The main content of the binder to develop TiO_2-based is linseed oil. The thick film was deposited on polyimide film and alumina substrate using a screen-printing technique, then annealed at 350 ^{0}C for one hour in ambient air. Graphite IDE was deposited at the bottom sample before a layer of TiO_2-MWCNT or TiO_2-B_2O_3 thick film on top of a substrate. I-V characteristics and resistance values were measured at room temperature. The resistance results showed that the addition of MWCNT and B_2O_3 in TiO_2 reduced the resistance value of the interdigitated electrode. It also showed that graphite IDE and TiO_2-MWCNT, TiO_2-B_2O_3 produced an Ohmic contact behaviour, convincing the suitability to use as sensor applications. The resistance values of both thick films showed an increasing trend with the additional TiO_2-based associated with a slower electron mobility effect of resistance increase in materials.

Keywords—Thick film; interdigitated electrode graphite; electrical properties;

1.0 INTRODUCTION

Recently, the flexible electronics circuit is the most popular in the industry due to its diversity in applications and design. Deposition techniques are made by various methods such as photolithography, screen printing, inkjet printing, and other methods [1][2]. The thick film carbon-based via screen printing fabrication process is a simple, low-cost, and time-saving method. Screen printing seems to be one of the most popular technologies allowing large-scale production in the market in the near future because of its advantages such as miniaturisation, versatility, low cost and particularly the possibility of mass production [3].

An interdigitated electrode material adopted is important as a function electrode to harvest the electron from the material. Metals are commonly used as electrodes, such as silver, gold, and platinum, due to their low resistivity [4]. Among these materials, the most popular material is silver because it has high conductivity from common electrodes and is most stable in the air. However, metal silver tends to crack when a flexible substrate is applied [5]. Besides that, metal is easily oxidized under a high-humidity environment [6]. The purpose of this research work is to identify the capability of graphite flakes as the replacement material for electrodes. The purpose of interdigitated electrodes in sensing applications has gained increased interest during the last two decades, developing electrodes one of the most commonly used as electrochemical sensor structures [7][8] such as gas sensors, humidity sensors and piezoelectric. Graphite electrodes are suitable to replace the metal conductives used in electronic applications.

2.0 LITERATURE REVIEW

The Ohmic contact is a low resistance junction that provides current conduction from metal to semiconductor and vice versa. Theoretically, the current should increase or decrease linearly with the applied voltage. The resistance, (R) of the sample is given by equation 1 where R is equal to resistance in Ohm Ω, V is voltage in volts and I is current in Amperes [9].

$$V = IR \quad (1)$$

3.0 MATERIALS

This research work will compare the I-V characteristics with show the Ohmic contact for graphite electrodes using two different materials prepared by using the screen printing technique. Graphite conductive paste purchased from Serdang Paste Technology Sdn. Bhd. were used as materials for interdigitated electrode preparation. TiO_2-MWCNT and TiO_2-B_2O_3 were used as sample thick films to deposit the layer of interdigitated electrode graphite. TiO_2-MWCNT where, TiO_2 (Aeroxide P25) and MWCNT provided by Sigma-Aldrich and Materials-A2Z, were prepared with a mixing ratio of 70:30. Fig. 1 shows the proposed organic binder; it was prepared by mixing the linseed oil 85 wt.% and m-xylene 12.5 wt.% for 250 rpm in 3 hours at 40 ^{0}C, then continued by mixing with α-terpineol 2.5 wt.% using magnetic stirrer for 250 rpm in 3 hours at 40 ^{0}C to obtain a homogeneous binder. Meanwhile, TiO_2-B_2O_3 was prepared by mixing TiO_2-B_2O_3 with an organic binder. Initially, 90 wt. %of TiO_2 was mixed with 10 wt. % of glass powder, Boron Oxide. The glass powder was added to the paste to produce good adhesion between the paste and substrate.

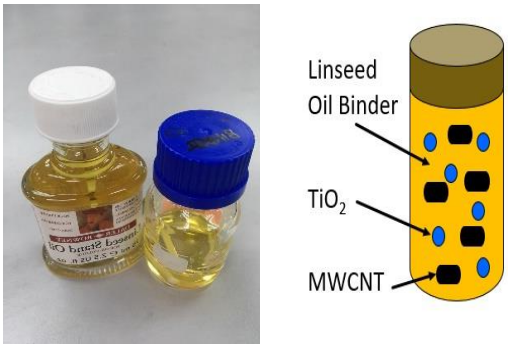

Fig. 1: Linseed Oil Binder

The screen printing fabrication method was used in paste deposition to fabricate a thick film. The thick film used in this work consists of two film layers, the first layer is the graphite electrode and the second layer is the material TiO_2-MWCNT or TiO_2-B_2O_3. The sample was left for about 15 minutes before proceeding to the annealing process at 350 ^{0}C for one hour.

4.0 EXPERIMENTAL

Two-point probe setup using Keithly Current Source I-V LabView as software instruments connected to Keithley 2400 Source Meter to measure the electrical properties of the sample as shown in Fig. 2 (a). I-V characteristics on the electrode were studied by copper wires attached to

both ends of the electrode. Two-point probes were attached to the sample as shown in Fig. 2(b), this is called the two-point probes technique, since as probe connections. A voltage source from Keithley 2400 Source Meter applies of voltage, 10 V across the sample, causing a current, *I* to flow through the sample. The amount of current, *I* that flows through the sample is measured by the controller module Lab View software, which was connected in series with the sample and voltage source.

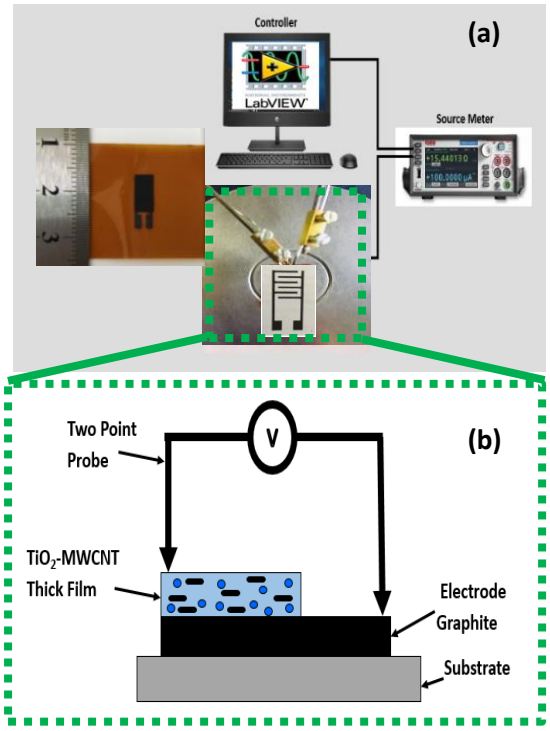

Fig. 2: (a) Two Point Probe Set-Up; and (b) Formation Two Point Probe.

5.0 RESULTS AND DISCUSSION

I-V characteristics effect between graphite electrode on TiO_2, TiO_2-MWCNT and TiO_2-B_2O_3 material using a two-point probes system can be represented by a graph. The performance of graphite results could be demonstrated with TiO_2-MWCNT and TiO_2-B_2O_3 material layer. A voltage supply of 10V was connected to interdigitated graphite electrode and another probe to the TiO_2 layer shows a lower range of current value from 102.62 pA to 2.48 mA on alumina substrate compared to that Kapton substrate for 2.06 nA to 2.48 mA as shown as Figure 3(a) and (b). The alumina substrate shown in the graph TiO_2 and TiO_2-MWCNT was stacked together and TiO_2-B_2O_3 was lower than that. Compared to the Kapton substrate, it does not have a stacked graph with resistance value decrease from TiO_2, TiO_2-B_2O_3 and TiO^2-MWCNT. Both graphs show the Ohmic contact behaviour of interdigitated electrode graphite on alumina and Kapton which can be proposed as material for sensor applications.

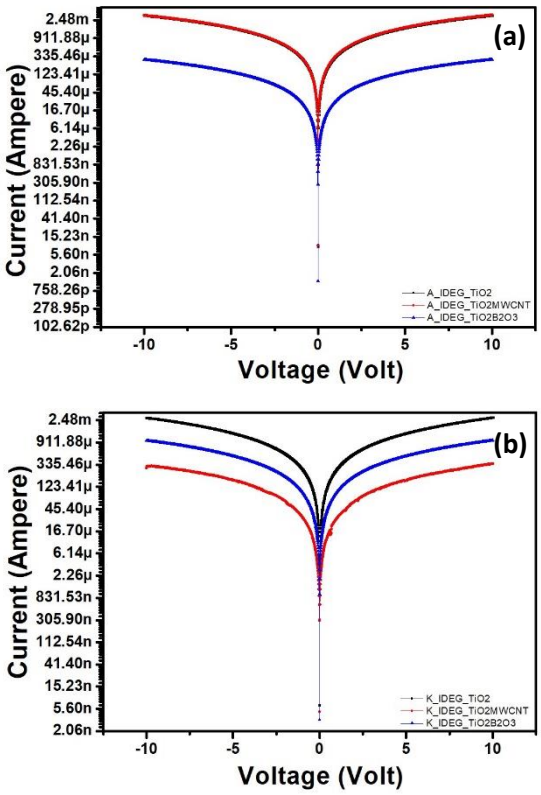

Fig. 3: Comparison I-V Characteristics (a)

Table 1 shows the measured resistance values by using a two-point probe for each sample. The resistance values of interdigitated electrodes without any TiO_2 layer are 17.03 and 17.88 KΩ using alumina and Kapton substrate respectively. Materials of interdigitated electrode and substrate represented as the first column the resistance value of graphite substrate on kapton and alumina respectively. The second column shows the resistance value of interdigitated electrode with TiO_2-MWCNT and TiO_2-B_2O_3 layer.

Resistance IDEG/TiO_2-MWCNT deposited on substrate alumina is $3.03x10^3$ Ohm compared to substrate kapton $3.53x10^3$ Ohm. That conditions show the same trend using IDEG/TiO_2-B_2O_3 on substrate alumina detect $2.07x10^3$ Ohm, compare to substrate kapton the value resistance increase to $2.32x10^3$ Ohm. This value shown the Ohmic contact behavior. Besides that, the material TiO_2 doped to B_2O_3 and mix to MWCNT show the low resistance when it mixes with MWCNT. It is because, MWCNT are conductive paste and have free electron to move around compare to B_2O_3 are glass powder only as adhesion contribution to paste increase the firing temperature.

Interdigitated electrode graphite on alumina shows a lower value of resistance compared to kapton substrate for both material TiO_2-based. The difference between both materials suggesting that the effect of contact resistance is more prominent in alumina substrate. This can be attributed to the high resistance value contributed from the material layer. The resistance value also shows an increasing trend after the deposition of TiO_2-MWCNT and TiO_2-B_2O_3 material layer.

TABLE I: Resistance Value Interdigitated Electrode Graphite for Material Elements TiO_2-MWCNT and TiO_2-B_2O_3.V

Material Layer/ Substrate	Resistance ($x10^{-3}$ Ω)		
	TiO_2	TiO_2-MWCNT	TiO_2-B_2O_3
IDEG/ Alumina	17.03	3.03	2.07
IDEG/ Kapton	17.88	3.53	2.32

6.0 CONCLUSION

The main finding of different TiO_2-based material using interdigitated electrode graphite at different substrate are presented as below:

i. All sample IDEG/TiO_2-MWCNT and IDEG/TiO_2-B_2O_3 at substrate alumina and kapton show the Ohmic contact behavior and suitable with Ohm's Law equations.
ii. Material TiO_2-B_2O_3 are good material suggested as sensor applications compare to TiO_2-MWCNT because of low resistance value.
iii. Interdigitated electrode graphite success to replace metal material as conductive electrode.

ACKNOWLEDGEMENTS

The author would like to thank Universiti Kuala Lumpur, and Majlis Amanah Rakyat (MARA) for the financial support. An acknowledgement contribution also goes to FNDL group, Institute of Nanoscience and Nanotechnology.

REFERENCES

1. Abdulhameed, A., Halin, I. A., Mohtar, M. N., and Hamidon, M. N., (2021) 'Airflow-assisted dielectrophoresis to reduce the resistance mismatch in carbon nanotube-based temperature sensors,' RSC Adv., vol. 11, no. 62, pp. 39311–39318.
2. H. Omran and K. N. Salama, "Design and Fabrication of Capacitive Interdigitated Electrodes for Smart Gas Sensors."
3. Chachuli, S. A. M.,(2021) 'Effects of MWCNTs/graphene nanoflakes/MXene addition to TiO2 thick film on hydrogen gas sensing,' J. Alloys Compd., vol. 882, p. 160671.
4. J. Oberländer et al., "Study of interdigitated electrode arrays using experiments and finite element models for the evaluation of sterilization processes," Sensors (Switzerland), vol. 15, no. 10, pp. 26115–26127, 2015, doi: 10.3390/s151026115.
5. R. Alrammouz, J. Podlecki, P. Abboud, B. Sorli, and R. Habchi, "A review on flexible gas sensors: From materials to devices," Sensors Actuators, A Phys., vol. 284, pp. 209–231, 2018, doi: 10.1016/j.sna.2018.10.036.
6. S. P. Lee, "Electrodes for semiconductor gas sensors," Sensors (Switzerland), vol. 17, no. 4, 2017, doi: 10.3390/s17040683.
7. S. A. M. Chachuli et al., (2021) "Effects of MWCNTs/graphene nanoflakes/ MXene addition to TiO_2 thick film on hydrogen gas sensing," J. Alloys Compd., vol. 882, p. 160671,
8. George, J., (2019) 'CNT-based inkjet-printed RF gas sensor: Modification of substrate properties during the fabrication process,' Sensors (Switzerland) Sensors 19, no. 8: 1768.

9. Abdulhameed, A., Halin, and Hamidon, M. N., (2022) 'The role of the electrode geometry on the dielectrophoretic assembly of MWCNT bundles from aqueous solution,' J. Electrostat., vol. 116, p. 103694.

Fabrication and Characterization Methods of PVA/TiO_2 Fibers for potential application of water treatment

Cik Rohaida **Che Hak**

Materials Technology Group, Industrial Technology Division, Malaysian Nuclear Agency

*Corresponding author's phone: +603-8911 2000 ext. 1190
E-mail: rohaida@nm.gov.my / rohaida@gmail.com

ABSTRACT

Titanium dioxide (TiO_2) is an ideal photocatalyst because of its stability in terms of chemical and optical properties. The performance of TiO_2 as fiber incorporated in a membrane may find better than in bulk form especially in applications of water treatment. There are many methods for fabrication of TiO_2 in a composite membrane such as freeze-drying, thermal evaporation, physical and chemical vapour deposition. Unfortunately, these methods are not favor because they require multiple steps which may produce impurities. Electrospinning is a simple and versatile technique to produce composite membrane comprise of TiO_2. In this study, we propose fabrication of PVA/ TiO_2 composite membrane using electrospinning method for the potential in water treatment. We studied two parameters which is polymer loading and sonication time to investigate the quality of the electrospun fibers. Then we investigated the ability of this composite to show UV photodegradation. Morphology studies confirmed that the TiO_2 particles are incorporated well into the fibers. XRD phase analysis showed the incorporation of anatase into the composite and finally this composite showed the ability to degrade the methylene blue under UV.

Keywords— TiO_2, electrospinning, fiber, photodegradation, membrane

1.0 INTRODUCTION

TiO_2 becomes the most promising photocatalyst due to its advantages of being photocatalytically stable, reasonably inexpensive, and relatively easy to produce and use [1]. It is a human and environmentally friendly and can be used to treat polluted air and split the water to generate hydrogen [2]. Most previous studies on photocatalytic of TiO_2 use one-dimensional (1-D) coating on a surface. However, dimensionally becomes a crucial factor in determining properties of nanomaterial including surface area [3]. Recently, electrospinning (ES) is becoming a popular technique to produce 2-D composite materials. The advantageous of ES is, it can produce nanofibers with diameter ranging from 50 to 500 nm which the small sizes fibers improved the photocatalytic performance of the TiO_2. Furthermore, the use of electrospun TiO_2 fibers has become an interest in various applications because of the mechanical, biological, and kinetic properties that being easily manipulated by altering the matrix composition and processing parameters [4]. In common condition of fiber fabrication using ES, it is combined with sol-gel technique to synthesize the nanoparticles. In our study, we introduced a new method to produce TiO_2 fibers using ES without combination with sol-gel. We used TiO_2 powder that synthesized earlier via hydrothermal method followed by calcination to obtain anatase phase. Polyvinyl alcohol (PVA) was chosen as the matrix.

2.0 LITERATURE REVIEW

ES is a method to produce 2-D composite materials. The interest of this technique to fabricate ceramic nanofibers

has grown up exponentially since 2002 [5]. This technology uses electric field to convert polymer solution (matrix) or melt into a fibre form. The principles of electrospinning is a syringe loaded with a polymer solution is pumped at a constant flow rate. A specific voltage applied will induce an electric field between the needle tip and the collector. The solution will be charged and the charge will accumulate at the surface of the liquid. As the voltage increased, the electrostatic repulsion of the solution will be increased. The liquid is retained by surface tension. When the electrostatic repulsion is higher than the surface tension, a liquid meniscus with conical shape is formed at the tip of the needle. The electric field and surface tension of the solution interact with each other leading to stretching in the solution jet which allows fibers to be formed. The whipping motion of the jets leads to the evaporation of the solvent and solidifies the fiber [6]. Usually TiO_2 fibers were synthesized by combining ES and sog-gel technique. The usual precursor used for TiO_2 was titanium isopropoxide (TIP), and the matrix used was polyvinylpyrrolidone (PVP) due to its high molecular weight (130,000 g/mol). The solvent used to dissolve PVP was ethanol. The anatase phase of TiO_2 was obtained by calcination of the fibres. In general, the quality of the electrospun fibres depend on three processing parameters: ES experiment set up (voltage supply, flow rate, needle size, needle tip-to-collector distance), sol-gel parameters and selection of TiO_2 precursors. The viscosity of the TiO_2 solution depends on the molecular weight of the polymer and the concentration of the mixture (polymer, solvent and precursor). The polymer concentration will determine the fibre diameter [7], and the diameter increases with the increase of TiO_2 precursor solution [8]. Knowing the complicated of sol-gel technique, Li et al. in 2012 [8] has developed the ES technique without combining with sol-gel. The precursor used was tetrabutyltitanate (TBT) and the matrix was polyvinylpyrrolidone (PVP), and ethanol was the solvent. Mesoporous TiO_2 nanofibres with anatase were successfully produced after calcination at 500°C, and the best photodegradation rate of rhodamine B in aqueous was 99% under ultraviolet light .

3.0 MATERIALS

TiO_2 powder (synthesized earlier via hydrothermal technique), deionized water, PVA, surfactant and methylene blue dye.

4.0 EXPERIMENTAL

The fabrication of PVA/TiO_2 fibers using ES technique was reported before in 2021 [9]. In current study we optimized the fabrication techniques with two parameters; varying the amount of PVA added from 10 - 16 wt% and sonication time was altered from 1 - 4 hours. The ratio of PVA:TiO2 mixture was 4:1 and TiO2: SDS mixture was 10:1. The morphology of the electrospun fibers were characterized using field emission scanning electron microscope (GeminiSEM 500, Carl Zeiss) and the titanium (Ti) element was determined using energy dispersive X-ray (X-Max 80, Oxford Instrument). The anatase phase was determined using x-Ray Diffractometer (X'Pert Pro, Panalytical). The electrospun fibers were then removed from the aluminium foil and was immersed in methylene blue (MB) dye solution for photodegradation experiment using 400W UV light for 5 hours exposure time. The degradation was determined based on the absorbance value at interval of 1 hour obtained using a UV-Vis spectrometer (Lambda 35, Perkin Elmer).

5.0 RESULTS AND DISCUSSION

The TiO_2 powder used in this study was characterized has anatase phase and the particles size was less than 50 nm as reported earlier in 2017 [10]. The XRD pattern shown in Fig. 1 was used to

identify the difference between PVA pure and PVA/TiO2 fibers.

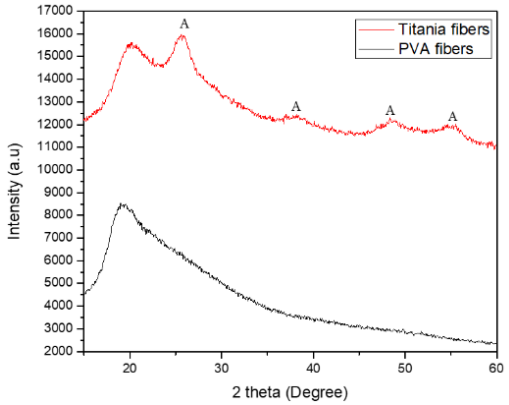

Fig. 1: XRD patterns for PVA fibers and titania fibers.

For TiO_2 fibers, the peaks are identified at 2θ = 25.8°, 38.15°, 48.53°, and 55.13° which identified as anatase phase (ICSD: 01-070-6826). The broad peak at 2θ = 25.8° is also observed on the pure PVA fibers, indicates that there is texturization occurred during electrospinning process [11]. Texturization is a mechanism of PVA changed its crystal structure to a preferred orientation to accommodate the presence of TiO_2 and surfactant during electrospinning process [12].

Fig. 2 shows the electron images of PVA/TiO_2 fibers. It is observed that as the wt% of PVA increases, the fiber diameter also increases, and the spherical shape beads was formed at low wt%. This is related to the viscosity of the polymer solution. This is supported by the previous studies which showed the number of beads decreases as the viscosity increased [13].

The fiber diameter in Fig. 2 was measured and found that the size increases with sonication time. The diameter increases from 222 nm when sonicated at 1 hour and increases to 795 nm when sonicated for 4 hours.

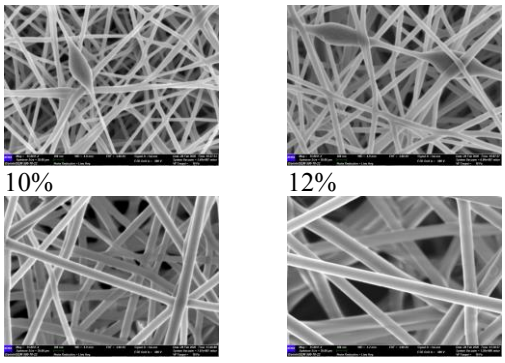

Fig. 2: Morphology of PVA nanofibers with different wt% of PVA.

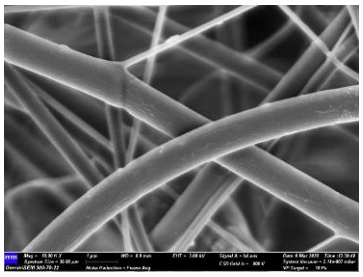

Fig. 3: PVA/TiO_2 with 4 hours sonication time

Sonication time is important to reduce the particle size of titania aggregates as smaller aggregates promote better incorporation of titania particles with PVA and thus formed fibers with larger diameter. Fig. 3 shows that fibers produced with 4 hours of sonication time have a rougher surface, attributed by the titania aggregates appearing on the surface of the fibers.

Fig. 4 shows the elemental analysis of the titania fibers. There are four elements presented on the PVA/TiO_2 fibers which are carbon (C), titanium (Ti), oxygen (O), and sulfur (S). The presence of Ti and O represents the TiO_2 distributed on the fiber surfaces, and sulphur is detected attributed from to the surfactant. The distribution of titania on the fiber is crucial as it can affect the efficiency of the catalyst when used in wastewater treatment application.

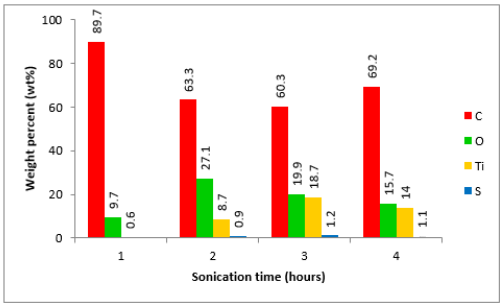

Fig. 4: Elemental analysis on titania fibers at different sonication times.

The photodegradation is calculated from the UV-Vis absorbance measurement. The photodegradation of MB is calculated from the UV-Vis absorbance measurement. The percentage of MB degraded in the solution for is 60.5% PVA pure fibers and 75.7% for PVA/TiO_2 fibers. The rate of photodegradation is calculated as 0.081/min and 0.127/min for PVA pure and PVA/TiO_2 fibers respectively.

6.0 CONCLUSION

The fabrication process of PVA/ TiO_2 fibers using electrospinning method was successfully developed. The amount of PVA loading affect the formation of beads, thus 16wt% of PVA gave the best fibers with least numbers of beads. The longest sonication time led to a better distribution of TiO_2 particles on the fiber, hence 4 hours was identified the appropriate time required to produce a homogenous PVA/TiO_2 fibers. This study proved that the fibers were able to degrade MB under UV exposure, and the presence of anatase TiO_2 loaded onto the fibers had increased the photodegradation rate.

ACKNOWLEDGEMENTS

I would like to thank Agensi Nuklear Malaysia for giving me permission to carry out this research, and for my student Nur Syafeika form Universiti Putra Malaysia for assisting me in doing all the experimental works.

REFERENCES

1. H. Albetran, Y. Dong, Low I.M. Journal of Asean Ceramic Societies 2015, (3):292.
2. D.A. Hanor, C.C. Sorrel. Journal of Material Science 2011, (46):855
3. S. Madhugiri S., Bun S., G.P. Smirniotis, J.P Ferraris. Microporous and mesoporous Materials, 2004, (6):77
4. Guarino, Vicenzo, Cruz, Maya, Iriczalili, Altobelli, Rosaria, Khartini Wan Abd Khodir, L. Ambrosio, Al.P. M.Alvara. Electrospun polycaprolactone nafobiers decorated by drug loaded chitosan nanoparticles reservoirs for antibacterial treatments. Nanotechnology 2017, 28
5. I.S. Chronakis, Journal of Materials Processing Technology 2005, (167) No 2-3:283.
6. B. Bera, Literature Review on Electrospinning Process (A Fascinating Fiber Fabrication Technique). *Imperial Journal of Interdisciplinary Research* 2016, (8) No. 2: 972
7. S.V. Fridrik, H. Jian, P. Michael Brenner, C. Gregory Rutledge. Physical Review Letter 2003, (90) No.14: 144502
8. Q. Li, D.J.G Satur, H. Kim, H.G. Kim. Material Letter 2012, (76): 169
9. C.R. Che Hak, S. Ridzuwan, S. S. Zainal Abidin, N.U. Saidin, S.A. Ahmad Fuzi. Effect of electron irradiation to the photocatalytic activity of the titanium oxide fibers. IOP Conference Series, Material Science Engineering 2020: 1106012016
10. C.R. Che Hak, S. S. Zainal Abidin, N.U. Saidin, S.A. Ahmad Fuzi, Y. Abdullah, M.Y.M. Sulaiman. The Effects of electron beam irradiation on structural and optical properties of TiO_2 particles. Materials Science Forum 2017, (88):297.
11. R.G Costa, C. Ribeiro, L.H Mattoso. Morphological and photocatalytic properties of PVA/TiO 2 nanocomposite fibers produced by electrospinning Journal of Nanoscience and Nanotechnology 2010 (8) No.10: 5144.
12. S. Ojha. Structure-property relationship of electrospun fibers. In M. Afshari (Ed.) Electrospun Nanofibers 2017 (1): 239.
13. N. Z. Al-Hazeem. Nanofibers and Electrospinning Method. In G. K. Kyzas, & A. C. Mitropoulos, *Novel Nanomaterials - Synthesis and Applications,* 1st ed., pp. 116-124. London: IntechOpen. 2018

$CaO-La_2O_3$ supported Co, Ni, and Pd catalysts for Methane Dry-Reforming Toward Syngas Production

Faris **Al-Doghachi** [*,a], Ali **Al-Najar** [a], and Yun Hin **Taufiq-Yap** [*,b,c]

[a] Department of Chemistry, Faculty of Science, University of Basra, 61004, Basra, Iraq.
[b] Catalysis Science and Technology Research Centre, Faculty of Science, UPM, 43400, Selangor, Malaysia.
[c] Chancellery Office, University Malaysia Sabah, 88400, Kota Kinabalu, Sabah, Malaysia.

*Corresponding authors:
Prof. Dr. Faris Al-Doghachi Tel: +60182987354 E-mail: faris.jassim@uobasrah.edu.iq
Prof. Dr. Yun Hin Taufiq-Yap Tel: +60389466809 E-mail: taufiq@upm.edu.my

ABSTRACT

The dry reforming of methane poses a critical challenge due to its endothermic nature and the propensity for coke formation. Developing catalysts and reaction conditions that promote efficient CH_4 and CO_2 conversion while mitigating carbon deposition is a central issue in achieving sustainable and economically viable carbon dioxide utilization. In this study, dry reforming of methane was conducted over $Ca_{1-x}La^{3+}{}_xO$ supported Co, Ni, and Pd catalysts, where x ranged from 0 to 0.15. The resulting catalysts underwent thorough characterization using XRD, XRF, FT-IR, TEM, and BET techniques. Prior to the reaction, the catalysts were reduced by H_2 at 700 °C. The dry reforming of methane reaction was carried out, the order of conversions of CO_2 and CH_4 at 900 °C of the reduced catalysts after being on the stream for 200 h was as follows: $Co,Ni,Pd/Ca_{0.85}La^{3+}{}_{0.15}O$> $Co,Ni,Pd/Ca_{0.93}La^{3+}{}_{0.07}O$> $Co,Ni,Pd/Ca_{0.97}La^{3+}{}_{0.03}O$> Co,Ni,Pd/CaO. with a 1:1 mole ratio of CH_4:CO_2 that displayed the best resistance to deactivation by carbon formation and formed high selectivity of H_2 and CO.

Keywords-Syngas; H_2 production; Dry-Reforming of methane(DRM), $CaO-La_2O_3$ catalyst.

1.0 INTRODUCTION

In Malaysia, biomass from palm oil has considerable potential for sustainable production of chemicals and fuels because of its renewability and copiousness. However, palm oil mill effluents (POME) originating from palm oil mills are a known wastewater pollutant. POME is mainly treated by anaerobic digestion in the palm-oil industry to reach the water quality standards for industrial effluent. However, one of the byproducts of this process is biogas primarily contains two greenhouse gases [i.e., 60–70% methane (CH_4), 30–40% CO_2 [1,2]. In the dry reforming of methane (DRM) method, CH_4 and CO_2 produce the highly costly syngas (containing CO and H_2) as feedstock. Accordingly, DRM is eliciting considerable interest because of its environmental benefits.

2.0 THEORY/LITERATURE REVIEW

Researchers have proposed the reforming of methane catalytically with CO_2. The method for the reforming of methane is the dry reforming method (DRM) (Eq. 1) [3].

$$CH_4 + CO_2 \rightarrow 2CO + 2H_2 \quad (1)$$

Nevertheless, there are certain limitations that have been found in the DRM reaction. One significant drawback arises from the occurrence of coke formation, which is the

result of the decomposition of methane gas (Eq. 2) and the Boudouard reaction (Eq. 3). In contrast, it has been discovered that the impact of nickel-based catalysts can be limited or reduced through the incorporation of promoters within the deactivation process. Lewis bases with high concentrations, such as CaO, have been enhanced through the chemisorption of CO_2. These modified bases exhibit the capability to mitigate coke deposition during their reaction with oxygen to produce CO. Similarly, the lanthanum elements, including ZrO_2 and La_2O_3, possess the capability to store and release oxygen, thereby exhibiting the same effects. Carbon is eliminated during the reaction between carbon deposits and lattice oxygen in these redox oxides [4].

$$CH_4 \rightarrow C + 2H_2 \quad (2)$$
$$2CO \rightarrow C + CO_2 \quad (3)$$

The use of nickel is highly recommended for the reforming process, as this active metal is readily available and inexpensive. However, the main disadvantage of nickel is that it causes the formation of carbon. Therefore, the aim of this work is to develop a catalyst that possessed high activity, selectivity, stability, and the ability to resist carbon accumulation on the catalyst during the dry reforming of methane. The $Co,Ni,Pd/Ca_{1-x}La^{3+}{}_xO$ catalysts were prepared by using the co-precipitation method that uses K_2CO_3 as a precipitant, followed by the impregnation of 1% of Pt, Pd, and Ni using $Pt(acac)_2$, $Pd(acac)_2$, and $Ni(acac)_2$, respectively. Subsequently, a study was carried out to investigate the impact of CO_2 and CH_4 concentrations, catalyst concentration, and conversion temperature on the catalytic performance of the prepared catalysts during the dry reforming process. Finally, the study examined the stability of the catalyst.

3.0 MATERIALS

$La(NO_3)_3.6H_2O$ (99.0%), $Ca(NO_3)_2.\ 6H_2O$ (99.0%) and K_2CO_3 (99.7%) were obtained from Merck Company. $Co(C_5H_7O_2)_2.H_2O$ (99.0%) and $Ni(C_5H_7O_2)_2.H_2O$ (99.0%) were provided by Acros Chemicals Company. At the same time, $Pd(C_5H_7O_2)_2.H_2O$ (99.5%) was obtained from the Aldrich company.

4.0 EXPERIMENTAL

This section outlines the preparation of stimulants catalyst for organizing $Ca_{1-x}La_xO$ stimulants (x = 0.00, 0.03, 0.07 and 0.15), and the method of co-precipitation (by using K_2CO_3) was used. It was found that La_2O_3 promoted CaO holder and was produced according to the method cited in the literature [5].

For the characterization of catalysts, various analytical techniques were employed. A diffractometer was adopted for these studies to get an idea about the crystal structure of a sample (Shimadzu model XRD6000). To get an estimate of the total surface area of the catalyst Brunauer-Emmett-Teller (BET) method using the Thermo Fisher Scientific S.P.A (model: Surface Analyzer). Transmission Electron Microscopy (TEM) (Hitachi H7100 TEM with an increasing voltage of 10 MV) was used to investigate the crystal system type and the catalyst's homogeneity.

For the catalytic evaluations, a fixed bed stainless steel micro-reactor (i.d. Ø = 6 mm, h = 34 cm) was used. A reactor was then equipped with a mass flow gas controller (SIERRA instrument) and an online gas chromatography (GC) (Agilent 6890N; G 1510N) provider with Varian capillary columns HPPLOT/Q and HP-MOLSIV. Prior to initiating the process, approximately 0.02 g of the catalyst was reduced by passing 5% H2/Ar at 700 °C for 3 hours. Finally, the conversions for CH_4 and CO_2, selectivity for H_2 and CO, and ratios for gas synthesis (H_2/CO) were calculated from Equations (4-8).

$$CH_4 \text{ Conversion } \% = \frac{(CH_4)\text{ in} - (CH_4)\text{ out}}{(CH_4)\text{ in}} \times 100 \quad (4)$$

$$CO_2 \text{ Conversion } \% = \frac{(CO_2)\text{ in} - (CO_2)\text{ out}}{(CO_2)\text{ in}} \times 100 \quad (5)$$

$$H_2 \text{ Selectivity } \% = \frac{(H_2)}{2[(CH_4)\text{ in} - (CH_4)\text{ out}]} \times 100 \quad (6)$$

$$CO \text{ Selectivity } \% = \frac{(CO)}{[CH_4\text{ (in} - \text{out)}] + [CO_2\text{ (in} - \text{out)}]} \times 100 \quad (7)$$

$$H_2/CO \text{ ratio} = \frac{(H_2 \text{ Selectivity } \%)}{(CO \text{ Selectivity } \%)} \quad (8)$$

5.0 RESULTS AND DISCUSSION

Fig. 1. depicts the X-ray diffraction (XRD) patterns of the catalysts with varying amounts of calcium and Lanthanum. The diffraction peaks were observed at specific angles, notably 2θ = 23.06, 29.3, 35.8, 39.3, 43.1, 47.1, 47.5, 48.5, 64.7, and 65.5°. This was due to the cubic form of calcium oxide (JCPDS file no.: 00-004-0636). Meanwhile, the diffraction peaks detected at 2θ = 15.6, 27.4, 27.9, 39.5, and 47.1° were due to the cubic form of Lanthanum oxide (JCPDS file no.: 00-006-0585). The peaks detected at 2θ = 18.1, 34.1, 50.8, and 54.2° were attributable to the cubic shape of the catalyst complex (La-Ca-O).

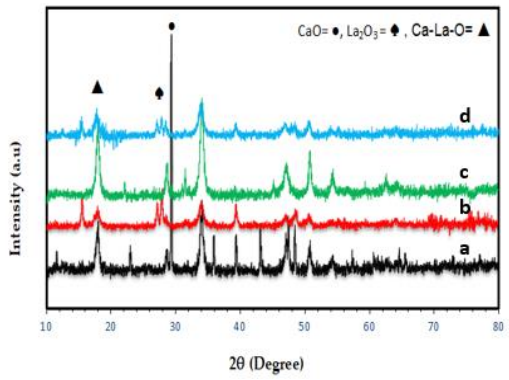

Fig. 1: XRD patterns of the catalysts: (a) Co,Ni,Pd/CaO, (b)Co,Ni,Pd/$Ca_{0.97}La^{3+}_{0.03}O$, (c) Co,Ni,Pd/$Ca_{0.93}La^{3+}_{0.07}O$, (d) Co,Ni,Pd/$Ca_{0.85}La^{3+}_{0.15}O$.

However, across all observed patterns, cobalt, nickel, and palladium did not exhibit any diffraction peaks. This absence can be attributed to the minuscule quantities of these metals present in the catalyst. This observation aligns with the findings documented by Grange [6].

Fig. 2. presents the FT-IR data corresponding to the catalysts. The spectra of the catalysts that were not reduced exhibited bands within the range of (3637 - 480 cm^{-1}), which were indicative of the presence of acetylacetonate ligands. The spectral peaks seen at wavenumbers 1654 and 1506 cm^{-1} in the FTIR analysis were attributed to the existence of carbonyl (C=O) and (C=C) bonds, respectively, in the acetylacetonate ligand of the primary catalyst (Co,Ni,Pd$(acac)_2$) complex [7,8].

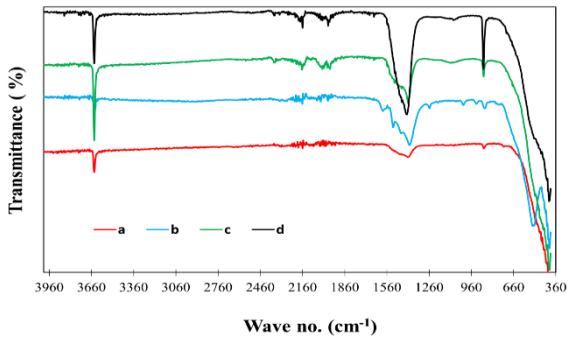

Fig. 2: FT-IR Spectra of Co,Ni,Pd/$Ca_{0.85}La^{3+}_{0.15}O$.

Fig. 3. shows the TEM image of the catalyst Co,Ni,Pd/$Ca_{0.85}La^{3+}_{0.15}O$ with cubic structures. The conditions used for these catalysts were calcination at 1150 °C with a uniform particle distribution without free La_2O_3.

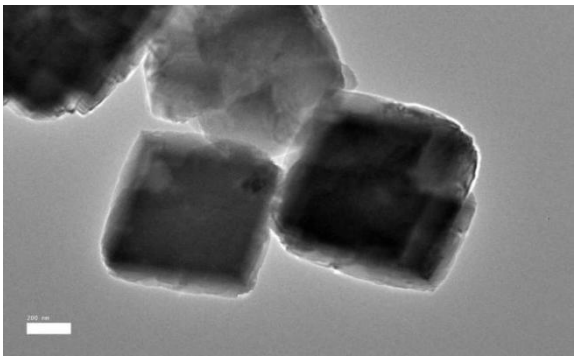

Fig. 3: TEM image of Co,Ni,Pd/$Ca_{0.85}La^{3+}_{0.15}O$.

The TEM results could confirm the formation of the CaO-La_2O_3 solid solutions [9], with cubic oxide particles on the Co, Ni, and Pd layers of the supported metal. The size of catalyst particles on the support Ca-La ranges from 45 to 85 nm [10].

Table 1. lists the surface area obtained from BET analysis of samples, pore volume, pore radius of the support, and CaO for different catalysts: Co,Ni,Pd/$Ca_{1-x}La_xO$. The surface area of catalysts Co,Ni,Pd/CaO with a cubic structure supported with TEM was 12.3 m^2/g, while the surface area for the support CaO was 12.1 m^2/g. The highest reading for the former was because of Co, Ni, and Pd loading on the specific surface area of the support CaO. In this instance, the surface areas of the catalysts Co,Ni,Pd/CaO were significantly lower than those of the conventional catalysts, which were measured to be 13.0, 12.4, and 16.3 m^2/g, respectively. This is because the layer of Co, Ni, and Pd particles partially covered the Calcium oxide pores. However, the BET surface area of the CaO promoted by La_2O_3 was almost identical to that of conventional bimetallic catalysts Co, Ni, and Pd [11].

Table 1: The main textural properties of fresh catalysts.

Sample name	Specific surface area (m^2/g)	Pore volume (cm^3/g)	Pore radius (Å)
CaO	12.1	0.22	9.9
Co,Ni,Pd/CaO	12.3	0.020	15.4
Co,Ni,Pd/$Ca_{0.97}La^{3+}_{0.03}O$	13.0	0.028	24.7
Co,Ni,Pd/$Ca_{0.93}La^{3+}_{0.07}O$	12.4	0.030	24.8
Co,Ni,Pd/$Ca_{0.85}La^{3+}_{0.15}O$	16.3	0.075	86.6

XRF was utilised for the elemental analysis of all catalyst components. Table 2 displays the percentage of Co, Ni, and Pd, which was slightly greater than one due to the incomplete precipitation of the Ca and La metal precursors by the co-precipitation method.

In order to examine the influence of catalyst concentration on conversion, Table 3 illustrates the effect of catalyst concentration during the conversion process.

Table 2: XRF analysis results.

Catalysts	XRF			
	Co%	Pd%	Ni%	CaO & La%
Co,Ni,Pd/CaO	0.2	0.2	0.21	99.39
Co,Ni,Pd/$Ca_{0.97}La^{3+}_{0.03}O$	0.05	0.05	0.23	99.67
Co,Ni,Pd/$Ca_{0.93}La^{3+}_{0.07}O$	1.23	1.23	2.89	94.65
Co,Ni,Pd/$Ca_{0.85}La^{3+}_{0.15}O$	0.41	0.42	0.25	98.92

The conversion of CH_4, CO_2, and the ratio of H_2/CO were in ascending order as in Co,Ni,Pd/CaO < Co,Ni,Pd/$Ca_{0.97}La^{3+}_{0.03}O$ < Co,Ni,Pd/$Ca_{0.93}La^{3+}_{0.07}O$ < Co,Ni,Pd/$Ca_{0.85}La^{3+}_{0.15}O$. The Co and Pd were combined with nickel on the support, CaO-La_2O_3. The experiments were conducted within specific parameters, including a temperature of 900 °C and a pressure of 1 atm. Additionally, the feed ratio of methane to carbon dioxide was maintained at a 1:1 ratio. In terms of methane conversion, the Co,Ni,Pd/$Ca_{0.85}La^{3+}_{0.15}O$ catalyst had the highest conversion (84%) while the Co,Ni,Pd/CaO catalyst had the lowest conversion (72%).

Another conclusion is that after 200 hours, most of the evaluated catalysts showed a minor deactivation. Overall, the conversion of CO_2 was more stable than methane, and the catalyst Co,Ni,Pd/$Ca_{0.85}La^{3+}_{0.15}O$ had the highest conversion of CO_2 (92%) while the catalyst Co,Ni, Pd/CaO had the lowest conversion (83%).

In all the tri-metallic CaO-La_2O_3 catalysts, as shown in Table 3, the product ratio of H_2/CO was more than 1. This demonstrated that in contrast to the other research [12], the Ni metal's CO_2 conversion process was less advantageous than the tri-metallic catalysts. The conversion rates of CH_4 and CO_2, as well as the ratio of H_2/CO, increased when lanthanum oxide concentration increased, as shown in Table 2. and the vast surface area demonstrated by the BET result was where the catalyst Co,Ni,Pd/$Ca_{0.85}La^{3+}_{0.15}O$ produced the

most outstanding results. This phenomenon indicates that the Reverse Water Gas Shift (RWGS) reaction can be significantly suppressed by adding La_2O_3 to CaO catalysts (eq. 9).

$$CO_2+H_2 \rightarrow CO+H_2O \quad (9)$$

The results of this study indicate the rate of carbon monoxide (CO) generation during the dry reforming of methane is influenced by the strong connection between the promoter, La_2O_3, and the support, CaO solid solution, according to Table 1, the largest surface area recorded was 16.3 m^2/g. Figure 4 illustrates the stability study conducted on the catalyst exhibiting the most superior catalytic performance. The results indicated that at a temperature of 900 °C, the conversion for both CH_4 and CO_2 was high.

Table 3:The catalytic results of the DRM reaction for the catalysts at 900 ˚C for the (1:1) ratio of CH_4: CO_2.

Catalyst	CH_4 Conversion %	CO_2 Conversion %	H_2/CO Conversion %
Co,Ni,Pd/CaO	72	83	0.69
Co,Ni,Pd/$Ca_{0.97}$ $La^{3+}_{0.03}O$	77	85	1.01
Co,Ni,Pd/$Ca_{0.93}$ $La^{3+}_{0.07}O$	83	88	1.09
Co,Ni,Pd/$Ca_{0.85}$ $La^{3+}_{0.15}O$	84	92	1.11

The activity and stability of the tri-metallic catalyst Co, Ni, and Pd were considerably superior to those of the mono-metallic catalyst Ni and the bi-metallic catalysts Pd-Ni and Co-Ni. This is consistent with the hypothesis that Co and Pd prevent the oxidation of Ni by increasing its electron density [13]. When there is a high concentration of La_2O_3, the conversion rate of CH_4 and CO_2 decreases, but when there is a decrease in the concentration of lanthanum oxide, it indicates that CO_2 is being converted through the active formation of substantial ionic oxides like $La_2O_3.CO_3$ attracts CO_2 to the top catalyst layer and then increases the conversion rate of CH_4. A reduction in the concentration of La_2O_3 may result from the high electron density of Co, Ni, and Pd [14]. The breakdown of $La_2O_3.CO_3$ species in DRM produced carbon dioxide and the different kinds of oxygen interacting with Co, Ni, and Pd-$La_2O_3.CO_3$ carbon deposits, reliving Co, Ni, and Pd activity sites. The La_2O_3-supported catalysts facilitated the adsorption of carbon dioxide. The lanthanum adsorption improves the dispersion stability of tiny mineral particles and its promotional effect on CO_2. In essence, lanthanum is an oxide that has been demonstrated to react vigorously during the supporting process of minerals. Both oxides and minerals have seen notable changes in their surface properties [15-17].

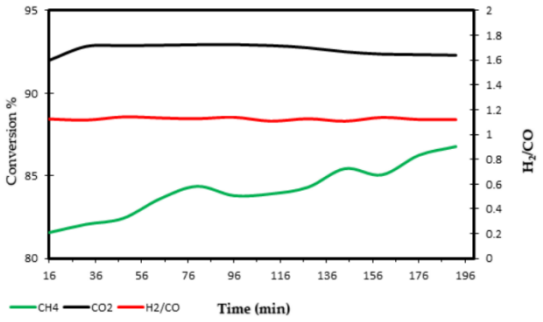

Fig. 4:Stability tests of Co,Ni,Pd/$Ca_{0.85}La^{3+}_{0.15}O$ catalysts at 900 ˚C for the 1:1 ratio of CH_4:CO_2 for 200 h. (GHSV = 15000 ml.$gcat^{-1}.h^{-1}$, 1 atm).

6.0 CONCLUSION

CO_2 reforming of methane was carried out using Co,Ni,Pd/$Ca_{1-x}La_xO$ catalysts to create synthesis gas. The physical and chemical characteristics of the catalysts were measured by XRD, FT-IR, BET, XRF, and TEM. The catalyst with the highest activity was Co,Ni,Pd/$Ca_{0.85}La^{3+}_{0.15}O$, which produced 92% and 84% supportable CO_2 and CH_4 conversion rates and a suitable H_2/CO ratio of 1.11 at 900 °C temperature and 1:1 ratio of CH_4:CO_2. The mixed catalyst results showed that the promoter's type and concentration significantly impact the catalytic characteristics.

REFERENCES

1. M. Chin, P. Poh, B. Tey, E. Chan, K. Chin. Biogas from palm oil mill effluent (POME): Opportunities and challenges from Malaysia's perspective Renew. Sust. Energy Rev. 2013, 26 717

2. P. Poh, M. Chong. Development of anaerobic digestion methods for palm oil mill effluent (POME) treatment Bioresour. Technol. 2009, 100, 1

3. A. Ashcroft, A. Cheetham, M. Green P. Vernon. Partial oxidation of methane to synthesis gas using carbon dioxide, Nature, 1991, 352, 225

4. Q. Chen, J. Zhang, Q. Jin , B. Pan, W. Kong, T. Zhao, Y. Sun. Effect of reflux digestion treatment on the catalytic performance of Ni-CaO-ZrO_2 nano composite catalysts for CO_2 reforming of CH_4 Catal. Today, 2013, 215, 251.

5. M. Tsyganok, T. Inaba, S. Tsunoda, K. Suzuki, T. Hayakawa. Dry reforming of methane over supported noble metals a novel approach to preparing catalysts, Catalysis Communications, 2003, 493-498.

6. P. Grange. Catalytic hydrodesulfuriza tion, Catalysis Reviews-Science and Engineering, 1980, 21, 135-181.

7. M. Nawfal, C. Gennequin, M. Labaki, B. Nsouli, A. Aboukaïs, E. AbiAad. Hydrogen production by methane steam reforming over Ru supported on Ni–Mg-Al mixed oxides prepared via hydrotalcite route, Int J Hydrog. Energy, 2015, 40, 1269-1277.

8. F. Al-Doghachi, U. Rashid, Z. Zainal, M. Saiman, Y. H. T. Yap. Influence of Ce2O3 and CeO2 promoters on Pd/MgO catalysts in the dry-reforming of methane. RSC Advances, 2015, 5(99), 81739-81752.

9. A. Djaidja, S. Libs, A. Kiennemann. Activity in dry reforming of methane on Ni-Mg/Al and Ni/MgO catalysts, Catalysis Today, 2006, 113, 194-200.

10. H. Kim, K. Kang, H. Kwak, Preparation of supported Ni catalysts with a core/shell structure and their catalytic tests of partial oxidation of methane, International journal of hydrogen energy, 2009, 34, 3351-3359.

11. K. Koo, H. Roh, Y. Seo, D. Seo, W. Yoon, S. Park. A highly effective and stable nanosized Ni/MgO-Al_2O_3 catalyst for gas to liquids (GTL) process, Int. J. Hydro. E, 2008, 33, 20-36.

12. Z. Bao, Y. Lu, J. Han, Y. Li, F. Yu. Highly Active and Stable Ni-based Bimodal Pore Catalyst for Dry Reforming of Methane. Applied Catalysis A: General, 2015, 491, 116-126.

13. A. Al-Najar, F. Al-Doghachi, A. Al-Riyahee, Y. H. Taufiq-Yap. Effect of La_2O_3 as a promoter on the Pt,Pd,Ni/MgO catalyst in dry reforming of methane reaction. Catalysts, 2020, 10(7), 750.

14. J. Kehres, J. Jakobsen, J. Andreasen, J. Wagner, H. Liu, A. Molenbroek, T. Vegge. Dynamical Properties of a Ru/$MgAl_2O_4$ Catalyst During Reduction and Dry Methane Reforming, J. Physical Chemistry, 2012, 116, 21407-21415.

15. F. Giordano, A. Trovarelli, C. Leitenburg, M. Giona. Model for the Temperature-Programmed Reduction of Low and High Surface Area Ceria, Catalysis, 2000, 193, 273-282.

16. I. Istadi, D. Anggoro, N. Amin, D. Ling. Catalyst deactivation simulation through carbon deposition in carbon dioxide reforming over Ni/CaO-Al_2O_3 catalyst, Bulletin of Chemical Reaction Engineering & Catalysis, 2011, 6,129-136.

17. F. Al-Doghachi, A. F. Jassim, Y. H. Taufiq-Yap. Enhancement of CO_2 Reforming of CH_4 Reaction Using Ni,Pd, Pt/$Mg_{1-x}Ce_x^{4+}O$ and Ni/$Mg_{1-x}Ce_x^{4+}O$ Catalysts. *Catalysts*, 2020, *10*(11), 1240.

Elucidating Interactions of Immobilized Lysozyme on Cellulose Spheres

Nurussuhaili **Nor Rosdi**, Nur Khairun Atiyah **Sagee Ahmad**, Sharifah Nabihah **Syed Jaafar***

Department of Applied Physics, Faculty of Science and Technology, 43000 Kajang, Universiti Kebangsaan Malaysia
Selangor, Malaysia

*Corresponding author's phone: +603-8921 4983
E-mail: nabihah@ukm.edu.my

ABSTRACT

Folding of lysozyme has been a major drawback and limits its application. Cellulose, which is a green molecule has the potential to be a carrier of lysozyme, because of its high functionality and chemical stability. The aim of this study is to elucidate the interaction of immobilized lysozyme on cellulose spheres (CS) by evaluating their physical and chemical interactions. Prior to dissolution, cellulose pulp undergoes acid treatment. Later, the cellulose solution was continued with the sol-gel emulsion technique and later impregnated with lysozyme for 12 hours. The ratio of cellulose solution and lysozyme used was 1:3, 1:5, and 1:7. After that, the formed and immobilized cellulose spherical (Lys-CS) was collected, washed, and dried. The zeta potential of lysozyme was found to be positively charged and the cellulose spheres were negatively charged. However, the Lys-CS samples were positively charged but the value was lower than Lysozyme. The Fourier transform infrared (FTIR) spectrum depicted, the interaction of CS and lysozyme occurred at 1650 and 1550 cm^{-1}. The findings proved the interaction of cellulose spheres and lysozyme had occurred.

Keywords—adsorption; cellulose; immobilized; lysozyme;

1.0 INTRODUCTION

Lysozyme is well known in various applications such as food, medicine, and veterinary because it has antimicrobial properties. But, the application of lysozyme is still limited due to its instability, low reusability [1], and short lifetime [2]. It also tends to cause aggregation caused by macromolecular crowding [3]. This can affect the quality and efficiency of lysozyme. Therefore, lysozyme has been largely immobilized on particles that act as carriers. Among them are zinc oxide (ZnO), silica [4], cellulose [5], and chitosan [6]. This enzyme immobilization technique can be divided into physical and chemical. The selection of appropriate techniques is important to increase the interaction between lysozyme and substrate particles to increase the stability of lysozyme.

Generally, cellulose nanoparticles offer a fascinating platform in biomedicine due to their unique properties such as high surface energy, surface-to-volume ratio, and high proportion of surface chemical groups that make them suitable as carriers. There are many researches that have focused on the use of cellulose nanomaterial derivatives with metal nanoparticle additions as antimicrobial agents. Mwafy et al. studied the antibacterial properties of cadmium oxide in TEMPO-oxidized cellulose nanofibers (TOCN) [7]. Other than that, carboxymethyl cellulose-based functional films that were prepared by incorporating curcumin and zinc oxide nanoparticles have also been reported to have antibacterial properties [8]. However, since nanometals can accumulate in many essential body organs, such as the spleen and liver, their

use is prohibitive. Nanometals that have accumulated in the atmosphere and the human body have significant harmful consequences [9].

2.0 MATERIALS

Cellulose (degree of polymerization, DP: 660) (α-cellulose>95%) was purchased from Georger Weil & Sons Ltd, Guildford, United Kingdom, lysozyme was provided by Sigma-Aldrich, containing ≥40,000 units/mg protein, sulfuric acid (H_2SO_4) (95%-98%), hydrochloric acid (HCl) (36%-38%), sodium hydroxide (NaOH), sorbitan monooleate (Span 80) (density: 0.992 g/cm^3) and paraffin oil were purchased from Sigma-Aldrich, United States, urea and acetone (99.9%) were purchased from Chemiz, United Kingdom.

3.0 EXPERIMENTAL

3.1 Samples Preparations

Cellulose was subjected to acid hydrolysis treatment using 40% H_2SO_4 for 1 hour at a temperature of 45°C. The treated cellulose was then washed using distilled water, before drying with a freeze dryer. 1.5g of the treated cellulose was added to the NaOH/Urea/water solution (7/12/81) and stirred at 9,000 rpm for 5 minutes and then, at 10,000 rpm for 20 minutes. The mixture was centrifuged at 10,000 rpm for 10 minutes to remove trapped air bubbles and to separate dissolved and undissolved cellulose solutions.

The cellulose solution was then filled into a plastic syringe (size 5 cc/ml with an inner diameter of 1.19 mm) and extruded at 2.0 ml/min into a beaker containing 1.5% Span 80 and paraffin oil. Then, the mixture was stirred for 3 hours using a mechanical stirrer at a temperature of 60°C for 15 minutes. After that, 100 ml of 10% HCl is mixed into the emulsion solution and two phases will be formed. The cellulose nanosphere solution on the lower phase was collected, filtered, and rinsed with acetone 3 times. To filter this cellulose nanosphere solution, a vacuum filter is used with filter paper that has a pore size of 0.22 μm.

A concentration of lysozyme (1 mg/ml) was prepared before the cellulose solution was added to the lysozyme solution at different ratios of cellulose solution to lysozyme (1:3, 1:5, and 1:7). The mixture was stirred for 15 minutes at 400 rpm and sonicated for 10 minutes at 40 kHz with 100W average ultrasonic power. After that, all this mixture will be impregnated at room temperature for 12 hours. Then, the resulting suspension solution was centrifuged at 14,000 rpm for 10 minutes. Two phases formed and only the bottom phase was used and named Lys-CS.

3.2 Samples Characterizations

Samples were measured using Fourier transform infrared spectroscopy GX/ Perkin Elmer with Attenuated Total Reflection (ATR) mode. FTIR was used to analyze the presence of functional groups and chemical structures in sample molecules by using standards of emission, reflectance, and ATR imaging. FTIR analysis was performed at a wavelength of 4000-800 cm^{-1}, a resolution of 4 cm $^{-1}$, and 32 scanning times.

The Zeta potential of the samples was determined by using Zeta Sizer Nano ZS (Malvern). The samples were diluted and analyzed at pH 7 with a temperature of 25°C using the light electrophoresis technique. Signals were collected at 12.8° and analyzed using Zetasizer Software. Then, the zeta potential value was calculated using the Smoluchowski equation.

Transmission electron microscopy (TEM) (JEM-2100, JEO, Tokyo, Japan) was used to observe the morphology of the samples. CS and Lys-CS were dropped onto perforated carbon foils supported on copper grids and allowed to dry at room temperature and then observed under TEM.

4.0 RESULTS AND DISCUSSION

Figure 1(a) shows the FTIR spectrum of lysozyme. The spectrum exhibits a broad peak around 3300 cm^{-1} due to N-H stretching from the free amino group in the amide A spectral region [10]. It also shows a significant peak in the spectral region of amide I and II which is 1640 and 1525 cm^{-1} indicating the occurrence of C=O, C-N stretching and N-H bending. Meanwhile, the FTIR spectrum of cellulose spheres (Figure 1(b)) consists of a broad peak at 3300 cm^{-1} (free OH), 2922 cm^{-1} (CH stretching), a weak peak of 1650 cm^{-1} (C=O), 1367 cm^{-1} (CH) and 1100 cm^{-1} (C-O).

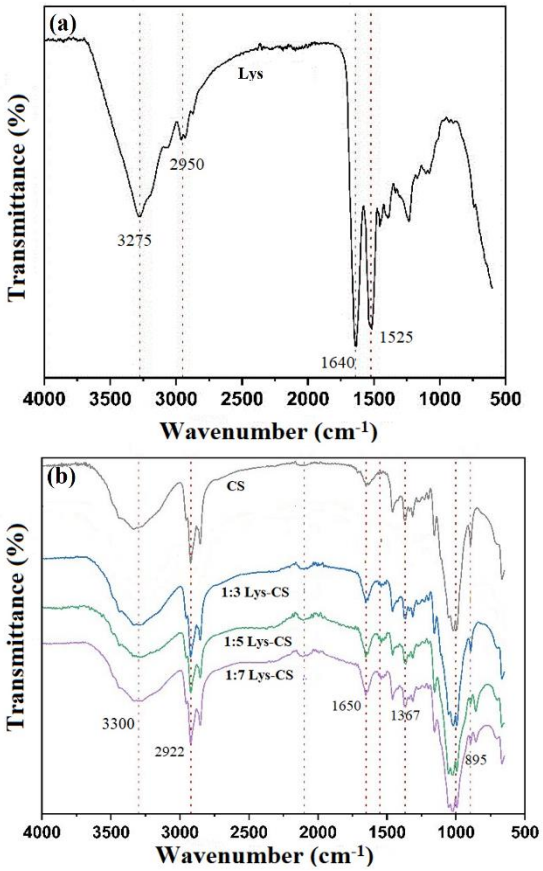

Fig. 1: FTIR spectrum of (a) lysozyme and (b) CS and Lys-CS

As for Lys-CS samples, the broader peak at 3300 cm^{-1} was due to the overlapping of OH and NH. A peak at 1650 and 1525 cm^{-1} was more pronounced than CS. This has proved the interaction of CS and lysozyme occurred.

The Zeta analysis found the zeta values for lysozyme was +17.00 and CS was -54.00. Lysozyme was positively charged because of the NH group meanwhile the CS was negatively charged because of the OH group. The zeta values for Lys-CS samples depicted also negative charges but the values were lower than CS. The results found the higher ratio of lysozyme, contributed to the lower the zeta values. This happened because of the interaction of lysozyme with the CS [11].

TABLE I: Zeta values of the samples

Samples	Zeta values (mV)
Lysozyme	+17.00
Cellulose spheres (CS)	-54.00
1:3 Lys-CS	-52.67
1:5 Lys-CS	-36.97
1:7 Lys-CS	-25.77

Figure 2(a) and (b) show the TEM images of CS and Lys-CS, respectively. The Lys-CS was found to be bigger than the CS itself. This is because the impregnation of lysozyme against CS has resulted in the existence of an additional layer which refers to a layer of lysozyme that has been impregnated on the entire surface of CS. Consequently, this additional layer disturbs the spherical shape of the CS and leads to the occurrence of an imperfect spherical structure.

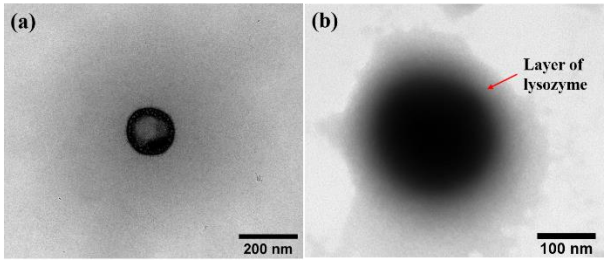

Fig. 2: TEM of (a) CS and (b) Lys-CS

5.0 CONCLUSION

The formation of perfect CS and the immobilization of lysozyme on CS were successfully done. The immobilization of

lysozyme on cellulose spheres was proved with the FTIR analysis and zeta potential. The TEM images confirmed the layer formation on CS has occurred.

ACKNOWLEDGEMENTS

The authors would like to thank the research university grant through Geran Universiti Penyelidikan (GUP-2021-041) and the Bioresources and Biorefinery Laboratory for the financial and facilities support, respectively.

REFERENCES

1. H. Zhang, Q. Luan, Y. Li, J. Wang, Y. Bao, H. Tang, F. Huang. Fabrication of highly porous, functional cellulose-based microspheres for potential enzyme carriers. International Journal of Biological Macromolecules 2022, (199): 61.
2. B. Shareghi, S. Farhadian, N. Zamani, M. Salavati N., S. Gholamrezaei. Stability and enzyme activity of lysozyme in the presence of Fe_3O_4 nanoparticles. Monatshefte Für Chemie - Chemical Monthly 2016,(147):465.
3. S. Venkataramani, J. Truntzer, D. Coleman. Thermal stability of high concentration lysozyme across varying pH: A Fourier transform infrared study. Journal of Pharmacy & Bioallied Sciences, 2013,(5):148.
4. M. Du, J. Liu, F. Wang, L. Bi, C. Ma, M. Song, G. Jiang. A sustained-release microcarrier effectively prolongs and enhances the antibacterial activity of lysozyme. Journal of Environmental Sciences 2023,(129):128.
5. P. Ferraboschi, S. Ciceri, P. Grisenti. Applications of lysozyme, an innate immune defense factor, as an alternative antibiotic. Antibiotics 2021,(10):1534.
6. A. Cerón A, L. Nascife, S. Norte, S. Costa A, J. H. Oliveira do Nascimento, F. D. P. Morisso, J. Baruque-Ramos, R. C. Oliveira, S. M. Costa. Synthesis of chitosan-lysozyme microspheres, physicochemical characterization, enzymatic and antimicrobial activity. International Journal of Biological Macromolecules 2021,(185):572.
7. E. A., Mwafy, M. S. Hasanin, A. M. Mostafa. Cadmium oxide/TEMPO-oxidized cellulose nanocomposites produced by pulsed laser ablation in liquid environment: Synthesis, characterization, and antimicrobial activity. Optics and Laser Technology 2019,(120): 105744.
8. S. Roy, J. W. Rhim. Carboxymethyl cellulose-based antioxidant and antimicrobial active packaging film incorporated with curcumin and zinc oxide. International Journal of Biological Macromolecules 2020,(148):666.
9. M. S. Hasanin, G. O. Moustafa. New potential green, bioactive and antimicrobial nanocomposites based on cellulose and amino acid. International Journal of Biological Macromolecules 2020,(144): 441.
10. N. A. Lopes, C. M. Barreto Pinilla, A. Brandelli. Antimicrobial activity of lysozyme-nisin co-encapsulated in liposomes coated with polysaccharides. Food Hydrocolloids 2019,(93): 1.
11. N. Henry, J. Clouet, C. Le Visage, P. Weiss, E., Gautron, D. Renard, T. Cordonnier, F. Boury, B. Humbert, H. Terrisse, J. Guicheux. Silica nanofibers as a new drug delivery system: a study of the protein-silica interactions. Journal of Materials Chemistry B 2017,(5): 2908.

Structural and Functional Group Characterization of Graphene Oxide Functionalized Melamine Sponge

Balarabe **El-yaqub**[1,2], Mohd Haniff **Wahid**[1*], Abdul Halim **Abdullah**[1], Wan Azlina **Wan Ab Karim Ghani**[3]

[1]Department of Chemistry, Faculty of Science, Universiti Putra Malaysia
[2] Department of Chemistry, Faculty of Science, Nigerian Defence Academy, Kaduna State, Nigeria
[3] Department of Chemical and Environmental Engineering, Faculty of Engineering, Universiti Putra Malaysia

*Corresponding author's phone: +603-9769 6784
E-mail: mw_haniff@upm.edu.my

ABSTRACT

Graphene oxide was successfully grafted onto melamine sponge using a simple dip coating technique. The material was characterized using XRD, FTIR and FESEM to confirm its structural, functional group and morphological characteristics. The presence of broad peaks in the XRD diffractogram confirms the amorphous nature of the composite. Meanwhile, FTIR spectra exhibited absorption peak attributed to C-N stretch of aliphatic amine which ascertain the interaction of melamine with graphene oxide. FESEM images also confirmed the presence of GO on the melamine sponge.

Keywords-melamine; GO nanosheets; adsorbents; porous carbon; melamine sponge

1.0 INTRODUCTION

There is a major global concern to overcome high concentrations of CO_2 gas in the atmosphere [1]. Graphene-based porous materials have received considerable interest as potential adsorbent [2]. To date, various materials have been used to functionalize graphene oxide to improve its properties. One of these materials is melamine. Melamine has been used to introduce nitrogen to GO structures which led to improvements in performance of GO in several applications such as catalysis [3], energy storage devices [4] and as an adsorbent [5]. These composite materials are made up of GO sheets and nanometer-sized nitrogen-linked metal and/or metal oxide particles.

2.0 THEORY/LITERATURE REVIEW

Several studies have explored the possibilities of adding nitrogen group to graphene nano-frameworks to increase its adsorption capacities. Melamine possesses certain characteristics such as abundance of nitrogen which can interact with CO_2 through acid-base reactions. Furthermore, melamine can be externally cross-linked with metal ions to produce robust structures and increase the reactivity of the composite material by providing cation sites for interaction with CO_2. Addition of pores to graphene-based structures has also been found to be effective to increase the adsorption performance of graphene materials [6].

Nitrogen doped porous carbon materials derived from graphene oxide/melamine resin composites for CO_2 adsorption at 298.15 K and 500 kPa showed good CO_2 adsorption ability of 5.21mmolg^{-1} as shown by batch adsorption test and exhibited quick adsorption kinetics, strong CO_2/N_2 selectivity and good recyclability[7]. Zhang et al. [8] worked on a simple post-treatment nitrogen doping approach to create nitrogen doped porous carbons obtained from sustainable biomass for effective CO_2 capture. Soybean meal was used as the precursor, KOH as the activator and melamine as the source of nitrogen. It was discovered that the physical and chemical characteristics of porous biochar were dramatically altered by the post-treatment nitrogen addition. It was discovered that the higher the nitrogen introduced, the higher the catalytic activity of the catalyst and thus the higher the CO_2 adsorption rate.

The present study's objective is to characterize a unique nitrogen doped carbon porous material to ascertain its structural and functional groups characteristics for potential application in different fields such as adsorbents, catalysis and energy storage.

3.0 MATERIALS

3.1 PREPARATION OF GO

Modified Hummers technique was used to produce graphene oxide [9]. In a nutshell, 3.0 g of pure graphite was dispersed in 400 mL of concentrated 9:1 H_2SO_4/H_3PO_4 acid. Then, 18.0g of $KMnO_4$ was slowly added while the mixture was agitated for 72 hours. After carefully adding 35 mL of H_2O_2, the mixture was agitated for 24 hours at room temperature in order to completely eliminate the excess $KMnO_4$ and stop the oxidation process. The graphene oxide was then centrifuged and rinsed with 1M HCl and extra DI water before neutrality was reached.

3.2 PREPARATION OF Melamine-GO (Me/GO)

The synthesis process of Me/GO composite is as illustrated in Fig. 1. Firstly, ethanol, epichlohydrin and NaOH (1M) were added together in the ratio of 13:1:0.1 to produce a linker solution. Then, the melamine sponge was dipped in the linker for two minutes followed by squeezing to remove excess solution. The sponge was then allowed to air dry for about 30 minutes in fumehood. The resulting MS was then dipped in 2 mg/ml solution of GO for two minutes and transferred to an oven for drying at 100 ^{0}C for 24 hours. The as-prepared dried composite was denoted Me/GO composite.

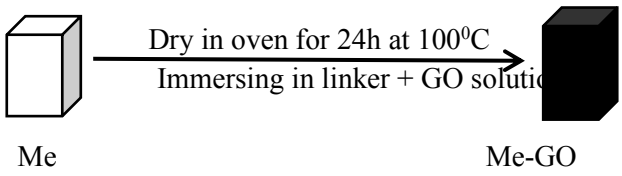

Fig. 1: Schematic illustration of the synthesis process of nitrogen-rich porous carbon materials derived from Me/GO composite.

3.3 PREPARATION OF Melamine-rGO (Me/rGO)

The reduction of the 3D melamine/graphene oxide was done by utilizing a standard National Microwave oven, model NN- C2000P, Japan, through microwave irradiation approach at 150^{0}C for 30 min with 15 min intervals [10].

3.4 CHARACTERIZATION OF THE MELAMINE-GO and rGO COMPOSITES

On a Bruker D8 ADVANCE (Bruker Co., Germany) X-ray diffractometer operating at 40 kV and 40 mA and using Ni-filtered Cu Kα radiation (l = 0.15λnm), wide-angle X-ray diffraction (XRD) patterns were captured. The 2θ range of 5-90^0 was used to capture the diffraction patterns. The Bragg's equation was then used to compute the interlayer spacing. FT-IR was employed to verify the GO grafting on the melamine surface. All samples were diluted in KBr (1% wt/wt.) and pressed into pellets, which were analysed in a Nicolet iS50 FT-IR spectrometer from Thermo Scientific. Spectra were collected in the mid-infrared region (4000–400 cm^{-1}) with 256 scans and a 4 cm^{-1} resolution. The surface morphological characteristics were studied by field emission scanning electron microscope with FESEM- JEOL JSM 6360LA, Japan.

4.0 RESULTS AND DISCUSSION

4.1 FTIR Analysis

The structural analysis of GO, Me, Me-GO and Me-rGO was performed by FTIR and shown in Fig 2. The GO sample showed two strong peaks at 3374cm^{-1} (O-H stretch vibration) and 1638cm^{-1} (C=C stretching vibration). Other peaks at lower wavenumbers show that
GO contain carbonyl and hydroxyl groups (619-423cm^{1}). Pure melamine sponge shows peaks at 3373cm^{-1} (N-H stretching vibrations of primary and secondary amide), 1686cm^{-1} (N-H bending), 1547cm^{-1} (C=N stretching vibration), 1478cm^{-1} (C-H bending), 1343cm^{-1} (C-H bending), 1157cm^{-1} (C-N stretching vibration), 1007cm^{-1} (C-O stretching vibration) and 811cm^{-1} (triazine ring vibration) which are typical characteristics of melamine [5]. The presence of crosslinking agents during the polymerization of melamine can be attributed to the peaks in the melamine sponge that are composed of carbon bonds. Most of the peaks found in melamine and GO are found in melamine-GO and melamine-rGO except 2363cm^{-1} (which can be attributed to O-H). This is due to the reduction process of melamine-GO to melamine-rGO by microwave heating. There are disappearance of some peaks that are found in GO and Me which are found in Me-GO and Me-rGO indicating that there was an interaction. Some peaks of GO and melamine were also expanded and weakened in the region of 970-1350cm^{-1} which should be linked to the creation of hydrogen bonds between GO and melamine[11]. In Me-GO spectrum, the intensity of peaks corresponding to C=C and triazine ring became weaker, indicating the formation of π-π stacking interaction between melamine and GO[8].

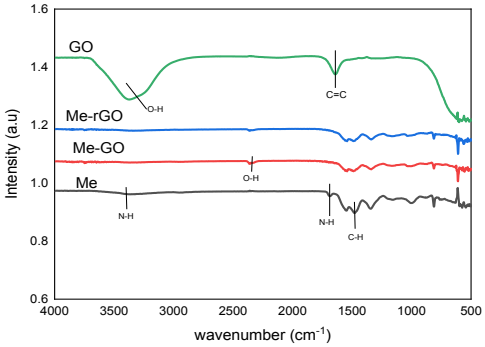

Fig 2: FTIR graph for GO, Me, Me-GO and Me-rGO

4.2 XRD results

The XRD pattern of melamine showed a broad peak at 23.4^0 which can be attributed to the orientation of melamine chains [5]. A weak peak centered at 14.5^0 for Me-GO and 14.9^0 for Me-rGO can also be attributed to the diffraction of the loaded GO sheets from (001) plane as compared to the peaks of GO and melamine. Also, the shifts in position of some peaks and the appearance of new peaks in Me-GO and Me-rGO also confirm the incorporation of GO on melamine sponge as shown in Fig 3.

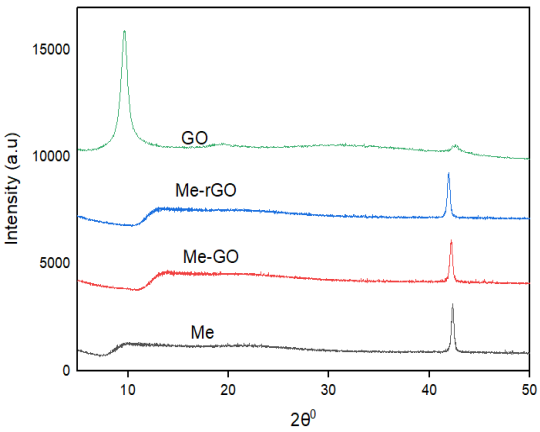

Fig 3: XRD graph for GO, Me, Me-GO and Me-rGO

4.3 FESEM results

FESEM images were also captured to examine the surface morphology of the samples (Fig. 4a-c). As observed by FESEM, melamine without any GO exhibited a 3D rich pore structure and when GO was impregnated into the sponge, the 3D structure was maintained and shows the presence of GO in between the pores of the melamine.

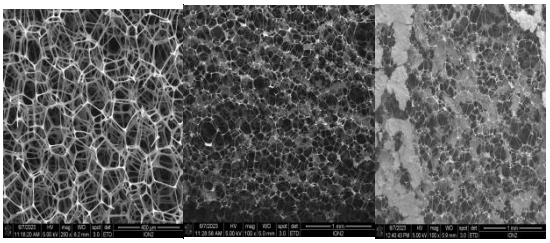

Fig 4a-c: FESEM images of Me, Me/GO and Me/rGO

5.0 CONCLUSION

This study reported the successful grafting of graphene oxide on the melamine sponge. Characterization using FTIR spectroscopy confirms the interaction between GO and melamine sponge in $1339cm^{-1}$ and $1162cm^{-1}$ attributing to C-N stretch from both melamine and GO while FESEM images also conforms the impregnation of the GO on melamine sponge. Meanwhile, the weak peaks at 14.5^0 and 14.9^0 for Me-GO and Me-rGO respectively, also conform to the loading of GO on the melamine sponge.

REFERENCES

[1] F. Raganati, F. Miccio, and P. Ammendola, "Adsorption of carbon dioxide for post-combustion capture: A review," *Energy & Fuels*, vol. 35, no. 16, pp. 12845–12868, 2021.

[2] Q. Kong *et al.*, "Strategies to improve the adsorption properties of graphene-based adsorbent towards heavy metal ions and their compound pollutants: A review," *J. Hazard. Mater.*, vol. 415, p. 125690, 2021.

[3] A. M. Bakry, F. S. Awad, J. A. Bobb, A. A. Ibrahim, and M. S. El-Shall, "Melamine-based functionalized graphene oxide and zirconium phosphate for high performance removal of mercury and lead ions from water," *RSC Adv.*, vol. 10, no. 62, pp. 37883–37897, 2020, doi: 10.1039/d0ra07546a.

[4] F. B. Ajdari *et al.*, "Melamine-functionalized graphene oxide: Synthesis, characterization and considering as pseudocapacitor electrode material with intermixed POAP polymer," *Appl. Surf. Sci.*, vol. 459, pp. 874–883, 2018, doi: 10.1016/j.apsusc.2018.07.215.

[5] X. Zhu, G. Zhou, G. He, L. Ma, B. Xu, and F. Sun, "Directly loading graphene oxide into

melamine sponge for fast and high-efficiency adsorption of methylene blue," *Surfaces and Interfaces*, vol. 36, no. October 2022, p. 102575, 2023, doi: 10.1016/j.surfin.2022.102575.

[6] N. Politakos, I. Barbarin, T. Cordero-Lanzac, A. Gonzalez, R. Zangi, and R. Tomovska, "Reduced graphene oxide/polymer monolithic materials for selective CO2 capture," *Polymers (Basel).*, vol. 12, no. 4, pp. 1–14, 2020, doi: 10.3390/POLYM12040936.

[7] L. Ouyang, J. Xiao, H. Jiang, and S. Yuan, "Nitrogen-doped porous carbon materials derived from graphene oxide/melamine resin composites for co2 adsorption," *Molecules*, vol. 26, no. 17, 2021, doi: 10.3390/molecules26175293.

[8] X. Zhang, Y. Xu, G. Zhang, C. Wu, J. Liu, and Y. Lv, "Nitrogen-doped porous carbons derived from sustainable biomass via a facile post-treatment nitrogen doping strategy: Efficient CO2 capture and DRM," *Int. J. Hydrogen Energy*, vol. 47, no. 58, pp. 24388–24397, 2022, doi: 10.1016/j.ijhydene.2022.05.222.

[9] D. C. Marcano *et al.*, " سنتز اکسید گرافن بهبود یافته است," *ACS Nano*, vol. 4, no. 8, pp. 4806–4814, 2010, [Online]. Available: https://pubs.acs.org/doi/abs/10.1021/nn1006368

[10] N. A. Pohan, M. H. Wahid, Z. Zainal, and N. A. Ibrahim, "Pickering-emulsionlated synthesis of 3D hollow graphene as an efficient oil absorbent," *RSC Adv.*, vol. 11, no. 7, pp. 3963–3971, 2021, doi: 10.1039/d0ra09265g.

[11] R. Yin, P. Sun, L. Cheng, T. Liu, B. Zhou, and X. Dong, "A Three-Dimensional Melamine Sponge Modified with MnOx Mixed Graphitic Carbon Nitride for Photothermal Catalysis of Formaldehyde," *Molecules*, vol. 27, no. 16, 2022, doi: 10.3390/molecules27165216.

Effect of Annealing Environment on Structural and Optical Properties of Solution-Grown NiO Nanoflowers

Norfarariyanti **Parimon**[1*], Mohamad Hafiz **Mamat**[2,3], Mohd Firdaus **Malek**[3,4]

[1] Nano Engineering and Materials Research Group, Faculty of Engineering, Universiti Malaysia Sabah, 88400 Kota Kinabalu, Sabah, Malaysia
[2] NANO-ElecTronic Centre (NET), School of Electrical Engineering, College of Engineering, Universiti Teknologi MARA, 40450 Shah Alam, Selangor, Malaysia
[3] NANO-SciTech Lab (NST), Centre for Functional Materials and Nanotechnology, Institute of Science (IOS), Universiti Teknologi MARA, 40450 Shah Alam, Selangor, Malaysia
[4] Faculty of Applied Sciences, Universiti Teknologi MARA, 40450 Shah Alam, Selangor, Malaysia

*Corresponding author's phone: +6013-9319711
E-mail: fara2012@ums.edu.my

ABSTRACT

Nickel oxide (NiO) nanoflowers with improved crystallinity were grown on the NiO seed-coated glass substrates by the immersion growth process. Argon (Ar) gas and ambient atmosphere were used during the heat treatment process of the samples. The properties of NiO nanoflowers annealed at 500 °C in an Ar and ambient atmosphere surrounding were analyzed using X-ray diffraction (XRD), field emission scanning electron microscopy, and ultraviolet-visible spectroscopy. The XRD patterns of the highly porous NiO nanoflowers showed they were in a cubic NiO-type polycrystalline structure. The crystallinity improved with Ar-annealed compared to the ambient atmosphere-annealed. The crystallite sizes estimated from the most prominent peak of XRD were 21.4 nm and 17.5 nm for the samples annealed in the ambient and Ar environments, respectively. The dislocation density is also higher for the sample annealed in Ar. The optical properties demonstrated that the average transmittance in the visible region (400 - 800 nm) was approximately 32 % and 37 % for the NiO samples annealed in the ambient and Ar environments, respectively. Further, the absorbance spectra showed a higher absorption edge when the sample was annealed in the Ar atmosphere, which is 410 nm compared to 360 nm when annealed in the ambient environment.

1.0 INTRODUCTION

The binary semiconductor compounds, especially metal oxide semiconductors, are made up of n-type and p-type, whose film deposition can be made by various techniques. Most of the metal oxides commonly engaged are ZnO, TiO_2, SnO_2, CuO, and NiO, which can be used in many application branches. Among the p-type metal oxide materials, NiO is one of the favorable candidates that has been extensively studied. NiO has been reported to have a wide bandgap (E_g) between 3.6 to 4.0 eV [1, 2] and has a particular specialty that can be used in different potential device applications such as sensors [3, 4] as well as electrochromic devices [5] and organic light-emitting diodes (OLED) [6].

During the deposition or growth process of the film, deficiencies in terms of oxidation and impurities might occur [7]. According to Yang et al. [1], the influence of the oxidation state of the cation under different ambient conditions may vary the physical properties of the transition metal oxides. Besides, the presence of impurities typically leads to a decrease in the melting point of certain bulk substances. One of the

ways to change the properties of the metal oxide semiconductors is to diversify the annealing process applied in the different environments, in which the process normally takes place after the growth process. In other words, the post-annealing treatment is the common parameter that can influence the nature of the material and further enhance its crystallinity [8, 9]. For instance, by providing argon (Ar) as isolated ambient gas, the contaminants could be removed, and crystal defects coming from external ambient can be eliminated. As such, the conductivity and transparency of the film could be improved, and the resistive properties could also be lowered, thus making a certain device application more stable and efficient [7].

Many existing studies have been intensively reported on the different annealing temperatures and various fabrication techniques of NiO [10]. Nonetheless, not many have researched the annealing temperature in different environments to see the effect on the physical properties of NiO. Hence, this work presents the properties of NiO nanoflowers that grew using the solution immersion method and annealed at 500 °C under ambient and Ar environments. Then, the influence of annealing in these environments on the structural and optical properties of the samples was observed and investigated.

2.0 EXPERIMENTAL

2.1 Synthesis of NiO Nanoflowers

Before NiO nanoflower grew, the NiO seed layer (SL) was deposited on the glass substrate using the sol-gel spin coating technique. The SL solution containing chemicals of nickel acetate, diethanolamine, and ethylene glycol monoethyl ether was stirred for 2 hours before five layers spin coating process was conducted. Then, the SL was dried at 150 °C and annealed at 400 °C. The next step was the growth of NiO nanoflowers by the immersion method at 95 °C for 2 hours, where the nickel nitrate hexahydrate, hexamethylenetetramine, and deionized water were used for the solution preparation. The solution underwent the sonication and stirring processes. Further, the available NiO nanoflowers were pre-baked at 150 °C and annealed at 500 °C for 1 hour in the ambient and Ar atmospheres, respectively. The annealing in the ambient atmosphere was done inside the furnace (Protherm), while the annealing in the Ar environment was done in the chemical vapour deposition (CVD), STF 40-1100. To ensure the absence of oxygen in CVD, the Ar flowed into the furnace at the gas flow rate of 100, with the samples placed inside before starting the annealing procedure.

2.2 Characterization of NiO Nanoflowers

The surface morphological studies of the samples were conducted using a field emission scanning electron microscope (FESEM), Zeiss Supra 40VP. The polycrystalline structures of NiO nanoflowers were analyzed using X-ray diffraction (XRD) patterns, PANalytical X'Pert PRO. Meanwhile, the ultraviolet-visible (UV-vis) spectrophotometer, Jasco/V-670 EX examined the optical properties.

3.0 RESULTS AND DISCUSSION

The XRD measurement was conducted to investigate the crystalline quality of the NiO nanoflowers that were deposited on the NiO SL and annealed under different environments. As shown in Fig. 1, the XRD patterns indicate that both NiO nanoflower samples display polycrystalline structures, which can be indexed to the cubic type of β-NiO (JCPDS NO.47-1049). Both samples show three prominent diffraction peaks at 2θ values of approximately 36.6°, 42.8°, and 62.3°, which were indexed to (111), (200), and (220) crystal planes, respectively. Meanwhile, two infirm diffraction peaks at

75.0° and 79.1° were indexed to (311) and (222), respectively. Among the two diffraction patterns exhibited, the three highest diffraction intensities at (111), (200), and (220) crystal planes were detected in the sample annealed in an Ar environment. It shows that the sample had a higher crystallization and led to the successful growth of NiO at 500 ºC-annealed under the Ar environment compared to the ambient atmosphere.

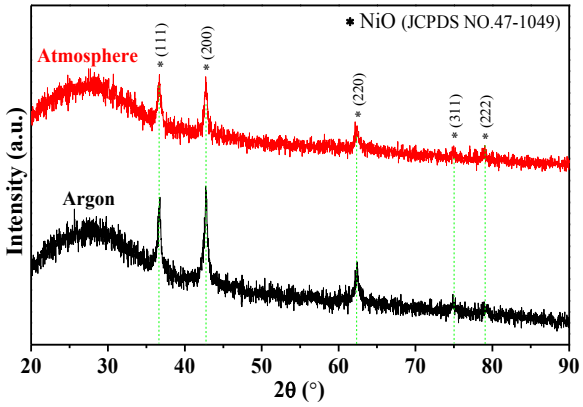

Fig. 1: The XRD patterns of NiO nanoflowers annealed at 500 °C in the ambient atmosphere and Ar gas

As supported by Park et al. [11], using Ar as the ambient gas during the heat treatment improves the diffraction peak intensity. According to Wang et al., the enhanced crystallinity and high defect state can cause good photovoltaic properties in terms of the efficiency of solar cells [12]. It shows that certain performance of applications can be optimized when the crystallinity improves. The crystallite size (D) could be assessed using the Scherrer formula (1) from the measured FWHM (β) values (in rad) of the high intensity at (200) crystal plane. λ is the X-ray wavelength with 1.54 Å, and θ is the diffraction angle.

$$D = \frac{0.94\lambda}{\beta cos\theta} \qquad (1)$$

From the summarized data in Table I, the calculated D in the Ar-annealed sample is much smaller (17.5 nm) than the D of the sample annealed in the ambient atmosphere (21.4 nm). This result is in line with the work by Goktas [13], where the grain size annealed in Ar is smaller than that annealed in the air due to less agglomeration. The smaller D will cause a higher surface area and thus enlarge the recombination rate at the grain interfaces or boundaries [12]. For certain applications, such as sensors, the higher surface area will lead to increase catalytic sites available for adsorption and desorption reactions [14]. Next, the dislocation density (δ), as tabulated in Table I, can be calculated through equation (2) which is for determining the number of defects in the crystal of NiO nanoflower.

$$\delta = \frac{1}{D^2} \qquad (2)$$

It shows that the higher number of defects belongs to the sample that annealed in Ar with 3.26×10^{15} Lines/m^2 due to the higher number of δ compared to the sample annealed in the atmosphere. This confirms that the structural defects could be seen vice versa from their crystallite sizes and are highly dependent on the annealing environment. From the larger number of defects, the force of attraction between delocalized electrons and nuclei will be increased the stability of the NiO nanoflower that is annealed in Ar [15].

TABLE I: The FWHM, crystallite size, and dislocation density of NiO nanoflowers at different annealing environments

Sample Annealed	(hkl)	2θ (°)	FWHM, β (°)	Crystallite size, D (nm)	Dislocation density, δ ×10^{15} (Lines/m^2)
Atmosphere	**(200)**	42.734	0.4167	21.4	2.18
Argon (Ar)	**(200)**	42.736	0.5094	17.5	3.26

As shown in Fig. 2, the surface morphological images of NiO nanoflowers at different annealing environments revealed that their shape and pattern were similar to flower-like nanostructures with very thin and porous petals. The unique structure with a bouquet of rounded flowers can be observed as the same as the nanocarnation-like NiO reported by Parimon et al. [16]. In addition, the average diameter of an individual flower-like NiO is also the same for both annealing environments of approximately 1.5 µm. Fig. 2 (a) and (b) show the NiO nanoflower images for the ambient atmosphere- and Ar-annealed samples, respectively. These images revealed that more prominent petals could be seen in the sample annealed in the Ar.

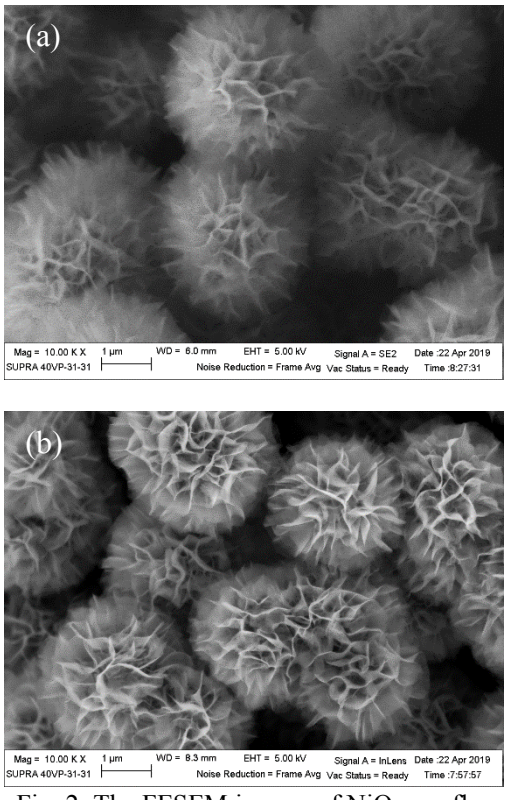

Fig. 2: The FESEM images of NiO nanoflowers annealed at 500 °C in the (a) ambient atmosphere and (b) Ar gas

Fig. 3 (a) and (b) demonstrate the optical transmittance and absorbance of the NiO nanoflowers at different annealing environments, respectively. The transmittance plot shows that the NiO nanoflowers exhibit transparency in the visible region with a slightly higher value when annealed in the Ar gas than annealed in the ambient atmosphere. The average transmittance percentage value in the visible region (VR) ~ (400 – 800 nm) was estimated to be at 32 % and 37 % for the ambient and Ar environments, respectively. It can be seen both optical transmissions are less than 50 %. The lowest transmittance percentage of the ambient environment may be due to the greater nanoflower thickness than annealed in an Ar environment [4]. It shows the changes in optical properties could be related to the variation in thickness after annealing in different environments.

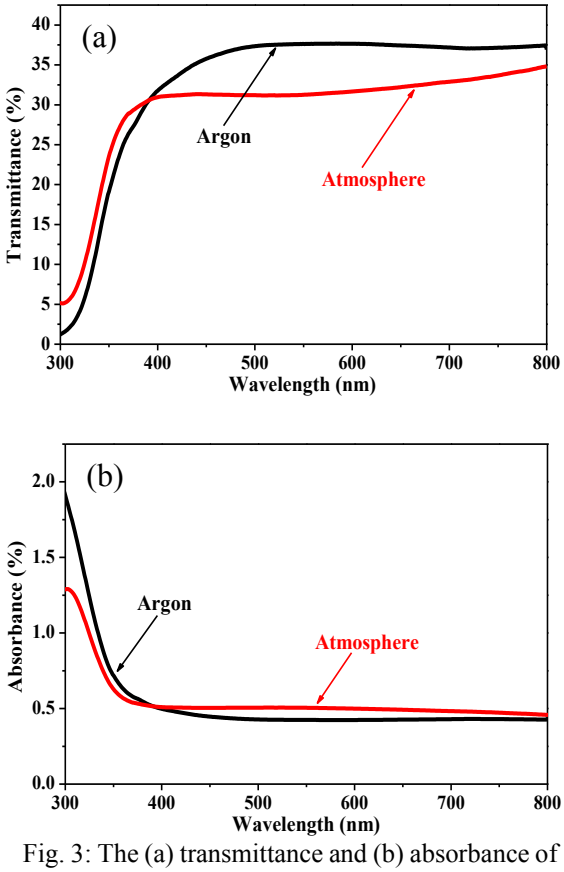

Fig. 3: The (a) transmittance and (b) absorbance of NiO nanoflowers annealed at different annealing environments

The absorbance spectra in Fig. 3 (b) revealed that NiO nanoflowers exhibit slightly different optical absorption values. The absorption in the VR can be related to some local energy levels caused by intrinsic

defects [17]. According to Cergel et al., the increase in absorption value depends on the oxygen vacancies on the nanostructure surfaces due to the annealing environment [18]. In addition, the spectra show the UV absorption edges at a wavelength below 410 nm for the Ar-annealed sample, while the absorption edge is below 360 nm for the ambient atmosphere-annealed sample. The optical absorption at the absorption edge correlated with the transition from the valence band to the conduction band [17]. From the results, it can be postulated that the optical properties can be changed by using different gases in the annealing process. For instance, the optical bandgap of the sample annealed in the Ar environment can be considerably smaller than the optical bandgap annealed in the ambient atmosphere.

4.0 CONCLUSION

The effects of annealing environments on the structural and optical properties of NiO nanoflowers prepared via a solution-grown immersion method were studied. The annealing temperature was performed at 500 °C for 1 hour under the ambient atmosphere and isolated Ar gas. The surface morphologies show that the nanoflower shape of NiO annealed in Ar is more prominent than the ambient atmosphere. The XRD patterns and optical properties for the sample annealed in the Ar environment exhibit improved crystallinity and higher transparency. The smaller crystallite size was produced in the Ar atmosphere as well as generated a higher density of defects. The absorption edge in the sample annealed in the Ar environment is at a longer wavelength than in the ambient environment. In conclusion, the crystallinity and properties of NiO could be improved with Ar environment annealing, thus promising performance optimization in particular applications such as sensors.

ACKNOWLEDGEMENTS

This research was funded by the internal grant of UMS (SBK0511-2022). Thanks to the NET Lab at the School of Electrical Engineering, UiTM, for providing the laboratory facilities to run this experiment.

REFERENCES

1. S. Yang, J. Kim, Y. Choi, H. Kim, D. Lee, J.-S. Bae, and S. Park. Annealing environment dependent electrical and chemical state correlation of Li-doped NiO. Journal of Alloys and Compounds, 2020. (815). pp. 152343.
2. M. H. Mamat, N. Parimon, A. S. Ismail, I. B. Shameem Banu, S. Sathik Basha, G. V. Vijayaraghavan, M. K. Yaakob, A. B. Suriani, M. K. Ahmad, and M. Rusop. Structural, optical, and electrical evolution of sol–gel-immersion grown nickel oxide nanosheet array films on aluminium doping. Journal of Materials Science: Materials in Electronics, 2019. (30):10. pp. 9916-9930.
3. M. Yin and Z. Zhu. Mesoporous NiO as an ultra-highly sensitive and selective gas sensor for sensing of trace ammonia at room temperature. Journal of Alloys and Compounds, 2019. (789). pp. 941-947.
4. N. Parimon, M. H. Mamat, A. S. Ismail, I. B. Shameem Banu, M. K. Ahmad, A. B. Suriani, and M. Rusop. Influence of annealing temperature on the sensitivity of nickel oxide nanosheet films in humidity sensing applications. Indonesian Journal of Electrical Engineering and Computer Science, 2020. (18):1. pp. 284-292.
5. K. Zrikem, G. Song, A. A. Aghzzaf, M. Amjoud, D. Mezzane, and A. Rougier. UV treatment for enhanced electrochromic properties of spin coated NiO thin films. Superlattices and Microstructures, 2019. (127). pp. 35-42.
6. Malvin, C.-T. Tsai, C.-T. Wang, Y.-Y. Chen, P.-C. Kao, and S.-Y. Chu. Improved hole-injection and external quantum efficiency of organic light-emitting diodes using an ultra-thin K-doped NiO buffer layer. Journal of Alloys and Compounds, 2019. (797). pp. 159-165.
7. O. Urper, O. Karacasu, H. Cimenoglu, and N. Baydogan. Annealing ambient effect on electrical properties of ZnO:Al/p-Si heterojunctions. Superlattices and Microstructures, 2019. (125). pp. 81-87.
8. F. Z. Souici, B. Benhaoua, H. Saidi, M. F. Boujmil, A. Rahal, A. Benhaoua, and M. S. Aida. Influence of Rapid Thermal Annealing in Argon Atmosphere on Properties of Electrodeposited Cuinse 2 Thin Films: Structural and Optical Study. Chalcogenide Letters, 2019. (16):2. pp. 79-87.
9. M. Sobri, A. Shuhaimi, K. M. Hakim, V. Ganesh, M. H. Mamat, M. Mazwan, S. Najwa, N. Ameera, Y. Yusnizam, and M. Rusop. Effect

of annealing on structural, optical, and electrical properties of nickel (Ni)/indium tin oxide (ITO) nanostructures prepared by RF magnetron sputtering. Superlattices and Microstructures, 2014. (70):0. pp. 82-90.
10. N. Parimon, M. H. Mamat, I. B. S. Banu, N. Vasimalai, M. K. Ahmad, A. B. Suriani, A. Mohamed, and M. Rusop. Annealing temperature dependency of structural, optical and electrical characteristics of manganese-doped nickel oxide nanosheet array films for humidity sensing applications. Nanomaterials and Nanotechnology, 2021. (11). pp. 1-13.
11. D. J. Park, J. Y. Lee, T. E. Park, Y. Y. Kim, and H. K. Cho. Improved microstructural properties of a ZnO thin film using a buffer layer in-situ annealed in argon ambient. Thin Solid Films, 2007. (515):17. pp. 6721-6725.
12. B. Wang, K. Y. Wong, S. Yang, and T. Chen. Crystallinity and defect state engineering in organo-lead halide perovskite for high-efficiency solar cells. Journal of Materials Chemistry A, 2016. (4):10. pp. 3806-3812.
13. A. Goktas. High-quality solution-based Co and Cu co-doped ZnO nanocrystalline thin films: Comparison of the effects of air and argon annealing environments. Journal of Alloys and Compounds, 2018. (735). pp. 2038-2045.
14. M. H. Mamat, A. S. Ismail, N. Parimon, N. Vasimalai, M. H. Abdullah, M. F. Malek, M. K. Yaakob, M. K. Ahmad, N. Nafarizal, A. B. Suriani, A. Mohamad, M. D. Birowosuto, and M. Rusop. Heterojunction of SnO2 nanosheet/arrayed ZnO nanorods for humidity sensing. Materials Chemistry and Physics, 2022. (288). pp. 126436.
15. M. Gomathi, P. V. Rajkumar, and A. Prakasam. Study of dislocation density (defects such as Ag vacancies and interstitials) of silver nanoparticles, green-synthesized using Barleria cristata leaf extract and the impact of defects on the antibacterial activity. Results in Physics, 2018. (10). pp. 858-864.
16. N. Parimon, M. H. Mamat, M. A. R. Abdullah, A. S. Ismail, W. R. W. Ahmad, I. B. S. Banu, and M. Rusop. Nanocarnation-like Nickel Oxide Thin Film: Structural and Optical Properties. International Journal of Engineering & Technology, 2018. (7):4.18. pp. 103-106.
17. S. Benramache, Y. Aoun, R. Gacema, and H.-d. Mourghadea. Synthesis and Annealing Temperature Effect on Structural, Optical and Electrical Properties of NiO Thin Films Deposited by Sol–Gel Technique. Nanosistemi, Nanomateriali, Nanotehnologii, 2021. (19):1. pp. 147-158.
18. M. Söyleyici Cergel and F. Atay. The role of the annealing process in different gas environments on the degradation of the methylene blue organic pollutant by brookite-TiO_2 photocatalyst. Ionics, 2019. (25):8. pp. 3823-3836.

Effects of Dispersed Solvents on Carbon Black Distributions

Nur Alia Irdina **Amini**, Sharifah Nabihah Syed **Jaafar***, Mohd Firdaus Mohd **Raih**

Department of Applied Physic, Faculty of Science and Technology, Universiti Kebangsaan Malaysia, 43600 Bangi, Selangor, Malaysia.

*Corresponding author's phone: +6012 6138236
E-mail: nabihah@ukm.edu.my

ABSTRACT

Carbon black (CB) particle is an emerging material produced by incomplete combustion and possesses unique characteristics such as high surface area. As a result, it has high surface activation energy and tends to agglomerate. This study aims to reduce the agglomeration of CB by undergoing solvent dispersion. The treatment of CB was prepared in ethyl acetate (EA) and dichloromethane (DCM) at 30 ℃. The CB dispersion stability was confirmed via phase separation, Fourier transform infrared (FT-IR) spectroscopy, Raman spectroscopy, and transmission electron microscopy (TEM). The colloidal suspension of CB in DCM (CB-DCM) shows better phase stability than the colloidal suspension of CB in EA (CB-EA). This is because the chemical changes have happened in the CB-EA, as confirmed by the FTIR and Raman spectroscopies. The TEM results confirmed show that the CB-DCM and CB-EA were aggregated. This study proves that the agglomeration of CB particles could be reduced through solvent dispersion.

Keywords— agglomeration; aggregation; colloidal; oxidation

1.0 INTRODUCTION

The In recent years, carbon nanomaterials with different formations and structures have been synthesized and characterized, for example, graphenes, fullerenes, carbon nanotubes (CNTs), carbon nanofibers, and carbon black (CB) particles and other related forms [1], [2]. CB is composed of spherical aggregation particles that can be produced from incomplete combustion of liquid, gaseous, and other materials [3]. CB is a quasi-graphitic form of nearly pure elemental carbon that can be obtained significantly from ambient air pollution through many processes, for example, pyrolysis of waste tire [4], [5], [6]. CB has become an attractive and promising nanomaterial for many applications such as batteries, catalysts, electrodes, drug carriers, and others [7], [8]. This is because of its high surface area, high packing density, good biocompatibility, and excellent electrical conductivity [9], [1]. Although CB is an excellent material, it has drawbacks, such as agglomeration due to high surface activation energy. The dispersion of CB has been a persistent challenge [10], [11], [12] because of its strong Van der Waals forces, which lead to aggregation (50-500 nm) and agglomeration (>1 μm).

Previously, the research has explored the various treatments of carbon black to enhance their dispersion, surface modification, and functionalization for desired properties of CB [13], [14], [15]. The most common treatments are acid and surface modification. Some surface modification techniques have been combined with top-down processes, such as milling and grinding, to eliminate the strong aggregates between primary particles and some by grafting [16]. Surface modification of CB by grafting with ethylenediamine (EDA) and acrylamide improves shear stability to 25% in brine medium [17]. The acid

treatment by oxidation of CB using oxidizing solutions can create hydrophilic groups such as hydroxyl, carbonyl, and carboxyl groups can improve CB dispersion in an aqueous medium Aqel et al. [18], Cardona-Uribe et al. [19], Sobkowicz et al. [14]. The negatively charged surface of CB was accomplished by acid treatment, in which oxygen functionalities were introduced during the oxidation process [20].

Even though acid treatment and surface modification can enhance carbon black dispersion, they are complex, expensive, require extreme conditions, usage of corrosive agents, and require a longer processing time to reduce aggregation of CB [20]. Moreover, excessive acid treatment can reduce the negatively charged surface CB due to the removal of oxygen in the functional group. This led to a decrease in the negative surface charge of CB and limited dispersing on an aqueous medium [16]. Herein we demonstrate a cost-effective and simple process to reduce the agglomeration of CB by solvent treatment. Little previous studies sought to compare the effect of solvents such as dichloromethane (DCM) and EA as solvents to reduce agglomeration, respectively.

2.0 MATERIALS

CB powder (purity 75%) with 200 mesh was obtained from Eco Power Synergy Sdn. Bhd. DCM and EA were purchased from R&M Chemicals (Malaysia).

3.0 EXPERIMENTAL

3.1 Treatment of Carbon Black

In different vials, 5 g of CB was typically dispersed in 50 ml of EA and DCM. They were sonicated for 30 minutes at 30 °C. Later, the dispersion was continued stirring with a magnetic stirrer for 30 minutes.

3.2 Characterizations

The stability of CB dispersion was conducted by looking at their phase separation. ATR-FT-IR (Perkin Elmer), with a wavenumber of 4000 – 600 cm^{-1} and 4 cm^{-1} resolution, was utilized to determine the chemical groups of CB and treated CB. Raman spectra were recorded with a Raman spectrometer (Thermo Scientific) at 3000-100 cm^{-1} with a 633 nm laser. The transmission electron microscope (TEM) (Talos L120C, Thermo Scientific) was used to observe the morphology changes of the CB particles.

4.0 RESULTS AND DISCUSSION

The stability of the CB dispersion after solvent dispersion is shown in Fig. 1. By observing the dispersion of CB in EA (CB-EA) and CB in DCM (CB-DCM). CB-DCM shows no phase separation from day 1 to day 7 (Fig. 1 (a). However, the CB-EA shows a rapid change in the state of stability dispersion where phase separations occur (Fig. 1 (b)). The top part is the dissolved CB meanwhile, the bottom part is the colloidal suspension of CB. EA has been considered a polar solvent, thus able to dissolve the CB. Polarity is related to the strong polar interaction and strong hydrogen bonding within the molecules [21]. During the dissolution in EA, the CB particles have been reduced and surrounded by the solvent molecules, thus confirming the reduction of van der Waals between CB particles [22]. Based on observation, the color of dissolved CB in EA was brownish. It indicates that the dissolved CB has undergone an oxidation reaction [23] during the dissolution.

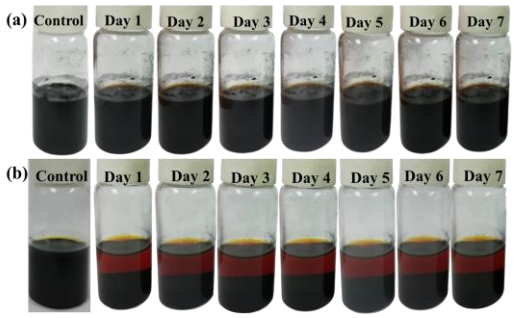

Fig. 1: Analysis of dispersion stability of CB in (a) DCM and (b) EA at day 1-7. The control sample in (a) CB-DCM and (b) CB-EA at day 0.

The FTIR analysis was carried out to confirm the functional group changes in the samples (Fig. 2). The spectrum of CB and CB-DCM depict almost similar patterns, except for the additional peaks at 2918 cm^{-1} and 2850 cm^{-1} at CB-DCM. Apparently, these two peaks exist in CB-DCM and CB-EA, which are assigned to the stretching of CH_2 and CH_3, respectively. On the other hand, CB-EA exhibits a new band at 1737 cm^{-1}, which was attributed to the stretching of the carboxylic group (-C=O). In addition, the sharp peaks at 1230 cm^{-1} and 1035 cm^{-1} were attributed to C-O. The addition of -C=O and C-O has proved the oxidation of colloidal CB in EA [24].

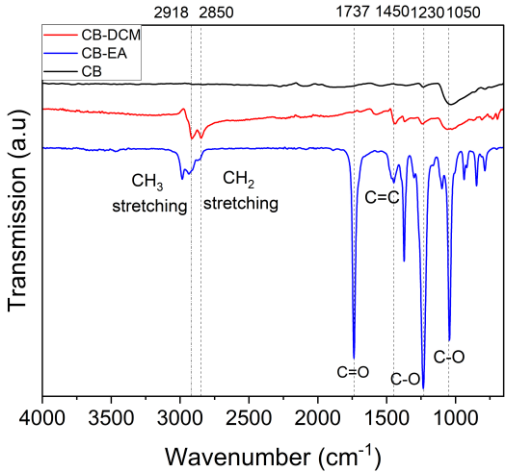

Fig. 2: FTIR analysis of CB, CB-DCM, and CB-EA after phase separation.

Fig. 3 shows the Raman spectra of the CB dispersed in different solvents after phase separation. The Raman spectrum of CB was characterized by two strong peaks, the G band, and the D band. The D-band was identified at 1349 cm^{-1}, 1350 cm^{-1}, and 1350 cm^{-1} for CB, CB-DCM, and CB-EA, respectively. These peaks were related to the disorder of carbon structure due to the vibration of carbon atoms with dangling bonds [25]. The G-band, which was positioned at 1577 cm^{-1}, 1598 cm^{-1}, and 1600 cm^{-1} for CB, CB-DCM, and CB-EA, were due to stretching of C=C bond in graphitic materials shows that CB in sp^2 hybridized structure [26]. The C=C in CB samples was pronounced in Raman spectra because Raman is active for polarized samples, like C=C. The ID/IG was found to be 0.76 for CB and 0.87 for CB-DCM and CB-EA. The higher ID/IG means a lower degree of graphitization has occurred [27], [28].

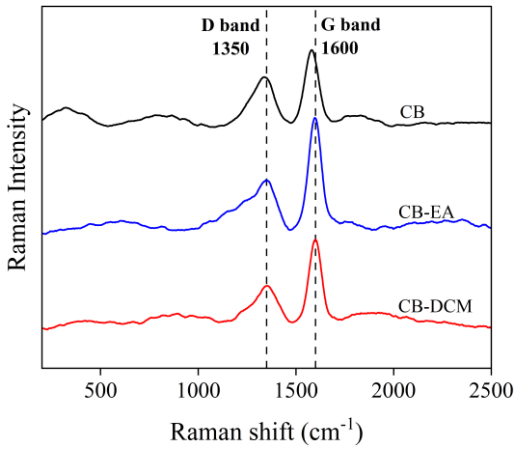

Fig. 3: Raman spectra of (i) CB, (ii) CB-EA, and (iii) CB-DCM

All samples were viewed under TEM to confirm that the agglomeration of CB has been reduced during the dispersibility. Based on Fig 4(a), the CB image was characterized by a spherical (agglomeration) clump at an average size of 971 nm. Baklanova et al. [29] and Hanada et al. [16] reported that the CB structure consists of many spherical particles that fuse together and tend to agglomerate. On the other hand, Fig. 4(b) and 4(c) demonstrate that the colloidal suspension of CB in DCM and CB in EA were in aggregation because the size has been reduced to 554.50 nm and 322.94

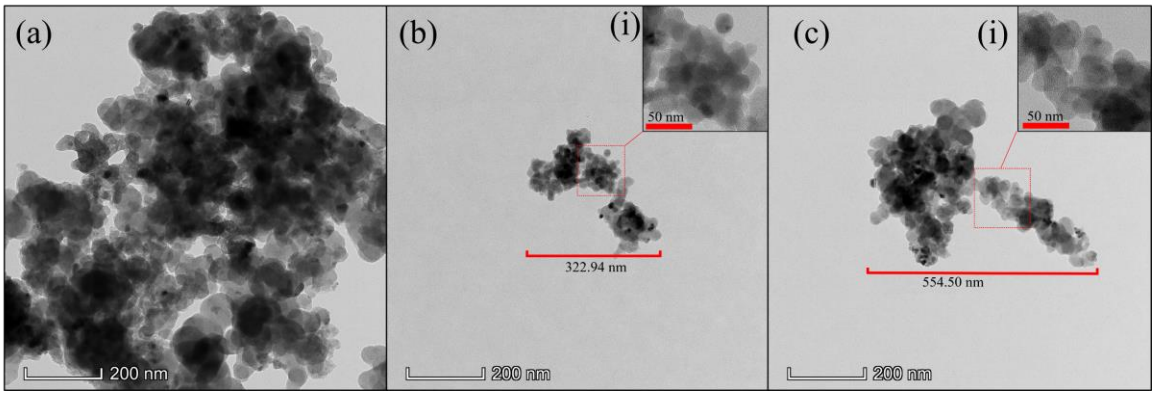

Fig. 4: TEM image of a) CB, b) CB-DCM, and c) CB-EA after solvent treatment.

nm, respectively. After solvent dispersion, CB-DCM and CB-EA encounter steric hindrance due to stabilizing dispersion in the solvent. Lee et al. [23] stated that the dispersant molecules must be strongly affixed to the surface of the CB particles, and sufficient steric hindrance between the CB particles needs to exist for dispersion stability to occur.

5.0 CONCLUSION

This study demonstrated the effect of DCM and EA on CB dispersibility. As for the treatment in DCM, the colloidal of CB was more stable and did not undergo chemical changes. Meanwhile, the colloidal of CB in EA was relatively unstable due to oxidation. However, both colloidal suspension CB in DCM and EA show a reduction in the ID/IG and succeed form to aggregation.

ACKNOWLEDGEMENTS

This work was funded by an internal research grant from Universiti Kebangsaan Malaysia through GUP-2021-041. The authors also would like to thank the Chemical Laboratory, Department of Applied Physics, Universiti Kebangsaan Malaysia (UKM) for support and facilities.

REFERENCES

1. Heidari, A., & Younesi, H. (2020). Synthesis, characterization, and life cycle assessment of carbon nanospheres from waste tires pyrolysis over ferrocene catalyst. Journal of Environmental Chemical Engineering, 8(2), 103669.
2. Maiti, D., Tong, X., Mou, X., & Yang, K. (2019). Carbon-Based Nanomaterials for Biomedical Applications: A Recent Study. Frontiers in Pharmacology, 9.
3. Khodabakhshi, S., Fulvio, P. F., & Andreoli, E. (2020). Carbon Black reborn: Structure and chemistry for renewable energy harnessing. Carbon, 162, 604–649.
4. Figarol, A., Pourchez, J., Boudard, D., Forest, V., Akono, C., Tulliani, J. M., Lecompte, J. P., Cottier, M., Bernache-Assollant, D., & Grosseau, P. (2015). In vitro toxicity of carbon nanotubes, nano-graphite and carbon black, similar impacts of acid functionalization. Toxicology in Vitro, 30(1), 476–485.
5. Gómez-Hernández, R., Panecatl-Bernal, Y., & Méndez-Rojas, M. Á. (2019). High Yield and Simple one-step Production of Carbon Black Nanoparticles from Waste Tires. Heliyon, 5(7).
6. Long, C. M., Nascarella, M. A., & Valberg, P. A. (2013). Carbon black vs. black carbon and other airborne materials containing elemental carbon: Physical and chemical distinctions. In Environmental Pollution (Vol. 181, pp. 271–286). Elsevier Ltd.
7. Benzigar, M. R., Talapaneni, S. N., Joseph, S., Ramadass, K., Singh, G., Scaranto, J., Ravon, U., Al-Bahily, K., & Vinu, A. (2018). Recent advances in functionalized micro and mesoporous carbon materials: Synthesis and applications. Chemical Society Reviews, 47(8), 2680–2721.
8. Hajmohammadi, Z., Fattahi, R., Zarei-Behjani, Z., & Hosseinzadeh, S. (2022). Carbon nanoparticles for medicine: current and future. Bulletin of Materials Science, 45(1), 8.
9. Axet, M. R., Dechy-Cabaret, O., Durand, J., Gouygou, M., & Serp, P. (2016). Coordination chemistry on carbon surfaces. Coordination Chemistry Reviews, 308, 236–345.

10. Chauhan, A. P. S., & Chawla, K. (2016). Comparative studies on Graphite and Carbon Black powders, and their dispersions. Journal of Molecular Liquids, 221, 292–297.
11. Gilmour, P. S., Ziesenis, A., Morrison, E. R., Vickers, M. A., Drost, E. M., Ford, I., Karg, E., Mossa, C., Schroeppel, A., Ferron, G. A., Heyder, J., Greaves, M., MacNee, W., & Donaldson, K. (2004). Pulmonary and systemic effects of short-term inhalation exposure to ultrafine carbon black particles. Toxicology and Applied Pharmacology, 195(1), 35–44.
12. Porter, D., Sriram, K., Wolfarth, M., Jefferson, A., Schwegler-Berry, D., Andrew, M. E., & Castranova, V. (2008). A biocompatible medium for nanoparticle dispersion. Nanotoxicology, 2(3), 144–154.
13. Kim, S., & Park, S. (2007). Effect of acid / base treatment to carbon blacks on preparation of carbon-supported platinum nanoclusters. 52, 3013–3021.
14. Sobkowicz, M. J., Dorgan, J. R., Gneshin, K. W., Herring, A. M., & McKinnon, J. T. (2009). Controlled dispersion of carbon nanospheres through surface functionalization. Carbon, 47(3), 622–628.
15. Zappielo, C. D., Nanicuacua, D. M., Santos, W. N. L. dos, Silva, D. L. F. da, Dall'Antônia, L. H., Oliveira, F. M. De, Clausen, D. N., & Tarley, C. R. T. (2016). Solid Phase Extraction to On-Line Preconcentrate Trace Cadmium Using Chemically Modified Nano-Carbon Black with 3-Mercaptopropyltrimethoxysilane. Journal of the Brazilian Chemical Society, October.
16. Hanada, Y., Masuda, S., Iijima, M., & Kamiya, H. (2013). Analysis of dispersion and aggregation behavior of carbon black particles in aqueous suspension by colloid probe AFM method. Advanced Powder Technology, 24(5), 844–851
17. Lima, M. C. F. S., Zaida do Amparo, S., Ribeiro, H., Soares, A. L., Viana, M. M., Seara, L. M., Paniago, R. M., Silva, G. G., & Caliman, V. (2016). Aqueous suspensions of carbon black with ethylenediamine and polyacrylamide-modified surfaces: Applications for chemically enhanced oil recovery. Carbon, 109, 290–299.
18. Aqel, A., El-Nour, K. M. M. A., Ammar, R. A. A., & Al-Warthan, A. (2012). Carbon nanotubes, science and technology part (I) structure, synthesis and characterisation. Arabian Journal of Chemistry, 5(1), 1–23.
19. Cardona-Uribe, N., Betancur, M., & Martínez, J. D. (2021). Towards the chemical upgrading of the recovered carbon black derived from pyrolysis of end-of-life tires. Sustainable Materials and Technologies, 28, e00287.
20. Wang, H., Xu, H., Jia, W., & Ren, S. (2018). Functionalized carbon black nanoparticles used for separation of emulsified oil from oily wastewater. Journal of Dispersion Science and Technology, 39(4), 497–506.
21. Lapuerta, M., & Canoira, L. (2016). The Suitability of Fatty Acid Methyl Esters (FAME) as Blending Agents in Jet A-1. In Biofuels for Aviation: Feedstocks, Technology and Implementation (pp. 47–84). Elsevier
22. Shukla, S., Bhattacharjee, S., Weber, A. Z., & Secanell, M. (2017). Experimental and Theoretical Analysis of Ink Dispersion Stability for Polymer Electrolyte Fuel Cell Applications. Journal of The Electrochemical Society, 164(6), F600–F609.
23. Lee, J., Bae, J., Kim, W., & Lee, S. (2022). A Study on Aqueous Dispersing of Carbon Black Nanoparticles Surface-Coated with Styrene Maleic Acid (SMA) Copolymer. Polymers, 14(24), 5455.
24. Sancaktar, E., & Basan, S. (2019). Comparison of Electrical Conductivity in Compounds of Carbon Black With Natural and Butadiene Rubbers. Frontiers in Materials, 6(October), 1–8.
25. Kang, J., Li, O. L., & Saito, N. (2013). Synthesis of structure-controlled carbon nano spheres by solution plasma process. Carbon, 60, 292–298.
26. Matthews, M. J., & Pimenta, M. A. (1999). Origin of dispersive effects of the Raman D band in carbon materials. 59(10), 6585–6588.
27. Aziz, S. B., Brza, M. A., Hamsan, M. H., Kadir, M. F. Z., Muzakir, S. K., & Abdulwahid, R. T. (2020). Effect of ohmic-drop on electrochemical performance of EDLC fabricated from PVA:dextran: NH4I based polymer blend electrolytes. Journal of Materials Research and Technology, 9(3), 3734–3745.
28. Zou, K., Cai, P., Wang, B., Liu, C., Li, J., Qiu, T., Zou, G., Hou, H., & Ji, X. (2020). Insights into Enhanced Capacitive Behavior of Carbon Cathode for Lithium Ion Capacitors: The Coupling of Pore Size and Graphitization Engineering. Nano-Micro Letters, 12(1), 1–19.

Exchange-Coupling Behaviour in $BaFe_{12}O_{19}$-$Y_3Fe_5O_{12}$ Nanocomposites Film Prepared by a Sol-Gel Method

Noratiqah Yusop and Noor Baa'yah Binti **Ibrahim***

Department of Applied Physics, Universiti Kebangsaan Malaysia, 43600 Bangi, Selangor, Malaysia

*Corresponding author: *baayah@ukm.edu.my*

ABSTRACT

In this study, the $BaFe_{12}O_{19}/Y_3Fe_5O_{12}$ nanocomposite film with various soft phase (YIG) compositions (11%, 17%, 20%, 33% and 43%) were synthesized through a sol-gel method followed by a spin coating technique and annealed at 900 ^oC for 2 hours. The microstructural analysis shows that film that contain low YIG content has good crystallinity without impurity phase. It was found that the magnetic properties of the nanocomposite film were influenced by soft phase composition. The exchange-coupling interaction that was achieved at an 11% of soft phase composition managed to improve the magnetic properties of the nanocomposite film higher than the single BaM phase. Further increment in the soft phase causes the dipolar interaction (soft-soft) to suppress the soft-hard interaction which causes the magnetic properties to be reduced. In this study, the best nanocomposite (BaM/YIG) film with good magnetic properties exhibited by the film with 11% of soft phase, with $(BH)_{max}$ value of 7.52 kJ/m^3 which is 9% higher than the single BaM phase (6.9 kJ/m^3). Magnetic properties analysis at high temperatures found that the Curie temperature of the best nanocomposite film is 720 K, slightly lower than the single BaM phase film (740 K).

Keywords—exchange-coupling, magnetic materials, thin film, sol-gel method, ferrites

1.0 INTRODUCTION

In 1991, Hawig & Kneller [1] introduced a theory involving a combination of hard magnetic phases with high H_c and soft magnetic phases with high M_s value in purpose to enhance the magnetic properties of a magnetic material, thus improves a material's magnetic energy product $(BH)_{max}$. In the production of nanocomposite magnets, a sol-gel method was identified as an ideal route to due to its advantage in producing material with smaller grain size, homogenous grains distribution [2–4], process simplicity and low cost [5,6]. There are two types of sol-gel approaches, first, a one-pot sol-gel [7] and second, a physical mixture [7,8]. A one-pot sol-gel method was reported has been successfully prepared a nanocomposite magnet with good magnetic properties [7,9] due to very homogenous grains distribution which contribute to a strong exchange-coupling. Torkian et al. (2018) [7] reported on hard/soft nanocomposite $SrFe_{10}Al_2O_{19}$/ $Co_{0.8}Ni_{0.2}Fe_2O_4$ that was prepared using a one-pot and a physical mixture sol-gel method. The nanocomposite magnet that was prepared via a one-pot sol-gel method showed enhancement in magnetic properties and smooth hysteresis loops compared to a nanocomposite magnet that was prepared via a physical mixture which showed kink at the second quadrant of the hysteresis loop. However, magnetic properties improvement also observed in a nanocomposite magnet that was prepared by a physical mixture. This reveals that the

exchange-coupling interaction is present in a nanocomposite that was prepared by a physical mixture.

In this study, the nanocomposite magnet of BaM/YIG film will be prepared by using a physical mixture of sol-gel. In our previous work, a nanocomposite magnet of (1-x) BaM/ x YIG film has been prepared by using a physical mixture sol-gel method [10]. However, in this study, the mixing method of BaM and YIG was altered by maintaining the BaM composition at 4.0. Hence, this makes the prepared nanocomposite film as 4.0 BaM/ *x* YIG. This study aims to study the exchange-coupling behaviour in a nanocomposite BaM/YIG film that was prepared via the proposed ratio composition.

2.0 EXPERIMENTAL PROCEDURE

2.1 Preparation of BaM solution and YIG solution

The preparation method of BaM and YIG solution has been reported in our previous work [10].

2.2 Preparation of 4.0 BaM / x YIG nanocomposite film

In this study, the 4.0 BaM / x YIG nanocomposite film will be prepared by mixing the soft phase YIG solution into the hard phase of the BaM solution. The x value of the soft phase was 0.50, 0.80, 1.0, 2.0 and 3.0, which is equivalent to 11%, 16%, 20%, 33% and 43%. Similar film deposition and annealing temperature has been reported in previous study [10].

The structural and phase composition of the film was identified using an X-Ray diffractometer (XRD-Bruker 8. The magnetic property of the composite film was studied using Vibrating Sample Magnetometer which performed at 300 K with the maximum applied field was 12 kOe.

3.0 MICROSTRUCTURAL ANALYSIS

The XRD pattern (Fig.1) of the nanocomposite BaM/YIG films reveals that film 4.0 BaM/0.5 YIG and 4.0 BaM/0.8 YIG shows good crystallinity without impurity phases (Fe_2O_3).

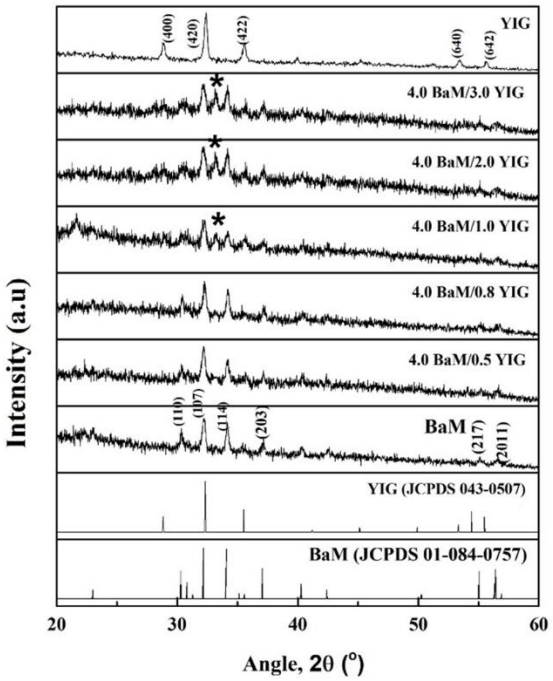

Fig. 1 Diffraction pattern of 4.0 BaM/ x YIG nanocomposite film. (*) refers to impurity phase Fe_2O_3

4.0 MAGNETIC PROPERTIES

In the nanocomposite magnetic properties analysis, the hysteresis loop's shape was used as the main indicator to identify the interaction between the soft and the hard phases. The smooth hysteresis loop that persists to a single-phase property indicates good exchange-coupling interaction between the hard and soft phases. In this case, the reversal of both phases' magnetic moment has occurred simultaneously at the same field. However, constricted loop at the second quadrant (bee-waist loop) of the hysteresis indicates

poor exchange-coupling between the two magnetic phases [11–13]. This insufficient exchange-coupling was attributed by the incoherent rotation of the magnetic moment of the two phases. The soft phase moments will rotate first at a lower field due to its low anisotropy, while the hard phase moments rotate at a higher field due to its high anisotropy than the soft phase. Fig. 2 shows the hysteresis graph of M versus H of all nanocomposite films. Based on the observation, the nanocomposite film of 4.0 BaM/ 0.5 YIG (in-plane and out-plane direction) and 4.0 BaM/ 0.8 YIG (in-plane direction) have smooth hysteresis loops to indicate good exchange coupling was achieved in between BaM and YIG phases, contributed by good exchange-coupling and homogenous grains distribution of the BaM and YIG grains. However, the film of 4.0 BaM/ 1.0 YIG, 4.0 BaM/ 2.0 YIG and 4.0 BaM/ 3.0 YIG showed kink on the second quadrant of hysteresis to indicate poor exchange-coupling due to significant dipolar interaction that may be contributed by the factor of grains distribution inhomogeneity and higher YIG phase composition. In the production of nanocomposite film, the soft phase compositions and the grains distributions play important roles to determine the magnetic properties of a nanocomposite magnet [12,14,15].

The second indicator used to identify the soft-hard phase interaction is a graph of dM/dH versus H. Fig.3 shows the dM/dH versus H graph of all nanocomposite films. Almost all nanocomposite film shows the appearance of two peaks in the graph. The appearance of the peak at a higher field represents exchange-coupling interaction between the two magnetic phases. The magnetic moment of the two phases experience simultaneous reversal of the magnetic moment of the soft and hard phases. Otherwise, the appearance of a peak at the lower field (near zero field) represents the dipolar interaction of the soft phase which does not experience exchange-coupling interaction with the hard phase.

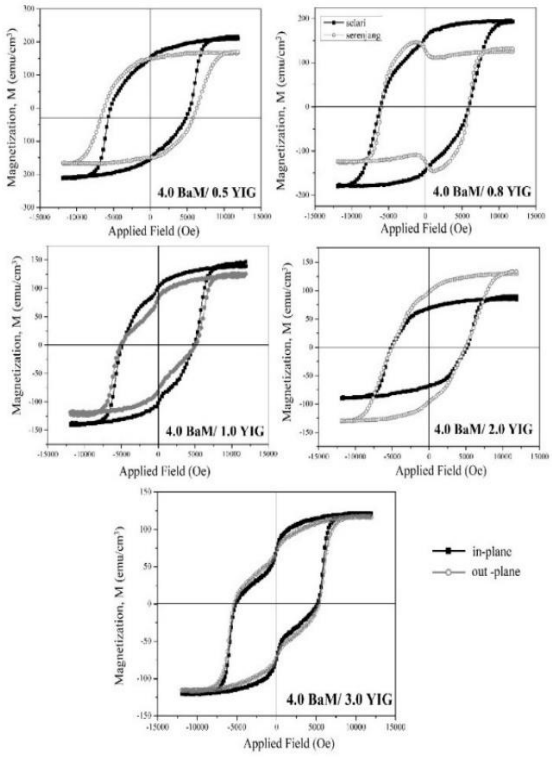

Fig. 2 Hysteresis loop of the 4.0 BaM / x YIG nanocomposite film

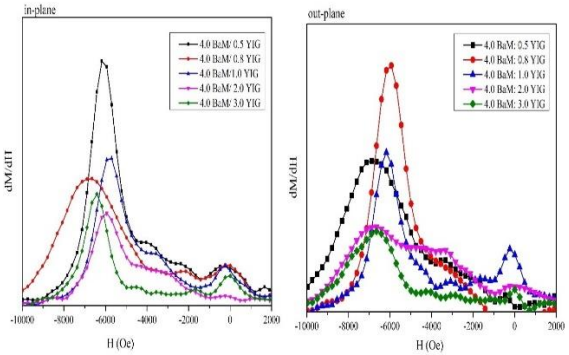

Fig.3 Graph of dM/dH versus H of 4.0 BaM/ x YIG nanocomposite film

Table 3 summarizes the magnetic properties of the prepared nanocomposite film. The 4.0 BaM/0.5 YIG shows the highest M_s value with 8% enhancement compared to the single BaM phase film (in-plane measurement). This enhancement is contributed by the exchange-coupling

interaction that was successfully achieved between BaM and YIG phases.

The H_c value of the nanocomposite 4.0 BaM/ x YIG film shows an unsystematic trend with an increment in YIG phase content. The nanocomposite of 4.0 BaM/ 0.5 YIG and 4.0 BaM/ 0.8 YIG films showed 6% and 16% enhancement in H_c value (in-plane direction), respectively higher than the H_c value of single BaM phase film (in-plane direction).

In this study, the nanocomposite of 4.0 BaM/ 0.5 YIG films shows improvement in $(BH)_{max}$ value with 9% (in-plane) and 11% (out-plane) enhancement compared to the single BaM phase attributed to the good exchange-coupling. Futher increment of soft YIG content cause the $(BH)_{max}$ value to decrease due to poor exchange-coupling.

Film	$M_{S\parallel}$ (±1 emu /cm^3)	$M_{S\perp}$ (±1 emu/ cm^3)	$M_{r\parallel}$ (± 1 emu/cm^3)	$M_{r\perp}$ (± 1 emu/cm^3)	$H_{C\parallel}$ (±1 Oe)	$H_{C\perp}$ (± 1 Oe)
BaM	194	215	156	154	5086	5388
4.0 BaM/ 0.5 YIG	210	166	152	150	5380	6290
4.0 BaM/ 0.8 YIG	125	193	130	148	5900	6043
4.0 BaM/ 1.0 YIG	133	121	100	82	4908	5030
4.0 BaM/ 2.0 YIG	84	129	70	97	5148	5030
4.0 BaM/ 3.0 YIG	120	116	73	70	5143	5300
YIG	128	84	54	30	38	4747

Fig.4 shows the M-H loop of the nanocomposite film 4.0 BaM/0.5 YIG measured at 10 K. A good hysteresis curve observed on the M-H loop indicates good interaction among the grains at lower temperature attributed by the homogeneous grains' distribution at optimum YIG composition. The dM/dH curve plot (Fig.5) shows only a single peak at a higher field, which indicates good interaction among the soft-hard was well achieved at low temperatures

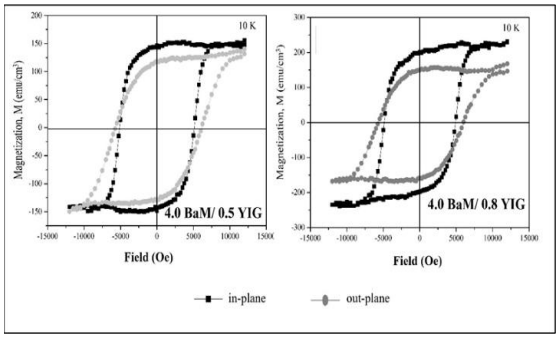

Fig. 4 Graf of M versus H of nanocomposite 4.0 BaM/0.5 YIG and 4.0 BaM/0.8 YIG films measured at 10 K

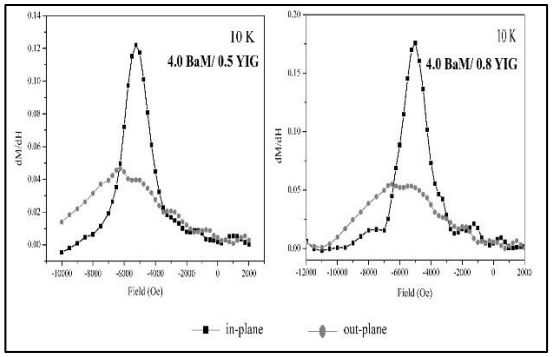

Fig. 5 dM/dH curves versus H of nanocomposite 4.0 BaM/0.5 YIG and 4.0 BaM/ 0.8 YIG films measured at 10 K

The Curie temperature (Fig.6) of the nanocomposite 4.0 BaM/ 0.5 YIG and 4.0 BaM/0.8 YIG was identified at 720 K and 730 K, respectively. The identified value is slightly lower than the T_c value of a single BaM-phase film in this study (740 K).

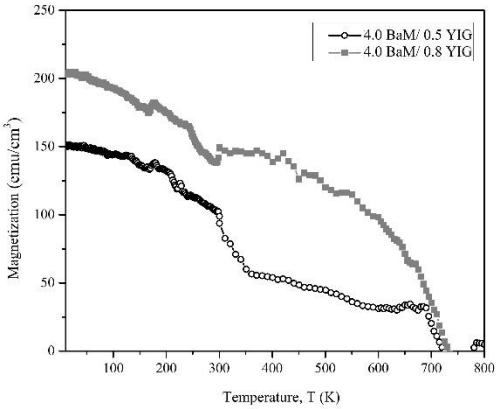

Fig.6 The magnetization (M) versus temperature (T) graph of the nanocomposite 4.0 BaM/0.5 YIG and 4.0 BaM/0.8 YIG films.

5.0 CONCLUSION

The nanocomposite BaM/YIG film has been successfully prepared using a sol-gel method. The nanocomposite of 4.0 BaM/0.5 YIG film shows improvement in magnetic properties thus enhancing the $(BH)_{max}$ value higher than the single BaM phase film. This enhancement was associated with exchange-coupling interaction that was well achieved at 11% of soft phase YIG composition. This finding reveals that the physical mixture sol-gel method can improve the magnetic properties of a nanocomposite magnet. The produced nanocomposite film with 11% of YIG composition has the potential to be applied as a permanent magnet due to its high coercivity value and enhanced $(BH)_{max}$ value.

ACKNOWLEDGEMENT

The authors would like to thank to the Ministry of Higher Education Malaysia for the financial support with grant no. [FRGS/1/2019/STG02/UKM/02/2] and Universiti Kebangsaan Malaysia for grant no. [GP-2020-K006916].

REFERENCES

[1] E.F. Kneller, R. Hawig, The exchange-spring magnet: A new material principle for permanent magnets, IEEE Transactions on Magnetics. 27 (1991) 3588–3600.

[2] M. Chithra, C.N. Anumol, B. Sahu, S.C. Sahoo, Exchange spring like magnetic behavior in cobalt ferrite nanoparticles, Journal of Magnetism and Magnetic Materials. 401 (2016) 1–8.

[3] G. Han, Y. Liu, W. Yang, S. Geng, W. Cui, Y. Yu, Fabrication, characterization, and magnetic properties of exchange-coupled porous BaFe8Al4O19/Co0.6Zn0.4Fe2O4 nanocomposite magnets, Nanoscale. 11 (2019) 10629–10635.

[4] V. Harikrishnan, R. Ezhil Vizhi, Temperature-dependent phase transition: Structural and magnetic properties of Ba0.5Sr0.5Fe12O19-CoFe2O4 nanocomposites, Journal of Physics and Chemistry of Solids. 127 (2019) 35–42.

[5] H. Irfan, R. Ezhil Vizhi, P. Saravanan, Processing and characterization of Ba0.5Sr0.5Fe12O19/Y3Fe5O12 nanocomposite ferrites towards permanent magnet applications, Journal of Materials Science: Materials in Electronics. 31 (2020) 10585–10592.

[6] N.B. Ibrahim, Y. Noratiqah, The microstructure and magnetic properties of yttrium iron garnet film prepared using water-alcohol solvents, Journal of Magnetism and Magnetic Materials. 510 (2020) 166953.

[7] S. Torkian, A. Ghasemi, Energy product enhancement in sufficiently exchange-coupled nanocomposite ferrites, Journal of Magnetism and Magnetic Materials. 469 (2019) 119–127.

[8] V. Sharma, S. Kumari, B.K. Kuanr, Exchange-coupled hard-soft ferrites; A new microwave material, Journal of Alloys and Compounds. 736 (2018) 266–275.

[9] Y. Li, A. Xia, C. Jin, Synthesis, structure and magnetic properties of hexagonal BaFe12O19 ferrite obtained via a hydrothermal method, Journal of Materials Science: Materials in Electronics. 27 (2016) 10864–10868.

[10] Y. Noratiqah, N.B. Ibrahim, Journal of Magnetism and Magnetic Materials The enhancement in magnetic properties of exchange-coupled (1 − x) BaFe 12 O 19 / x Y 3 Fe 5 O 12 magnetic nanocomposite film, Journal of Magnetism and Magnetic Materials. 570 (2023) 170534.

[11] R. Xiong, W. Li, C. Fei, Y. Liu, J. Shi, Exchange-spring behavior in BaFe12O19-

Ni0.5Zn0.5Fe2O4 nanocomposites synthesized by a combustion method, Ceramics International. 42 (2016) 11913–11917.

[12] H. Yang, T. Ye, Y. Lin, M. Liu, P. Kang, G. Zhang, Enhancements of (BH)max and remanence in BaFe12O19/CaFe2O4/CoFe2O4 nanocomposite powders by exchange-coupling mechanism, Materials Chemistry and Physics. 171 (2016) 27–32.

[13] M.A. Radmanesh, S.A. Seyyed Ebrahimi, Synthesis and magnetic properties of hard/soft SrFe 12O 19/Ni 0.7Zn 0.3Fe 2O 4 nanocomposite magnets, Journal of Magnetism and Magnetic Materials. 324 (2012) 3094–3098.

[14] N.A. Algarou, Y. Slimani, M.A. Almessiere, A. Baykal, S. Guner, A. Manikandan, I. Ercan, Enhancement on the exchange coupling behavior of SrCo0.02Zr0.02Fe11.96O19/MFe2O4 (M = Co, Ni, Cu, Mn and Zn) as hard/soft magnetic nanocomposites, Journal of Magnetism and Magnetic Materials. 499 (2020) 166308.

[15] M.A. Almessiere, Y. Slimani, A. Baykal, Structural, morphological and magnetic properties of hard/soft SrFe12-xVxO19/(Ni0.5Mn0.5Fe2O4)y nanocomposites: Effect of vanadium substitution, Journal of Alloys and Compounds. 767 (2018) 966–975.

[16] S. Torkian, A. Ghasemi, R.S. Razavi, Magnetic properties of hard-soft SrFe10Al2O19/Co0.8Ni0.2Fe2O4 ferrite synthesized by one-pot sol-gel auto-combustion, Journal of Magnetism and Magnetic Materials. 416 (2016) 408–416.

Immobilization of Zno Microrods on Rigid Meshes Using Hydrothermal Method

Jiao **Liu**, Shao-Liang **Liang**, Swee-Yong **Pung***
School of Materials and Mineral Resources Engineering,
Engineering Campus, Universiti Sains Malaysia, 14300 Nibong Tebal, Pulau Pinang, Malaysia.
*Corresponding author's phone: +604 5995215
E-mail: sypung@usm.my

ABSTRACT

Although ZnO photocatalyst demonstrates promising results in organic pollutants removal, its application in industry for wastewater treatment is still limited. One of the major issues are the deterioration of photocatalytic performance over time as the ZnO particles tend to drain away by the flowing wastewater during the treatment. To address this issue, ZnO microrods were immobilized on the kanthal meshes using hydrothermal technique. The effect of synthesis temperature on the growth of ZnO microrods was studied. The ZnO microrods rods that synthesized at 100 ^{o}C was selected for photocatalytic test. It demonstrated reasonable photodegradation on methylene blue (MB) under UV irradiation. However, the ZnO microrods demonstrated poor repeatability in removal of MB dye after 5 cycles.

Keywords— ZnO; hydrothermal; photocatalysts; immobilization

1.0 INTRODUCTION

ZnO is an II-VI semiconductor with wide bandgap (3.37 eV) and large exciton binding energy (60 meV) at room temperature. It is also a transparent metal oxide with good conductivity, piezoelectric property, bio-safe and bio-compatible material [1]. Attributed to these unique properties, it is a potential candidate for applications such as photocatalysts [2], light emitting diodes [3], field effect transistors [4], solar cells [5], gas sensors [6] and electric nanogenerators [7].

Many research works have been done to explore ZnO potential as photocatalysts for removal of organic pollutants such as dyes, insecticides, and volatile organic compounds [2] and heavy metal ions [8], inactivation of bacterial [9] and fungal [10], generation of oxygen and hydrogen through water splitting [11] and self-cleaning glass substrates [12]. Nevertheless, the application of ZnO photocatalysts are still limited because of (i) poor responsive to visible light due to its wide bandgap energy, (ii) rapid recombination of charge carriers, and (iii) deterioration of photocatalytic performance over time. To address issues (i) and (ii), approaches such as doping [13] and coupling with metals or metal oxides [8] have been attempted by researchers.

Deterioration of photocatalytic performance of ZnO photocatalyst over time happened particularly when it is used in particle form. ZnO particles tend to be carried away by wastewater, causing decrease of photodegradation efficiency and generation of secondary pollutants. This limits its applications in wastewater treatment technology. The washed-away particles became secondary pollutants where additional filtration process is needed to remove these particles from water. This will incur additional time and cost of the process and cause the process more difficult.

To address this problem, ZnO photocatalysts were immobilized onto various supporting substrates such as silicon wafers [13], glass slides [14], polymeric fibers such as polyethylene terephthalate [15], stainless steel wires [16], carbon [17] and clay [18] to minimize

the loss during wastewater treatment process. In this work, ZnO sub-micron rods were grown on kanthal meshes by hydrothermal technique. The effect of growth temperature on the morphology of ZnO microrods were studied. The ZnO microrods with the largest areal density was selected for the photocatalytic test for MB removal under UV irradiation. Feasibility study was also performed to assess its long-term reliability (reusability test) to decompose organic pollutants.

2.0 MATERIALS AND EXPERIMENTAL

2.1 Synthesis of ZnO sub-micron rods using hydrothermal technique

Kanthal meshes (FeCrAl alloy) were used as substrates due to their ability to withstand high temperature (melting point: 1435 ^{o}C) and good corrosion resistance. The meshes were cut into the size of 1 cm X 1 cm. They were cleaned by sonication in acetone for 15 min, followed by ethanol for another 15 min.

In a typical reaction procedure, an aqueous solution of zinc nitrate hexahydrate (50 mM, 100 ml) (Sigma Aldrich) was mixed with an aqueous solution of hexamethylenetetramine (50 mM, 100 ml) (Sigma Aldrich). The mixture solution was transferred to a Teflon-line stainless steel flask. Subsequently, the kanthal meshes were immersed in the precursor solution and autoclaved at 80 ^{o}C for 5 hrs. Lastly, kanthal meshes were cleaned with deionized water, and dried at room temperature. The effect of synthesis temperature (80, 100 and 120 ^{o}C) on the growth of ZnO microrods on the kanthal meshes were studied.

2.2 Materials characterization

The crystal structures of samples were characterized using X-ray diffractometer (D8 Advance, Bruker) with Cu-K_{α} radiation (15.4056 nm) at 40 kV and 40 mA, ranging from 20◦ to 90◦ at room temperature. The surface morphologies of samples were determined by field emission scanning electron microscopy (FESEM, Zeiss Supra 35 VP) and transmission electron microscope (TEM, Tecnai G2 F20 X-Twin).

2.3 Photocatalytic study

In a typical photocatalytic assessment, a 250 ml of 5 ppm of methylene blue (MB) solution was prepared under dark condition. 3ml of initial methylene blue solution was withdrawn as reference. 4 pieces of kanthal meshes (with ZnO microrods) were then put into the solution. A plastic mesh was used to separate the kanthal meshes and magnetic stirrer to avoid damages done on the ZnO microrods. The mixture was stirred under dark for 30 min to achieve desorb-adsorb equilibrium. Subsequently, the mixture was exposed to UV light ($\lambda \sim 300$ nm) under continuous stirring for 1 hour. In every 15 min interval, 3 ml of solution was withdrawn and stored in a cuvette. The absorbance of degraded MB solution was measured using UV–vis spectrophotometer (Varian Cary 50). The photodegradation efficiency of MB by ZnO microrods that grown on kanthal meshes was calculated using Equation (1).

$$\text{Photodegradation efficiency, } (\eta\%) \cdot = \left(1 - \frac{A_t}{A_o}\right) x\ 100\ \% \qquad (1)$$

where A_o and A_t are the characteristic absorbance of MB dye solution ($\lambda = 665$ nm) at t = 0 min and after t min of reaction, respectively. The kinetics of the photodegradation of MB were explored based on the first order kinetic model using Equation (2).

$$\ln\left(\frac{A_t}{A_o}\right) = -kt \qquad (2)$$

The kanthal meshes were washed and reused for the repeatability test using the above procedure.

3.0 RESULTS AND DISCUSSION

3.1 Effect of growth temperature

The XRD patterns of samples deposited on kanthal mesh synthesized at different growth temperatures using hydrothermal method is shown in Fig. 1. All the samples deposited on kanthal mesh at various growth temperatures exhibited diffraction peaks that could be indexed to ZnO (ICSD 04-007-1614). The presence of remaining diffraction peaks were matched with crystal planes of aluminum iron phase (ICSD 04-003-7166) and chromium (ICSD 98-002-3333). The origin of the aluminum iron and chromium were from the kanthal mesh.

Fig. 2 (a, b) show the surface morphology of bare kanthal mesh under different magnifications. The sieve size was 0.5 mm. The diameter of the kanthal wire was 200 µm ± 10 µm. The surface of wire was not smooth as seen in Fig. 2 (b). Surface imperfections such as grooves, and delamination could be clearly observed. In addition, the crystal grains of the wire were found elongated in unidirectional because of the extrusion process during fabrication of the wire.

In general, ZnO microrods with hexagonal tips were grown on the kanthal meshes using hydrothermal technique as shown in Fig. 2 (c) – (f). The size, and areal density atomic % are plotted in Fig. 3 for better comparison. At 80 ºC, ZnO microrods with large diameter (1.73 ± 0.16 µm) and short length (1.20 ± 0.034 µm) were obtained (sample size, n = 30). In addition, the areal density is 0.123 ± 0.003 rods per µm^2. At this low temperature, a slower growth rate was expected.

The ZnO microrods synthesized at 100 ºC have a longer length but smaller diameter as compared to those grew at 80 ºC as observed in Fig. 2 (e, f). The length and diameter of the ZnO microrods are 3.27 ± 0.52 µm and 0.914 ± 0.059 µm, respectively (n = 30). The areal

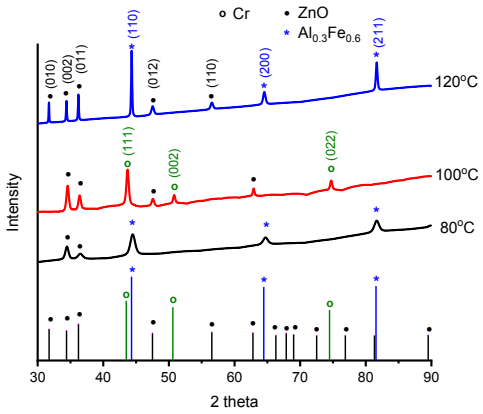

Fig. 1 XRD diffraction patterns of ZnO synthesized at 80, 100 and 120 ºC.

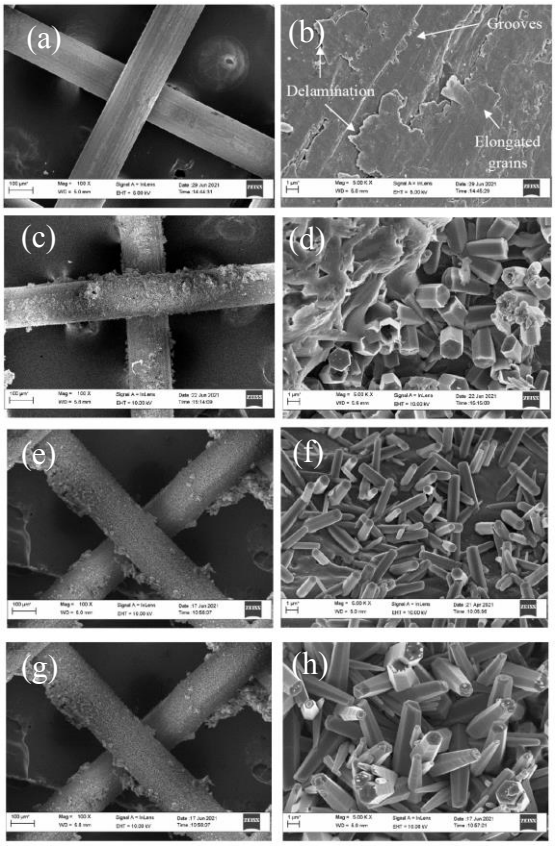

Fig. 2 Surface morphology of (a, b) bare kanthal mesh and ZnO microrods that grown on kanthal meshes at (c, d) 80, (e, f) 100 and (g, h) 120 ºC.

density is 0.285 ± 0.044 rods per µm^2. A higher growth temperature promoted more nucleation and growth rate, increasing the number of microrods per µm^2 (areal density) and longer microrods. The ZnO microrods synthesized at 120 ºC have needle-like structure with a larger bases and smaller hexagonal tips. The length and

diameter of the ZnO microrods are 3.88 ± 0.76 µm and 0.954 ± 0.285 µm, respectively (n = 30). The areal density is 0.140 ± 0.027 rods per µm^2. It is noted that some of the adjacent ZnO microrods merged to form larger microrods.

The ZnO microrods synthesized using optimum condition were selected for TEM as shown in Fig. 4. The ZnO microrods have needle-like structure. The length and diameters of these ZnO microrods are 5.620± 0.165 µm and 1.113± 0.054 µm, respectively. It is known that the preferred growth direction of ZnO is in [0001] and perpendicular to its (002) [20, 21], as labelled in Fig. 4 (a). It is found that the surface of (002) of ZnO microrods was rougher as compared to its side wall, i.e., {01$\bar{1}$0}. This is explainable as the (002) experienced faster growth rate attributed to its larger surface energy (3.76 J/m^2) [22] as compared to {01$\bar{1}$0} (2.97 J/m^2) [23].

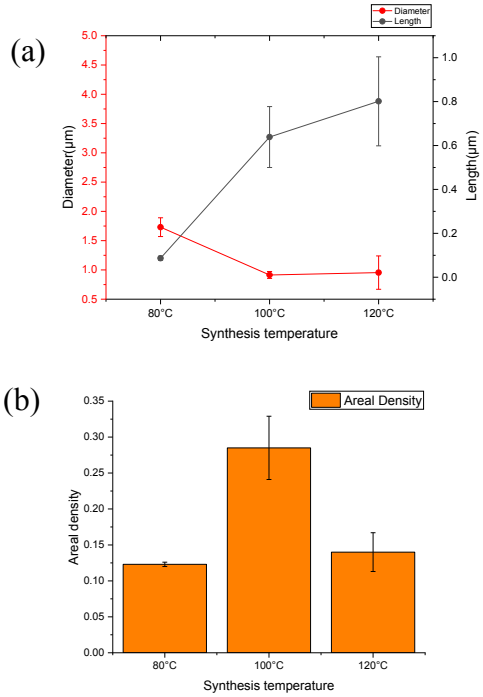

Fig. 3 (a) Size, and (b) areal density of ZnO microrods that grown on kanthal meshes at different growth temperature.

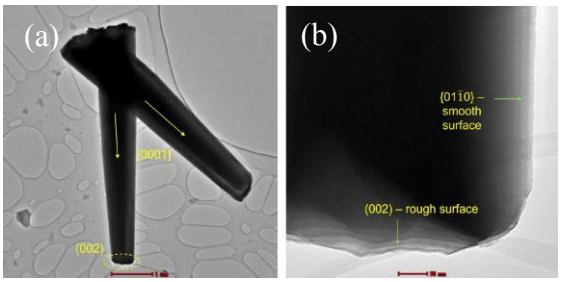

Fig. 4 TEM images of ZnO microrods observed under (a) 7 and (b) 97 kX.

Fig. 5 (a) shows the photodegradation efficiency of MB by ZnO microrods, showing 17.43 % photodegradation efficiency after 90 min of UV irradiation. The linear fitting in Fig. 5 (b) indicates that the photodegradation of MB followed first order kinetic reaction with a rate constant of 1.82 x 10^{-3} min^{-1} (R^2 = 0.96608).

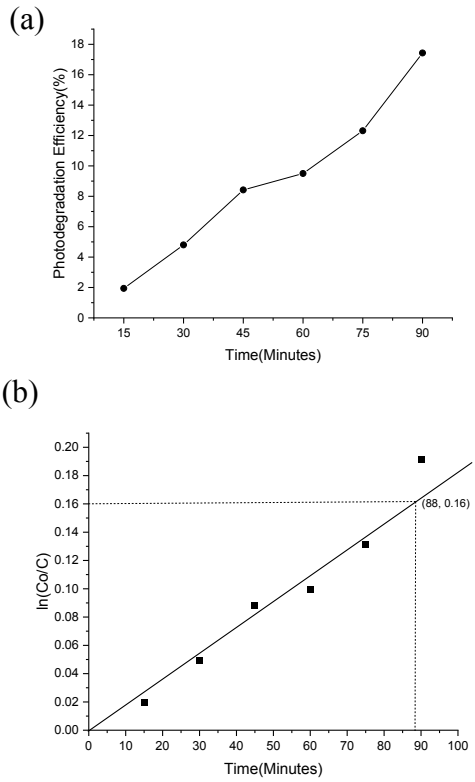

Fig. 5 (a) Photodegradation efficiency, and (b) kinetic plot of MB degraded by ZnO microrods grown on kanthal meshes under UV light.

Fig. 6 (a) displays the photodegradation efficiencies of ZnO microrods after 5 consecutive cycles. The photodegradation efficiency deteriorated after each cycle and recorded a 7.87% photodegradation efficiency at the 5th cycle. The decrease of photodegradation was attributed to the loss of ZnO microrods from the kanthal meshes. As shown in Fig. 2 (e, f), some of ZnO microrods were deposited rather than grown on kanthal meshes. These deposited ZnO microrods tended to drop off from the surface of kanthal meshes, causing decay of photodegradation efficiency over time as shown in Fig. 6 (b).

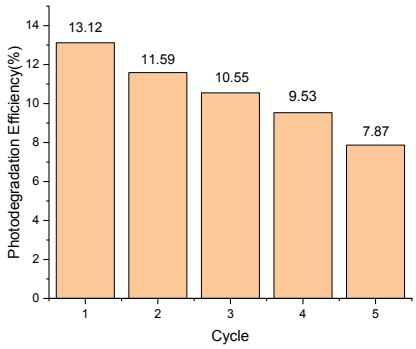

Fig. 6 Reusability test of ZnO microrods that grown on kanthal mesh after 5th cycle in MB removal.

4.0 CONCLUSION

The ZnO microrods were grown on kanthal mesh using hydrothermal method. The optimum synthesis condition was using mixture of 50mM of zinc nitrate hexahydrate and hexamethylenetetramine at 100ºC for 5 hours as it possessed the largest areal density. The photocatalyst recorded a 17.43% of photodegradation efficiency in MB dye removal with rate constant of 0.00182 min^{-1} under UV irradiation after 90 minutes. The photodegradation of MB by ZnO microrods followed first order kinetic model. The ZnO microrods that deposited (but not grown on) the kanthal mesh was the main contribution of poor reusability.

ACKNOWLEDGEMENTS

The authors gratefully acknowledge the financial support of Ministry of Higher Education, Malaysia for providing the research funding under Fundamental Research Grant Scheme (FRGS) (FRGS/1/2020/TK0/USM/02/27) to conduct this project.

REFERENCES

1. D. K. Sharma, S. Shukla, K. K. Sharma, and V. Kumar. A review on ZnO: Fundamental properties and applications. Materials Today: Proceedings 2022, (49): 3028.
2. Y. Zhang, M. K. Ram, E. K. Stefanakos, and D. Y. Goswami. Synthesis, characterization, and applications of ZnO nanowires. Journal of Nanomaterials 2012, (2012).
3. S. H. Park, S. H. Kim, and S. W. Han. Growth of homoepitaxial ZnO film on ZnO nanorods and light emitting diode applications. Nanotechnology 2007, (18) 5.
4. N. M. J. Ditshego. Zinc oxide nanowire field effect transistor used as a pH sensor. International Journal of Electrical and Electronic Engineering and Telecommunications 2022, (11)2: 162.
5. M.Z. Toe, S.Y. Pung, K. Yaacob, and S.S. Han. Effect of dip-coating cycles on the structural and performance of ZnO thin film-based DSSC. Arabian Journal for Science and Engineering 2021, (46): 6741.
6. X. Jiaqiang, C. Yuping, C. Daoyong, and S. Jianian. Hydrothermal synthesis and gas sensing characters of ZnO nanorods. Sensors and Actuators B Chemical 2006, (113)1: 526.
7. M. S. Al-Ruqeishi, T. Mohiuddin, B. Al-Habsi, F. Al-Ruqeishi, A. Al-Fahdi, and A. Al - Khusaibi. Piezoelectric nanogenerator based on ZnO nanorods. Arabian Journal of Chemistry 2019, (12)8: 5173.
8. A. Thi Le, S.-Y. Pung, S. Sreekantan, A. Matsuda, D. Phu Huynh, and D. Phu Huynh. Mechanisms of removal of heavy metal ions by ZnO particles. Heliyon 2019, (5).
9. F.C.O. Soh, J.H. Kee, M.T. Thein, Y.L. Ying, C.F. Le, D.N.D Nguyen, B.H. Goh, S.Y. Pung, and Y.F. Pung. Antibacterial activity by ZnO nanorods and ZnO nanodisks: A model used to illustrate "Nanotoxicity Threshold". Journal of Industrial and Engineering Chemistry 2018, (62):333.
10. P. Singh, and A. Nanda. Antimicrobial and antifungal potential of zinc oxide nanoparticles in comparison to conventional zinc oxide particles. Journal of Chemical and Pharmaceutical Research 2013, (5)11: 457.

11. J. Kegel, I. M. Povey, and M. E. Pemble. Zinc oxide for solar water splitting: A brief review of the material's challenges and associated opportunities. Nano Energy 2018, (54): 409.
12. G. Broasca, G. Borcia, N. Dumitrascu, and N. Vrinceanu. Characterization of ZnO coated polyester fabrics for UV protection. Applied Surface Science 2013, (279):272.
13. R. Khokhra, P. B. Barman, and R. Kumar. Synthesis of ZnO nanostructures on silicon wafer by wet chemical method. International Journal of Engineering Research and Technology 2013.
14. H. K. Hakki, S. Allahyari, N. Rahemi, and M. Tasbihi. Surface properties, adherence, and photocatalytic activity of sol–gel dip-coated TiO_2–ZnO films on glass plates. Comptes Rendus Chimie 2019, (22)5:393.
15. Y.L. Chan, S.Y. Pung and S. Sreekantan. Degradation of organic dye using ZnO nanorods based continuous flow water purifier," Journal of Sol-Gel Science & Technology 2013, (66)3:399.
16. S. N. Q. A. Abd Aziz, S. Y. Pung, N. N. Ramli, and Z. Lockman. Growth of ZnO nanorods on stainless steel wire using chemical vapour deposition and their photocatalytic Activity. Scientific World Journal 2014, (2014).
17. P. Raizada, P. Singh, A. Kumar, G. Sharma, B. Pare, S.B. Jonnalagadda, P. Thakur. Solar photocatalytic activity of nano-ZnO supported on activated carbon or brick grain particles: role of adsorption in dye degradation. Applied Catalysis A 2014, (486):159.
18. M. Akkari, P. Aranda, A.B.H. Amara, and E. Ruiz-Hitzky. Clay -nanoarchitectures as photocatalysts by in situ assembly of ZnO nanoparticles and clay minerals. Journal of Nanoscience and Nanotechnology 2018, (18): 223.
19. A. T. Le, T. D. H. Le, K.-Y. Cheong, and S.-Y. Pung. Immobilization of zinc oxide-based photocatalysts for organic pollutant degradation: A review. Journal of Environmental Chemical Engineering 2022, (10)5: 108505.
20. S. Xu, and Z.L. Wang. One-dimensional ZnO nanostructures: solution growth and functional properties. Nano Research 2011, (4): 1013.
21. S.Y. Pung, K.L. Choy, X. Hou and C. Shan. Preferential growth of ZnO films by the atomic layer deposition technique. Nanotechnology 2008, (19): 435609.
22. B. Yamina, A, Abderrahim, B. Omar and B. Lazhar. A Comprehensive DFT study of wurtzite ZnO. Der Pharma Chemica 2018, (10)1:16.
23. S. H. Na, and C. H. Park. First-principles study of the surface of wurtzite ZnO and ZnS - implications for nanostructure formation. Journal of Korean Physical Society 2009, (54)9:867.

The Effect of Nano Silica as Nanofiller on Tensile, Flexural and Compression Properties of Basalt and Glass Fiber Reinforced Composites Using Industrial Polyester Resin

Mohamad Asrofi **Muslim**[1], Aidah **Jumahat**[1*], Shahrul Azam **Abdullah**[1], Mohd Azrul **Jaafar**[2], Mochamad **Chalid**[3], Jamaliah Md **Said**[1]

[1]School of Mechanical Engineering, College of Engineering, University Technology MARA, Shah Alam, Selangor, Malaysia
[2] Centre for Instructor and Advanced Skill Training, Shah Alam, Selangor, Malaysia
[3]Department of Metallurgical and Material Engineering, Faculty of Engineering, Kampus Baru UI, Universitas Indonesia, Depok, Indonesia

*Corresponding author's phone: + 60 12-229 0890
E-mail: aidahjumahat@uitm.edu.my

ABSTRACT

Granite waste is becoming increasingly relevant as the global demand for granite increases. This study aimed to develop a new composite using nano-silica as a nanofiller in basalt and glass fiber reinforced composites using industrial polyester resin. Composite fabrication processes using hand lay-up and vacuum silicon mould. Analysis testing results show that nano silica increases tensile, flexural and compression strength values. The maximum weight percentage value is 1wt%. More than 3wt% nano silica will decrease the strength value. Samples with more than 3wt% nano silica tend to agglomerate. Replacement of using glass to basalt will increase by 28% in tensile strength. Using nano silica in this application will help decrease the waste in granite industries and contribute sustainable resources. This new composite is suitable for truck body carriers and is more environmentally.

Keywords—nano silica; basalt fibre; glass fibre; polyester; vacuum silicon mould

1.0 INTRODUCTION

Granite is extensively utilised globally within construction, architecture, and as an ornamental substance. The material is highly regarded due to its exceptional durability, pleasing aesthetic qualities, and notable resistance to both heat and scratches. Nevertheless, using granite raises certain apprehensions about its environmental implications, including its impact on the ecosystem, habitat degradation, soil erosion, water contamination, and potential health hazards (Agasnalli et al., 2022). Although granite presents various advantages, it is crucial to carefully consider its environmental impact, health implications, labour conditions, and long-term sustainability factors to achieve a balanced approach to its utilisation.

Basalt fibre is a multifaceted substance obtained from naturally occurring volcanic rock known as basalt. The material possesses distinct characteristics that make it suitable for various applications on a global scale, particularly in the Automotive and Aerospace industries. These properties enable the material to effectively reduce weight without compromising its strength. Automobile components such as body panels, interior parts, and structural elements find application in various automotive contexts (Plappert et al., 2020).

The utilisation of basalt fibre globally is progressively expanding due to its inherent benefits, including its notable tensile strength, fire resistance, and resistance to chemicals and corrosion. The

sustainability, ample availability, and minimal environmental footprint relative to alternative fibres render it a compelling option across multiple industries.

Nano silica, called silica nanoparticles or colloidal silica, is a silicon dioxide variant characterised by particle dimensions falling within the nanometer scale. The material possesses distinct characteristics that render it suitable for various industrial applications, including its use as a rubber and plastics reinforcing agent (Kaka et al., 2021). Incorporating nano silica particles has been shown to positively impact the mechanical characteristics of rubber and plastic materials, leading to improvements in their strength, stiffness, and durability (Abdel-Rahim et al., 2022).

2.0 MATERIALS AND METHODS

Carbon Tech Global Sdn was supplied with industrial polyester resin and Hardener M60 Butanox; meanwhile, woven glass fibre and basalt fibre were supplied by Innovative Poltrusion Sdn Bhd. Nano silica was extracted from granite dust supplied by JKR Malaysia.

2.1 COMPOSITE FABRICATIONS PROCESS

The fibre-reinforced composites were prepared using a hand lay-up and vacuum silicon mould supplied by CTG SD.BHD, as shown in Figure 1. The polyester resin was mixed with a hardener in a ratio of 50:1 by weight, recommended by the supplier, to ensure the resin was fully cured.

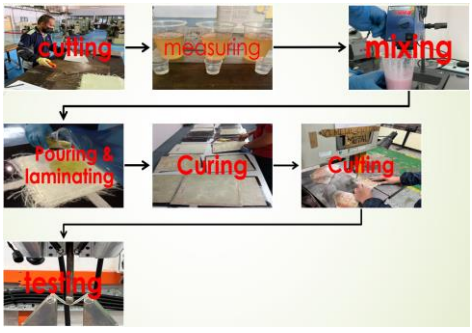

Figure 1:Composite Fabrication process

3.0 EXPERIMENTAL

A total of 12 system sample size 300 x 300 mm were prepared and cut, following ASTM-D3039 for tensile, ASTM-D790 for flexural, and ASTM D3410 for compression. Each system was designed with five identical samples following the dimension ASTM respectively.

3.1 TENSILE STRENGTH MEASUREMENTS

In the case of BFRC and GFRC composites, the ASTM D-3039 standard is used for conducting tensile testing[19], [20]. The SHIMADZU 3366 machine is used for testing, and the specimen used for tensile testing has the following dimensions: Length of 250mm, width of 25mm, thickness of 2mm, and gauge length (distance between the grips) of 50mm. The crosshead speed for the tensile test is set at 5mm/min, which is the rate at which the grips move apart during the trial. A standard sample size of five specimens is used in most testing methodologies to ensure statistical validity and to reduce any outliers' impact. Calculate the tensile strength and elongation of the Basalt Fibre Reinforce Composite (BFRC), Glass Fibre Reinforce Composite (GFRC) and Polyester (PE) resin.

3.2 FLEXURAL PROPERTIES MEASUREMENTS

A standard test procedure used to ascertain the flexural properties of composites is ASTM D790-03 [22]. In the test, a rectangular specimen is bent until it fractures, and the force and displacement are recorded. The recorded data determined flexural strength (FS) and flexural modulus (FM). The SHIMADZU, The 3366-10kN machine, was used to test the materials' mechanical properties. In this specific test, the samples were rectangular and had dimensions of 80 mm (length) x 13 mm (width) x 5 mm (thickness). The test was conducted at a cross-head speed of 2 mm/min, the rate at

which the machine's crosshead moves during the trial. At least five samples were prepared for each formulation, which refers to the specific composition and processing conditions used to produce the material.

3.3 COMPRESSION MEASUREMENTS

Composite materials are widely used in various industries due to their exceptional strength-to-weight ratio. The ASTM D3410 standard provides a comprehensive protocol to assess these materials' compressive properties. This compression test method is outlined in ASTM D3410 for composite materials with dimensions 110mm length, 10mm width, and 2mm thickness. Following the specified dimensions and test protocol can accurately assess the material's compressive strength, modulus, and deformation behaviour. This information is crucial for designing and selecting composite materials in various applications where compression forces may be encountered. Understanding the behaviour of composite materials under compression is essential for ensuring structural integrity and overall performance in real-world scenarios (D'Mello et al., 2019).

4.0 RESULTS AND DISCUSSION

The results are the mean values of five samples tested for each type of composite laminate. The difference in the sample is the weight percentage of nano silica mixed in the resin before the pouring process during the hand lay-up fabrication process. The tensile, flexural, and compression properties of composite laminates, PE, BFRC, and GFRC were studied. The finding thoroughly discussed the effect of different characters.

1. Effect of nano silica on polyester composite.
2. Effect of nano silica on Basalt Fibre Reinforced Composite.
3. Effect of nano silica on Glass Fibre Reinforced Composite; and
4. Effect of nano silica compared to Industrial Sample.

4.1 Effect nano silica on Polyester Composite

The polyester composite's tensile, flexural, and compressive strength are shown in *Figure 2*. The result shows that the highest tensile value is 1wt% with 62.97Mpa compared to 57.46MPa at unmodified polyester composite—the improvement of 9.5% increases when nano silica is incorporated in polyester resin. In 3wt%, the value decreased to 54.40MPa and continued to decrease to 48.59Mpa in 5wt% of nano silica. Nano silica tends to agglomerate and approves when 3wt% and more powders are added. The flexural value for unmodified PE is 88.10 MPa, and 105.10 MPa at 1wt% contain nano silica with an increasing value of 19.3%. The value continuously decreased to 88.46MPa and 83.92MPa. The compressive strength value also increased from 86.67MPa to 108.42MPa with an increasing percentage of 25% at 1wt% containing nano silica.

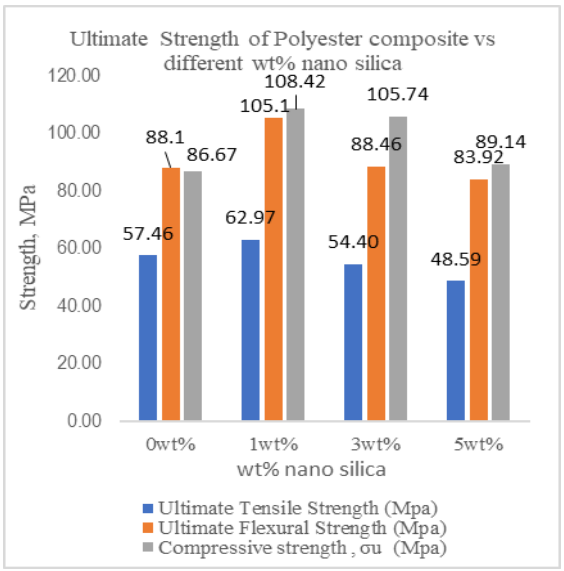

Figure 2: Tensile strength PEC

Including nano silica leads to a decrease in value to 105.74MPa and 89.14MPa. The experimental findings indicate that incorporating nano-silica in polyester composites resulted in a notable improvement in the mechanical properties, specifically tensile, flexural, and compressive strength. The observed enhancements ranged from 9% to 25%. The rationale behind utilising nano-silica in this context is attributed to its expansive surface area, which enables it to effectively occupy the voids within the polyester material up to a specific weight percentage. In the present experiment, the optimal weight percentage deemed appropriate is 1wt%. (Quadflieg et al., 2023).

4.2 Effect of nano-silica on (BFRC)

The tensile, flexural, and compressive properties of the BFRC composite are shown in *Figure 3*. Based on the results, the highest tensile value is in 1wt%, with 337.67Mpa increasing from 314.43MPa at unmodified BFRC. The percentage improved by 7.4% when polyester resin incorporated nano silica. In 3wt%, the value continuously decreases to 300.65 and 275.42 in 5wt% of nano silica.

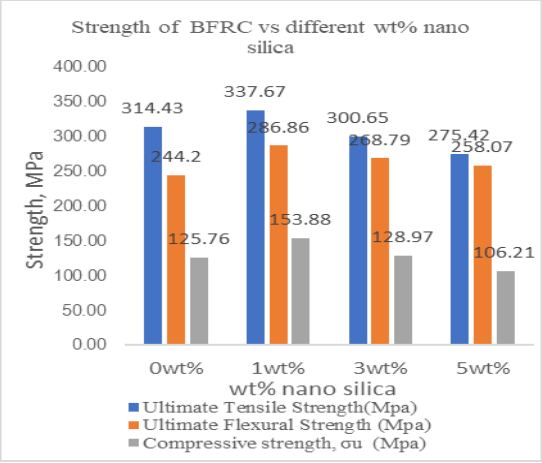

Figure 3: Tensile, Flexural, and compressive strength BFRC

The flexural value exhibited a significant increase of 17.5%, ranging from 244.20MPa to 286.86MPa. Subsequently, the value exhibited a consistent downward trend, reaching magnitudes of 268.79MPa and 258.07MPa. The compressive strength value exhibited a notable increase, rising from 125.76MPa to 153.88MPa, representing a percentage increase of 22.4%. At a weight percentage of 5%, the value decreases to 128.97MPa and 106.21MPa. The impact of incorporating nano-silica into polyester composites was observed to result in a variation in tensile, flexural, and compressive strength properties, ranging from 7% to 22.4%. The reason for this phenomenon is attributed to the expansive surface area of nano-silica particles, which enables them to effectively occupy the available space within the polyester matrix up to a specific weight percentage (wt.%), as observed in this experimental study, where the saturation point was determined to be 1wt%. (Erkliğ, 2022).

4.3 Effect of nano-silica on GFRC

The tensile, flexural, and compressive properties of the GFRC composite are shown in *Figure 4*. The highest tensile value is 1wt% with 306.37Mpa compared to 244.98MPa at unmodified GFRC. The value is increased by 25%, while nano silica is incorporated in polyester resin. In 3wt%, the value decreased to 276.93 and still decreased to 206.17 in 5wt% of nano silica. The flexural value went from 223.64MPa to 249.19MPa, with an increasing value of 11.4%. After that, the value continuously decreased with values of 238.03MPa and 224.03MPa. The compressive strength value also increased from 99.78MPa to 114.50MPa with an increasing percentage

of 14.75%. The value decreases to 113.36MPa and 96.79MPa at 5wt%.

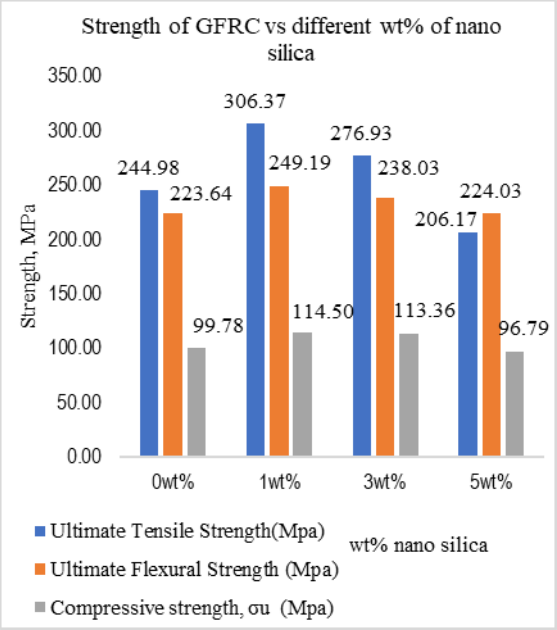

Figure 4: Tensile, flexural, and compressive strength of GFRC

The impact of incorporating nano-silica into polyester composites resulted in a variation of tensile, flexural, and compressive strength properties, ranging from 11.4% to 25%. The rationale behind using nano-silica in this study is attributed to its extensive surface area, which allows for effective incorporation into the polyester matrix up to a specific weight percentage (wt.%), specifically 1wt%.

4.4 Effect of nano-silica Compared to Industrial Sample

Figure 5 displays the graph illustrating the tensile properties, explicitly comparing the industrial sample to the maximum strength values of PE, BFRC, and GFRC. The BFRC material exhibits the highest tensile strength value, specifically at a concentration of 1wt%, measuring 337.67Mpa. The PE sample exhibits the lowest strength, measuring 62.97MPa. This is succeeded by the industrial sample, CTG by 1wt%, which records a strength of 91.79MPa. The GFRC sample with 1wt% demonstrates the highest strength, measuring 306.37MPa. The tensile value of PE exhibits a percentage increase of 433%, while BFRC demonstrates a percentage increase of 487.6%.

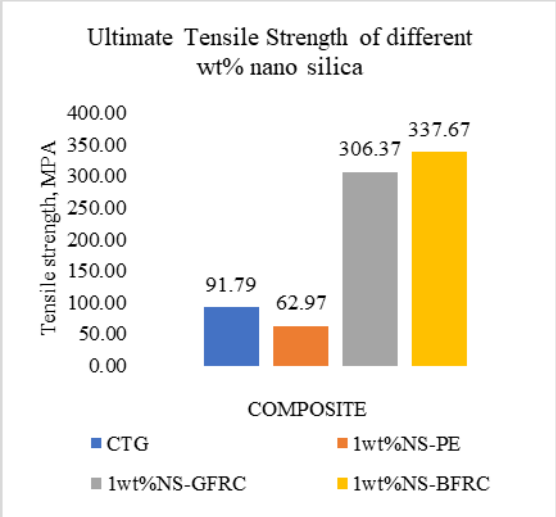

Figure 5: Tensile Strength Comparison maximum wt.% with industrial sample

The graph for the flexural, with the comparison between the industrial sample and the highest value of the strength of PE, BFRC, and GFRC, is shown in Figure 6.

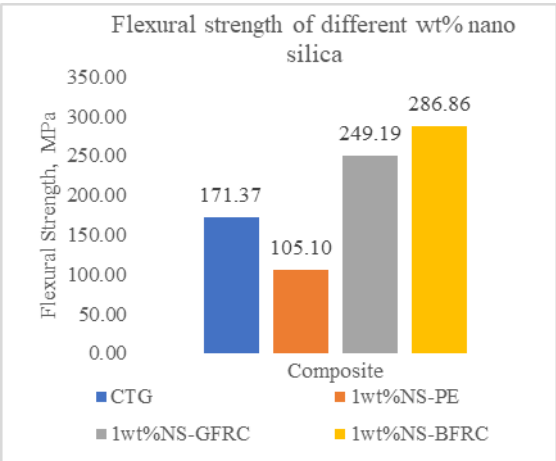

Figure 6: Flexural Strength Comparison maximum wt.% with industrial sample

The flexural strength of the CTG sample was measured to be 117.37MPa, while the GFRP sample exhibited a flexural strength of 249.19MPa, representing a 45% increase when incorporating 1wt% nano silica. Subsequently, the value exhibited a consistent upward trend, reaching values ranging from 286.86 MPa-1wt%-BFRC and a notable increase of 67.4%.

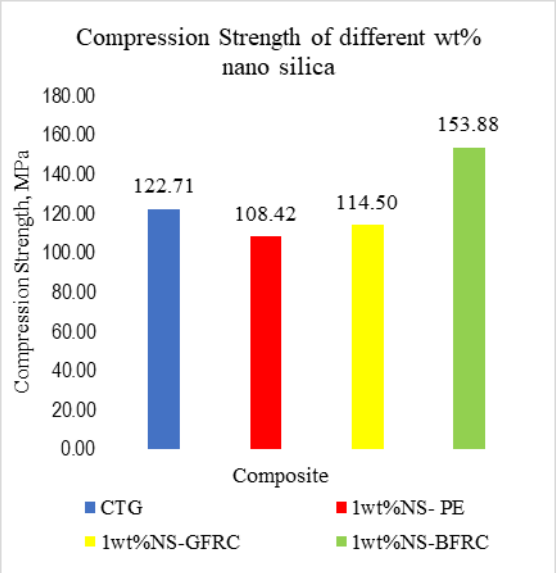

Figure 7: Compression strength of different wt.% nano silica

Based on *Figure 7*, The compressive strength value also increased from 105.93MPa to 114.50MPa with an increasing percentage of 8%. The value is increasing to 153.88.36MPa for BFRC with a 45% increment.

5.0 CONCLUSION

Incorporating nano-silica will increase the tensile, flexural and compression strength values in PE, BFRC and GFRC.

ACKNOWLEDGEMENTS

The authors would like to thank Universiti Teknologi MARA (UiTM) for the research support. This research work is financially supported by the KEPU Grant no: 600-RMC/KEPU 5/3 (016/2021) and DINAMIK Grant.

REFERENCES

1. Abdel-Rahim, R. H., Attallah, M. S., & Mohammed, R. A. (2022). Investigation the Effect of Nano Silica Dioxide Additives on the Properties of Epoxy Resin for Using in Industrial Applications. *Materials Science Forum*, *1050 MSF*, 103–113. https://doi.org/10.4028/www.scientific.net/MSF.1050.103
2. Agasnalli, C., Hema, H. C., Lakkundi, T., & Chandrappa, K. D. (2022). Integrated assessment of granite and basalt rocks as building materials. *Materials Today: Proceedings*, *62*, 5388–5391. https://doi.org/10.1016/j.matpr.2022.03.546
3. D'Mello, J., D'Souza, A. G., Gowda, S. H., & Pinto, D. (2019). Experimental investigation of compression, flexural strength and damping behaviour of granite particulate epoxy matrix composite. *AIP Conference Proceedings*, *2080*. https://doi.org/10.1063/1.5092895
4. Erkliğ, A. (2022). Influence of Nano-Silica on the Mechanical Properties of Jute/Glass Fiber Reinforced Epoxy Hybrid Composites. Çukurova Üniversitesi. In *Mühendislik Fakültesi Dergisi* (Vol. 37, Issue 2).
5. Kaka, D., Fatah, R. A., Gharib, P., & Mustafa, A. (2021). Mechanical Properties of Polyester Toughened with Nano-Silica. *Iraqi Journal of Industrial Research*, *8*(3). https://doi.org/10.53523/ijoirvol8i3id67
6. Plappert, D., Ganzenmüller, G. C., May, M., & Beisel, S. (2020). Mechanical properties of a unidirectional basalt-fiber/epoxy composite. *Journal of Composites Science*, *4*(3). https://doi.org/10.3390/jcs4030101
7. Quadflieg, T., Srivastava, V. K., Gries, T., & Bhatt, S. (2023). Mechanical Performance of Hybrid Graphene Nanoplates, Fly-Ash, Cement, Silica, and Sand Particles Filled Cross-Ply Carbon Fibre Woven Fabric Reinforced Epoxy Polymer Composites Beam and Column. *Journal of Materials Science Research*, *12*(1), 22. https://doi.org/10.5539/jmsr.v12n1p22

Optimisation in Compressive Strength of Seawater and Zeolite based Geopolymer Foam reinforced with Nanocellulose

Chai Hua **Tay**[1], Norkhairunnisa **Mazlan**[2,3,4*], Aimrun **Wayayok**[5], Mohd Salahuddin **Basri**[6], Mohd Mustafa **Albakri Abdullah**[7]

[1]Institute of Tropical Foresty and Forest Product, Universiti Putra Malaysia, 43400 Serdang, Selangor, Malaysia
[2] Department of Aerospace Engineering, Faculty of Engineering, Universiti Putra Malaysia, 43400 UPM Serdang, Selangor
[3] Institute of Nanoscience and Nanotechnology (ION2), Universiti Putra Malaysia, 43400 UPM Serdang, Selangor
[4] Aerospace Malaysia Research Center, Universiti Putra Malaysia, 43400 UPM Serdang, Selangor
[5] Department of Biological and Agriculture Engineering, Universiti Putra Malaysia, 43400 Serdang, Selangor, Malaysia
[6] Department of Process and Food Engineering, Universiti Putra Malaysia, 43400 Serdang, Selangor, Malaysia
[7] Construction Materials Engineering and Technology at Center of Excellence, UniMAP, 01000 Kangar, Perlis, Malaysia
line 2-City, Country

*Corresponding author's phone: +603-9769 6403
E-mail: norkhairunnisa@upm.edu.my

ABSTRACT

Geopolymer Foam (GF) is an innovative and extension product of geopolymer with additional porosity. This provides the material with the advantages that comes with being porous while benefiting from the basic properties of a common geopolymer. Although numerous studies are reported on geopolymer foam, none has reported on the optimization in its compressive strength which is essentially critical in determining its suitability for various applications. The scope of this research is to optimize and validate the best combination of factors that produces the highest compressive strength of GF. A Central Composite Design (CCD) comprising four factors and five levels, which are Seawater/Potassium Silicate (SW/KSil: 1, 1.05, 1.1, 1.15, 1.2), Potassium Hydroxide/Potassium Chloride (KOH/KCl: 20/80, 40/60, 60/40, 80/20, 100/0), Sodium Laureth Ether Sulfate/Benzalkonium Chloride (SLES/BAC: 0/100, 25/75, 50/50, 75/25, 100/0), and Hydrogen Peroxide/Nanocellulose (H_2O_2/NC: 0/100, 25/75, 50/50, 75/25, 100/0), and five levels respectively, with two replications chosen, totalling up to 62 experimental runs. ANOVA data revealed that all factors are significant with p-value < 0.05. The optimized design is found to be at SW/KSil=1.03, KOH/KCl=90.30/9.70, SLES/BAC=0/100 and H_2O_2/NC of 0/100. The experimental validation showed an average error of 3.369%.

Keywords— Response Surface Methodology; Geopolymer Foam; Nanocellulose; Compressive Strength; Optimization

1.0 INTRODUCTION

Compressive strength is a critical property in ensuring the functionality of GF in applications it is intended for. It has been intensively studied that the compressive strength of geopolymer is influenced by factors like the chemical composition of aluminosilicates, the amount of aggregates present, the type and concentration of alkaline solutions, the curing temperature

and period, and the ratio of water to solid [1]. In the context of GF, an extensive study is required on the similar matter as there are additional factors that influence the compressive strength of the material. This is because of the presence of new chemicals like foaming agent and surfactants which are required to produce foam and stabilize foam respectively. Consequently, the distribution and dimension of resultant pores will affect the compressive strength of GF. To the best of authors' knowledge, no study is reported on the optimization of compressive strength in geopolymer foam.

2.0 THEORY/LITERATURE REVIEW

Geopolymer is an aluminosilicate binder that resulted from the synthesis between aluminosilicates and alkaline solutions [2]. Ocassionally, acidic medium is used as well in producing geopolymer material [3]. The growing attention that geopolymer received is well founded as the material offers advantages which include the utilization of industrial byproducts [4] and low carbon footprint [5] resulting in positive environmental impact. In addition to that, geopolymers are also reported for its higher strength compared to Ordinary Portland Cement [6].

Geopolymer Foams (GF) as the name suggests, are foamed, porous, aerated and lightweight versions of geopolymers. By introducing varying porosity dimension and distribution, GF offers numerous appealing applications as lightweight concrete [7], adsorption of toxic materials [8], thermal insulator [9], catalyst [10] and pH regulator [11]. However, with the introduction of porosity within the geopolymer structure, it is only natural that its strength will degrade.

In this study, the optimization in compressive strength of seawater and zeolite based geopolymer foam reinforced with nanocellulose is conducted. Through Response Surface Methodology (RSM), the effect of four factors on the compressive strength of geopolymer foam is studied. These four factors consist of eight materials which are Seawater, Potassium Silicate, Potassium Hydroxide, Potassium Chloride, Sodium Laureth Ether Sulfate, Benzalkonium Chloride, Hydrogen Peroxide and Nanocellulose.

3.0 MATERIALS

Zeolite powder obtained from West Java, Indonesia, was sieved through 200 mesh openings to obtain finer particle size. Seawater was collected from Dataran 1 Malaysia, Melaka, Malaysia. Potassium Silicate (KSil), Potassium Hydroxide (KOH), and Potassium Chloride (KCl) were purchased from Sigma Aldrich. The elemental compositions of Zeolite, Seawater and KSil are displayed in Table 1. Foaming agent Hydrogen Peroxide (H_2O_2) with 30% concentration was purchased from R&M Chemicals, Sodium Lauryl Ether Sulphate (SLES) was purchased from Evachem, while Benzalkonium Chloride (BAC) with 80% concentration was purchased from Chemiz. Nanocellulose (NC) with width <50 nm and length >100 um, and concentration of 2.0 %(w/v) in distilled water was produced by ZoepNano.

TABLE I: Elemental compositions of Zeolites, Seawater and Potassium Silicate

Zeolite						
Component	CaO	SiO_2	Fe_2O_3	Al_2O_3	K_2O	MgO
Concentration (%)	70.400	16.900	6.220	2.260	1.580	0.949
Seawater						
Component	Cl	Na	Mg	K		
Concentration (%)	1.89	1.33	0.096	0.08		
Potassium Silicate						
Component	SiO_2	K_2O				
Concentration (%)	23.49	10.77				

4.0 EXPERIMENTAL

4.1 Design of Experiment using Response Surface Methodology

The experiment was designed using four factors, which are SW/KSil (V_1), KOH/KCl (V_2), SLES/BAC (V_3) and H_2O_2/NC (V_4) in MINITAB software. The response compressive strength is assumed to be influenced by these factors. A Central Composite Design (CCD) comprising the four factors and five levels, with two

replications were chosen, totalling up to 62 experimental runs. The factors were chosen based on literature review while their levels were decided based on preliminary testing, which allows for workability during stirring and structure rigidity when immersed under water. The factors and their levels are displayed in Table 2. An Analysis of Variance (ANOVA) was used to calculate the significance of the main factors and their interactions. The value of 95% was set as the significance level, which reflects the ρ-value of 0.05.

TABLE II: Factors and Levels

Factors	Unit	Note[a]	Levels				
			-2	-1	0	1	2
SW/KSil	g	V_1	1	1.05	1.1	1.15	1.2
KOH/KCl	%/%	V_2	20/80	40/60	60/40	80/20	100/0
SLES/BAC	%/%	V_3	0/100	25/75	50/50	75/25	100/0
H_2O_2/NC	%/%	V_4	0/100	25/75	50/50	75/25	100/0

[a] Notation

4.2 Geopolymer Foam Formulation

Zeolite and KSil are kept constant at a ratio 5:1. Therefore, the varying SW/KSil ratio is translated as constant KSil but varying seawater content. The SW/KSil ratio was calculated based on their weight in grams. KOH/KCl was prepared at 10wt% of KSil. This produces KOH solution with concentration ranging from 0.297M to 1.782M. The KOH/KCl ratio was calculated based on their percentage to 10wt% of KSil. For example, when 10wt% of KSil is equal to 10g, a KOH/KCl ratio 20/80 means 2g of KOH and 8g of KCl are used. SLES/BAC is weighed at 0.05wt% of basic geopolymer slurry while H_2O_2/NC at 0.4 wt% of basic geopolymer slurry. Basic geopolymer slurry consists of Zeolites, Seawater, KSil, KOH and KCl. SLES/BAC and H_2O_2/NC ratios are calculated similarly as KOH/KCl.

4.3 Geopolymer Foam Fabrication

The fabrication was done following the method published by the author [12].

4.4 Compressive Testing Analysis

The compressive test was performed in accordance with ASTM D695 by using Instron Universal Testing Machine (UTM) with a load cell of 30kN. The compressive specimens were loaded at a rate of 1.3mm/min. The specimens have dimensions of 1.5 cm (height), 1cm (width) and 1cm (length).

4.5 Morphological Analysis

Morphological analysis was conducted using FEI NOVA NANOSEM230. Samples were first placed on aluminum sample stubs by using carbon conductive tape. Then the samples were coated with platinum, before being vacuumed in a sample chamber for viewing.

5.0 RESULTS AND DISCUSSION

The compressive strength of selected samples is shown in Table 3.

TABLE III: The compressive strength of selected samples

Sample	Factors				CS[b]
	SW/KSil	KOH/KCl	SLES/BAC	H_2O_2/NC	
S1	1.1	60/40	50/50	50/50	0.05842
S2	1.1	60/40	50/50	100/0	0.03908
S3	1.05	80/20	75/25	75/25	0.04695
S4	1.1	60/40	50/50	0/100	0.19412
S5	1.15	80/20	25/75	75/25	0.0366
S6	1.1	60/40	50/50	50/50	0.06331
S7	1.05	40/60	75/25	25/75	0.0537
S8	1.1	60/40	100/0	50/50	0.0631

[b] Compressive Strength (MPa)

5.1 Statistical Analysis of Compressive Strength

The ANOVA table is displayed in Table 4. The results showed that all four terms, three squared terms and three interaction terms are highly significant at p-value < 0.05. However, the square term V_2*V_2 and interactions terms V_1*V_2, V_1*V_3, and V_1*V_4 are less significant with p-value of 0.067, 0.879, 0.072 and 0.229 respectively. Values for R^2 = 0.9036 and R^2(adj)=0.8749 are very high, indicating that 90.36% of the sample variation in the response was attributed to the independent variables. The term H_2O_2/NC has the highest absolute

coefficient value of 0.046918, indicating that it has the strongest effect on the compressive strength of geopolymer foam. Equation represents the regression model for compressive strength. The equation can be used to calculate and analyze the effect of factors on compressive strength of geopolymer foam.

TABLE IV: ANOVA table for Compressive Strength

Term	Notation	Coef.	SE Coef.	*p*
Constant		0.081005	0.006794	0
SW/KSil	V_1	-0.011182	0.003669	0.004
KOH/KCl	V_2	0.027446	0.003669	0
SLES/BAC	V_3	-0.026533	0.003669	0
H_2O_2/NC	V_4	-0.046918	0.003669	0
Square Term				
SW/KSil*SW/KSil	V_1*V_1	-0.006988	0.003361	0.043
KOH/KCl*KOH/KCl	V_2*V_2	0.006293	0.003361	0.067
SLES/BAC*SLES/BAC	V_3*V_3	0.007274	0.003361	0.036
H_2O_2/NC*H_2O_2/NC	V_4*V_4	0.008851	0.003361	0.011
Interaction Term				
SW/KSil*KOH/KCl	V_1*V_2	0.000685	0.004494	0.879
SW/KSil*SLES/BAC	V_1*V_3	0.008284	0.004494	0.072
SW/KSil*H_2O_2/NC	V_1*V_4	0.005478	0.004494	0.229
KOH/KCl*SLES/BAC	V_2*V_3	-0.02256	0.004494	0
KOH/KCl*H_2O_2/NC	V_2*V_4	-0.030361	0.004494	0
SLES/BAC*H_2O_2/NC	V_3*V_4	0.035934	0.004494	0
R^2 = 90.36% R^2(adj)= 87.49%				

$$Y_{CS} = 0.081005 - 0.011182V_1 + 0.027446V_2 - 0.026533V_3 - 0.046918V_4 - 0.006988V_1V_1 + 0.006293V_2V_2 + 0.007274V_3V_3 + 0.008851V_4V_4 + 0.000685V_1V_2 + 0.008284V_1V_3 + 0.005478V_1V_4 - 0.02256V_2V_3 - 0.030361V_2V_4 + 0.035934V_3V_4. \quad (1)$$

5.2 Effect of Factors on Compressive Strength

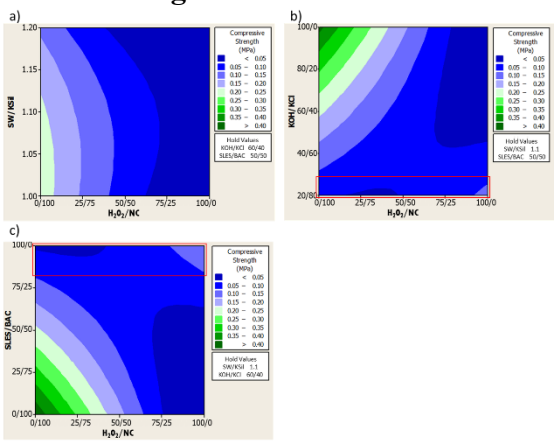

Fig. 1: Compressive strength contour plot with H_2O_2/NC versus a) SW/KSil, b) KOH/KCl and c) SLES/BAC

In Fig. 1a), Fig. 1b) and Fig. 1c), all parts of the contour plots (except for those within red rectangles) display high compressive strength at low H_2O_2/NC ratio. As a foaming agent, the presence of high H_2O_2 is expected to induce high porosity in the geopolymer structure. Depending on the content of other factors such as water and surfactant, the stabilization of foam will be impacted. However, generally from Fig. 1a), Fig. 1b) and Fig. 1c), the increasing H_2O_2 content leads to a lower compressive strength. This is similarly reported by published work [13, 14, 15, 16].

At a low H_2O_2/NC ratio, the high presence of NC in all the contour plots of Fig. 1a), Fig. 1b) and Fig. 1c) displays a region of highest compressive strength achieved. This indicates that NC enhanced the compressive strength of geopolymer foam. Fig. 2 displays the microscopical images of S26 that are composed of SW/KSil = 1.05, KOH/KCl = 40/60, SLES/BAC = 75/25 and H_2O_2/NC = 75/25. In Fig. 2a), it can be observed that there is presence of geopolymers adhered to the NC. A clearer display of the adhesion can be seen in Fig. 2b). This is an indication that there is strong interfacial adhesion between the nanoparticle with geopolymer matrix, as supported by other published work [17]. Fig. 2a) also depicts the well distributed NC in geopolymer, which may also contribute to the enhanced compressive strength.

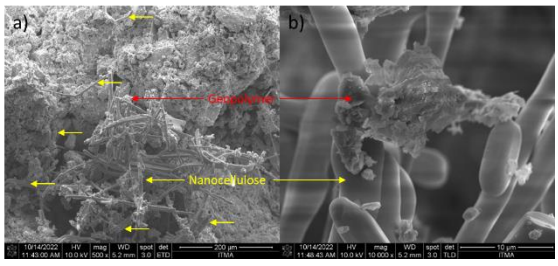

Fig. 2: Microscopical images showing geopolymer adhesion onto nanocellulose at a) 500x and b) 10,000x magnification.

In Fig. 1a), the higher seawater content (which also means higher water content), displays a slight decrease in compressive strength. This is due to the higher presence of excessive water content that is not

involved in geopolymer backbone, leading to higher water evaporation which leaves behind vacancies in the geopolymer structure. Consequently, this lowers the compressive strength.

In Fig. 1b), at low KOH/KCl ratio, increasing H_2O_2/NC content leads to an increasing compressive strength. During low KOH/KCl ratio, the dissolution of zeolite is low. The increasing presence of foaming agent which leads to high foaming then distributes the slurry to its surroundings. The coupling effect results in distribution of geopolymer slurry that fills in the void of unreacted zeolite, filling in spaces that previously would contribute to low compressive strength. As a result, this leads to higher compressive strength with increasing H_2O_2 content. As KOH/KCl increases, increasing H_2O_2/NC leads to a decreasing compressive strength. This is because at higher KOH/KCl ratio, the dissolution of zeolite is higher. This means that there are less vacancies due to lower unreacted zeolite. When H_2O_2/NC ratio is increased, the decreasing compressive strength is due to increasing presence of pores. The higher the H_2O_2 content, the more foaming occurred, leading to higher pore formation which leads to lower compressive strength.

In Fig. 1c), at low SLES/BAC, increasing H_2O_2/NC content shows a decreasing compressive strength. At low SLES/BAC ratio, the surface tension of geopolymer slurry is high, thus increasing H_2O_2 content and therefore increasing foaming is not able to be sustained by the surfactant, leading to collapsing foam. At higher SLES/BAC ratio, increasing H_2O_2/NC content shows a slightly increasing compressive strength. It is possible that the viscosity at maximized SLES/BAC and H_2O_2/NC reached a viscosity where foaming is optimized, thus the pores are well distributed with low chance of foam coalescence among them. This reduces the weak point in geopolymer which increases the compressive strength.

Optimization of the Compressive Strength

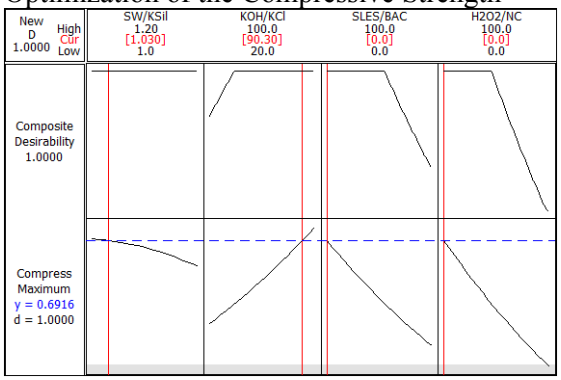

Fig. 3: Optimization plot of compressive strength

Optimization plot for compressive strength is shown in Fig. 3. The objective is to optimize compressive strength. The composite desirability calculated is 1, proving that the parameters used are well within the experimental range. The optimized values are SW/KSil of 1.03, KOH/KCl of 90.30/9.70, SLES/BAC of 0/100 and H_2O_2/NC of 0/100.

Experimental Validation

TABLE V: Experiment Validation.

Sample	Experimental value (MPa)	Predicted Value (MPa)	Error (%)
SV1	0.705	0.692	1.922
SV2	0.665	0.692	3.810
SV3	0.661	0.692	4.374
Average error			3.369

From Table 5, the average error for compressive strength is around 3.4% which is well below 15%. This concludes that the regression model used in this method can optimize the compressive strength.

6.0 CONCLUSION

RSM was successful in identifying the significant factors of compressive strength in Geopolymer Foam. Result shows that SW/KSil, KOH/KCl, SLES/BAC and H_2O_2/NC are all significant factors in this study. The term H_2O_2/NC has the strongest effect on the compressive strength of geopolymer foam. Through experimental validation with an average error of 3.369%, it is concluded that the developed regression model has successfully optimized the compressive strength accurately.

ACKNOWLEDGEMENTS

This project was supported by KPT under FRGS/1/2019/TK05/UPM/02/14. The authors declare no conflict of interest.

REFERENCES

1. Ahmed, H. U., Mohammed, A. S., Qaidi, S. M., Faraj, R. H., Hamah Sor, N., & Mohammed, A. A. (2023). Compressive strength of geopolymer concrete composites: a systematic comprehensive review, analysis and modeling. European Journal of Environmental and Civil Engineering, 27(3), 1383-1428.
2. Davidovits, J. (2009). Geopolymer chemistry and applications book. Geopolymer Institute, St Quentin, France.
3. Nikolov, A. (2020). Alkali and acid activated geopolymers based on iron-silicate fines—By-product from copper industry. Int. Sci. J. Mach. Technol. Mater, 14, 37-39.
4. Azad, N. M., & Samarakoon, S. S. M. (2021). Utilization of industrial by-products/waste to manufacture geopolymer cement/concrete. Sustainability, 13(2), 873.
5. Sotelo-Piña, C., Aguilera-González, E. N., & Martínez-Luévanos, A. (2019). Geopolymers: Past, present, and future of low carbon footprint eco-materials. Handbook of Ecomaterials, 4, 2765-85.
6. Bakri, A. M., Kamarudin, H., Binhussain, M., Nizar, I. K., Rafiza, A. R., & Zarina, Y. (2013). Comparison of geopolymer fly ash and ordinary portland cement to the strength of concrete. Advanced Science Letters, 19(12), 3592-3595.
7. Masoule, M. S. T., Bahrami, N., Karimzadeh, M., Mohasanati, B., Shoaei, P., Ameri, F., & Ozbakkaloglu, T. (2022). Lightweight geopolymer concrete: A critical review on the feasibility, mixture design, durability properties, and microstructure. Ceramics International, 48(8), 10347-10371.
8. Ramos, F. J. H. T. V., Marques, M. D. F. V., Rodrigues, J. G. P., de Oliveira Aguiar, V., da Luz, F. S., de Azevedo, A. R. G., & Monteiro, S. N. (2022). Development of novel geopolymeric foam composites coated with polylactic acid to remove heavy metals from contaminated water. Case Studies in Construction Materials, 16, e00795.
9. Bai, C., Franchin, G., Elsayed, H., Zaggia, A., Conte, L., Li, H., & Colombo, P. (2017). High-porosity geopolymer foams with tailored porosity for thermal insulation and wastewater treatment. Journal of Materials Research, 32(17), 3251-3259.
10. Utsumi, T., Terasawa, T., Kudo, I., Suzuki, T., Nakayama, T., Suematsu, H., & Ogawa, T. (2020). Preparation of potassium and metakaolin based geopolymer foam with millimeter sized open pores for hydrogen recombining catalyst supports. Journal of the Ceramic Society of Japan, 128(2), 96-100.
11. Bumanis, G. (2015). The effect of alkaline material particle size on adjustment ability of buffer capacity. Materials Science, 21(3), 405-409.
12. Tay, C. H., Mazlan, N., Wayayok, A., Basri, M. S., Mustafa, M., & Abdullah, A. (2022). Nanocellulose reinforced zeolite based geopolymer concrete: Density analysis through response surface methodology. Materials Today: Proceedings, 66, 2873-2882.
13. Surya, I., & Ismail, H. (2019, May). The degree of filler dispersion, rheometric and mechanical properties of carbon black-filled styrene-butadiene rubber composites in the presence of alkanolamide. In IOP Conference Series: Materials Science and Engineering (Vol. 523, No. 1, p. 012063). IOP Publishing.
14. Walbrück, K., Drewler, L., Witzleben, S., & Stephan, D. (2021). Factors influencing thermal conductivity and compressive strength of natural fiber-reinforced geopolymer foams. *Open ceramics*, *5*, 100065.
15. Liu, Y. L., Liu, C., Qian, L. P., Wang, A. G., Sun, D. S., & Guo, D. (2023). Foaming processes and properties of geopolymer foam concrete: Effect of the activator. *Construction and Building Materials*, *391*, 131830.
16. Anggarini, U., Pratapa, S., Purnomo, V., & Sukmana, N. C. (2019). A comparative study of the utilization of synthetic foaming agent and aluminum powder as pore-forming agents in lightweight geopolymer synthesis. *Open Chemistry*, *17*(1), 629-638.
17. Sapiai, N., Jumahat, A., Manap, N., & Usoff, M. A. I. (2015). Effect of nanofillers dispersion on mechanical properties of clay/epoxy and silica/epoxy nanocomposites. *J. Teknol*, *76*, 107-111.

Neolamarckia Cadamba Nanofibrillated Filter Paper for Textile Wastewater Treatment via Cross-Flow Filtration System: Performance and Fouling Mechanism

Siti Solehah Ahmad **Norrahma**[1], Nor Hazren Abdul **Hamid**[1,*], Nur Hanis Hayati **Hairom**[2], Latifah **Jasmani**[3]

[1] Faculty of Engineering Technology, Universiti Tun Hussein Onn Malaysia, Pagoh Higher Education Hub, KM 1, Jalan Panchor, 84600, Muar, Johor, Malaysia
[2] Microelectronic and Nanotechnology-Shamsuddin Research Centre (MiNT-SRC), Faculty of Electrical and Electronic Engineering, Universiti Tun Hussein Onn Malaysia, 86400, Parit Raja, Batu Pahat, Johor, Malaysia
[3] Pulp and Paper Branch, Forest Products Division, Forest Research Institute Malaysia, 52109, Kepong, Selangor, Malaysia

*Corresponding author's phone: +60174023278
Email: norhazren@uthm.edu.my

ABSTRACT

An approach presented on the textile wastewater treatment by using nanofibrillated (NFC) filter paper prepared from renewable resources (*Neolamarckia cadamba*) via cross-flow filtration system with different operating parameters (cellulose dosage, pH and initial feed concentration). The best operating conditions of the cross-flow filtration system were obtained at an initial pH 6.5 and 100% of initial feed concentration of textile wastewater with a 60:40 cellulose dosage of NFC filter paper. The mechanisms of membrane fouling were investigated using model fitting according to the Wiesner and Aptel equations revealed that cake formation occurred rapidly at both stages of the fouling mechanism. Thus, overall results revealed that this study has a great deal of promise to serve as a benchmark for an efficient and viable way to treat textile wastewater.

Keywords—Nanocellulose fibre; Filtration; Textile wastewater; Flux; Membrane fouling mechanism

1.0 INTRODUCTION

Large amounts of industrial effluent containing dye have been released because of the textile industries' usage of synthetic chemical dyes in the various textile processing activities, such as dyeing, printing, bleaching, and finishing procedures.

In collaboration with the Forest Research Institute Malaysia (FRIM), the starting material for this research came from plantation forests in Malaysia that are renewable resources. *Neolamarckia cadamba*, also known as the kelempayan tree locally, was the type of renewable resource that was extracted into the NFC form and then subjected to an enzymatic pre-treatment in order for the production filter paper.

The originality and novelty of this study come from the fact that the modification of nanofibrillated cellulose (NFC) from the renewable resource of Malaysian plantation forest (*Neolamarckia cadamba*) in the form of filter paper and its performance to treat textile wastewater via cross-flow filtration system. The effects of

different parameters such as cellulose dosage, initial pH and initial dye concentration was also investigated in the present study. Blocking mechanism approaches was used to explain the development of nanocellulose filter paper fouling which leads to the permeation flux decline.

2.0 THEORY/LITERATURE REVIEW

Approximately 10,000 different dyes are currently employed in the textile industry [1]. In order to remove dye from wastewater solution, industrial practitioners have used a variety of important treatments, including photocatalytic reactors that use novel nanomaterials, advanced oxidation processes (AOP), electrocoagulation, and nanofiltration membrane technology [2].

Recent studies on nanocellulose-based materials for novel nanotechnology wastewater treatment have been carried out as its great potential green technology for removing different types of pollutants due to their high surface area, binding and adsorbing capabilities [3]. The fabrication of nanopapers from nanocellulose-based materials have been widely explored for various [4], [5], [6], [7]. Unfortunately, these nanopapers were too dense to permit high water permeance and, thus, efficiency. While providing enough surface area for dissolved ions to adsorb during water passage through the filter, it may be hypothesised that covering a substrate made of typical natural fibres with charged nanocellulose would enable high permeance while maintaining high porosity and pore size [8].

Wiesner and Aptel equations were used to determine the fouling mechanism. The model was consisted of complete blocking, standard blocking, intermediate blocking and cake formation mechanism.

3.0 MATERIALS

Sulphuric acid (96%) was purchased from Fisher Scientific (UK) and fully hydrolysed polyvinyl alcohol (PVA) was obtained from Sigma Aldrich (US). Sodium hydroxide, sodium sulphide, ethanol and toluene were purchased from R&M Chemical (UK), glacial acetic acid from Ajax Finechem (Australia) and sodium chlorite from Merck (USA).

4.0 EXPERIMENTAL

4.1 Textile wastewater sample

Textile wastewater originated and was produced in a textile factory in Johor, Malaysia.

4.2 NFC filter paper modification

Nanofibrillated cellulose (NFC) from *Neolamarckia cadamba* was prepared according to the prior research [9] for kraft pulping and bleaching process. The process continues by using enzymatic pre-treatment from *Aspergillus niger* cellulase enzyme.

4.3 Experimental set-up

The permeation experiment was initiated by wetting out the NFC filter paper at 3 bars pressure for 30 minutes with distilled water and conducted via cross-flow filtration system (Sterlitech™ HP4750, USA) which consists of 20.60 cm^2 effective membrane area. A schematic of the filtration system was shown in Fig. 1.

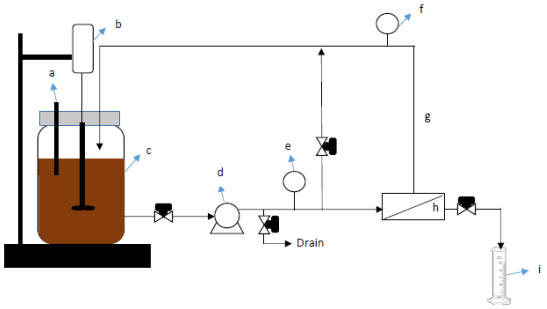

Fig. 1 Schematic diagram of cross-flow filtration system: a) feed, b) overhead stirrer with stand, c) reactor, d) pump, e & f) pressure gauge, g) recycle flow, h) membrane filtration system and i) measuring cylinder.

4.4 Analytical methods

The colour intensity of the samples was measured using a UV-Vis spectrophotometer (DR6000, Hach Company, USA).

4.5 Flux decline analysis

The pure water flux (J_0) of each NFC filter paper sample were specified by calculating the volume of permeate (V) per unit area (A) per unit of time (t) according to the following equation:

$$J_0 = \frac{V}{At} \quad (1)$$

The instantaneous permeate flux (J) at each run was calculated in the time intervals t_1 and t_2 by:

$$J = \frac{V_2 - V_1}{A(t_2 - t_1)} \quad (2)$$

Subsequently, in order to investigate the NFC filter paper performances under various parameters, the flux was normalised through Equation (6). The graph was plotted as normalised flux against operating time for comparison and analysis of the permeate flux decline.

$$Normalised\ flux = \frac{Solution\ flux, J}{Pure\ water\ flux, J_0} \quad (3)$$

4.7 Membrane fouling mechanism

The primary programme used to calculate and plot the graph of the y-axis and the x-axis in accordance with the blocking filtration rules versus time was MATLAB R2023b.

5.0 RESULTS AND DISCUSSION

5.1 Permeability performance of NFC filter paper

Water permeability test is used to measure the fabricated NFC filter paper ability to retain or interact with the cross-flow filtration system without the presence of pollutants. Smaller value of water permeability of NFC filter paper may indicate more fibrous and less void spaces exist between the NFC molecules which increases the barrier of water molecules entering the filter paper surface.

5.2 Effect of cellulose dosage

In Fig. 2 showed the final normalized flux reading after 2 hours operating for NFC filter paper dosage of 50:50, 60:40, 70:30 and 80:20 was 0.0879, 0.7397, 1.2479 and 0.5403, respectively. The results showed in Table 1 below indicated the colour removal percentage after 2 hours operation.

This condition could be explained by different size of wastewater molecules which interacted and pass through the fibrous network of cellulose and limited void spaces, thus resulting in blocking and fouling effect on the filter paper surface. Therefore, it could be concluded that the optimum condition for cellulose dosage of NFC filter paper was at 60:40 in this present study.

Table 1 Percentage of wastewater removal under various cellulose dosages

Cellulose dosage	Colour removal (%)
50:50	53.99
60:40	90.56
70:30	89.45
80:20	84.76

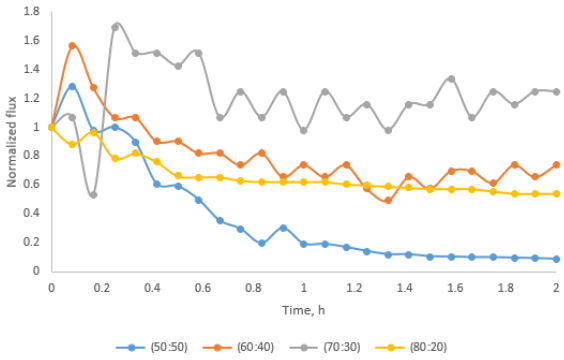

Fig. 2 The normalised flux against time for the different cellulose dosage of NFC filter paper

5.3 Effect of initial pH

Fig. 3 shows the value of normalized flux can be best described in the descending order of pH 3 (1.0926) > pH 6.5 (0.7397) > pH 4 (0.7221) > pH 9 (0.4969) > pH 10 (0.3719). According to [10], flux reduction or fouling decline phenomenon would occur when the pH of solution was adjusted from 3 (acidic) to 10 (alkaline) which indicated that higher pH solution improved the flux reading. The removal of the pollutants achieved by these lowest and highest pH value were considered high and low as in 87.75% and 81.24%, respectively.

In term of decolourization efficiency, pH 6.5 showed highest colour removal percentage as much 90.56% with the normalized flux at 0.7396. Meanwhile, other pH values showed lower percentage colour removal which below 90% value. Therefore, this indicated that pH 6.5 is the optimum initial pH of textile wastewater removal for the cross-flow filtration system.

Table 2 Percentage of wastewater removal under various pH solution.

Solution pH	Colour removal (%)
3	87.75
4	89.29
6.5	90.56
9	81.87
10	81.24

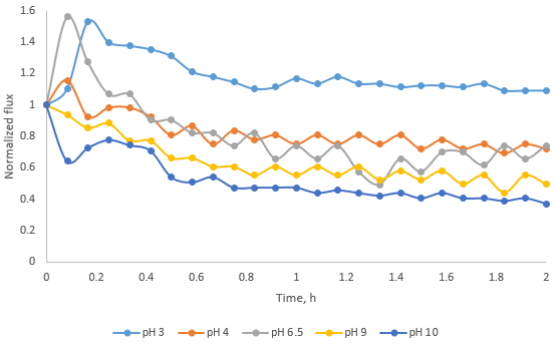

Fig. 3 The normalised flux against time for the different pH initial feed concentration of wastewater

5.4 Effect of initial feed concentration

Fig. 4 illustrated the normalized flux decline analysis could be indicated in the descending order started with initial concentration of 80% (0.8432) >100% (0.7397) >50% (0.7063). Basically, the concentration polarization of the pollutant's molecules on the NFC filter paper was the potentially reason for the contribution of the flux decline which cause the pore blocking in the fibrous network of the cellulose and created further resistance for the liquid transportation through the filter paper [11].

Table 3 showed that as the initial feed concentration of wastewater solution increased, the percentage of colour removal also increased. Overall, the optimum condition regarding the removal of wastewater solution by using cross-flow filtration system for this study was best described at 60:40 cellulose dosage of NFC filter at pH 6.5 with 100% initial feed solution.

Table 3 Percentage of wastewater removal under different initial feed concentration

Wastewater dilution (%)	Colour removal (%)
100	90.56
75	82.14
50	79.70

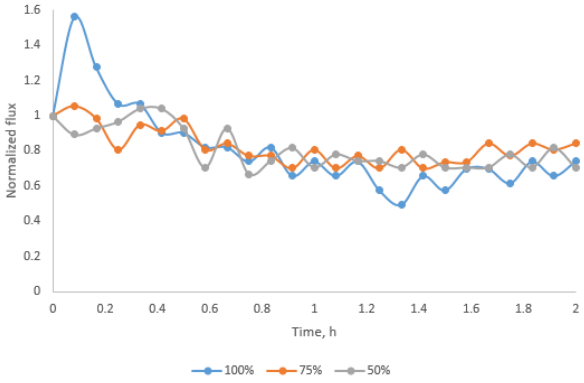

Fig. 4 The normalised flux against time for the different initial concentration of textile wastewater

5.5 Fouling mechanism

Fig. 5 showed the fitting of experimental data based on the equations of Wiesner and Aptel, meanwhile Table 11 presented the corresponding correlation coefficients (R^2) and fitted parameter constant, *K*, to indicate the best fit model. The highest value of R^2 means that the model was suitable to describe the fouling mechanism.

According to the data in Table 4, the cake filtration mechanism was fitted well to the experimental results with R^2 value of 0.9782. As expected, the result indicated that a rapid cake formation occurred at the initial stage and the second stage held the progress of cake formation growing. This phenomenon can be explained by the fact that due to the variation of pollutants particles size of textile wastewater solution which are larger than the size of the NFC fibre networks and the void spaces. The deposition of the pollutants molecules on the filter paper surface which resulted from the higher interaction between them and consequently formed a dense and thick cake layer on the surface could be occured [12].

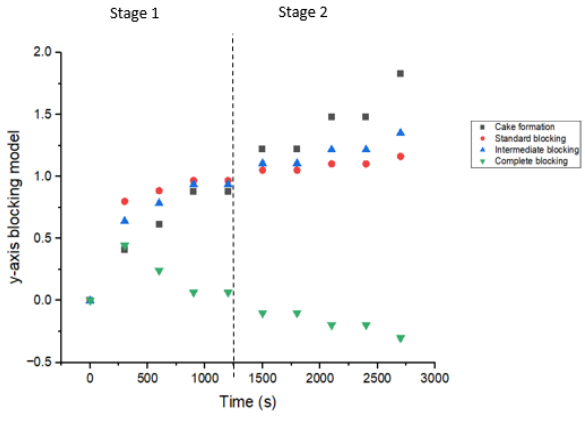

Fig. 5 Fouling mechanism model for NFC filter paper at optimum conditions

Table 4 Rate constant for NFC filter paper under optimum condition

Blocking filtration laws	Stage 1	
	R^2	K (s^{-1})
Intermediate blocking	0.8574	3.543
Standard blocking	0.7430	3.586
Complete blocking	< 1.0	< 0.1
Cake filtration	0.9782	3.401
Blocking filtration laws	**Stage 2**	
	R^2	K (s^{-1})
Intermediate blocking	0.9166	0.8648
Standard blocking	0.9108	0.4052
Complete blocking	0.9029	< 0.1
Cake filtration	0.9218	1.984

6.0 CONCLUSION

The optimum operational conditions of NFC filter paper in the cross-flow filtration system were determined at pH 6.5 of 100% of initial feed concentration textile wastewater with 60:40 cellulose dosage content showed maximum dye rejection (90.56%) and minimum membrane flux decline (0.7397). The Wiesner and Aptel equations showed that under ideal circumstances, both steps of the membrane fouling mechanism for the NFC filter paper conformed to the cake filtration model. Therefore, this research has proved and presented a novel, alternative and advance method in nanofiltration technology by using NFC as medium in filter paper formation to solve dye and wastewater removal treatment problems in the industry.

ACKNOWLEDGEMENTS

Author would like to acknowledge Forest Research Institute Malaysia (FRIM) for providing the lab instrument for the preparation of NFC filter paper. The authors would like to thank the Ministry of Education Malaysia for supporting this research under Fundamental Research Grant Scheme (Code Grant: RACER/1/2019/TK10/UTHM//1 and partially sponsored by Universiti Tun Hussein Onn Malaysia

REFERENCES

[1] I. N. H. M. Amin and M. H. M. Nizam, "Assessment of membrane fouling indices during removal of reactive dye from batik wastewater," *Journal of Water Reuse and Desalination*, vol. 6, no. 4, pp. 505–514, Dec. 2016, doi: 10.2166/wrd.2016.072.

[2] S. Samsami, M. Mohamadi, M. H. Sarrafzadeh, E. R. Rene, and M. Firoozbahr, "Recent advances in the treatment of dye-containing wastewater from textile industries: Overview and perspectives," *Process Safety and Environmental Protection*, vol. 143. Institution of Chemical Engineers, pp. 138–163, Nov. 01, 2020. doi: 10.1016/j.psep.2020.05.034.

[3] A. S. Norfarhana, R. A. Ilyas, and N. Ngadi, "A review of nanocellulose adsorptive membrane as multifunctional wastewater treatment," *Carbohydrate Polymers*, vol. 291. Elsevier Ltd, Sep. 01, 2022. doi: 10.1016/j.carbpol.2022.119563.

[4] A. Mautner and A. Bismarck, "Bacterial nanocellulose papers with high porosity for optimized permeance and rejection of nm-sized pollutants," *Carbohydr Polym*, vol. 251, Jan. 2021, doi: 10.1016/j.carbpol.2020.117130.

[5] A. Mautner *et al.*, "Natural fibre-nanocellulose composite filters for the removal of heavy metal ions from water," *Ind Crops Prod*, vol. 133, no. March, pp. 325–332, 2019, doi: 10.1016/j.indcrop.2019.03.032.

[6] H. Sehaqui, A. Mautner, U. Perez De Larraya, N. Pfenninger, P. Tingaut, and T. Zimmermann, "Cationic cellulose nanofibers from waste pulp residues and their nitrate, fluoride, sulphate and phosphate adsorption properties," *Carbohydr Polym*, vol. 135, pp. 334–340, 2016, doi: 10.1016/j.carbpol.2015.08.091.

[7] A. Mautner, T. Kobkeatthawin, and A. Bismarck, "Efficient continuous removal of nitrates from water with cationic cellulose nanopaper membranes," *Resource-Efficient Technologies*, vol. 3, no. 1, pp. 22–28, 2017, doi: 10.1016/j.reffit.2017.01.005.

[8] A. Mautner *et al.*, "Natural fibre-nanocellulose composite filters for the removal of heavy metal ions from water," *Ind Crops Prod*, vol. 133, pp. 325–332, Jul. 2019, doi: 10.1016/j.indcrop.2019.03.032.

[9] J. Latifah, M. Nurrul-Atika, A. Sharmiza, and I. Rushdan, "EXtraction of nanofibrillated cellulose from kelempayan (neolamarckia cadamba) and its use as strength additive in papermaking," *Journal of Tropical Forest Science*, vol. 32, no. 2, pp. 170–178, 2020, doi: 10.26525/JTFS32.2.170.

[10] * Teow, Y. Haan, W. Zhong Huo, S. Takriff, and A. W. Mohammad, "Fouling behaviours of two stages microalgae/membrane filtration system applied to palm oil mill effluent treatment."

[11] R. V. Kumar, L. Goswami, K. Pakshirajan, and G. Pugazhenthi, "Dairy wastewater treatment using a novel low cost tubular ceramic membrane and membrane fouling mechanism using pore blocking models," *Journal of Water Process Engineering*, vol. 13, pp. 168–175, Oct. 2016, doi: 10.1016/j.jwpe.2016.08.012.

[12] H. Mokarizadeh and A. Raisi, "Industrial wastewater treatment using PES UF membranes containing hydrophilic additives: Experimental and modeling of fouling mechanism," *Environ Technol Innov*, vol. 23, Aug. 2021, doi: 10.1016/j.eti.2021.101701.

Enhancing Nucleation of Graphitic Carbon on Carbon Nanotube Basal Planes via Temperature and Gas Flow Rate Control

Ismayadi **Ismail**[1*], Md Shuhazlly **Mamat@Mat Nazir**[2]

[1]Institute of Nanoscience and Nanotechnology (ION2), Universiti Putra Malaysia, 43400 Serdang, Selangor Darul Ehsan, Malaysia.
[2]Department of Physics, Faculty of Science, Universiti Putra Malaysia, 43400 Serdang, Selangor Darul Ehsan, Malaysia

*Corresponding author's phone: +603 9769 7546
E-mail: ismayadi@upm.edu.my

ABSTRACT

Graphenated carbon nanotubes (g-CNTs) amalgamate the unique attributes of 2D graphitic carbon from graphene and 1D carbon nanotubes (CNTs). Single-wall CNTs (SWCNTs) exhibit electronic conductivity, while multi-wall CNTs (MWCNTs) offer structural reinforcement and energy storage. Large-scale graphene synthesis limitations propel the creation of 3D g-CNTs by merging graphene with MWCNTs, resulting in materials with amplified surface area and charge capacity. G-CNTs show potential for supercapacitors and fuel cells, boasting accelerated electron transfer kinetics due to heightened edge density. Our study introduces an innovative single-step floating catalyst chemical vapor deposition (FCCVD) method for synthesizing g-CNT sheets, providing a high-volume-density framework of carbon nanotubes possessing graphene properties. The synthesized sheet-bulk structure holds industrial potential and signifies progress in g-CNT synthesis techniques. The investigation explores temperature and hydrogen gas flow effects on the CNT-to-g-CNT transition, paving the way for scalable g-CNT sheet production.

Keywords— Graphenated Carbon Nanotubes; Single-Step FCCVD Method; Temperature and Gas Flow Effects

1.0 INTRODUCTION

Graphenated carbon nanotubes (g-CNTs) combine 2D graphitic carbon with 1D carbon nanotubes (CNTs). Single-wall CNTs (SWCNTs) are conductive for electronics, while multi-wall CNTs (MWCNTs) offer structural reinforcement and energy storage. Challenges in large-scale graphene synthesis limit its commercial use. Integrating graphene with MWCNTs creates 3D g-CNTs with high surface area and charge capacity. Promising for supercapacitors and fuel cells, g-CNTs exhibit faster electron transfer kinetics due to their edge density. Our work presents a novel single-step FCCVD method to synthesize g-CNTs sheets, a high-volume-density framework of carbon nanotubes with graphene properties. This industrially favorable sheet-bulk form has potential applications, marking advancement in g-CNT synthesis techniques.

2.0 THEORY/LITERATURE REVIEW

The potential of graphenated carbon nanotubes (g-CNTs) lies in their hybrid nature, merging 2D graphitic carbon from graphene with 1D carbon nanotubes (CNTs). Single-wall CNTs (SWCNTs) are prized for their conductivity, suitable for electronic devices, yet demanding precise synthesis control. On the contrary, multi-wall CNTs (MWCNTs) are simpler to produce, suitable for structural reinforcement and

energy storage. Large-scale graphene utilization is restricted due to synthesis complexities, prompting the creation of a 3D g-CNT framework, blending high surface area and edge density, along with scalability and cost-effectiveness [1]. The integration of graphene edges into g-CNTs enhances charge density, elevating surface area and charge capacity. By incorporating graphitic layers with dense CNT volumes, these materials become viable candidates for energy storage applications, particularly in supercapacitors and fuel cells, with faster electron transfer kinetics attributed to heightened edge density [2]. This study addresses the scarcity of reports on macro-scale g-CNT sheets synthesized via a single-step process like FCCVD [3]. Past methods include two-step approaches, including plasma treatments to produce graphitic nanosheets on CNTs [4]. This investigation focuses on the influence of hydrogen gas flow rate and temperature parameters on CNTs-g-CNTs transition, employing a single-step FCCVD process to create industrially adaptable g-CNT sheets that offer ease of scalability [5].

3.0 METHODOLOGY

The g-CNT sheet was fabricated through a direct spinning method using floating catalyst chemical vapor deposition (FCCVD). To prepare the carbon solution, 40 ml of ethanol was employed as the carbon source. The catalyst mixture comprised 2.4 wt% ferrocene and 1.2 wt% thiophene, with a 2:1 ratio. This mixture underwent sonication for 1 hour to ensure homogeneity before being injected into the FCCVD system through a syringe pump. The FCCVD setup included a quartz tube furnace measuring 1.2 m in length, with an outer diameter of 50 mm and an inner diameter of 40 mm. A 1.5 cm diameter stainless steel fitting was placed at the FCCVD inlet, and a rotating spindle was positioned at the quartz tube's end to collect the g-CNT sheet. Refer to Fig. 1 for the schematic construction and optical image of the synthesized g-CNTs.

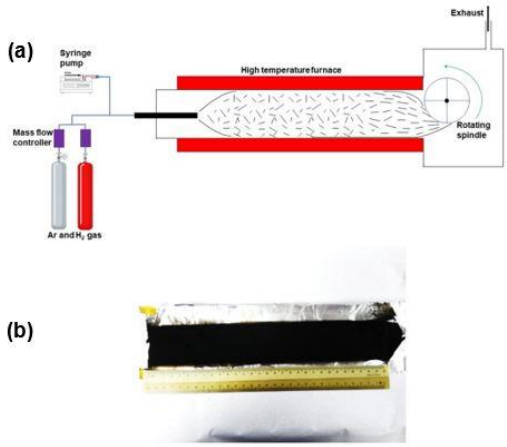

Fig. 1: (a) A schematic diagram of spinning g-CNTs sheet and (b) optical image of synthesized g-CNTs.

Initially, the furnace was heated to a temperature range of 1150–1250°C with an argon gas flow rate of 200 sccm. Once the desired temperature was attained, hydrogen gas was introduced at a flow rate of 200–300 sccm (based on synthesis parameters). The reaction was initiated by injecting the precursor at a rate of 10 ml/h. The synthesized g-CNTs were retrieved from the rotating spindle after cooling the furnace to room temperature under argon flow. Figure 1(b) displays an optical image of the resulting g-CNTs sheet.

To analyze structural properties, HRTEM (JEM 2100F FETEM) at 200 kV accelerating voltage were employed and EDX was used. Raman spectroscopy (Alpha 300R by Witec) used a He-Ne laser with a 532.1 nm emission for excitation. Spectral collection utilized charge-coupled device detectors (CCDs) with an integration time of 5 s per acquisition. Thermo-gravimetric analysis assessed weight loss of the g-CNTs sheet, employing a heating rate of 20°C/min in compressed air at a 50 ml/min rate. Detailed synthesis conditions and sample designations are summarized in Table 1.

Table 1: Synthesis parameters, elemental analysis, purity, Raman analysis, and electrical properties of synthesized samples.

Sample denomination	Parameters			EDX		Purity (%) from EDX analysis	Diameter (nm)	I_D/I_G	Purity (%) calculated from TGA results	I_G'/I_G	Conductivity (S cm^{-1})
	Temperature (°C)	Hydrogen flow rate (sccm)	Injection rate of precursor (ml/hr)	C weight%	Fe weight%						
1250(300)	1250	300	10	100.00	0	93.09	49.61	1.04	93.9	0.71	1.9
1150(300)	1150	300	10	90.99	9.01	92.94	24.63	0.70	88.6	0.82	4.35
1150(250)	1150	250	10	100.00	0	94.85	24.81	0.84	97.1	0.73	0.33
1150(200)	1150	200	10	100.00	0	92.43	25.93	0.88	95.4	0.87	2.63

4.0 RESULTS AND DISCUSSION

Comparing 1150(300) and 1250(300) samples synthesized at 1150°C and 1250°C, same hydrogen flow rate (Fig. 2 (a,b,c,d)), 1150(300) couldn't form g-CNT. Unlike 1250(300), insufficient thermal energy at 1150°C prevented graphitic foliation on CNTs' outer walls. A CNT-to-g-CNT transition occurs between 1150°C and 1250°C due to higher thermal energy at 1250°C. Thermal energy at 1150°C isn't enough for foliation due to short synthesis time compared to 1250°C with same gas flow rate.

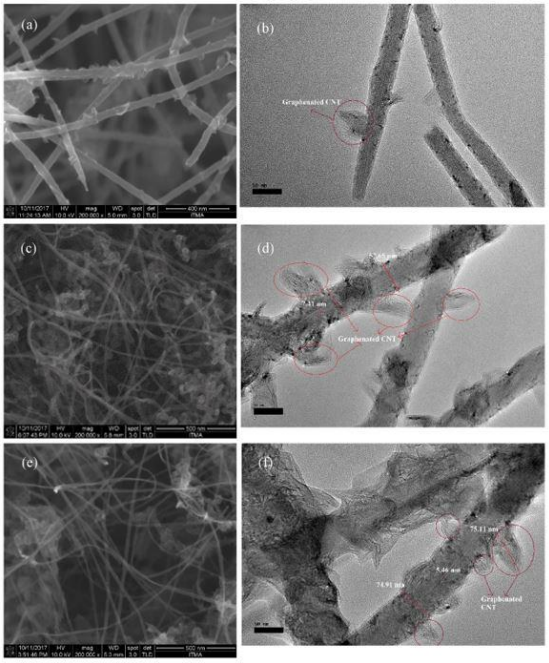

Fig. 2: FESEM and HRTEM images of g-CNTs sheets synthesized using different synthesis parameters of: (a), (b) sample 1250(300); (c), (d) sample 1150(300); (e), (f) sample 1150(250); (g),(h) sample 1150(200).

crystallinity than arc discharge CNTs (Fig.2(a,c,e,g)), with highly curved g-CNTs. Longer g-CNTs are crucial for aerogel formation, enabling extended residence time on the spindle. Agglomeration among g-CNT bundles is common. Due to nanotube bending, high stress results in localized deformations, reducing system energy (sum of in-plane stress and bending energies of CNT walls) [6]. This lowers sheet's mechanical strength, a challenge in superfiber materials.

Altering hydrogen flow rate was carried out to explore residence time impact by reducing flow at 1150°C. At 200 and 250 sccm, nanotubes with foliate leaves formed, akin to 1250(300) g-CNTs. Diameter measured: 1250(300) - 49 nm; 1150(300), 1150(250), 1150(200) - 24 nm (Table 1). Hydrogen flow didn't alter CNT diameter, unlike temperature. FESEM, HRTEM images showed foliates straight, linear, hollow. Density of foliates in 1250(300) higher than 1150(200), 1150(250). Results align with Parker et al., larger CNT diameter increases foliate probability [7–9]. Few layered graphene (FLG) edge planes or leaves cause structural defects, bridging CNS and CNTs [2,7].

Temperature increase from 1150°C to 1250°C triggers CNTs to g-CNTs transition. At constant 1150°C, hydrogen flow rate increase (200, 250, 300 sccm) shifts g-CNTs to CNTs. Similar studies showed g-CNTs obtained using ethanol [8], engine/grapeseed oil [10]. Temperature's impact on 1D CNTs, 2D CNSs, and 3D g-CNTs reported, with

synthesis temperature vital for both CNTs and g-CNTs [2].

From HRTEM images in Figure 2(a,b), 1250(300) had fewer foliates than 1150(250) and 1150(200) due to larger diameter. Large nanotube diameters generate graphene layers along tubes. High synthesis temp breaks C-H bonds, provides carbon radicals. Hydrogen etches CNTs' surface, causing basal plane defects. Surface defects nucleate foliates that extend, grow faster than existing CNT walls [11]. Residual stress on outer wall due to higher outer sidewall CNT growth induces buckling, carbon layer protrusion, then nucleation site for foliate graphene. Hydrogen plasma treatment in [12] also forms carbon nanosheets via C-H replacement. Ammonia radicals etch, nucleate, deposit on sidewalls, provide graphene foliates in g-CNTs [2]. Hydrogen's presence induces foliate formation due to CNT curvature, sidewall defects [4].EDX analysis tested elemental composition in g-CNTs sheets indicated mainly carbon and iron, revealing no foreign elements during g-CNTs growth (Table 1).

Raman spectroscopy assessed g-CNTs crystallinity, revealing D-band (~1350 cm^{-1}) and G-band (~1580 cm^{-1}) associated with disordered and graphitized structures, respectively. G' band at 2652 cm^{-1} shows second-order peak in crystalline carbon (Fig. 3) [13,14].

g-CNTs sheets (1250(300), 1150(250), 1150(200)) show I_D/I_G ~ 0.84–1.04, higher than 1150(300) (0.70), due to high flake density on CNT stem, increasing defect peak [14]. D-peak intensity in multi-walled g-CNTs affected by wall disorder, curvature [15]. Crystallinity gauged via crystallite size inversely related to D-peak/G-peak ratio and FWHM values. High I_D/I_G in 1250°C synthesis suggests smaller foliates [7,16]. Higher $I_{G'}/I_G$ ratio indicates more sp^2 domains after foliate growth, especially 1150(200) [13]. FCCVD-synthesized CNTs have inevitable defects, seen as D peak [3]. High temp, large-diameter generate foliates [2]. Plasma etching breaks C-H, leads to CNT-FLG defects [11].

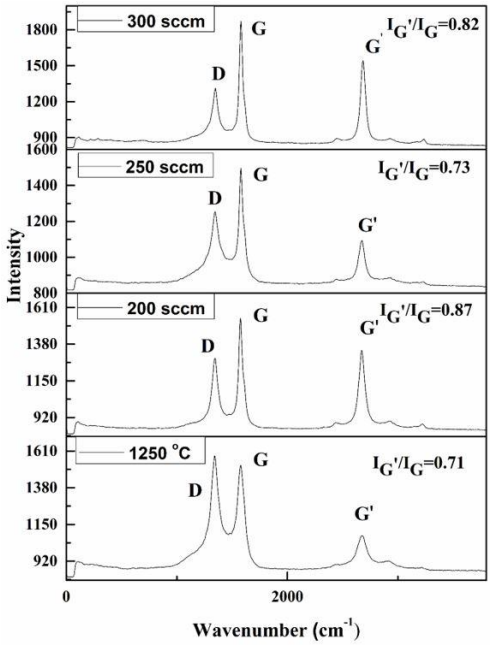

Fig. 3: Raman spectra of samples 1250(300), 1150(300), 1150(250), and 1150(200) at different synthesis parameters and their ratio of $I_{G'}/I_G$.

Thermogravimetric analysis (TGA) reveals g-CNT composition, decomposition, and oxidation (Fig. 4). CNTs decomposed at 500–800°C, affected by diameter and defects. TGA curves of g-CNTs display weight loss at 720–744°C, aligning with decomposition temperature >700°C. Sample 1150(250) exhibits most stable linear curve up to 744°C. Samples 1150(200) and 1250(300) are thermally stable up to 725°C and 720°C respectively, consistent with Raman analysis indicating higher IG'/IG ratio for thermally stable CNT sheets. G-CNT sheet compositions: 1150(250) - 97.1% g-CNTs, 5.1% iron catalyst; 1150(200) - 95.4% g-CNTs, 7.6% iron catalyst; 1250(300) - 94.9% g-CNTs, 6.9% iron catalyst. Weight gain before decomposition due to g-CNT oxidation. Defective foliate leaves adsorb gaseous

substances, increasing weight. High decomposition temperature implies multi-walled g-CNTs' resistance to combustion, higher oxidative stability. Iron nanoparticles catalyze CNT oxidation, contributing to rapid decomposition. G-CNTs' stability and decomposition behavior are important for various applications.

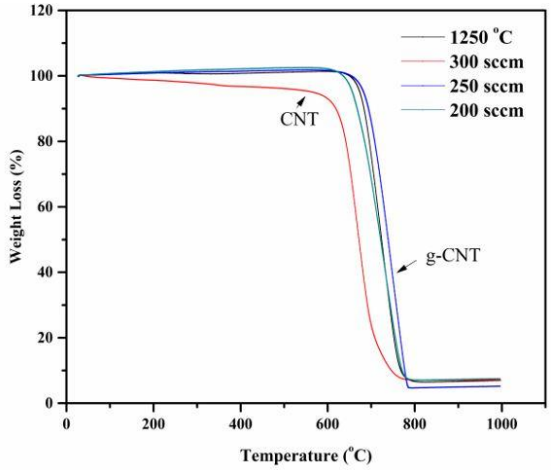

Figure 4: TGA curves of samples 1250(300), 1150(300), 1150(250), and 1150(200) with different synthesis parameters of reaction temperature and hydrogen gas flow rate.

Sample 1150(300) displays initial weight loss (~50°C) due to absorbed water [21]. Linear decline (200°C-353°C) signifies amorphous carbon presence, while multi-walled CNT decomposition starts at 668°C. Sample components: 0.86% amorphous carbon, 88.58% CNTs, 7.06% iron catalyst. Carbon impurities in 1150(300) may increase $I_{G'}/I_G$ ratio, distinct from g-CNTs sheets in other samples. Implication of varied composition on material characteristics is noteworthy.

5.0 CONCLUSION

In summary, this study underscores the potential of graphenated carbon nanotubes (g-CNTs) as a promising avenue for advanced materials in energy storage and electronic applications. By integrating 2D graphitic carbon from graphene with 1D carbon nanotubes (CNTs), a 3D framework of g-CNTs with enhanced surface area and charge capacity is achieved. The innovative single-step floating catalyst chemical vapor deposition (FCCVD) process presented here for synthesizing g-CNT sheets offers industrial scalability and ease of fabrication. The investigation of the CNTs-g-CNTs transition under varying temperature and hydrogen gas flow rate has shed light on the critical factors influencing the synthesis of these materials. The role of temperature in promoting the transition from CNTs to g-CNTs is highlighted, with higher temperatures yielding more favorable results. The impact of hydrogen gas flow rate on residence time and subsequent foliation of g-CNTs is evident, providing insights for controlled synthesis. Furthermore, the diverse structural and morphological analyses elucidated the characteristics of the synthesized g-CNTs. The implications of differing compositions on g-CNT properties, such as crystallinity and stability, are well-documented. The higher oxidative stability observed in g-CNTs, combined with their resistance to combustion, underscores their potential for various applications.

ACKNOWLEDGEMENTS

The authors are thankful to Universiti Putra Malaysia for providing Putra Berimpak Grant (Vot: 9689000).

REFERENCES

1. H.B. Abdullah, I. Ramli, I. Ismail, N.A. Yusof. Synthesis and mechanism perspectives of a carbon nanotube aerogel via a floating catalyst chemical vapour deposition method, Bulletin of Materials Science 42 (2019).
2. S.M. Ubnoske, A.S. Raut, B. Brown, C.B. Parker, B.R. Stoner, J.T. Glass. Perspectives on the Growth of High Edge Density Carbon Nanostructures: Transitions from Vertically Oriented Graphene Nanosheets to Graphenated Carbon Nanotubes, The Journal of Physical Chemistry C 118 (2014) 16126–16132.

3. M.J. Schulz, B. Ruff, A. Johnson, K. Vemaganti, W. Li, M.M. Sundaram, G. Hou, A. Krishnaswamy, G. Li, S. Fialkova, S. Yarmolenko, A. Wang, Y. Liu, J. Sullivan, N. Alvarez, V. Shanov, S. Pixley. Chapter 2 - New Applications and Techniques for Nanotube Superfiber Development, in: M.J. Schulz, V.N. Shanov, Z.B.T.-N.S.M. Yin (Eds.), William Andrew Publishin*, Boston, 2014: pp. 33–59.
4. S. Trasobares, C.P. Ewels, J. Birrell, D. Stephan, B.Q.Q. Wei, J.A. Carlisle, D. Miller, P. Keblinski, P.M. Ajayan. Carbon nanotubes with graphitic wings, Advanced Materials, 16 (2004) 610–613.
5. W. Muangrat, W. Wongwiriyapan, S. Morimoto, Y. Hashimoto. Graphene nanosheet-grafted double-walled carbon nanotube hybrid nanostructures by two-step chemical vapor deposition and their application for ethanol detection, Scientific Reports 9 (2019) 7871.
6. M. Flygare, K. Svensson. Quantifying crystallinity in carbon nanotubes and its influence on mechanical behaviour, Materials Today Communications 18 (2019) 39–45.
7. C.B. Parker, A.S. Raut, B. Brown, B.R. Stoner, J.T. Glass. Three-dimensional arrays of graphenated carbon nanotubes, Journal of Materials Research 27 (2012) 1046–1053.
8. I. Ismail, J.M. Yusof, M.A. Mat Nong, N.L. Adnan. Synthesis of carbon nanotube-cotton superfiber materials, in: Synthesis, Technology and Applications of Carbon Nanomaterials 2018: pp. 61–76.
9. H.B. Abdullah, R. Irmawati, I. Ismail, N.A. Yusof. Utilization of waste engine oil for carbon nanotube aerogel production using floating catalyst chemical vapor deposition, Journal of Cleaner Production 261 (2020) 121188.
10. H.B. Abdullah, R. Irmawati, I. Ismail, M.A. Zaidi, A.A.A. Abdullah. Synthesis and morphological study of graphenated carbon nanotube aerogel from grapeseed oil, Journal of Nanoparticle Research 23 (2021) 244.
11. K. Yu, G. Lu, Z. Bo, S. Mao, J. Chen. Carbon Nanotube with Chemically Bonded Graphene Leaves for Electronic and Optoelectronic Applications, The Journal of Physical Chemistry Letters 2 (2011) 1556–1562.
12. L. Zeng, D. Lei, W. Wang, J. Liang, Z. Wang, N. Yao, B. Zhang. Preparation of carbon nanosheets deposited on carbon nanotubes by microwave plasma-enhanced chemical vapor deposition method, Applied Surface Science 254 (2008) 1700–1704.
13. Z. Bo, Y. Yang, J. Chen, K. Yu, J. Yan, K. Cen. Plasma-enhanced chemical vapor deposition synthesis of vertically oriented graphene nanosheets, Nanoscale 5 (2013) 5180–5204.
14. N. Soin, S.S. Roy, T.H. Lim, J.A.D. McLaughlin. Microstructural and electrochemical properties of vertically aligned few layered graphene (FLG) nanoflakes and their application in methanol oxidation, Materials Chemistry and Physics 129 (2011) 1051–1057.
15. A.M. Rao, A. Jorio, M.A. Pimenta, M.S.S. Dantas, R. Saito, G. Dresselhaus, M.S. Dresselhaus. Polarized Raman Study of Aligned Multiwalled Carbon Nanotubes, Physical Review Letters 84 (2000) 1820–1823.
16. N. Soin, S.S. Roy, C. O'Kane, J.A.D. McLaughlin, T.H. Lim, C.J.D. Hetherington. Exploring the fundamental effects of deposition time on the microstructure of graphene nanoflakes by Raman scattering and X-ray diffraction, CrystEngComm 13 (2011) 312–318.

Green Chemistry Biosynthesis of Stable Silver Nanoparticles by *Saccharomyces Cerevisiae* Grown in Static Magnetic Fields

Atika **Ahmad**, Jahirul Ahmed **Mazumder**, Siobhan **O' Sullivan**, Mayssa Haschem **Galeb**, Wafa Yaser **Abushar**, David **Sheehan***

Department of Chemistry, Khalifa University of Science and Technology, Abu Dhabi 127788, United Arab Emirates 100059886@ku.ac.ae
Department of Chemistry, Khalifa University of Science and Technology, Abu Dhabi 127788, United Arab Emirates jahirul.mazumder@ku.ac.ae
Department of Chemistry, Khalifa University of Science and Technology, Abu Dhabi 127788, United Arab Emirates
siobhan.osullivan@ku.ac.ae
Department of Chemistry, Khalifa University of Science and Technology, Abu Dhabi 127788, United Arab Emirates mayssa.haschem@ku.ac.ae
Department of Chemistry, Khalifa University of Science and Technology, Abu Dhabi 127788, United Arab Emirates 100060603@ku.ac.ae

*Corresponding author's phone: +971 2 312 4333
E-mail: david.sheehan@ku.ac.ae

ABSTRACT

Biosynthesis of metal nanoparticles has received significant attention for its ability to offer cost-effective, sustainable, eco-friendly, and industrially scalable technology. In the present work, we report a novel green chemistry approach to synthesize nanoparticles using *Saccharomyces cerevisiae* cultured in the presence of static magnetic fields (SMF). Cell-free media from the SMF-treated cultures supported biosynthesis of extremely stable and monodispersed silver nanoparticles (AgNPs) compared to the control cell-free media obtained from SMF untreated cultures. Magnetic field strength for the formation of smallest AgNPs was 7 mT. AgNPs from SMF-treated cultures were crystalline and smaller compared to the ones synthesized by control media without SMF treatment.Dynamic light scattering (DLS) sizes of 36 nm (SMF) and 57 nm (without SMF) transmission electron microscopy (TEM) gave ranges of 5-15 nm (SMF) versus 10-25 nm (control). A remarkable difference in stability of AgNP was observed over a period of 75 days between SMF-treated and untreated control media through DLS and estimation of polydispersity index.

Keywords— green synthesis, silver nanoparticles, static magnetic fields, fungi, nanoparticles

1.0 INTRODUCTION

Metal nanoparticles (diameter < 100 nm) are emerging as crucial players in the fields of electronics, health sciences and pharmaceutical industries due to their excellent optical, barrier, antibacterial and advanced sensing properties. Due to their small size, they may agglomerate and lose their stability over time resulting in loss of their functionality. It is desirable to obtain mono dispersed, highly uniform, crystalline, and stable nanoparticles. Synthesis of nanoparticles can be achieved through various chemical and physical methods which necessitates massive energy inputs with considerable ecological footprints. Green synthesis of nanoparticles utilizing plants, bacteria, fungi etc. is favored over chemical synthesis due to its intrinsic advantages of non-toxicity, sustainability, increased

stability, biocompatibility, and low energy requirements [1,2].

Silver nanoparticles (AgNPs) are among the most captivating class of metal nanoparticles due to their broad spectrum of antimicrobial, antifungal and antiviral properties. Low intensity magnetic fields have become a crucial component of our ecosystem due to widespread use of personal electronic devices. Based on their property to be able to change over time they are classified as static magnetic fields (SMF) and dynamic magnetic fields [3]. SMF has been reported to induce oxidative stress in fungi *Saccharomyces cerevisiae,* a species of yeast which belongs to the kingdom fungi.

Currently, there exists a huge research gap in literature around SMF induced stress and its potential utilization in biosynthesis of metal nanoparticles. Only recently, Kthiri [4] observed for the first time that the addition of silver nitrate in cell free extract of SMF treated *S. cerevisiae* produces highly crystalline, extremely small (2-5 nm) and potent antibacterial AgNPs. Thus, present study reports the biosynthesis of stable AgNP using green chemistry synthesis approach through *Saccharomyces cerevisiae* extract in the presence of SMF.

2.0 THEORY/LITERATURE REVIEW

Fungi synthesize nanoparticles as a survival strategy, reducing metal salt-induced toxicity through oxidation state changes. Fungal cell membranes, rich in proteins, aid metal detoxification during stress. Heterocyclic compound-derived functional groups like ≡CeOeC≡, =C=O, ≡C–O–R are identified in fungal protein extracts [5].

2.1 *S. cerevisiae* as biological nano factories for biosynthesis of nanoparticles

"*S. cerevisiae*," or baker's yeast, is renowned for cellular physiology and genetics. Its straightforward encapsulation mechanism involves glycoproteins and beta-glycans for nanoparticle stabilization. Cell membrane oxidoreductases transform metal salts into elemental form [6]. Nanoparticles interacting with S. cerevisiae develop a "protein corona" [7–9], influenced by stressors like heat shock, oxidation, and magnetic fields.

2.2 *S. cerevisiae* stress response

Under oxidative stress, *S. cerevisiae* accumulates glycerol via Hog1 MAP kinase pathway [10]. Hsp synthesis increases during stress, regulated by DNA-binding proteins Msn2p and Msn4p [11]. YAP family contributes to Hsps-independent stress response. Oxidative stress activates glutathione and thioredoxin pathways [12]. WSC proteins govern stress-activated PKC1-MAP kinase pathway for heat shock and cell wall integrity [13].

2.3 Role of SMF in stress response

SMF reduces *S. cerevisiae* viability [14] and alters gene expression. SMF impacts antioxidant markers like GPX, CAT, and SOD [15]. "Protein corona" of biogenic nanoparticles is influenced by SMF-induced magnetic stress. SMF presence leads to hsp70 and early response gene overexpression [16], enhancing specific enzyme activity.

3.0 MATERIALS

Silver nitrate ($AgNO_3$), yeast extract, peptone, and dextrose (YPD media) were purchased from Sigma Aldrich, Life Science. Saccharomyces cerevisiae (strain BY4741. Genotype: MATa his 3Δ1 leu2Δ0 met15Δ0 ura3Δ0) was obtained from ATCC. A commercially available Helmholtz coil (radius 6.8 cm) (Leybold, Germany) able to produce SMF in the range of 0-10 mT and a combined DC power supply (12 V and 2 A) were used to generate SMF.

4.0 EXPERIMENTAL METHODS

The *Saccharomyces cerevisiae* (strain BY4741. Genotype: *MATa his 3Δ1 leu2Δ0 met15Δ0 ura3Δ0*) obtained from ATCC were cultured in YPD broth (1% bacto-yeast extract, 2% bacto-peptone, 2% glucose). The cultures with increased growth were treated to a parallel and homogenous magnetic induction in the range of 0-10 mT and magnetic field was generated by Helmholtz coils. The terrestrial magnetic field at the experimental location was 0.065 mT. The control cultures were identically prepared without exposure to a magnetic field. Cell-free supernatants were obtained from each culture by centrifugation (10,000 g) and 1mM of $AgNO_3$ was added to the supernatant. The supernatants were kept in the dark at room temperature for 24 h. AgNPs were collected through wash cycles and sequential centrifugation (10,000 g).

4.1 CHARACTERIZATION OF SILVER NANOPARTICLES

4.1.1 UV-visible absorbance spectral analysis

AgNPs were detected through visual color change observation of the cell filtrate after treatment with 1mM silver nitrate. Characterization was carried out in the range of 300-700nm using UV-Visible spectrophotometer (Bruker UV-5500PC (USA).

4.1.2 Dynamic Light Scattering

A Zetasizer Nano S from Malvern Instruments Ltd. was used to perform dynamic light scattering (DLS) analysis on 1mg/ml AgNP samples in a low-volume quartz cuvette. The analysis was performed at 25 °C for 10 cycles. AgNP synthesized at different field strengths (3-9 mT) were studied.

4.1.3 Stability assessments of AgNP

Control and test samples of AgNPs were dissolved in ddH_2O at a concentration of 1 mg/ml and subjected to DLS measurements over a period of 75 days. The resulting colloidal sample of AgNP (Control and Test) were analyzed to assess changes in AgNP hydrodynamic size and polydispersity index (PDI).

4.1.4 X-Ray Diffraction (XRD)

Powdered AgNP was used for XRD analysis in a Bruker D8 advance diffractometer over a wide range of Bragg angles ($20° \leq 2\theta \leq 80°$), the h, k, l indices correlating to the 2-theta value was analyzed and matched with the corresponding Joint Committee on powder diffraction (JCPDS) file number.

4.1.5 Transmission Electron Microscopy (TEM)

A transmission electron microscope (FEI Tecnai) operating at 200kV was used to study the size and shape of AgNPs. The sample preparation for TEM was carried out by drop coating the diluted AgNPs on carbon-coated copper grid.

5.0 RESULTS AND DISCUSSION

Cell-free *S. cerevisiae* culture supernatants were employed in the current study to synthesize AgNPs. After 18 hours of incubation at 25°C, the color of the *S. cerevisiae* supernatant changed from light yellow to brown with the addition of 1 mM silver nitrate aqueous solution (Fig. 1). A surface plasmon resonance peak at 412 nm, consistent with the known absorbance peaks of AgNP were observed. The inset to Fig. 1 illustrates color change from pale yellow to golden yellow and then to brown, signifying the biosynthesis of AgNP. Additionally, two controls were used; in one, the experimental setup was maintained while the temperature was raised to 50°C, and in the other, 1 mM silver nitrate aqueous solution was combined with YPD broth; no resonance peak was evident in either of these circumstances (results not shown here). It has been stated previously elsewhere that the surface plasmon resonance (SPR)-induced excitation of the solution's color change from yellow to brown makes it possible to visualize the reduction of Ag^+ into AgNP clearly [5].

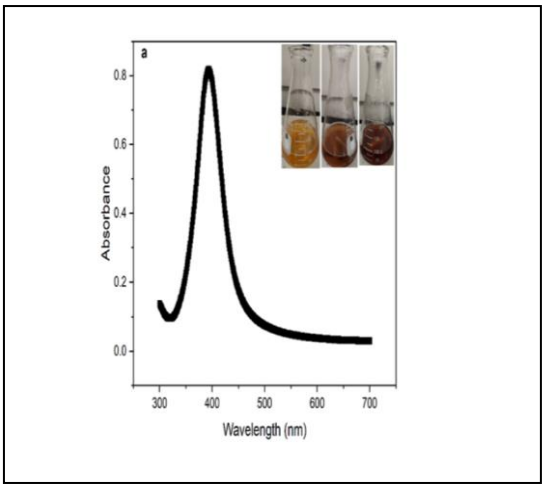

Fig. 1: UV Vis spectrum of AgNP synthesized using *S. cerevisiae*, under the influence of SMF. A maximum absorption peak was observed at 412 nm. Inset represents colour change during the AgNP synthesis.

Thus, SPR helps to identify the reduction of Ag^{+} into AgNPs visually. During the culture of *S. cerevisiae,* a range of magnetic field strengths (3-9 mT) were employed and AgNP biosynthesis was followed to identify the optimal field strength yielding the most favorable hydrodynamic size and PDI. This analysis was performed using DLS. Fig. 2 revealed the hydrodynamic size and PDI at various magnetic field strengths. DLS suggested that 7 mT was optimum for uniform size distribution and most stable PDI.

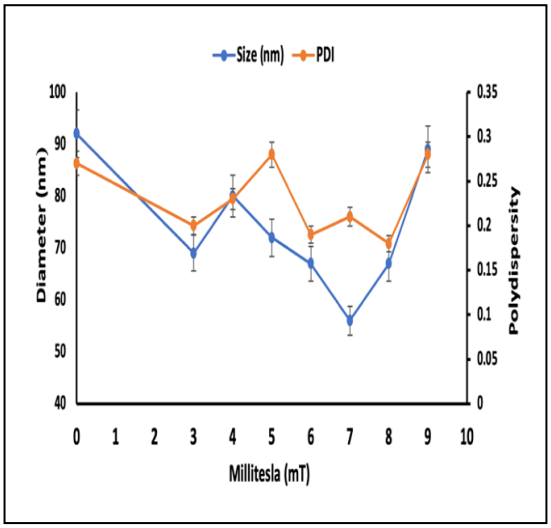

Fig. 2: Dynamic light scattering graph which shows minimal hydrodynamic size and PDI, was observed at 7mT. The results were represented as means of three replicate (n = 3) ± SD. The significance level was maintained as p-value <0.05.

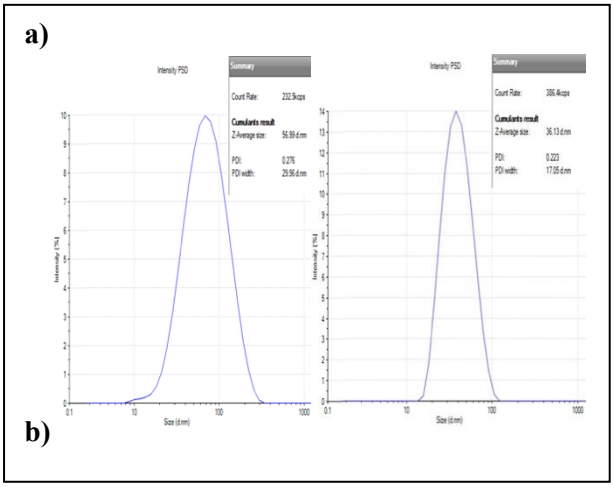

Fig. 3: Dynamic Light Scattering graph showing Z average size of AgNP. (a) $AgNP_{control}$ has a Z average size of 56 nm and (b) $AgNP_{test}$ has a Z average size of 36 nm

To evaluate the effect of magnetic field strength, AgNPs were synthesized in the presence of SMF (test, 7mT) and compared to a control sample synthesized without the magnetic field, by DLS. Fig. 3b revealed that the test AgNP sample exhibited a hydrodynamic size of 36 nm, indicating smaller nanoparticles. The PDI value of 0.22 indicated a nearly monodisperse particle distribution with minimal size variations. In comparison, the control sample (fig. 3a), synthesized in the absence of the magnetic field, exhibited a larger hydrodynamic size of 56 nm. The PDI value of 0.27 indicated a moderate level of polydispersity, suggesting a broader size distribution compared to the test AgNP.

TEM was used to compare $AgNP_{control}$ and $AgNP_{test}$ (Fig. 4). In the absence of SMF, the majority of AgNP had diameters ranging from 10 to 25 nm (Fig. 4a). However, in the presence of SMF, the majority particles exhibited diameters in the range 5 to 15 nm (Fig. 4b). Notably, nanoparticles appeared mostly spherical in both cases, but those synthesized under SMF conditions seemed to have a more uniform shape and size distribution.

The crystalline nature and phase purity of both control and test samples of AgNP were analyzed using XRD. Distinct peaks corresponding to crystallographic planes at (111), (200), (142), and (220) for both

control (Fig. 5a) and test samples (Fig. 5b) were observed. These closely matched the standard JCPDS card number 04-0783. A few additional peaks in the control sample (denoted by *) which may be due to impurities were not observed in test sample. The presence of well-defined peaks at specific crystallographic planes further confirm successful biosynthesis of crystalline AgNPs.

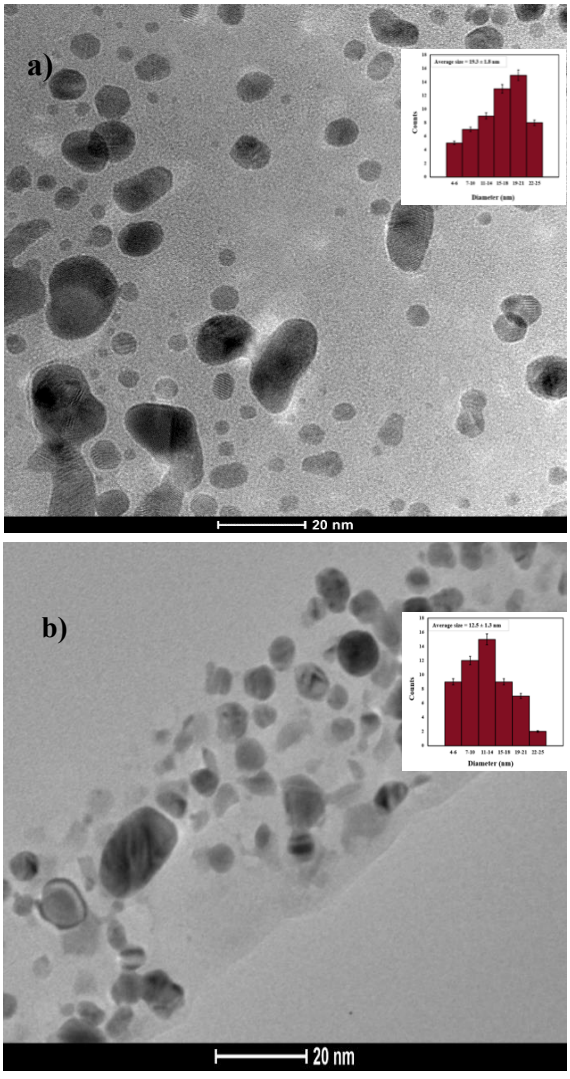

Fig. 4: Transmission electron microscopy image of a. AgNP $_{Control}$, b. AgNP$_{Test}$. Inset shows histogram, showing mean average particles range in between 19.3±1.8 nm to 12.5±1.3 nm.

A stability study of AgNPs revealed significant differences in hydrodynamic size and PDI between the SMF and control samples over a period of 75 days. After the 75th day, it was observed that the size of the AgNP$_{Test}$ sample remained relatively stable at approximately 63 nm. In contrast, the hydrodynamic size of the AgNP$_{Control}$ sample displayed a consistent increase, eventually reaching 327 nm (Table 1). Fig.6 shows associated PDI analysis. It is worth mentioning that the AgNPs were maintained at a temperature of 4º C in solution form at a normal pH. No further capping agents were used to increase the stability of AgNPs over time. AgNP$_{Test}$ exhibited a consistent PDI of 0.2, indicating a stable and uniform size distribution. On the other hand, the AgNP$_{Control}$ exhibited a significantly higher PDI of 0.62, indicating noticeable polydispersity and agglomeration.

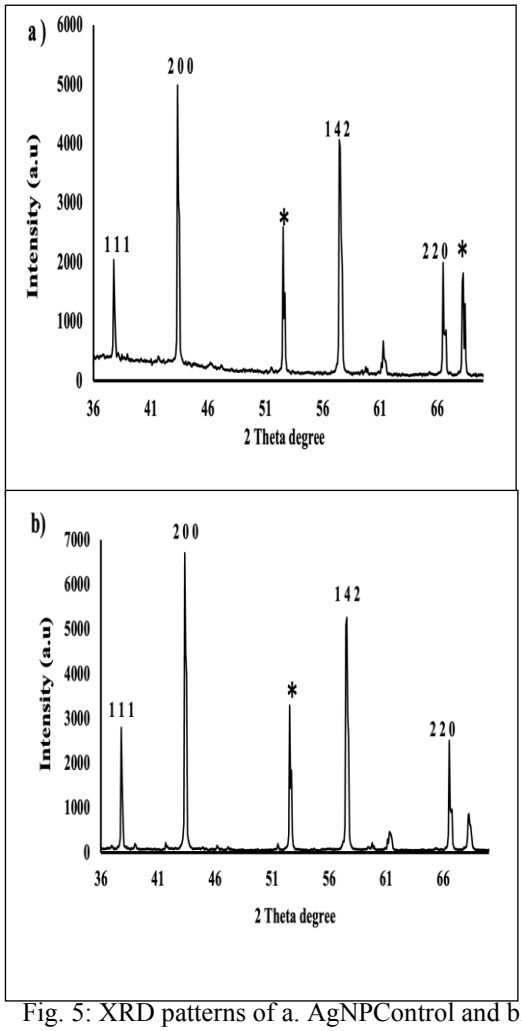

Fig. 5: XRD patterns of a. AgNPControl and b. AgNPTest. The h,k,l indices correlating to the 2-theta value is analyzed and matched with the corresponding JCPDS file number 04-0783.

TABLE 1: The hydrodynamic size was recorded using DLS over a period of 75 days. The results were represented as means of three replicates (n = 3) ± SD. The significance level was maintained as p-value <0.05. Statistical analysis of the data was performed using an independent t-test to compare test and control. The t-test revealed a significant difference between the two groups AgNP (Control) and AgNP (Test) (p = 0.0282), indicating a statistically significant effect

Days	Size (nm) of AgNP (Test)	Size (nm) of AgNP (Control)
1	36±1.5	56±3.2
15	57±1.76	81±3.8
30	61±1.54	92±4.1
45	63±2.1	98±3.9
50	61±2.3	110±2.7
65	60.8±1.87	263±5.3
75	63.2±1.01	327±4.21

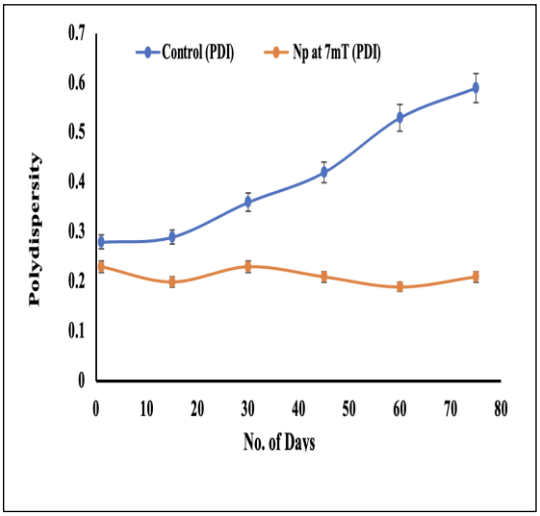

Fig. 6: The polydispersity index (PI) analysis shows that after 75 days, $AgNP_{Test}$ had a PDI of 0.2, which suggested that they were quite stable, as opposed to $AgNP_{Control}$, which reached a PDI of 0.62, suggesting agglomeration and loss of stability. Data are reported as the means of three replicates (n = 3) ± standard deviation. p-value <0.05 was kept as the significance threshold.

5.0 CONCLUSION

The current study reports successful biosynthesis of stable AgNPs using *S. cerevisiae* culture as a reducing agent under the influence of SMF. Optimizing the magnetic field strength (7 mT) yielded AgNPs with favorable size and PDI which opens up possibilities for tailoring the characteristics of AgNPs according to specific application requirements. This observation suggests that the presence of the magnetic field enhances dispersion and prevents agglomeration, thus improving stability of AgNPs. Future work would involve monitoring the general applicability of this method exploiting different species of yeast.

The authors declare no conflict of interests.

References

1. O.V Kharissova, H.V.R. Dias, B.I. Kharisov, Pérez: The Greener Synthesis of Nanoparticles. Trends Biotechnol 2013. pp. 240–248
2. H. Duan, D Wang, Y.Li: Green Chemistry for Nanoparticle Synthesis. Chem Soc Rev 2015. pp. 5778–5792.
3. E.N. Parker, E.N. The Origin of Magnetic Fields The Astrophysical Journal 1970. pp. 383 .
4. A. Kthiri, S. Hamimed, A. Othmani, A. S. O'sullivan, D Sheehan: Novel Static Magnetic Field Effects on Green Chemistry Biosynthesis of Silver Nanoparticles in Saccharomyces Cerevisiae. Scientific Reports 2021(1):20078
5. J.R. Robinson, O.S Isikhuemhen, F.N Anike,. Fungal-Metal Interactions: A Review of Toxicity and Homeostasis. J Fungi (Basel) 2021 (3):2025
6. A. Roychoudhury: Yeast-Mediated Green Synthesis of Nanoparticles for Biological Applications. Indian J. Pharm. Biol. Res 2020. pp. 26–31.
7. T. Kopac: Protein Corona, Understanding the Nanoparticle–Protein Interactions and Future Perspectives: A Critical Review. Int J Biol Macromol 2021.pp. 290–301.
8. S.Zanganeh, R. Spitler, M. Erfanzadeh, A.M.Alkilany, M. Mahmoudi, Protein Corona: Opportunities and Challenges. International Journal of Biochemistry and Cell Biology 2016. pp 143–147.
9. M.P Monopoli, C.Åberg, A Salvati, K.A. Dawson: Biomolecular Coronas Provide the Biological Identity of Nanosized Materials. Nat Nanotechnol 2012. pp.779–786,
10. H Saito, F. Posas. Response to Hyperosmotic Stress. Genetics 2012. pp. 289–318,
11. Y Hirata, T Andoh, T Asahara, A Kikuchi: Yeast Glycogen Synthase Kinase-3 Activates

Msn2p-Dependent Transcription of Stress Responsive Genes. Mol Biol Cell 2003, pp. 302–312.
12. K.A Morano, C.M. Grant, W. Moye-Rowley Scott: The Response to Heat Shock and Oxidative Stress in Saccharomyces Cerevisiae. 2012 pp.1157-1195
13. Lodder, A.L.; Lee, T.K.; Ballester, R. Characterization of the Wsc1 Protein, a Putative Receptor in the Stress Response of Saccharomyces Cerevisiae; 1999;
14. J.Novák, L.Strašák, L.Fojt, I. Slaninová, V. Vetterl, Effects of Low-Frequency Magnetic Fields on the Viability of Yeast Saccharomyces Cerevisiae. Bioelectrochemistry 2007. pp 115–121
15. D.R Weisbrot,O. Khorkova, H.Lin, A.S.Henderson, R. Goodman, The Effect of Low Frequency Electric and Magnetic Fields on Gene Expression in Saccharomyces Cerevisiae; Elsevier Sequoia S.A, 1993.
16. A. Kthiri, S. Hamimed, A. Othmani, A. S. O'sullivan, D Sheehan: Biochemical and Biomolecular Effects Induced by a Static Magnetic Field in Saccharomyces Cerevisiae: Evidence for Oxidative Stress. PLoS One 2019:e0209843

Valley and Spin Transport Characteristics Based on a Quantum Dot Contact Structure Regulated by Piezoelectric Field

Ruhao **Liu**, Yan **Zhang***

School of Physics, University of Electronic Science and Technology of China
Cheng du, China

*Corresponding author's E-mail: zhangyan@uestc.edu.cn

ABSTRACT

Piezotronics and piezo-phototronics have attracted great interest and are widely used in self-powered technology, low power consumption, and artificial intelligence. piezoelectric field is an important role to modulate charge-carrier transport properties in two-dimensional(2D) materials. In this study, piezotronics effect on the transport of valley and spin properties in monolayer transition metal dichalcogenides which include MoS_2, $MoSe_2$, $MoTe_2$, WS_2, WSe_2 and WTe_2, based on a quantum dot contact structure is studied. The interface piezoelectric fields of different transition metal dichalcogenides in the structure, as well as the valley and spin conductance and the valley and spin polarizability under the corresponding piezoelectric field regulation are calculated theoretically. Our work not only demonstrate the significant advantage of the strong piezoelectric field on the modulation of valley and spin quantum states, but also provide a guidance for device design and material selection of high performance quantum piezotronic devices.

Keywords—valleytronics; spintronics; spiezotronics

1.0 INTRODUCTION

The electron's degree of freedom is of great importance in various areas[1]. Transition Metal Dichalcogenides (TMDs) have been the subject of extensive research due to their readily accessible electronic degree of freedom. This attribute enables dynamic control, a feature that was initially discovered in graphene, marking a major breakthrough in the field [2, 3]. In addition to the electron charge and spin, the valley has also garnered significant attention [4, 5]. The valley pertains to the various degenerate energy states in the vicinity of the local maximum of the conduction or valence bands occupied by electrons. Monolayer(ML) TMDs, being atomically thin semiconductors and devoid of inversion symmetry, have been extensively investigated in the realm of quantum devices [6].

It is reported that valley and spin polarization is achieved in a Quantum dot contact (QPC) structure, the possibility of electric field controlled QPC in TMDs offers a new way for valley- and spin-based quantum information processing [7]. Current research has shown that the intensity of the electric field is a crucial factor in controlling the valley and spin [8]. However, there are limited existing research methods that can achieve a strong electric field. The piezoelectric field, which arises from the polarization of charges in response to strain, offers an excellent solution. Recently, it has been highlighted that piezoelectric field can reach the order of MV/cm in ML MoS_2, exhibiting favorable valley and spin characteristics [9]. However, to date, there is an insufficient amount of comprehensive research conducted on the characteristics of robust piezoelectric fields in 2D materials and their potential implications for the design of devices.

In this study, The QPC structure that regulate valley and spin by strong

piezoelectric field is proposed. The influence of piezoelectric field on the transport and polarization of valley and spin in TMDs are invesgated in QPC structure. Our research offers a comprehensive theoretical guidance for investigating the manipulation of valley and spin transport through the application of piezoelectric effects.

2.0 MODEL AND METHIDS OF SPIN AND VALLEY TRANSPORT

2.1 Model

For the QPC structure, it is a BN/TMDs/BN quantum well. A TMDs layer is sandwiched between two BN layers, in this way, it is a quantum well structure, the related structures have been extensively explored theoretically and experimentally [10, 11]. Ferromagnetic materials are placed in the QPC channels to create the exchange field. By applying strain, a piezoelectric field is generated along the QPC channel interface to control valley and spin transport. Figure 1(a) shows the QPC structure of ML MoS_2. Fig. 1(b) shows the corresponding potential and electric field, where W is the QPC channel width in QPC structure. In order to study the effect of longitudinal electric polarization field on spin and valley regulation, we set the width of QPC to a fixed value of 5 nm and placed ferromagnetic materials at the QPC channel to magnetize the single-layer TMDs, in this way, piezoelectric field in the y direction as well as the electric field intensity is obtained, as shown in Fig. 1(b). The transverse length in Fig. 1(a) correspond to the x direction. In Fig. 1(b), and the longitudinal widths correspond to the y direction. Although we only draw the MoS_2 form, other materials of TMDs are similar. The strain was set to 8% in Fig. 1(b).

2.2 Methods

For the QPC structure, the valley- and spin-dependent transport properties is obtained through the Schrödinger equation

$$H\psi = E\psi \tag{1}$$

H is a Hamiltonian, E is an eigenvalue, Ψ represents wave function. When the electric states near the band edge in the QPC structure, it can be described using the effective Hamiltonian.

$$\begin{aligned} H = v\left(\tau k_x\sigma_x + k_y\sigma_y\right) + \frac{\Delta}{2}\sigma_z \\ -\lambda_v\tau\frac{\sigma_z - 1}{2}s - \lambda_c\tau\frac{\sigma_z + 1}{2}s - sh + U \end{aligned} \tag{2}$$

$\sigma_x, \sigma_y, \sigma_z$ are Pauli matrices, spin up and spin down are described by s=±1 , τ is valley index, v is Fermi velocity, Δ is energy gap, λ is coupling constant. h is the exchange field. U is the piezoelectric potential.

When strain is applied on the QPC structure, the piezoelectric potential in the QPC structure can be written as [12]

$$U_{piezo} = \begin{cases} \frac{e_{11}s_{11}}{2\pi\varepsilon_r\varepsilon_0}\ln|y| + U_1, -W_{qpc} < y \le 0 \\ \frac{e_{11}s_{11}}{2\pi\varepsilon_r\varepsilon_0}\ln\left|\frac{y}{W_{qpc} - y}\right|, 0 < y \le W_{qpc} \\ \frac{e_{11}s_{11}}{2\pi\varepsilon_r\varepsilon_0}\ln|y - W_{qpc}| + U_2, W_{qpc} \le y < 2W_{qpc} \end{cases} \tag{3}$$

All the parameters can be obtained in Ref [9]. Based on the above discussion, the total conductance is obtained through the utilization of the Landauer-Buttiker formula [8]:

$$G_{\tau s} = G_0\sum_{mn}\left|t_{mn}^{\tau s}\right|^2 \tag{4}$$

$t_{mn}^{\tau s}$ is the dependent scattering coefficient from of valley and spin. $G_0 = e^2/h$ is the conductance unit. Valley- and spin-dependent conductance can be obtained by using the formula $G_K = (G_{K\uparrow} + G_{K\downarrow})/2$. $G_s = (G_K + G_{K'})/2$. The valley and spin polarization, denoted as P_v and P_s, respectively, can be used as metrics to

characterize the effectiveness of valley and spin filtering capability [8]

$$P_v = \frac{G_K - G_{K'}}{G_K + G_{K'}} \quad (5)$$

$$P_s = \frac{G_\uparrow - G_\downarrow}{G_\uparrow + G_\downarrow} \quad (6)$$

3.0 RESULTS AND DISCUSSION

Fig. 1(a) illustrates the structure of the BN/MoS_2/BN quantum well. The constriction between the two gates serves as a QPC. Fig. 1(b) depicts the piezoelectric field and the corresponding intensity of the piezoelectric field.

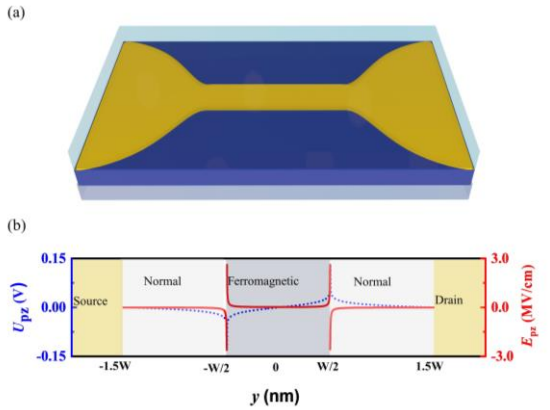

Fig. 1: (a) Schematic illustration of QPC structure based on BN/MoS_2/BN. (b) Piezoelectric potential and piezoelectric field intensity in QPC structure, the piezoelectric field is along the longitudinal direction of the device, where W = 5 nm is the channel width of QPC structure, the maximum potential at the channel interface is 0.14 V, and the maximum piezoelectric field intensity is 2.6 MV/cm. and the data in (b) were obtained under tensile strain of 8%.

Fig. 2 displays the conductance of valley and spin of ML TMDs in QPC structure. The exchange field and Fermi level are still 100 meV and −0.975 eV, respectively. When −10% to 10% strain is applied, the transport phenomenon can be observed. ML TMDs showed better strain-regulated spin and valley degree of freedom screening in QPC structure. When the compressive strain is 7%-10% and 0-2.5%, only K-valley conductance occurs in MoS_2, and when the strain is −10% to 7.5% in WSe_2, complete K-valley conductance also occurs, more specifically, only K ↑ conductance occurs when the compressive strain is −2.5% to 2.5%. Complete K′ ↑ conductance occurs in $MoSe_2$ and $MoTe_2$, corresponding to 2%-10% compressive strain and 4%-9% tensile strain, respectively. The conductance of WS_2 and WTe_2 in QPC structure oscillates with the change of strain, and there is no obvious region of high polarizability.

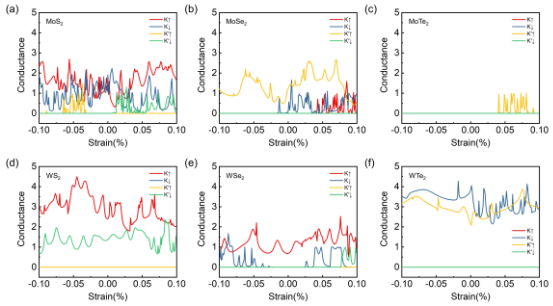

Fig. 2: Valley- and spin-dependent conductance of ML TMDs under the Fermi level of −0.975 eV based on the QPC structure. (a)-(h) is MoS_2, $MoSe_2$, $MoTe_2$, WS_2, WSe_2, WTe_2 respectively.

Fig. 3 shows the polarization diagram of valley and spin under strain in QPC structure according to the conductance data of Fig. 3 as well as (5) and (6). The corresponding relationship between curves and data is the same as that in Fig. 3. As for WS_2 and WTe_2, the polarization effect has weak response to strain. In WS_2, the two polarization curves coincide completely, while in WTe_2, the two polarization curves are symmetric about the X axis, indicating that these two materials are not ideal enough for QPC structure. $MoTe_2$ and WSe_2 show ideal spin and valley polarization properties under strain in QPC structure the strain induced valley and spin a region of valleys polarization region are more obvious. When strain is 4%-10%, 100% spin up and K′ valley polarization are obtained in $MoTe_2$. When the strain is −10% to 8%, 100% K valley polarization is obtained in WSe_2. In addition, for WSe_2, the response of the spin up polarization to strain is also obvious, and there are several high polarizability intervals, among which complete polarization is achieved in the range of −2% to 2.5%. MoS_2 and $MoSe_2$

also show better polarization characteristics. Especially for $MoSe_2$, when strain is applied from −2% to −10%, pure K' valley and spin up polarization is obtained. In MoS_2, nearly pure spin up polarization can also be obtained between −6% to −10% and −3% to 1%.

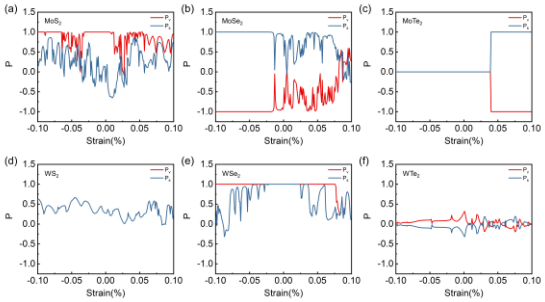

Fig. 3: Valley and spin polarization of ML TMDs based on the QPC structure with the corresponding Fermi level of −0.975 eV. (a)-(h) is MoS_2, $MoSe_2$, $MoTe_2$, WS_2, WSe_2, WTe_2 respectively.

4.0 CONCLUSION

In this work, valley and spin transport properties under piezoelectric field of ML TMDs in the QPC structure were invesgated. We found MoS_2 and $MoSe_2$ show more obvious spin and valley polarization. In addition, $MoTe_2$ in QPC structure also shows a good prospect under tensile strain due to the relatively large relaxed-ion piezoelectric coefficients. We find that QPC structure reflects a relatively better effect, The QPC structure based on MoS_2, $MoSe_2$, especially $MoTe_2$, shows a good range of spin and valley polarization under strain regulation, and the WSe_2 also has a relatively good screening range, which provides a good reference for regulating the spin and valley simultaneously with a single strain regulation mode. In this paper, we theoretically propose a spin and valley control device based on ML TMDs. This research offers valuable theoretical guidance for the development of innovative quantum piezoelectric devices.

REFERENCES

1. I. Žutić, J. Fabian, S. D Sarma. Spintronics: Fundamentals and applications[J]. Reviews of Modern Physics, 2004, 76(2): 323.
2. A. K Geim. Graphene: status and prospects[J]. Science, 2009, 324(5934): 1530-1534.
3. M. Chhowalla, H. S Shin, G. Eda, et al. The chemistry of two-dimensional layered transition metal dichalcogenide nanosheets[J]. Nature Chemistry, 2013, 5(4): 263-275.
4. K. F Mak, D. Xiao, J. Shan. Light–valley interactions in 2D semiconductors[J]. Nature Photonics, 2018, 12(8): 451-460.
5. J. R Schaibley, H. Yu, G. Clark, et al. Valleytronics in 2D materials[J]. Nature Reviews Materials, 2016, 1(11): 1-15.
6. T. P Cysne, M. Costa, L. M Canonico, et al. Disentangling orbital and valley Hall effects in bilayers of transition metal dichalcogenides[J]. Physical Review Letters, 2021, 126(5): 056601.
7. K. Wang, T. Taniguchi, K. Watanabe, et al. Engineering quantum confinement in semiconducting van der Waals heterostructure[J]. arXiv preprint arXiv:1610.02929, 2016.
8. T. Yokoyama. Controllable valley and spin transport in ferromagnetic silicene junctions[J]. Physical Review B, 2013, 87(24): 241409.
9. R. H Liu, G. W Hu, M. J Dan, et al. Piezotronic spin and valley transistors based on monolayer MoS_2[J]. Nano Energy, 2020, 72: 104678.
10. J. Yin, C. Tan, D. Barcons-Ruiz, et al. Tunable and giant valley-selective Hall effect in gapped bilayer graphene[J]. Science, 2022, 375(6587): 1398-1402.
11. P. Michetti, B. Trauzettel. Devices with electrically tunable topological insulating phases[J]. Applied Physics Letters, 2013, 102(6).
12. J. D Jackson. Classical electrodynamics, 3nd ed. New York: Wiley, 1999, p. 460.

Antimicrobial Activity of Biomediated-Synthesized Silver Nanoparticles using *Persicaria odorata* Aqueous Extract

Nik Ahmad Nizam Nik **Malek**[1,2*], Mariana **Mohd**[1], Muhammad Hariz **Asraf**[1]

[1] Dept. of Biosciences, Faculty of Science, Universiti Teknologi Malaysia, UTM, Skudai Johor
[2] Centre for Sustainable Nanomaterials (CSNano), Ibnu Sina Institute for Scientific and Industrial Research (ISI-ISIR), Universiti Teknologi Malaysia, UTM, Skudai

*Corresponding author's phone: +6013-7805466
E-mail: niknizam@utm.my

ABSTRACT

Silver nanoparticles (AgNP) is an inorganic antimicrobial agent that can be synthesized through a biological approach that is more environmentally friendly, as compared to a chemical approach. This paper reports the biosynthesis of AgNP using Kesum (*Persicaria odorata* plant) aqueous extract. The colour of the $AgNO_3$-Kesum extract mixture changed from yellowish to reddish-brown, indicating the formation of AgNP and proven by surface plasmon resonance (SPR) peak in the range of 420 to 470 nm. The optimized synthesis conditions of 0.9 mL *P. odorata* 4% resulted in the highest SPR intensity. Attenuated Total Reflectance-Fourier Transform Infrared Spectroscopy (ATR-FTIR) showing the bioactive from the plant extract in the AgNP sample. Transmission Electron Microscopy (TEM) image showed that the AgNP had an average size of 20 ± 5 nm and a predominantly spherical shape and appeared both in dispersed and aggregated forms. The antifungal activity of the AgNP sample was evaluated against *Candida albicans* (ATCC 90028) using Disc Diffusion Technique (DDT). Higher sample concentrations resulted in larger inhibition zones, indicating stronger antifungal activity against *C. albicans*. Thus, *P. odorata* aqueous extract could be used as a bio-reducing agent for AgNP formation and it is shown to have promising antifungal properties.

Keywords—Silver nanoparticles; *Persicaria odorata*; antifungal

1.0 INTRODUCTION

Among the different types of metallic nanoparticles, silver nanoparticles (AgNP) is the most studied ones due to their remarkable properties, especially their inhibitory effect on microbes [1]. There are various preparation approaches available for the synthesis of different types of nanoparticles, including physical, chemical and biological methods. However, physical and chemical methods have many drawbacks including being toxic, costly and time-consuming that endanger both human health and the surroundings [2]. The risk can be decreased by using less dangerous chemicals in the biosynthesizing of AgNPs [3]. Hence, biological methods for synthesising AgNPs utilizing plant extract are becoming more and more significant nowadays as the alternative to the physical and chemical synthesising methods of AgNPs.

Kesum or *Persicaria odorata* (or *polygonum minus*) is one of the organic sources suitable to act as a reducing agent in converting silver nitrate ($AgNO_3$) into AgNP. In general, Kesum is constituted not only of aromatic compounds but also some minor components such as flavonoids, aliphatic aldehydes and phenols [4]. Due to this characteristic, this study aimed to synthesise AgNP using Kesum extract and characterise the morphological features of synthesised nanoparticles. Moreover, the antifungal potential of the green synthesis AgNP was also determined in this study.

2.0 EXPERIMENTAL

Kesum leaves were bought from Pasar Taman Universiti in Skudai, Johor. The leaves were dried under the sunlight for 12 hours and placed in the oven for 20 minutes to make sure the leaves were fully dried. The dried leaves were crushed and ground to obtain the fine powder. For the preparation of Kesum leaves extract solution (10%, w/v), 50 g of the Kesum powder was added to 500 mL of ultrapure water. Next, the mixture was heated and boiled at 100°C for 20 minutes by using a hotplate magnetic stirrer. The solution was filtered with Whatman® No. 1 filter paper.

In the preparation of 1.0 mM $AgNO_3$ solution, about 0.17 g of $AgNO_3$ in 1 L ultrapure water. Then, 1.0 mL of 10% Kesum extract was added to a falcon tube containing 10 mL of the 1.0 mM $AgNO_3$ solution. The dilution was performed on the 10% Kesum extract to obtain different concentrations (2%, 4%, 6%, and 8%).

The mixtures were allowed to be left at room temperature for 24 hours. During this time, a colour change occurs, indicating the formation of AgNP. To confirm the reduction of silver ions, the solutions were analysed using a UV-Visible spectrophotometer (Jenway). Distilled water was used as a blank sample and the absorbance was measured in the wavelength range of 350 nm to 800 nm. The initial steps of the procedure were repeated using Kesum extract at the optimum concentration but varying the volumes of the extract to determine the best volume for AgNP synthesis. Then, another synthesis parameter which is reaction time was also assessed to optimize the biosynthesis process.

The colloidal AgNP at the optimum concentration and volume was centrifuged at 10,000 rpm and at 40°C for 15 minutes and the precipitates were collected. The powder was dried in an oven at 50°C for 24 h. The characterization of the prepared AgNPs was performed using several analytical techniques including Attenuated Total Reflectance-Fourier Transform Infrared Spectroscopy (ATR-FTIR) and Transmission Electron Microscopy (TEM) [1]. The antifungal activity of the AgNP has been evaluated against *Candida albicans* ATCC 90028 based on Disc Diffusion Technique (DDT) technique following method by Jalal et al. [5].

3.0 RESULTS AND DISCUSSION

Fig. 1 shows the appearance of the colour change of the mixture from yellowish to reddish-brown after 24 hours indicating the reduction of silver ion (Ag^+) to silver nanoparticles (Ag^0) due to excitation of surface plasmon vibrations in the AgNP [8].

Fig. 1: The colour change of colloidal which denotes the formation of AgNP

Based on Fig. 2, there are different intensities with each synthesis parameter. The higher intensity peaks correspond to the higher yield of AgNP formation. Therefore, the highest yield of AgNP could be achieved by synthesis of AgNP using Kesum leaves extract at 4% concentration with 0.9 mL and for 9 days. According to Fig. 2(a), the high concentration led to the lower intensity indicating possible aggregation forming larger particle sizes. For the reaction time (Fig 2(c)), the peak intensity is not significantly different from each other. The suitable reaction time is 24 hours (1 day), and it will be stable in the long term.

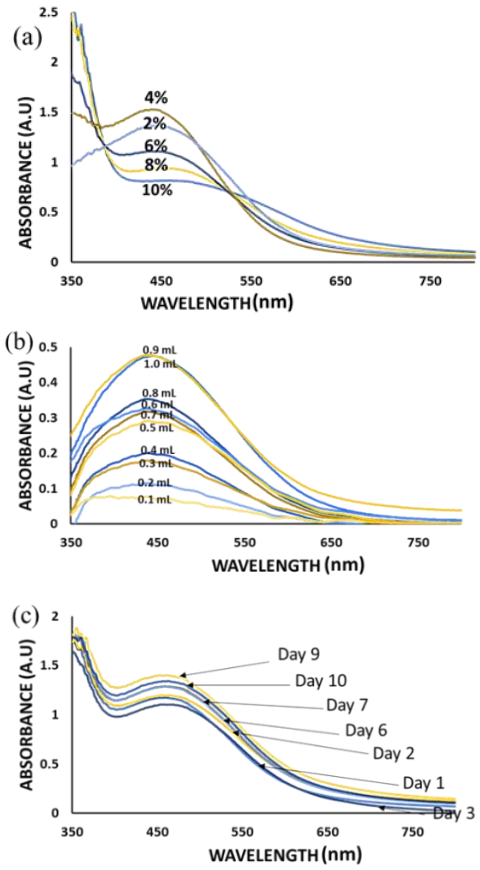

Fig. 2: UV-Vis spectra of the biosynthesized AgNP measured at (a) different concentrations, (b) different volumes, and (c) different time intervals

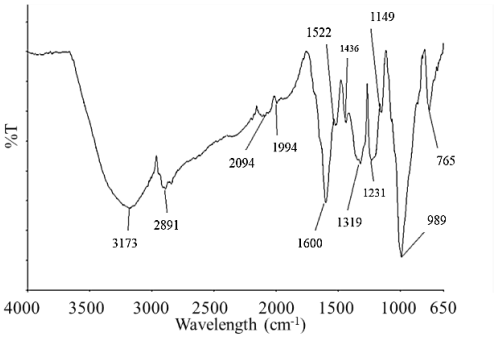

Fig. 3: FTIR spectrum of the biosynthesized AgNP

In Fig. 3, the presence of OH at 3173 cm^{-1} indicates the presence of alcohols and phenols which play an important role in the reduction reaction. The peak at 2891 cm^{-1} represented C-H of the alkyl group and peak around 2094 cm^{-1} represented C=C from alkene or aromatic amine [1]. Bands in the range of 1600 cm^{-1} can be the indicative of carbonyl groups (C=O), commonly found in ketones, aldehydes and carboxylic acids. These functional groups may participate in the reduction of silver ions and serve as potential capping agents for the AgNPs [6]. The band at 1319 cm^{-1} indicates the presence of carboxylate groups (COO^-), which are commonly found in organic acids. This group can act as a stabilizer and provide a negative charge on the surface of AgNP, preventing their aggregation [7].

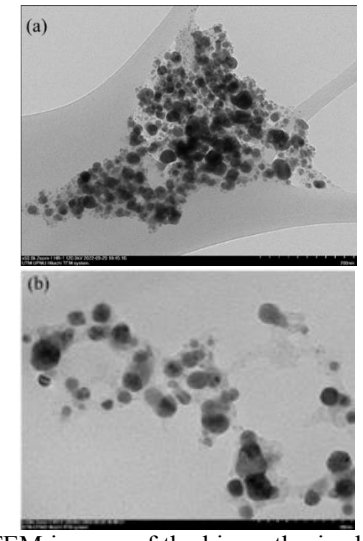

Fig. 4: TEM images of the biosynthesized AgNP at (a) 50,000x and (b) 100,000x magnifications.

Based on Fig. 4, a relatively narrow size distribution with most the nanoparticles falling within the range of 15-25 nm is indicated. The relatively small particle sizes and narrow size distribution indicated a controlled synthesis process and suggested the presence of a stabilizing agent in the Kesum leaf extract. The TEM images revealed that the biosynthesized AgNP using Kesum leaves extract exhibited a predominantly spherical shape. Most of the nanoparticles appeared as well-defined spheres with smooth surfaces. The spherical shape is favourable for many applications due to its uniformity, higher stability and enhanced surface-to-volume ratio.

The antifungal activity of the biosynthesized AgNP was performed against the fungus *C. albicans*, and the DDT images are given in Fig. 5.

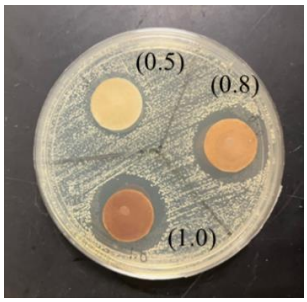

Fig. 5: DDT images for the antifungal activity of AgNP against *C. albicans* at different concentrations.

The DDT image in Fig. 5 shows the clear zone of inhibition around the discs containing the biosynthesized AgNP at all tested concentrations. As the concentration of the AgNP increased, the size of the inhibition zones also increased. This observation suggests that the biosynthesized AgNP exhibits dose-dependent antifungal activity against *C. albicans*. The higher the concentration of AgNPs is more effective in inhibiting the growth of the fungal pathogen.

4.0 CONCLUSION

In this study, AgNP was successfully synthesized using Kesum extract as a bio-reducing agent. The optimum AgNP synthesis parameters were 4% concentration and 0.9 mL volume of the plant extract after 24 hours of reaction time. The particle size of the AgNP was of 20 ± 5 nm and a relatively narrow size distribution between 15-25 nm. The biosynthesized AgNP using Kesum leaf extract has antifungal activity against *C. albicans* with dose-dependent activity.

ACKNOWLEDGEMENTS

We would like to thank Universiti Teknologi Malaysia under Industry-International Incentive Grant (IIIG), UTM, 03M93 for financially supporting this project.

REFERENCES

1. F.A. Lubis, N.A.N.N. Malek, N.S. Sani, K. Jemon. Biogenic synthesis of silver nanoparticles using *Persicaria odorata* leaf extract: Antibacterial, cytocompatibility, and in vitro wound healing evaluation. Particuology 2022, (70): 10-19.
2. N.H. Ab Razak, N.A.N.N. Malek, J. Matmin, J., W.R.Z.W. Dagang, N.A. Zawawi, T.S. Chundawat. Brief review on bioresources green synthesis of silver nanoparticles. Journal of Advanced Research in Materials Science 2021 (79): 1-10.
3. R. Vishwanath, B. Negi. Conventional and green methods of synthesis of silver nanoparticles and their antimicrobial properties. Current Research in Green and Sustainable Chemistry 2021 (4): 100205.
4. R. Ahmad, A.R. Rosandy, I. Sahidin, N.S. Ab Ghani, N.M. Noor, S.N. Baharum. Bioassay analysis and molecular docking study revealed the potential medicinal activities of active compounds Polygonumins B, C and D from *Polygonum minus* (*Persicaria minor*). Plants 2022 (12): 59
5. M. Jalal, M.A. Ansari, M.A., Alzohairy, S.G. Ali, H.M. Khan, A. Almatroudi, M.I. Siddiqui. Anticandidal activity of biosynthesized silver nanoparticles: effect on growth, cell morphology, and key virulence attributes of Candida species. International Journal of Nanomedicine, 2019 (14) 4667-4679.
6. S.M. Din, N.A.N.N. Malek, M. Shamsuddin, J. Matmin, A.A. Hadi, M.H. Asraf. Antibacterial silver nanoparticles using different organs of *Ficus deltoidea* Jack var. kunstleri (King) Corner. Biocatalysis and Agricultural Biotechnology 2022 (44): 102473.
7. A.O. Akintola, B.D. Kehinde, P.B. Ayoola, A.G. Adewoyin, O.T. Adedosu, J.F. Ajayi, S.B. Ogunsona. Antioxidant properties of silver nanoparticles biosynthesized from methanolic leaf extract of *Blighia sapida*. IOP Conference Series: Materials Science and Engineering 2020 (805): 012004).

Role Of Graphene Oxide Addition on Microstructural Properties of $YBa_2Cu_3O_{7-\delta}$ Superconductor

N. A. **Zulkarnain**[1], S. Z. **Ismail**[1], N. H. A. **Kadir** [3] M.M. Awang **Kechik** [4], Aima **Ramli**[2*]

[1] Faculty of Science and Marine Environment, University Malaysia Terengganu, 21030 Kuala Nerus, Terengganu, Malaysia
[2]ANOMA Faculty of Science and Marine Environment, University Malaysia Terengganu, 21030 Kuala Nerus, Terengganu, Malaysia
[3]BIOSES RIG Faculty of Science and Marine Environment, University Malaysia Terengganu, 21030 Kuala Nerus, Terengganu, Malaysia
[4] Department of Physics, Faculty of Science, Universiti Putra Malaysia, Serdang 43400, Selangor, Malaysia

*Corresponding author's phone: +60 133439844
E-mail: aima.ramli@umt.edu.my

ABSTRACT

Yttrium Barium Copper Oxide ($YBa_2Cu_3O_{7-\delta}$) is a group of crystalline chemical compounds of high-temperature superconductors (HTSc). However, $YBa_2Cu_3O_{7-\delta}$ superconductor suffers from low grain conductivity and weak links of the grains, thus resulting in disruption of superconducting performance. Thus, in this research, the high-temperature superconductor $YBa_2Cu_3O_{7-\delta}$ was added with graphene oxide (x = 0.0, 0.2, 0.4, 0.6, 0.8, and 1.0 wt.%) and synthesized via solid state method. All samples then being characterized using thermogravimetric analysis (TGA), X-ray diffraction (XRD), and scanning electron microscope (SEM). The thermogravimetric analysis indicated that the samples have identical thermal decomposition observing the weight lost with optimum sintering temperature at 900 ^{o}C. It was found that orthorhombic structure is preserved in all samples with predominant Y-123 phase and secondary phase of graphene oxide in added samples with the main peak of $2\theta = 32.45^{o}$ plane of (013). Samples became porous and their grain sizes increased as the addition of graphene oxide increased. As a conclusion, it was shown that the addition of the graphene oxide nanoparticle in $YBa_2Cu_3O_{7-\delta}$ increases the grain growth of $YBa_2Cu_3O_{7-\delta}$. This may be attributed to enhancement in superconducting volume fraction in the sample, as graphene oxide nanoparticles reside near the grain boundary region to increase the weak link between superconducting grains.

Keywords—$YBa_2Cu_3O_{7-\delta}$, superconductor, sustain, solid-state method, nanoparticles.

1.0 INTRODUCTION

In a superconducting state, a superconducting material shows zero electrical resistivity. The resistance of the superconductor material will reduce to zero when these superconductor materials are cooled below its critical temperature [1] and related to the magnetic flux penetrating in a superconductor. A superconductor cannot carry current with zero electrical resistance if the flux lines always move. Hence, by the addition of impurities or other kinds of impendent, flux lines can be pinned. As nanoparticles were added to the sample, the behavior of the superconductor critical current density in the applied magnetic field was found to increase, which can be due to the presence of flux pinning centers [2]. By pinning the flux line effectively, vortex movement can be prevented. Hence, the critical current

density is increased. Zero magnetic field also known as critical field occurs at the magnetic field where superconductivity is reacted. $YBa_2Cu_3O_{7-\delta}$ (YBCO) is the most desirable superconductor among the different types of high-temperature superconductors because of its good physical properties, such as the higher value of superconducting transition temperature, good response to the higher value of the magnetic field applied, and mechanical stability at room temperature [3]. Based on the previous research many additions had been conducted towards the $YBa_2Cu_3O_{7-\delta}$ superconductor.

2.0 THEORY/LITERATURE REVIEW

Many additions of impurities had been conducted such as the addition of Neodymium(III) oxide $Nd2O3$ nanoparticles on microstructural properties of YBCO (123) by using co-precipitation method which the samples with the weight percentage of 0.2 until 1.0 percent structure became more porous and the grain sizes significantly decreased [4]. In this research, the addition of x = 0.0, 0.2, 0.4, 0.6, 0.8, and 1.0 wt % graphene oxide (GO) was experimented upon the $YBa_2Cu_3O_{7-\delta}$ superconductor. More homogeneity and better relations between the superconductivity grains are generated by GO doping, and the porosity between them is reduced [5]. Furthermore, Colie stated that the auto-combustion reaction followed by calcination to the micrometric pores and independent or interconnected particles will lead to porous material via SEM [6]. GO is a unique material that can be viewed as a single monomolecular layer of graphite with various oxygen-containing functionalities [7]. The presence of an oxygen functional group procreates graphene oxide to be chemically active and mechanically stable. The oxygen in the functional groups of GO is parted and GO is reduced into reduced graphene oxide (RGO) when undergoes the sintering process with a temperature more than 650 °C. Hence, the removed oxygen enters the copper oxide (CuO) chains of YBCO leading to the reduction of oxygen vacancies and increasing the superconducting parameters [8].

3.0 MATERIALS

All the samples of $YBa_2Cu_3O_{7-\delta}$ were prepared via solid-state method by mixing with the suitable amount of yttrium oxide (Y_2O_3), (Alfa Aesar, 99.9%), barium carbonate ($BaCO_3$) (Alfa Aesar, 99.8 %), and copper oxide (CuO), (Alfa Aesar, 99.7 %) referring to the stoichiometry formula of 1:2:3 for YBa2Cu3O7-δ as shown in Equation 1. Graphene sheets (Aldrich, 4-10% edge-oxidized) were added to the calcined samples that had been grounded.

$$\frac{1}{2}Y_2O_3 + 2BaCO_3 + 3CuO + \frac{1}{2}O_2 \rightarrow YBa_2Cu_3O_7 + 2CO_2 \quad (1)$$

4.0 CHARACTERIZATION

4.1 Thermogravimetry Analysis (TGA)

The thermal properties of the precursor powder were analyzed by Mettler Toledo TGA/DSC 1 from 30 ºC to 900 ºC at a heating rate of 10 ºC/min. The samples of 2g were approximately placed in aluminum pans under a dynamic flow of nitrogen 50mL/min.

4.2 X-Ray Diffraction (XRD)

The thermal properties of the precursor powder were analyzed by Mettler Toledo TGA/DSC 1 from 30 ºC to 900 ºC at a heating rate of 10 ºC/min. The samples of 2g were approximately placed in aluminum pans under a dynamic flow of nitrogen 50mL/min.

4.3 Scanning Electron Microscope (SEM)

SEM measurement was performed by using JEOL JSM-6360LA. The pellets were carefully fractured into small pieces using a pestle and mortar. To get better imaging for the surface and cross-section, the fractured pellets were then coated with

an ultra-thin coating of gold before analyzing the samples to increase the thermal conduction and improve the secondary electron that was detected by SEM. The results that SEM investigated were the surface morphology, homogeneity, grain sizes, and orientation of the samples.

5.0 RESULTS AND DISCUSSION

5.1 Thermogravimetry Analysis (TGA)

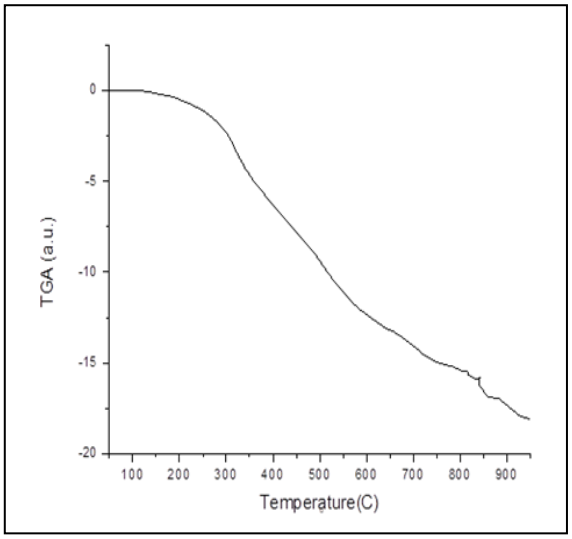

Fig. 1: Thermogravimetric analysis (TGA) of $YBa_2Cu_3O_{7-\delta}$ powder.

The TGA results of the weight loss of YBa2Cu3O7-δ plotted using the Origin 8.5 software. Figure 1 shows the dehydration of moisture and water from the lattice of copper oxide occurring at temperatures below 200 °C.

Then, the complete decomposition of barium carbonate, BaCO3 to barium oxide, BaO occurred at 760 °C and fully decomposed at 855 °C. The graph showed that there was a small mass loss above 900 °C which might have resulted from YBa2Cu3O7-δ phase formation.

5.2 X-ray Diffraction (XRD)

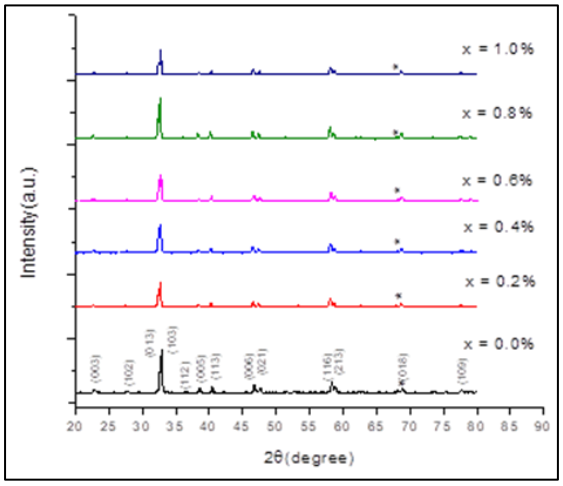

Fig. 2: X-ray diffraction of $YBa_2Cu_3O_{7-\delta}$ when added with graphene oxide (x = 0.0, 0.2, 0.4, 0.6, 0.8 and 1.0 wt.%).

Figure 2 shows the XRD patterns of the $YBa_2Cu_3O_{7-\delta}$ when added with graphene oxide (x = 0.0, 0.2, 0.4, 0.6, 0.8 and 1.0 wt.%). All the XRD results were analyzed using the Crystallographica Search-Match software. It was found that all samples showed orthorhombic structure with pre-dominant Y-123 phase with space group symmetry for orthorhombic crystal system, Pmmm, and impurities of the unreacted graphene appeared with the addition of the x = (0.0, 0.2, 0.4, 0.6, 0.8 and 1.0 wt.%) graphene oxide. The peak at the plane of (013) and the main peak of 2θ = 32.45º were all maintained which indicates the orthorhombic structure.

Table 1: Lattice parameters, a, b, and c axes for $YBa_2Cu_3O_{7-\delta}$ superconductor with the addition of graphene oxide (x = 0.0, 0.2, 0.4, 0.6, 0.8, and 1.0 wt.%).

$YBa_2Cu_3O_{7-\delta} + x$ wt% of GO	*a* (Å)	*b* (Å)	*c* (Å)	V (Å^3)	δ = [(b – a)/(b +a)]
$x = 0.0$	3.82150	3.88500	11.68440	173.47277	0.00824
$x = 0.2$	3.81700	3.88300	11.63300	172.47474	0.00857
$x = 0.4$	3.82449	3.89384	11.50150	171.27979	0.00899
$x = 0.6$	3.81071	3.88025	11.51360	170.68953	0.00904
$x = 0.8$	3.82590	3.89594	11.47940	171.10593	0.00907
$x = 1.0$	3.85000	3.77087	11.67300	169.46686	0.01038

Besides, there are other characteristics reflections confirms the orthorhombicity at (003), (005), (113), (006), (116), (213), (021), and (109). Comparing the diffraction pattern of composite samples with the pure YBCO, all peaks correspond to the pure YBCO but the intensity of the peaks has slightly changed may be interference of the graphene oxide [6]. Due to the grain size of the graphene being very small, it only leads to slight changes in the position of the peak. From the graph, the small peak was observed and a labelled star at $2\theta = 68.75^{o}$ corresponded to the secondary phase which was the addition of graphene oxide.

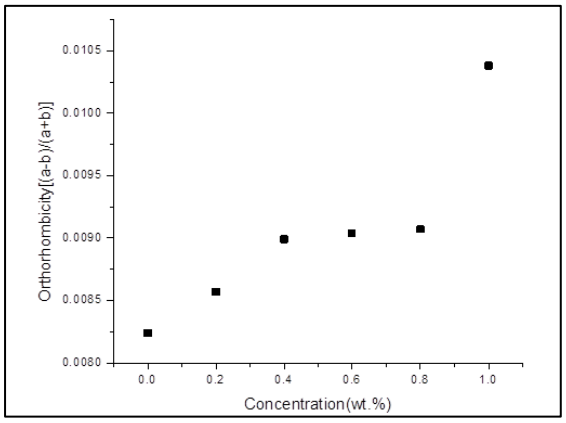

Fig. 3: Calculated orthorhombicity versus $YBa_2Cu_3O_{7-\delta}$ when added with graphene oxide (x = 0.0, 0.2, 0.4, 0.6, 0.8 and 1.0 wt.%).

Table 1 shows the lattice parameters a, b, and c and the unit cell volumes of samples. The constants a, b, and c vary with the different concentrations of graphene oxide percentage determining that the graphene oxide had already incorporated with the $YBa_2Cu_3O_{7-\delta}$ crystal structure. Figure 3 shows the calculated orthorhombicity versus $YBa_2Cu_3O_{7-\delta}$ when added with graphene oxide (x = 0.0, 0.2, 0.4, 0.6, 0.8, and 1.0 wt.%). Furthermore, the addition of graphene oxide may result in a change of the oxygen content in the Y123 system that might affect the lattices constant [9]. As the content of oxygen is a superior parameter which increases the superconducting properties of HTSc, the addition of graphene oxide to $YBa_2Cu_3O_{7-\delta}$ increases the oxygen content. This has been proven by the increasing orthorhombicity value in Table 1.

5.3 Scanning Electron Microscope (SEM)

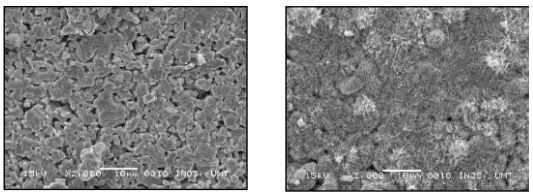

(a) (b)

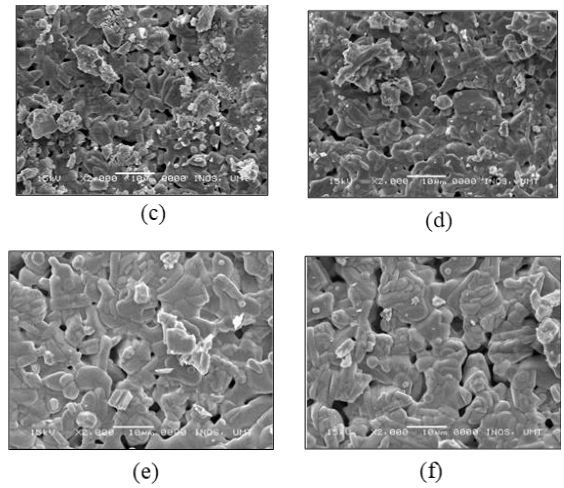

Fig. 4: SEM micrographs of the surface of the $YBa_2Cu_3O_{7-\delta}$ when added with (a) 0.0 wt%, (b) 0.2 wt%, (c) 0.4 wt%, (d) 0.6 wt%, (e) 0.8 wt%, and (f) 1.0 wt% of graphene oxide.

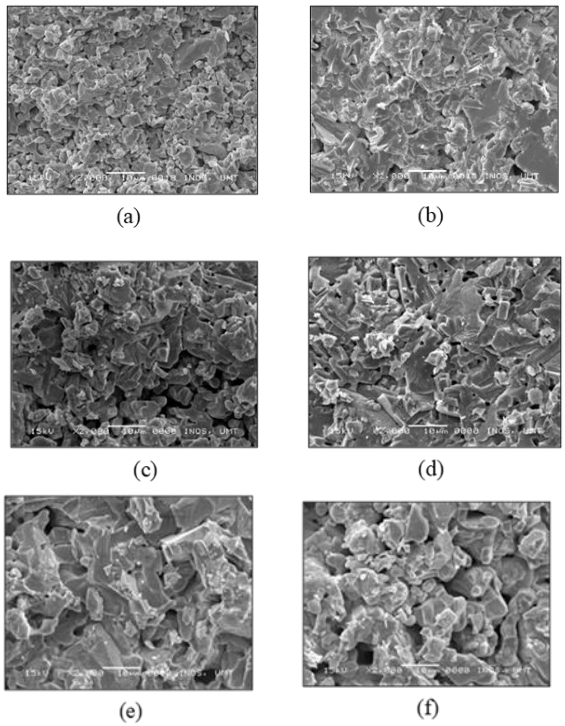

Fig. 5: SEM micrographs of the cross-section of the $YBa_2Cu_3O_{7-\delta}$ when added with (a) 0.0 wt%, (b) 0.2 wt%, (c) 0.4 wt%, (d) 0.6 wt%, (e) 0.8 wt%, and (f) 1.0 wt% of graphene oxide.

The scanning electron microscope was used to analyze the grain size and morphology of the samples through their surface and cross-section. The analyzing process used the magnification of 2000X and about 100 grains were measured using Image J software. Figure 4 and 5 shows the surface and cross-section of the samples respectively according to their weight percentage.

Based on the results all the samples became porous and their grain sizes increased as the addition of graphene oxide increased. It shows that the addition of the graphene oxide nanoparticle in $YBa_2Cu_3O_{7-\delta}$ increases the grain growth of $YBa_2Cu_3O_{7-\delta}$. It proved that as the concentration of graphene oxide increased, the average grain size of the samples also increased. This may be attributed to enhancement in superconducting volume fraction in the sample, as graphene oxide nanoparticles reside near the grain boundary region to increase the weak link between superconducting grains which displays the granular structure with the enhancement of particle size after the addition of graphene oxide [10]. The interlinking among the superconducting grains is increased and due to the inclusion of graphene oxide [11]. In addition, the grain size is also affected by the inhomogeneity of the samples during sample preparation.

6.0 CONCLUSION

The preparation of $YBa_2Cu_3O_{7-\delta}$ when added with graphene oxide (x = 0.0, 0.2, 0.4, 0.6, 0.8 and 1.0 wt.%) was successfully done via solid state method. All the samples were characterized by thermogravimetric analysis (TGA), X-ray diffraction (XRD), and scanning electron microscope (SEM). The result obtained from the TGA shows that the thermal decomposition behavior of $YBa_2Cu_3O_{7-\delta}$ during the TG measurement is analyzed. The XRD result proved that all the samples demonstrated that the samples have an orthorhombic structure with a Y-123 phase. The SEM shows that there is the presence of graphene oxide through the increase of the grain size and porosity as the amount of graphene oxide increases. Particularly, this improvement may be attributed to good

interlinked between the superconducting grains, as the irregularities and voids are filled by the graphene oxide.

ACKNOWLEDGEMENTS

The authors would like to thank the support to Advanced Nano Materials (ANoMa) Research Group of the Faculty of Science and Marine Environment and also the Instrumentation and Control Laboratory of the Faculty of Ocean Engineering Technology and Informatics, University Malaysia Terengganu for all the equipment and also the support given.

REFERENCES

1. Galsin, J. S. (2019). Solid state physics: An introduction to theory. Academic Press.
2. Abd-Ghani, S. N., Abd-Shukor, R., & Kong, W. (2012). Effects of Fe_3O_4 Nano particles addition in high-temperature superconductor $YBa_2Cu_3O_{7-\delta}$. *Advanced Materials Research*, 501, 309-313.
3. Dadras, S., Liu, Y., Chai, Y., Daadmehr, V., & Kim, K. (2009). Increase of critical current density with doping carbon nanotubes in $YBa_2Cu_3O_{7-\delta}$. *Physica C: Superconductivity*, 469(1), 55-59.
4. Ramli, A., Shaari, A. H., Baqiah, H., Kean, C. S., Kechik, M. M. A., & Talib, Z. A. (2016). Role of Nd2O3 nanoparticles addition on microstructural and superconducting properties of YBa2Cu3O7-δ ceramics. Journal of Rare Earths, 34(9), 895–900.
5. Dadras, S., & Gharehgazloo, Z. (2016). Effect of AU nanoparticles doping on polycrystalline YBCO high-temperature superconductor. *Physica B: Condensed Matter*, 492, 45-49.
6. Colie, M., Mihaiescu, D., Surdu, A., Trusca, R., Vasile, B., Istrati, D., Ficai, A., Plapcianu, C., & Andronescu, E. (2016). High-temperature superconducting materials based on Graphene / YBCO nanocomposite. *Materials Today: Proceedings*, 3(8), 2628-2634.
7. Ray, S. (2015). Applications of Graphene and graphene-oxide-based nanomaterials
8. Sahoo, B., Routray, K. L., Samal, D., & Behera, D. (2019). Effect of artificial pinning centers on YBCO high-temperature superconductor through substitution of graphene nano-platelets. *Materials Chemistry and Physics*, 223, 784-788.
9. Jin, F., Zhang, H., Wang, W., Liu, X., & Chen, Q. (2017). Improvement in structure and superconductivity of $YBa_2Cu_3O_{6-\delta}$ ceramics superconductors by optimizing sintering processing. *Journal of Rare Earths*, 35(1), 85–89.
10. Gaffoor, M. Z., Jarvis, A. L., & Archer, J. C. (2023). Investigating the critical transitional temperature increase in graphene oxide doped bulk YBCO. *Results in Physics*, *44*, 106140.
11. Sahoo, B., Singh, A. K., & Behera, D. (2020). Graphene oxide modified superconducting and elastic parameters of YBCO superconductor. *Materials Chemistry and Physics*, 240, 12

Impact of Micrometer and Nanometer-Sized Particles on the Electrical Properties of Prosopis Africana Biochar Thick Films

Suleiman **Babani**[1,3*], Mohd Nizar **Hamidon**[1,2*], Alyani **Ismail** [2], Haslina **Jaafar** [2], Intan Helina **Hasan**[1], Farah Nabilah **Shafiee**[1], Zainab **Yunusa**[3], Umar **Musa**[3], Jamila **Lamido**[1,3], Azlinda **Abu Bakar** [1], Ismail **Lawal** [2,4]

[1] Institute of Nanoscience & Nanotechnology (ION2), Universiti Putra Malaysia, 43400 UPM Serdang, Selangor, Malaysia
[2] Faculty of Engineering, Universiti Putra Malaysia, 43400 UPM Serdang, Selangor, Malaysia
[3] Department of Electrical Engineering, Faculty of Engineering, Bayero Universiti Kano, PMB 3011 Kano, Nigeria
[4] National Agency for Science and Engineering Infrastructure (NASENI): HEDI Kano, Nigeria.

*Corresponding author's phone: +60196648600 / +60104260737
E-mail: mnh@upm.edu.my / sbabani.ele@buk.edu.ng

ABSTRACT

The goal of this work was to develop a thick film using Prosopis africana biochar PAC and to investigate the influence of particle size on the electrical properties of the thick layer of P. africana. In this study, biochar particles of micrometer and nanometer sizes were prepared, from which a conductive paste was prepared and deposited on an alumina substrate using a screen-printing technique. The PAC material was sieved to < 20 µm for the micrometer size and then milled for 3 hrs at the nanometer scale. The electrical properties of thick biochar films were characterized and compared. The results show that the micrometer-sized particles are dense and uniform films with better interparticle contact and higher electrical conductivity than thick films with nanosized particles. In future work, it will be necessary to examine the effects of different firing temperatures and the adhesion of the thick film to its substrate. A longer firing time enhanced the conductivity of thick PAC layers.

Keywords— PAC; thick films; substrate; resistance.

1.0 INTRODUCTION

Owing to their tremendous electrical and mechanical properties, carbon materials, especially carbon nanomaterials, are in high demand [1]. There has been a rapid development in technology using carbon-based materials. over the past few years, particularly in the fields of electronics and biomedicine. Several applications of carbon-based nanomaterials include transistors [2], sensors [3], and radio-frequency identification tags (RFIDs) [4]. Nanomaterials made from carbon, such as carbon nanotubes (CNT and graphene, are in high demand because of their low cost and exceptional electrical, mechanical, and optical properties [2], [3]. The fabrication of thick films is a cost-effective and scalable method of incorporating biochar into electronic devices. The electrical properties of thick films can be significantly affected by the particle size of biochar, and the improvement in a thick film is proportional to its active layer, which adds value to its desired properties [5]. In this study, the effects of two different particle sizes, nanometric and micronic, on the electrical properties of thick films were investigated. The biochar is derived from

Prosopis Africana, a common biomass waste has gained attention as a potential material for various applications [6]–[9].
The novelty of this research lies in exploring how particle sizes, ranging from micrometers to nanometers, affect the electrical properties of thick films made from PAC, which have not yet been studied, to the best of our knowledge.

2.0 METHOD AND MATERIAL

Prosopis Africana biochar (PAC) particles were prepared and characterized to study the effects of particle size on the electrical properties of a thick layer. Biochar was obtained by subjecting Prosopis africana biomass waste to controlled pyrolysis. To obtain micronic particle sizes, the biochar particles were sieved to an average particle size of < 20 μm, whereas the biochar was milled for 3 hrs using a milling machine SPEX08000D to make the nanoparticles of the PAC biochar to be used as the material in the thick film fabrication process. Two pastes containing 40 wt% micrometer-sized particles and 40 wt% nanometer-sized particles of PAC were prepared by combining them with 60 wt% of an organic binder consisting of alpha-terpineol, m-xylene, and linseed stand oil to form pastes suitable for screen printing. The obtained mixture was stirred for 24 h at 40 °C and 300 rpm using a magnetic stirring device [10]. Later, the pastes were applied to an alumina substrate using the screen-printing technique. The Holding time refers to the duration for which a material or sample is maintained at a specific firing temperature during the heat treatment process. The choice of holding time can significantly affect the outcome of the firing process and the properties of the material being treated. Three distinct holding times were chosen: 30, 60, and 90 min, with a constant firing temperature maintained at 350 °C for the three different holding times. The sheet resistance and resistance of the thick layers were determined using four-point probe measurements. The equipment used in this work was a four-point probe (LORESTER-GX MCP-T700) for the measurement of resistance. In conclusion, this study aims to bridge the knowledge gap regarding the influence of particle size on the electrical properties of Prosopis africana biochar thick films. Through a systematic methodology encompassing biochar preparation, film fabrication, electrical characterization, and mechanistic investigation, this study seeks to provide valuable insights into optimizing biochar-based thick films for enhanced electrical performance in various applications.

3.0 RESULTS AND DISCUSSION

Three different holding times were chosen for firing at 350 °C, and the resistances of the nano- and micron-sized PAC thick films were compared. Because of the drying process of the binder, organic solvents and other volatile substances that may hinder the desired properties were removed. Nanometer-sized particles were observed in milled PAC powder samples. The nanosized meter exhibited higher resistance values than the micrometer. The milling process created defects on the particle surfaces, decreasing conductivity and preventing electron movement. The high surface-area-to-volume ratio of nanoparticles leads to increased reactivity and van der Waals forces on the particle surfaces, causing the particles to agglomerate [5]. This causes the particles to agglomerate, affecting the consistency of the paste [11] and ultimately affecting the resistance of the thick film, as shown below. Additionally, a longer firing hold time enhances the conductivity of the thick PAC layers [12].

Table 1: The Values of Pac Resistance of Thick Layers

Samples	Temperature (^{O}C)	Holding Time (min)	Resistance (kΩ)
X	350	30	8.110

		60	4.381
		90	0.920
Y	350	30	220.30
		60	143.50
		90	71.75

X = micrometer-sized and Y = nanometer-sized

The micrometer-sized particles resulted in a highly conductive film, which was attributed to better interparticle contact. A larger particle size facilitated better electron transport pathways and reduced the overall resistance of the film. The existence of nonconductive pores and lower interparticle contacts can be attributed to this phenomenon. The increased surface area and porosity of the film contributed to a higher capacitance, suggesting its potential for energy storage applications [13]. Figure 1 shows the measurement configurations for the data collected using a four-point probe. The resistances of the samples are listed in Table 1.

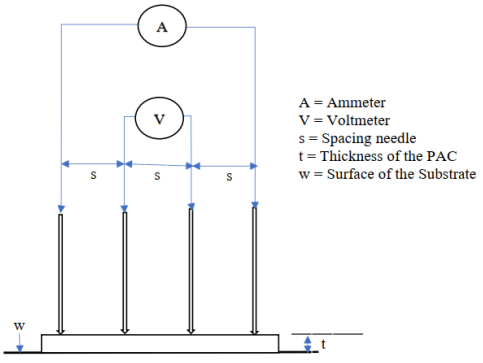

Fig.1 Measurement set up for 4-point probes.

In summary, the study investigates the effects of micrometer and nanometer-sized particles on the electrical properties of Prosopis Africana biochar thick films, aiming to uncover correlations and key findings that contribute to a deeper understanding of the relationship between particle size, electrical behavior, dispersion, and alignment, and conductivity analysis.

4.0 CONCLUSION

In conclusion, the particle size of Prosopis africana biochar has a significant influence on the electrical properties of thick films deposited on an alumina substrate. The micrometer-sized particles result in a dense and uniform film with better interparticle contact and higher electrical conductivity. On the other hand, nanometer-sized particles lead to a porous film structure with enhanced capacitive behavior owing to the increased surface area and porosity. The choice of particle size can be tailored to the specific application requirements of electronic devices and energy storage systems. The particle size affects the properties of the thick film because of the surface energy, where a smaller particle size has a larger surface area. A micron-thick film is better than a nanometric-thick film in terms of how the paste can be printed on the substrate and how well it conducts electricity. For further work to determine the flexibility of the thick film itself, it will be necessary to examine the effects of different firing temperatures and the adhesion of the thick film to its substrate.

ACKNOWLEDGEMENTS

This work was funded by the Petroleum Technology Development Fund (PTDF), Nigeria, for financial support, and the Institute of Nanoscience and Nanotechnology (ION2), Universiti Putra Malaysia (UPM), Malaysia.

REFERENCES

1. N. Haziqah, A. Aziz, H. Jaafar, S. Shafie, M. N. Hamidon, and R. M. Sidek, “Electrical Properties of Carbon Nanotube (CNT) Nano-Ink on Different Substrates.”
2. E. Artukovic, M. Kaempgen, D. S. Hecht, S. Roth, and G. Grüner, “Transparent and flexible carbon nanotube transistors,” *Nano Lett.*, vol. 5, no. 4, pp. 757–760, 2005.
3. V. Scardaci, R. Coull, J. N. Coleman, L. Byrne, and G. Scott, “Carbon Nanotube network-based sensors,” *Proc. IEEE Conf. Nanotechnol.*, pp. 1–3, 2012.

4. L. Yang, R. Zhang, D. Staiculescu, C. P. Wong, and M. M. Tentzeris, “A novel conformal RFID-enabled module utilizing inkjet-printed antennas and carbon nanotubes for gas-detection applications,” *IEEE Antennas Wirel. Propag. Lett.*, vol. 8, pp. 653–656, 2009.
5. F. N. Shafiee *et al.*, “Effect of nanometric and micronic particle size on physical and electrical properties of graphite thick film,” *Int. J. Nanotechnol.*, vol. 17, no. 11–12, pp. 825–839, 2020.
6. A. A. Rahim and Z. N. Garba, “Optimization of preparation conditions for activated carbon from Prosopis africana seed hulls using response surface methodology,” vol. 3994, no. March 2016.
7. Z. N. Garba and A. A. Rahim, “Journal of Analytical and Applied Pyrolysis Process optimization of K 2 C 2 O 4 -activated carbon from Prosopis africana seed hulls using response surface methodology,” *J. Anal. Appl. Pyrolysis*, vol. 107, pp. 306–312, 2014.
8. P. Africana and C. Briquettes, “Effects of Particle Size on the Thermal Properties of Sawdust, Corncobs and Effects of Particle Size on the Thermal Properties of Sawdust , Corncobs and Prosopis Africana Charcoal Briquettes .,” no. January, 2014.
9. P. O. Nnamani, F. C. Kenechukwu, O. C. Chika, and F. C. Otuu, “Performance of Prosopis africana peel powder (PAPP) as a novel sorbent for remediating malachite green contaminated aqua system,” *Sci. Res. Essays*, vol. 7, no. 48, pp. 4130–4137, 2012.
10. F. N. Shafiee, “Effect of nanometric and micronic particles size on physical and electrical properties of graphite thick film Mohd Nizar Hamidon * Mohd Haniff Wahid Abdul Halim Shaari Mehmet Ertugrul Nor Hapishah Abdullah and Mohd Asnawi Mohd Kusaimi Muhammad Syazwan Mus,” vol. 17, pp. 825–839, 2020.
11. C. Pretschuh, C. Schwarzinger, A. A. Abdala, and S. Vukusic, “Characterization of Conductive Nanographite Melamine Composites,” *Open J. Compos. Mater.*, vol. 04, no. 01, pp. 61–71, 2014.
12. I. H. Hassan, “PREPARATION AND CHARACTERIZATION OF NANOSIZED GRAPHITE BASED THICK FILM FOR FLEXIBLE ELECTRONICS Intan,” *Solid State Sci. Technol.*, vol. 26, no. 2, pp. 50–56, 2018.
13. Z. Husain *et al.*, “Materials Science for Energy Technologies Nano-sized mesoporous biochar derived from biomass pyrolysis as electrochemical energy storage supercapacitor,” vol. 5, pp. 99–109, 2022.

Preparation and Characterization of Electrospun PAN/Sago Lignin Nanofibers

Dzaidatu Aqmal **Ramlee**[1], Nurul Aida **Nordin**[1], Norizah **Abdul Rahman**[1,2*] and Hasliza **Bahruji**[3]

[1]Department of Chemistry, Faculty of Science, Universiti Putra Malaysia, Serdang 43400, Selangor, Malaysia.;

[2]Nanomaterials Processing and Technology Laboratory, Institute of Nanoscience and Nanotechnology, Universiti Putra Malaysia, UPM, Serdang 43400, Selangor, Malaysia.

[3]Centre of Advanced Material and Energy Science, University Brunei Darussalam, Jalan Tungku Link, Gadong BE 1410, Brunei Darussalam.

*Corresponding author's phone: +603-97696775
E-mail: a_norizah@upm.edu.my

ABSTRACT

Polyacrylonitrile (PAN)/Sago Lignin (SL) nanofibers were prepared via consecutive electrospinning method. The PAN to SL ratios were varied during electrospinning to obtain an optimum morphology of the fibers. The fiber diameter of PAN/SL was found to be greatly dependent on the ratio of SL incorporated in the fibers. The diameter of the fiber varied from 500 nm to 700 nm. A uniform bead-free nanofibers morphology was achieved at 20 wt% of lignin content. FTIR analysis results suggest that the two polymers only have physical blending without any chemical interactions. The degradation steps of the fibers were faster (steeper) than sago lignin only, but overall, the PAN/SL still maintains its thermal stability. DSC results show that PAN and SL were homogenously blended. The electrospun PAN/SL nanofibers show great potential to be used as the carbon nanofibers precursor.

Keywords—electrospinning; polyacrylonitrile; nanofibers; sago lignin; carbon fibers

1.0 INTRODUCTION

In recent years, nano-scaled materials have shown extensive research interest and showed great promise to be applied in a wide range of applications including medical, environmental, food packaging, and many more [1-2]. Among nano-scaled materials, electrospun nanofibers materials have attracted widespread attention due to their high porosity, gas permeability, and specific surface area [3]. Furthermore, electrospun nanofibrous membranes possess several attractive qualities, such as controllable fiber diameter and porosity, interconnected open pore structure, and high permeability of gases [4]. In addition, the varieties of the electrospun fiber properties can be achieved by blending two polymers. The ratio of the two polymers will greatly affect the morphology and also the properties of the electrospun nanofibers.

2.0 THEORY/LITERATURE REVIEW

Carbon fibers are industrially important and have gained significant attention in applications, from sports equipment to the aerospace industry. Most (90%) of the carbon fibers produced worldwide are obtained from polyacrylonitrile (PAN) and the rest from other raw materials, such as phenolic, rayon, or pitch fibers. Although PAN fibers are used extensively as a source of carbon fibers because their carbon yield is almost twice that of rayon [5]. Electrospun polyacrylonitrile (PAN)-based nanofiber

with a uniform diameter of ca. 800 nm was carbonized and steam-activated to produce activated carbon nanofiber with tailored microporosity and abundant nitrogen-containing functional groups as highly efficient adsorption sites [6].

PAN has some advantages as a carbon fibers precursors such as high carbon yield, easy-to-obtain uniform carbon fibers, and commercial viability. However, the drawbacks of PAN precursor are the price of PAN is high and it is produced from petroleum-based resources (non-renewable). Recently, researchers are intended to explore an alternative to PAN that is less expensive and has renewable resources [7-8].

Lignin is the second most abundant terrestrial biopolymer after cellulose and an essential renewable source of aromatic configurations in nature. Lignin is a by-product of the paper industry with a high molecular weight [9]. The usage of lignin as a precursor to carbonaceous materials has expanded interest not only due to its low cost but also owing to the presence of functional groups, such as carboxyl, hydroxyl, and carbonyl groups [10]. Lignin is the only natural source of aromatic compounds; it can serve as a renewable and sustainable source of specialty liquid fuels and chemicals [11]. To date, lignin cannot be electrospun alone and need to be blended with other polymers such as PAN.

In this study, sago lignin (SL) was extracted from sago waste and utilized to investigate the blending of SL with PAN in the production of PAN/SL nanofibers. The PAN and SL ratio was varied to study the effect of SL in the nanofibers. The PAN/SL fibers were characterized by using FTIR, scanning electron microscopy (SEM), thermogravimetric analysis (TGA), and differential scanning calorimetry (DSC) to determine the chemical. morphology and thermal properties of the fibers. The importance of this study is to understand the PAN/SL nanofibers before the conversion of the fibers to become carbon nanofibers (future work).

3.0 MATERIALS

Sago waste was obtained from Malaysia Nuclear Agency Bangi Complex. Benzene, polyacrylonitrile (PAN), M_w = 150000 g/mol, and dimethylformamide (DMF) were purchased from Sigma-Aldrich.

4.0 EXPERIMENTAL

4.1 Electrospun of PAN/SL nanofibers

Sago lignin was isolated from sago waste according to the previously reported method [19] with a slight modification. For the preparation of PAN/SL nanofibers, PAN was first dissolved in DMF solution to prepare 7.5% (wt/v) PAN solution. Sago lignin was then blended with 7.5% (wt/v) PAN solution in which the ratio of PAN:SL (wt/wt) was varied at different wt%; 9:1, 8:2, 7:3, 6:4, and 5:5. For electrospinning process, the polymer solution was filled in the 5 mL syringe attached with 0.8 mm needle diameter. The distance from the collector to the needle tip was fixed at 10 cm, the voltage applied was fixed at 18kV and the solution was electrospun at 2 mL h^{-1} flow rate.

4.2 Characterizations

The morphology of the nanofibers was examined using scanning electron microscopy (SEM) (JEOL JSM 6400, Tokyo, Japan). The samples were coated with a thin layer of gold and the samples were scanned by 2,500X, 5,000X, and 10,000 X magnification. 20 readings of nanofibers diameter were determined using ImageJ software to determine the average fiber diameter. The functional group of nanofibers was analyzed using attenuated total reflectance Fourier transform infrared (ATR-FTIR) spectrometer (Per-kin Elmer Spectrum RXI, Waltham, MA, USA) in the range of 4000 to 280 cm^{-1}. The thermal properties of sago lignin and PAN/ Sago

lignin nanofibers were determined using differential scanning calorimetry (DSC) (Model DSC Mettler Toledo 822). The small amount of sample was sealed in an aluminum pan and was heated in the range of 50 to 250 °C. The heating rate was 10 °C min^{-1} with a nitrogen flow of 50 mL min^{-1}. The thermal stability of sago lignin and PAN/sago lignin nanofibers were determined using thermogravimetric analysis (TGA) (Model TGA Mettler Toledo). Less than 10 mg sample was weighed, then sealed in an aluminum pan. The sample was heated at the range of 50 °C to 250 °C, with a heating rate of 10 °C min^{-1} under a nitrogen flow of 50 mL min^{-1}.

5.0 RESULTS AND DISCUSSION

The electrospun PAN/SL fibers were prepared by blending different ratios of PAN: SL mixtures to determine the optimum structure and morphology. The ratio of PAN to SL varied from 9:1, 8:2, 7:3, 6:4, and 5:5 as shown in Figure 1. The average diameter of PAN/SL nanofibers of 9:1 ratio was 718 ± 44 nm, 8:2 ratio was 698 ± 47 nm, 7:3 ratio was 505 ± 53 nm, 6:4 ratio was 472 ± 68 nm and 5:5 ratio was 455 ± 41 nm. The SEM micrographs showed the formation of small beads on the surface of nanofibers for 9:1, 7:3, 6:4, and 5:5 PAN/SL fibers. Meanwhile, the uniform and bead-free fibers were achieved using the 8:2 ratio.

The relationship between the PAN/SL ratio with the diameter of electrospun PAN/SL fiber is shown in Figure 2. The average nanofibers diameter was significantly affected by the composition of SL. The fiber diameter gradually decreased when a higher amount of lignin was used. The average fiber diameter was reduced to below 500 nm when the SL composition reached 30% and above. Similar results were observed by de Gonzaga et al. [12], where they found that the addition of lignin to PAN reduced the viscosity of the PAN solution in DMF. The low viscosity of the polymers (PAN/lignin) solution produces thinner electrospun fibers compared to PAN only.

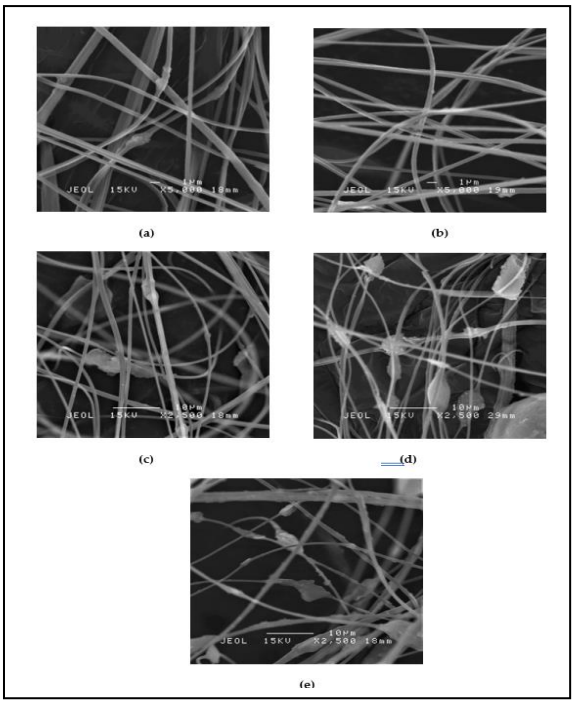

Fig. 1: SEM micrographs of PAN/SL fibers: (a) 9:1, (b) 8:2, (c) 7:3, (d) 6:4, (e) 5:5 of PAN:SL ratios.

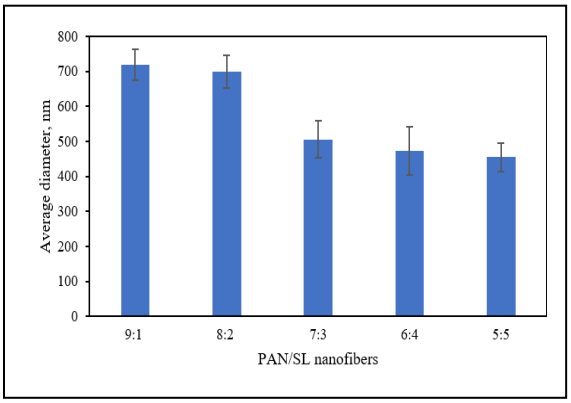

Fig. 2: Effect of different PAN/SL ratios on the average diameter of fibers.

Figure 3 illustrates the IR spectra for PAN/SL nanofibers. The interpretation of the FTIR spectra is based on the chemical structure of PAN and sago lignin. Based on the spectra, it presents mainly three stretching peaks, the first located around 3200 cm^{-1} and 2930 cm^{-1}, which can be attributed to C–H stretching of PAN and methyl groups present in sago lignin and the second located around 1450 cm^{-1} assigned to

the aromatic ring stretching of C-C. The third stretching band appeared around 1620 cm^{-1} and 1660 cm^{-1} corresponding to the C=C in the benzene ring. Moreover, the presence of an absorption band around 1080 cm^{-1} is due to the C-O bond of the ether and phenolic group presence in sago lignin [13]. There is no shifting or new peak formed in the IR spectra of the PAN/SL nanofibers suggesting that the blending is only involved with physical blending and does not have any chemical interactions between the two polymers.

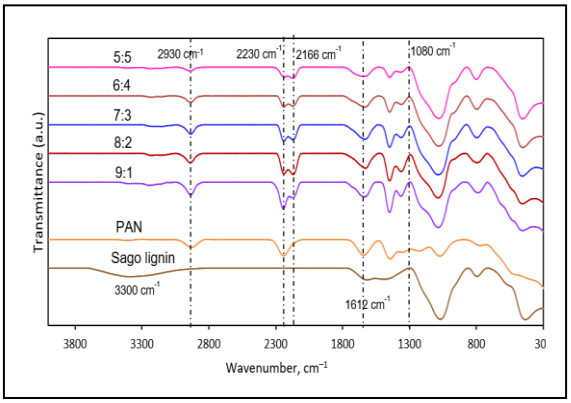

Fig. 3: ATR-FTIR spectra of sago lignin and PAN/SL nanofibers at different PAN to SL ratios.

Figure 4 shows the TGA thermogram of sago lignin and PAN/sago lignin nanofibers at different ratios. Based on the thermogram, the first weight loss temperature of sago lignin at 50 - 120 °C, which is due to the evaporation of moisture. This is expected since lignin is a hydrophilic polymer that can adsorb moisture. The second weight loss occurred between 250 to 300 °C, which is attributed to the evolution of volatiles and the initial decomposition of lignin [14]. The degradation of lignin mainly involved the degradation of β-O-4. The decomposition of lignin is much slower compared to blended PAN/SL nanofibers and the thermogram graph shows a less steep curve. This can be explained by the composition of lignin which contains various oxygen functional groups in its structure. The degradation rate mainly depended on the content of β-O-4 in the lignin [15].

The second degradation onset temperature is also contributed by the decomposition of PAN involved with the scission of C-N bonds. This can be seen in Figure 4, the greater weight loss for PAN/SL nanofibers compared to SL only.

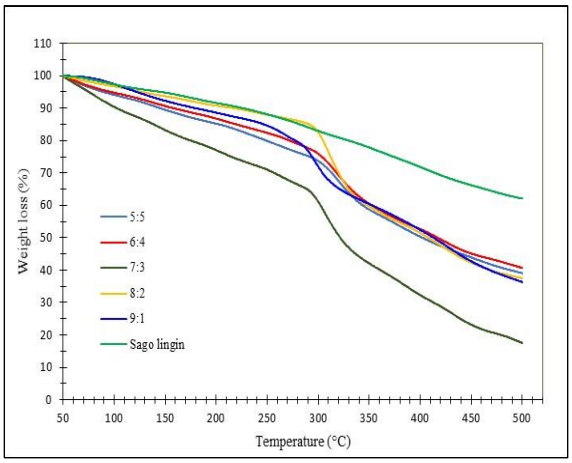

Fig. 4: TGA Thermogram of sago lignin and PAN/sago lignin nanofibers at different PAN/sago lignin ratios.

Figure 5 shows the DSC thermogram of PAN/sago lignin nanofibers. The thermograms of all nanofibers with different ratios show almost the same pattern, in which the endothermic peaks can be observed at temperatures around 60 - 80 °C, which corresponds to the glass transition temperature (T_g). Only one T_g was observed for all the fibers showing that the PAN and SL are miscible at the molecular scale and the mobility of the PAN and SL polymer chains are averaged. The removal of water and a series of low-temperature radical coupling occurs at this stage. The thermograms show a sharp and narrow exothermic peak around 300 °C. This is due to the cyclization reaction of the adjacent nitrile group with no other reactions occurring in a nitrogen atmosphere and forming a ladder structure, which causes a lot of heat to evolve from PAN [16]. The increased incorporation of SL in the fibers caused significantly reduced the intensity of the exothermic peak of cyclization and shifted the maximum peak temperature to a higher temperature.

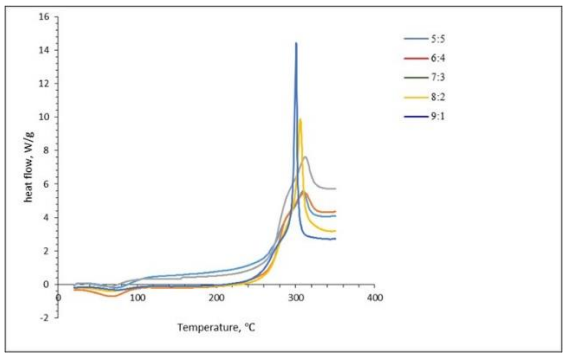

Fig. 5: DSC thermogram of PAN/Sago lignin nanofibers at different ratios.

6.0 CONCLUSION

PAN and sago lignin can be electrospun smoothly by using an electrospinning technique with various PAN-to-SL ratios. Variation of PAN/SL ratios showed that the optimum 8:2 PAN/SL nanofibers have uniform morphology with no apparent beads structures. The degradation steps of the fibers are steeper than SL only, but overall, the PAN/SL still maintains its thermal stability. DSC results show that PAN and SL were homogenously blended. The results show that PAN/SL nanofibers have great potential to be used as the carbon nanofibers precursor.

ACKNOWLEDGEMENTS

The authors are grateful for the financial support from the Ministry of Education Malaysia (FRGS/1/2019/STG01/UPM/02/7). The authors also greatly acknowledge the Nuclear Agency Malaysia for providing the sago waste.

REFERENCES

1. Baig, N., Kammakakam, I., and Falath, W., "Nanomaterials: a review of synthesis methods, properties, recent progress, and challenges", *Mater. Adv.*, vol. 2, pp. 1821–1871, 2021. https://doi.org/10.1039/D0MA00807A
2. Chen, M., Wang, C., Fang, W., Wang, J., Zhang, W., Jin, G., and Diao, G., "Electrospinning of Calixarene-Functionalized Polyacrylonitrile Nanofiber Membranes and Application as an Adsorbent and Catalyst Support", *Langmuir*, vol. 29, no. 38, pp. 11858–11867, 2013. doi: 10.1021/la4017799
3. Abdul Rahman, N., Gizdavic-Nikolaidis, M., Ray, S., Easteal, A.J., and Travas-Sejdic, J., "Functional electrospun nanofibres of poly(lactic acid) blends with polyaniline or poly(aniline-co-benzoic acid)", *Synth. Met.*, vol. 160, no.17-18, pp. 2015-2022, 2010. https://doi.org/10.1016/j.synthmet.2010.07.031
4. Gopal, R., Kaur, S., Feng, C. Y., Chan, C., Ramakrishna, S., Tabe, S., and Matsuura, T., "Electrospun nanofibrous polysulfone membranes as pre-filters: Particulate removal", *Journal of Membrane Science*, vol. 289, no. 1-2, pp. 210–219, 2007. doi: 10.1016/j.memsci.2006.11.056
5. Han, S. P., Xu, L. H., Cao W. Y., et al. "Aggregate states of PAN in the process of fiber formation", *New Carbon Materials*, vol. 21, pp. 54-58, 2006.
6. Lee, K. J., Shiratori, N., Lee, G. H., Miyawaki, J., Mochida, I., Yoon, S.-H., and Jang, J., "Activated carbon nanofiber produced from electrospun polyacrylonitrile nanofiber as a highly efficient formaldehyde adsorbent", *Carbon*, vol. 48, no. 15, pp. 4248–4255, 2010.
7. Zakaria, A.F., Kamaruzaman, S., and Abdul Rahman, Polyacrylonitrile/Lignin/Poly(Ethylene Glycol)-Based Porous Activated Carbon Nanofiber for Removal of Nickel(II) Ion from Aqueous Solution", *Polymers*, vol. 13, pp. 3590, 2021. https://doi.org/10.3390/polym13203590
8. Nordin, N.A., Abdul Rahman, N., and Abdullah, A.H., "Effective Removal of Pb(II) Ions by Electrospun PAN/Sago Lignin-Based Activated Carbon Nanofibers", *Molecules*, vol. 25, pp. 3081, 2020. https://doi.org/10.3390/molecules25133081
9. Ruiz-Rosas, R., Bedia, J., Lallave, M., Loscertales, I., Barrero, A., Rodríguez-Mirasol, J., and Cordero, T., "The production of submicron diameter carbon fibers by the electrospinning of lignin", *Carbon*, vol. 48, no. 3, pp. 696–705, 2010. doi: 10.1016/j.carbon.2009.10.014
10. Duval, A., and Lawoko, M., "A review on lignin-based polymeric, micro and nanostructured materials", *React. Funct. Polym.*, vol. 85, pp. 78, 2014.
11. Luo, H., and Abu-Omar, M. M.,

"Chemicals From Lignin", *Encyclopedia of Sustainable Technologies*, pp. 573–585, 2017. doi: 10.1016/b978-0-12-409548-9.10235-0

12. de Gonzaga, L.A.C., Martins, M.C.F., Correa, A.C. et al. "Production of carbon nanofibers from PAN and lignin by solution blow spinning", *J. Polym. Res.* Vol. 28, pp. 237, 2021.
13. Ramasubramaniam, G. (2013). Influence of Lignin modification on PAN-Lignin copolymers as potential carbon fiber precursors. Graduate Theses and Dissertations. 13438. https://lib.dr.iastate.edu/etd/13438
14. Zhou, M., Pu, F., Wang, Z., and Guan, S., "Nitrogen-doped Porous Carbons Through KOH Activation with Superior Performance in Supercapacitors," *Carbon*, Vol. 68, pp. 185-194, 2014.
15. Brebu, M., and Vasile, C., "Thermal degradation of lignin—a review". *Cellul. Chem. Technol.*, vol. 44, pp. 353, 2010.
16. Zhang, H., Quan, L., Gao, A., Tong, Y., Shi, F. and Xu, L. "Thermal Analysis and Crystal Structure of Poly(Acrylonitrile-Co-Itaconic Acid) Copolymers Synthesized in Water", *Polymers*, vol. 12, pp. 221, 2020. https://doi.org/10.3390/polym12010221

Aluminium-Doped Zinc Oxide (AZO) Prepared by Hydrothermal Method as a Potential of Potentiometric pH Sensors

Muhammad **Azmi**[1*], Naif **H. Al-Hardan**[1], Lim **Kar Keng**[2], Firdaus **Md Raih**[1] Ain **Zafirah** [1]

[1]Department of Applied Physics, Faculty of Science and Technology, Universiti Kebangsaan Malaysia, 43600 UKM, Bangi Selangor, Malaysia
[2] Pusat Pengajian Citra Universiti, Universiti Kebangsaan Malaysia, 43600 UKM, Bangi Selangor, Malaysia

*Corresponding author's phone: +6019-3661127
E-mail: azmi@ukm.edu.my

ABSTRACT

Numerous investigations have been conducted to increase the sensitivity and stability of metal oxide semiconductors as pH-sensing membranes. This article will describe the pH sensing and characterization of undoped zinc oxide (ZnO) and aluminium-doped zinc oxide (AZO) as potentiometric pH sensors. The hydrothermal technique was used to grow undoped ZnO and aluminium doped ZnO thin film nanostructures with doping concentrations of 1% and 3% Al on the cleaned FTO substrates. The pH potentiometric sensing was performed in a wide pH range of 4-12 and produced sensitivity, including stability of the nanostructures. The prepared samples were also characterized by X-ray diffraction analysis (XRD), field effect scanning electron microscope (FESEM), energy dispersive X-ray (EDX) to explore the influence of aluminium concentration on structural and morphology characteristics and then prepared as electrodes for pH sensing. From the XRD result, the sharp peaks and high peak intensities demonstrated well crystalline of the synthesized ZnO nanorods. Furthermore, the FESEM reveals the growth of array nanorods perpendicular over the surface of FTO. The sensitivity of the pH sensor with 3 at% AZO exhibits higher sensitivity (43.80 mV/pH), and larger linearity (0.9507).

Keywords—potentiometric;aluminium doped zinc oxide; pH sensor; hydrothermal

1.0 INTRODUCTION

Zinc oxide nanostructures (ZnO) has been used in various applications such as chemical and electrochemical sensor, high-power electronics, nanogenerators and development of biosensors applications [1], [2]. ZnO is a n-type semiconductor with wide and direct energy bandgap (3.37eV) and also have great chemical, electrical, and mechanical capabilities [3]. However, intrinsic ZnO has a high resistance, low conductivity and it can be enhanced by doping ZnO with group III metal elements [4]. Based [5], [6] aluminium (Al) has been the most used dopant element because it was affordable and can improve electrical qualities by improving ZnO conductivity. Furthermore, there are several growth methods for ZnO nanostructures such as chemical bath deposition (CBD), magnetron sputtering, sol-gel and hydrothermal method [7], [8]. Hydrothermal process is the preferred and versatile method as it is simple, low cost fabrication, environmental friendly with a repeatable results [9].

2.0 THEORY/LITERATURE REVIEW

To improve sensor performance, sensing materials must be used in the design of sensor devices. For

particular sensor applications, a variety of sensing materials, including polymers, nanomaterials, and composites, have been created. By altering the structure of the sensing materials, either physically or chemically, it is possible to further enhance their physicochemical qualities.As such a suitable dopant such as Al may improved ZnO sensitivity as a potentiometric pH sensor.

In this paper, we studied the growth of undoped ZnO and aluminium doped ZnO (1% and 3% Al) on FTO substrate as a pH sensor via the hydrothermal technique. The sensitivity and linearity of the pH-sensing sensor were investigated.

3.0 MATERIALS

The precursor solution was made to growth ZnO by combining zinc nitrate hexahydrate ($Zn(NO_3)_2•6H_2O$) and hexamethylenetetramine (HMTA). Then the addition of aluminium nitrate nanohydrate ($Al(NO_3)_2•9H_2O$) for growth aluminium doped ZnO into precursor solution. All the materials are from Sigma Aldrich.

4.0 EXPERIMENTAL

FTO conductive glass was cleaned with acetone, methanol, and ethanol before it ultrasonically cleaned with deionized water. The hydrothermal technique was utilised to grow undoped ZnO and aluminium doped ZnO nanorods. The precursor solution was made to growth ZnO by combining 0.025 M zinc nitrate hexahydrate ($Zn(NO_3)_2•6H_2O$) and 0.025 M hexamethylenetetramine (HMTA). Similar procedures were followed, with the addition of aluminium nitrate nanohydrate ($Al(NO_3)_2•9H_2O$) for growth aluminium doped ZnO into precursor solution. The concentration of Al dopant was labelled as undoped ZnO, 1% Al, and 3% Al respectively. The growth process was carried out in a oven at 95 °C for 6 hours. The samples were then cooled to room temperature and cleaned numerous times with deionized water. The sample has been dried for 20 minutes at 100 °C in a conventional oven. The samples were then produced as an electrode after that were immersed in reverse osmosis (RO) water for 12 hours before the detecting membranes were tested.

5.0 RESULTS AND DISCUSSION

Fig.1 reveals the FESEM images of (a) Undoped ZnO, (b) 1% Al, (c) 3% Al. Based on fig. 1, the images of undoped ZnO reveals the clear presence of hexagonal nanorods, confirming a c-axis growth by hydrothermal method at 95°C along the [002] direction. When the Al doping concentration is increased by 1% and 3%, the amount of sharp hexagonal nanorods is being reduced. The enhancement of Al doping exhibits nanorod hexagonal shape, existing with several nanosheets of ZnO. Based on the EDX spectra, well-defined peaks of Zn, O and Al were noticed. There was no other impurity-related peak found in the EDX spectra.

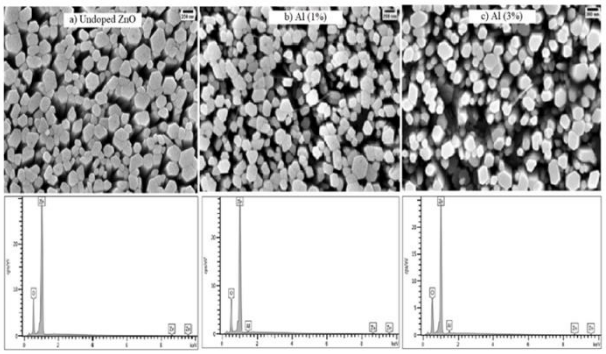

Fig. 1: The FESEM hexagonal nanorods images of (a) undoped ZnO, aluminium doped ZnO (b) 1% Al and (c) 3% Al with EDX spectra

The X-ray diffraction (XRD) peaks of the produced undoped and Al doped ZnO NRs were depicted in fig. 2. The diffraction peaks (002) indicate the presence of a wurtzite-structured hexagonal phase of ZnO. These nanorods are incredibly pure, as no secondary phase was discovered. The intensity of the (002) peak was found to be particularly high in comparison to the other peaks. The other diffraction peaks have been observed such as (004) may imply that

some ZnO nanorods were produced in other directions. The peaks position at 2θ values shows at 34.6° and 72.70° corresponding to the plane [002] and [004]. Based on the diffraction peaks, it was perfectly matched with the standard Joint Committee on Powder Diffraction (JCPDS) card No.35-1451.

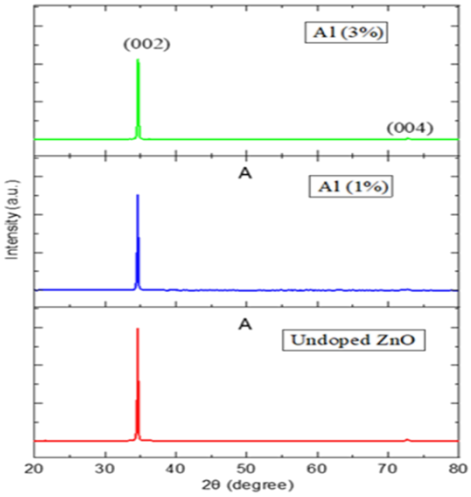

Fig. 2: X-ray diffraction patterns of undoped ZnO, 1% and 3% of aluminium doped ZnO

Fig. 3 shows the pH sensitivities of the undoped ZnO and aluminium doped ZnO nanostructure pH sensor using different pH standard buffer solution (from pH 4 to pH 12). The sensitivity for the undoped ZnO was 26.03 mV/pH with linearity of 0.9576. However, the sensitivity was enhanced for 1% Al at 30.99 mV/pH, linearity 0.9399, while the sensitivity for 3% is 43.80 mV/pH, linearity 0.9507. The results suggest that ZnO doped with 3% Al has greater sensitivity and linearity. Therefore, based on [10] it proves that adding Al to ZnO can have flexible sensor and increase the voltage response and stability of the pH sensor. Furthermore as seen in FESEM images, by adding Al into ZnO, altered the morphology and affected the sensitivity.

Stability were indicates as long-term testing of the undoped ZnO and aluminium doped ZnO pH sensor while the pH value keeps in constant [11]. The pH sensor was immersed in pH 7 buffer solution for 12 hours before measuring the response voltage with a pH sensor potentiometric measurement instrument. Fig. 4 shows the graph between the response voltage and time for different pH values of the buffer solution. The stability for the undoped ZnO were 7.97 mV/h and aluminium doped ZnO at 1%, 3% were 3.43 mV/h and 2.82 mV/h, respectively. pH sensor aluminium doped ZnO at 3% exhibited the highest stability whereas undoped ZnO had the lowest stability. A large number of crystal defects might correlate with the higher drift rate [12].

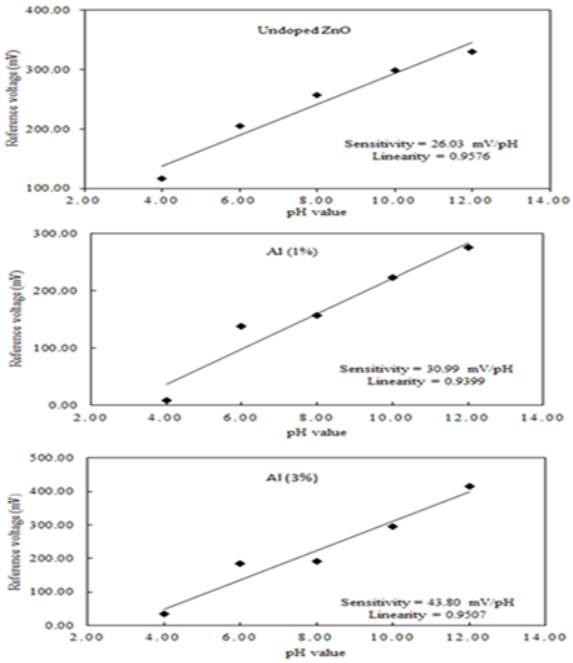

Fig. 3: The response voltage with pH value in the range pH 4 to pH 12 of undoped ZnO, 1% and 3% aluminium doped ZnO

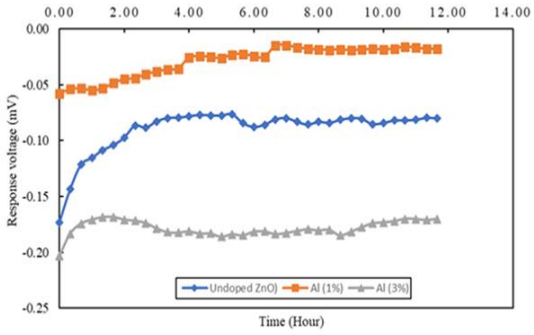

Fig. 4: The stability rate of undoped ZnO and aluminium doped ZnO NS at 1% and 3%

6.0 CONCLUSION

The undoped ZnO and aluminium doped ZnO were synthesized over the FTO substrate by a simple hydrothermal method at 95 ℃. Based on the FESEM and XRD results, reveal the polycrystalline with a hexagonal shape nanorods structure. Moreover, the sensitivity for the aluminium doped ZnO at 3% exhibits the higher sensitivity 43.80 mV/pH and with the linearity 0.95, respectively, thereby as a result, the addition of aluminium to ZnO was able to increase the sensitivity of the sensor. Furthermore, the linearity for the pH sensor is 0.95 which shows our sensors have a good accuracy. Consequently, the fabrication of pH sensing ZnO and aluminium doped ZnO could have a high potential and be advantageous for the usage of disposable biosensors.

ACKNOWLEDGEMENTS

This work was supported by the Universiti Kebangsaan Malaysia (UKM) through grant number GPS_DPK-2023-002 The authors are also thankful to the Centre for Research and Instrumentation Management (CRIM) at UKM for providing the FESEM, and XRD measurements.

REFERENCES

1. T. Illakkiya, S. Hemalatha, P. U. Rajalakshmi, and R. Oommen, "Nanostructured Zno thin films by spin coating technique," Emerg. Mater. Res., vol. 5, no. 1, 2015, pp. 57–61, doi: 10.1680/jemmr.15.00022.
2. J. T. Illakkiya, S. Hemalatha, P. U. Rajalakshmi, and R. Oommen, "Nanostructured Zno thin films by spin coating technique,"*Emerg. Mater. Res.*, vol. 5, no. 1, 2015, pp. 57–61, doi:10.1680/jemmr.15.00022.
3. Belkhaoui, N. Mzabi, H. Smaoui, and P. Daniel, "Enhancing the structural, optical and electrical properties of ZnO nanopowders through (Al + Mn) doping," Results Phys., vol. 12, no. January, 2019, pp.1686–1696, doi: 10.1016/j.rinp.2019.01.085.
4. S. M. Ahmed, "Characterization of Al-doped ZnO nanorods grown by chemical bath deposition method," Innovaciencia Fac. Ciencias Exactas Físicas y Nat., vol. 6, no. 1, 2018, pp. 1–9, Dec. doi: 10.15649/2346075X.463.
5. N. H. Al-Hardan, M. Azmi Abdul Hamid, M. Firdaus-Raih, and L. Kar Keng, "Jurnal Teknologi Aluminium-Modified ZnO Nanoparticles Synthesized Through Co-Precipitation," Alum. - Modif. Zno Nanoparticles Synth. Through Co-Precipitation, vol. 2, 2021, pp. 1–6, [Online]. Available: https://doi.org/10.11113/jurnalteknologi.v84.19323
6. M. B. Agarwal, M. Malaidurai, A. Sharma, and R. Thangavel, "Effect of Al doping on hydrothermal growth and physical properties of doped ZnO nanoarrays for optoelectronic applications," *Mater. Today Proc.*, vol. 21, 2020, pp.1781–1786, doi: 10.1016/j.matpr.2020.01.231.
7. P. Y. Yang et al., "PH sensing characteristics of extended-gate field-effect transistor based on al-doped ZnO nanostructures hydrothermally synthesized at low temperatures," IEEE Electron Device Lett., vol. 32, no. 11, 2011, pp.1603–1605, doi: 10.1109/LED.2011.2164230.
8. 8. P. N. Mishra, P. K. Mishra, and D. Pathak, "The Influence of Al Doping on the Optical Characteristics of ZnO Nanopowders Obtained by the Low-Cost Sol-Gel Method," Chemistry (Easton)., vol. 4, no. 4, 2022pp.1136–1146, doi: 10.3390/chemistry4040077.
9. L. Zan, Q. Wei, and W. Xiaohong, "Controllable hydrothermal synthesis of Al-doped ZnO with different microstructures, growth mechanisms, and gas sensing properties," RSC Adv., vol. 5, no. 69, 2015, pp. 56325–56332, doi: 10.1039/c5ra06233k.
10. A. Alkahlout, N. Al Dahoudi, I. Grobelsek, M. Jilavi, and P. W. de Oliveira, "Synthesis and Characterization of Aluminum Doped Zinc Oxide Nanostructures via Hydrothermal Route," J. Mater., vol. 2014, pp. 1–8, doi: 10.1155/2014/235638.
11. Y. T. Tsai, S. J. Chang, L. W. Ji, Y. J. Hsiao, and I. T. Tang, "Fast Detection and Flexible Microfluidic pH Sensors Based on Al-Doped ZnO Nanosheets with a Novel Morphology," ACS Omega, vol. 4, no. 22, 2019, pp. 19847–19855, doi: 10.1021/acsomega.9b02778.
12. C. Kao et al., "Sensing Membrane Applied in Electrolyte-Insulator-Semiconductor Structures," 2022.

Synthesis and Characterization of Silicon Quantum Dots Using Hydrothermal Method

Hassan **Grema**[1], Siti Haziyah **Mohd Chaculi**[1], Jaafar **Abdullah**[1,2], Nor Azah **Yusof**[1,2]

[1]Department of Chemistry, Faculty of Science, Universiti Putra Malaysia, 43400 UPM Serdang, Selangor, Malaysia.
[2]Institute of Nanoscience and Nanotechnology (ION2), University Putra Malaysia, 43400 Serdang, Selangor, Malaysia.

*Corresponding author's phone: +603-9769 6980
E-mail: jafar@upm.edu.my

ABSTRACT

Recently, research in developing novel nanomaterials which provided a wide range of choices of nanomaterials based on their desired properties is interesting. Silicon quantum dots (SiQDs) have become one of the most popular nanomaterials in biological applications for their excellent biocompatibility and optical properties. In this study, water-soluble silicon quantum dots with fluorescence properties were synthesized using a one-pot hydrothermal process. The synthesis involved reacting 3-aminopropyltriethoxysilane (APTES) as precursor and sodium citrate as reducing agent. The optical features of the SiQDs, including their absorption and emission characteristics were investigated using UV-Vis and fluorescence spectroscopy. It displayed an absorption pattern from 200 to 400 nm with a prominent shoulder around 329 nm and a maximum emission peak at 382 nm with an excitation of 305 nm. The structural characteristics of the synthesized SiQDs was investigated using FTIR indicating surface functionalization and the bonding composition have strong absorbance at 1101 cm^{-1} and 1001 cm^{-1} ascribed to the Si–O bending vibrations that proved successfully prepared of SiQDs. The surface morphology by TEM showed a uniformity, near-spherical shape, and a size range from 11.81 nm to 12.95 nm. The present findings of the synthesized SiQDs have the potential to be applied in the sensing field in the future.

Keywords—Silicon quantum dots; fluorescence; functionalization; APTES; hydrothermal

1.0 INTRODUCTION

Quantum dots are nanoparticles or nanocrystals with sizes ranging from 2 to 12 nm and typically composed of a few hundred to thousands of atoms. Their unique optoelectronic property is characterized by an extremely high surface-to-volume ratio, which is dependent on their size. Silicon, the second most abundant element in the Earth's crust, was first obtained in its pure form by Berzelius in 1823. With advancements in nanotechnology, silicon nanoparticles have found applications in various fields such as biology, chemistry, and medicine. Among them, photoluminescent (fluorescent) silicon nanoparticles are particularly noteworthy for their outstanding optical stability and biodegradability in physiological environments [1].

Over the past few years, there has been a growing fascination with silicon quantum dots (SiQDs), which represent a novel category of photoluminescent nanoparticles in scientific exploration. SiQDs with zero dimensions have garnered significant interest and are being explored as substitutes for semiconductor quantum dots and traditional organic dyes in the realms of sensing and bioimaging. Carbon dots from silane not only have similar

photoluminescence to other fluorescent nanomaterials but also offer added advantages like being non-toxic, stable in light, biocompatible, and widely available [2].

Their appealing attributes, such as excellent water solubility, low toxicity, stable photoluminescence, good biocompatibility, and broad absorption spectrum, have captured the attention of researchers. As a result of these valuable traits, Si quantum dots have found extensive application in fluorescence imaging and detection. The indirect bandgap in silicon's bulk causes poor photoluminescence. Still, the quantum confinement effect in SiQDs allows for effective fluorescence emission with a large quantum yield, which is also crucial [2]. Existing literature reveals that these quantum dots are commonly synthesized using electrochemical [3], hydrothermal [4,5,6], ultraviolet irradiation [7,8] and microwave techniques [9,10] either in their original form or after suitable modifications [11].

In this work, eco-friendly SiQDs was prepared using 3-aminopropyl triethoxysilane (APTES) as the silicon source and sodium citrate as a reducing agent through the hydrothermal process. The technique is more efficient, cost-effective, and environmentally friendly. The obtained SiQDs was characterized to understand the structural, optical and electronic properties. The techniques employed are transmission electron microscopy (TEM) for the investigation of morphology and particle size, Fourier transform infrared spectroscopy (FTIR) to determine the surface functional groups, and UV-Vis and fluorescence spectroscopy for optical properties.

2.0 MATERIALS AND METHODS

2.1. Reagents and solutions

3-Aminopropyltriethoxysilane (APTES, 99%), sodium citrate tribasic dihydrate (≥99.0%) were purchased from Sigma–Aldrich (USA). Deionized water was used for the whole experiment was from Milipore Alpha Q (18.2 MΩ. cm). The SnakeSkinTM dialysis tubing (3500 MWCO, 22 mm x 35 feet dry diameter, 34 mm dry flat width, 37 ml/cm) was used for dialysis solution of SiQDs.

2.2 Characterization

The UV-vis absorption spectra were measured using UV–visible spectro-photometer (Thermo ScientificTM MultiskanTM GO) at room temperature in the wavelength range of 200-800 nm while the fluorescence spectra were acquired by Tecan equipped with Tecan black 96 well plates using SPARKCONTROL Magellan software. An FT-IR spectrometer was employed to determine and analyze the molecular composition of the molecules bound to the surfaces of the nanoparticles Brucker, ATR FTIR Alpha).

2.3 Synthesis of silicon quantum dots (SiQDs)

The process of synthesizing SiQDs involves the following steps. Initially, APTES (6 mL) and 1.104 g sodium citrate were dissolved in deionized water and the mixture was stirred for 10 minutes. Next, this solution was placed into a polytetrafluoroethylene autoclave and heated at 180°C for a duration of 5 hours, resulting in a clear and transparent solution. Lastly, the obtained mixture was subjected to dialysis in ultrapure water for 48 hours to eliminate any remaining impurities.

3.0 RESULTS AND DISCUSSION

The optical properties of the synthesized SiQDs were evaluated by spectro-photometer UV–Vis and fluorescence, respectively. Fig. 1 shows the synthesized colloidal solution of SiQDs was light yellow transparent under natural light but emitted blue fluorescence under the portable UV-lamp (inset Fig. 1). Similar observation with blue fluorescence emitted when exposed to UV-lamp as reported in previous study [12]. UV−Vis spectrum was

recorded to study the optical properties of SiQDs as shown in Fig. 1(a). It shows a continuous absorption pattern from 200 to 400 nm with a prominent shoulder around 329 nm. As can be seen, the SiQDs showed a broad UV absorption band with two absorption peaks at 250 and 350 nm corresponding to the π – π* and n – π* transitions of the SiQDs. When exposed to UV light, SiQDs absorb light at two specific wavelengths (250 nm and 350 nm), which correspond to different types of electronic transitions. The π-π* transitions involve electron lifting from π orbitals to π* orbitals, while n-π* transitions involve electron lifting from non-bonding orbitals to π* orbitals [13]. Another study reported that the typical absorption band with two absorption peaks at 280 and 350 nm was presented in the UV–Vis absorption spectrum [14].

The emissions characteristic of the SiQDs is shown in Fig. 1(b). The maximum emission peak of the prepared SiQDs was at 382 nm can be obtained under excitation at 305 nm as the optimal excitation wavelength for the following experiments [15]. The fluorescence spectra of SiQDs at different excitation wavelengths were also measured.

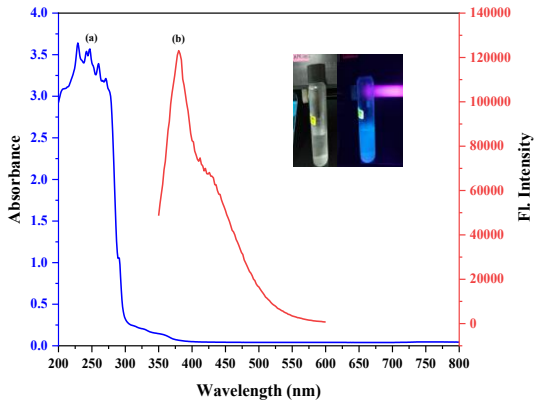

Fig. 1. UV-Vis spectrum of SiQDs (a), fluorescence emission of SiQDs (b)

The analyze the surface groups and bonding makeup of SiQDs, the Fourier Transform Infrared (FTIR) spectrum of SiQDs was investigated. As shown in Fig. 2, the stretching vibrations of O-H are responsible for the absorption peak at 3443 cm^{-1} was observed [16]. The peak in absorption at 1301 cm^{-1} related to C-N vibration, while the peak at 2910 cm^{-1} is attributable to C-H unsaturated stretching vibration [17]. The stretching vibration of C-O was identified as the source of the signal at 1566 cm^{-1} [18]. Most notably, the Si-O bending vibrations that successfully prepared SiQDs were responsible for the high absorbance at 1109 cm^{-1} and 1012 cm^{-1} [12]. These results demonstrated that there were plenty of hydroxyl groups and amino groups on the surface of the SiQDs and these functional hydrophilic groups on the surface greatly implied the excellent water. These findings showed that there were several functional hydrophilic groups, such as hydroxyl and amino groups on the surface of the SiQDs, which strongly suggested that the SiQDs had exceptional water solubility.

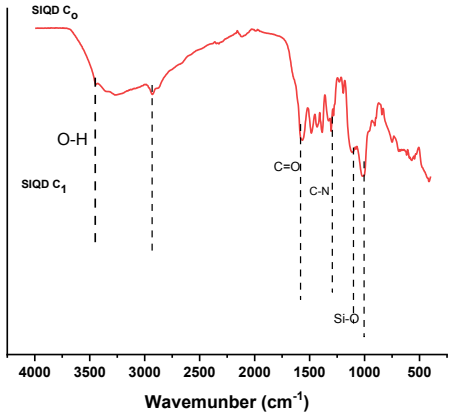

Fig. 2. FTIR spectrum of SiQDs

The morphology and size distribution of the SiQDs were observed by high resolution transmission electron microscopy (HRTEM). As shown in Fig. 3, the SiQDs shows a satisfactory uniformity with good dispersion, near spherical morphology and their size range from 11.81 nm to 12.95 nm. A previous study showed that prepared SiQDs were characterized by having a spherical shape and almost uniform in size [14].

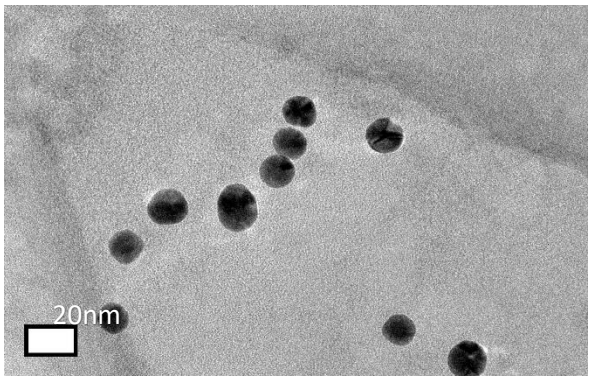

Fig. 3. HRTEM images of SiQDs at 20 nm scale

4.0 CONCLUSION

In brief, this study effectively produced new fluorescent silicon quantum dots achieved through a one-pot hydrothermal process using 3-aminopropyltriethoxy-silane (APTES) as the silicon source. The produced SiQDs exhibited fluorescence characteristics, which made them potentially relevant for a number of applications in optoelectronics and bioimaging. They were great prospects for biological applications and environmental sensing because to the SiQDs high stability and water solubility. The study of the production and characterization of silicon quantum dots shows their useful features and potential applications, adding important information to the field of nanomaterials and nanotechnology.

REFERENCES

[1] Y. Zhang, N. Cai, & V. Chan. (2023). Recent Advances in Silicon Quantum Dot-Based Fluorescent Biosensors, *Biosensors* 13, no. 3, 311.

[2] T.H. Le, D.T.T. Le, & T. N. Van. (2021). Synthesis of Colloidal Silicon Quantum Dot from Rice Husk Ash. *Journal of Chemistry*, *2021*, 1–9.

[3] S. Morozova, M. Alikina, A. Vinogradov & M. Pagliaro. (2020). Silicon Quantum Dots: Synthesis, Encapsulation, and Application in Light-Emitting Diodes, *Front. Chem.* 8, 1–8, 2020.

[4] C. Chen, Y. Zhang, Z. Zhang, R. He & Y. Chen. (2018). Fluorescent Determination of Glucose Using Silicon Nanodots, *Anal. Lett.* 51(18), 2895–2905.

[5] Y. Zhou, M. Qi & M. Yang. (2022). Fluorescence determination of lactate dehydrogenase activity based on silicon quantum dots, Spectrochimica Acta A 268, 120697.

[6] S. Terada, Y. Xin, & K. Saitow. (2020). Cost-Effective Synthesis of Silicon Quantum Dots. *Chemistry of Materials*, *32*(19), 8382–8392.

[7] Y. Li, W. Li, H. Zhang, Y. Liu, L. Ma & B. Lei. (2020). Amplified light harvesting for enhancing Italian lettuce photosynthesis using water soluble silicon quantum dots as artificial antennas, *Nanoscale* 12(1), 155–166.

[8] J. Wu, J. Dai, Y. Shao & Y. Sun. (2015). One-step synthesis of fluorescent silicon quantum dots (Si-QDs) and their application for cell imaging, *RSC Adv.* 5(102), 83581–83587.

[9] W. Li, D. Liu, D. Dong & T. You. (2020). Microwave-assisted synthesis of fluorescent silicon quantum dots for ratiometric sensing of Hg (II) based on the regulation of energy transfer, *Talanta* 226, 122093.

[10] J.L. Wilbrink, C.C. Huang, K. Dohnalova & J.M.J. Paulusse. (2020). Critical assessment of wet-chemical oxidation synthesis of silicon quantum dots. *Faraday Discussions*, *222*, 149–165.

[11] Y. Wang, H. Wang, J. Guo, J. Wu, L.J. Gao, Y.H. Sun, J. Zhao & G.F. Zou. (2015). Water-Soluble Silicon Quantum Dots with Quasi-Blue Emission. *Nanoscale Research Letters*, *10*(1), 300.

[12] Y. Liu, L. Cao, M. Zan, J. Peng, P. Wang, X. Pang, Y. Zhang, L. Li, W.F. Dong & Q. Mei. (2021). Cyan-emitting silicon quantum dots as a fluorescent probe directly used for highly sensitive and selective detection of chlorogenic acid. *Talanta* 233.122465

[13] Z. Zhang, C. Wei, W. Ma, J. Li, X. Xiao & D. Zhao. (2019). One-step hydrothermal synthesis of yellow and green emitting silicon quantum dots with synergistic effect. *Nanomaterials*, *9*(3) 9030466.

[14] H.E. Şatana Kara, B. DemiRhan & B. Er DemiRhan. (2020). Highly luminescent water-dispersed silicon quantum dots for fluorometric determination of oxytetracycline in milk samples. *Turkish Journal of Chemistry*, *44*(6), 1713–1722.

[15] Y. Liu, M. Zan, L. Cao, J. Peng, P. Wang, X. Pang, Y. Zhang, L. Li, Q. Mei & W.F. Dong. (2022). F-doped silicon quantum dots as a novel fluorescence nanosensor for quantitative detection of new coccine and application in food samples. *Microchemical Journal* 179*,* 107453.

[16] C. Pan, X. Qin, M. Lu & Q. Ma. (2022). Water Soluble Silicon Nanoparticles as a Fluorescent Probe for Highly Sensitive Detection of Rutin, *ACS Omega*, 7(32), 28588–28596.

[17] X. Miao, X. Yan, D. Qu, D. Li, F. F. Tao & Z. Sun. (2017). Red Emissive Sulfur, Nitrogen

Codoped Carbon Dots and Their Application in Ion Detection and Theraonostics," *ACS Appl. Mater. Interfaces*, 9(2), 18549–18556.

[18] Y. Liu, L. Wei, W. Peng, M. Chunhui, W. Xueyun, X. Mingcong, L. Sha, X. Zhuo & L. Shouxin. (2019). Hydrothermal synthesis of nitrogen and boron co-doped carbon quantum dots for application in acetone and dopamine sensors and multicolor cellular imaging," *Sensors Actuators, B*, 281, 34–43.

Enhancing the Luminescence of Carbon Quantum Dots from Biochar by Tuning the Functional Group Via Hydrothermal Synthesis

Nur Afif Nadhrah **Kamaruzaman**[1], Nurafifah Dilla **Diwi**[2], Jaafar **Abdullah**[3], Suraya **Abdul Rashid** [2*]

[1]Institute of Nanoscience and Nanotechnology (ION2), Universiti Putra Malaysia, Serdang 43400 UPM, Selangor, Malaysia; afifnadhrah@gmail.com
[2] Department of Chemical & Environmental Engineering, Faculty of Engineering, Universiti Putra Malaysia, Serdang 43400, Selangor, Malaysia; suraya_ar@upm.edu.my; nurafifahdilladiwi@gmail.com
[3] Faculty of Science, Universiti Putra Malaysia, Serdang 43400, Selangor, Malaysia; jafar@upm.edu.my

*Corresponding author's phone: +603-9769 6285
E-mail: suraya_ar@upm.edu.my

ABSTRACT

Empty fruit bunch (EFB) is a promising carbon source for preparing carbon quantum dots (CQD). CQD is widely used in the application of solar cells and agriculture as CQD exhibits fascinating properties such as biocompatibility, photostability, and easily tunable optical properties. In this study, a facile hydrothermal method was utilized to synthesize red-shifted CQD (R-CQD) and red-shifted nitrogen-doped CQD (R-NCQD) from biochar and sulfuric acid (H_2SO_4) as a solvent. Heteroatom-doped modification using urea as the nitrogen source is an efficient approach to enhance the electron transfer and thus notable redshift of the optimal excitation wavelength and the strongest emission peak. R-CQD and R-NCQD were characterized by Perkin Elmer LS55 PL spectroscopy and FTIR spectrum 100. The reactions were carried out at 200 °C for 10 hours in Teflon-lined stainless steel autoclave reactor. Under 450 nm excitation, R-CQD and R-NCQD showed maximum fluorescence emission at 518 nm and 575 nm. This research demonstrates the sustainable agrowaste utilization through a better understanding of hydrothermal synthesis processes.

Keywords — carbon quantum dot (CQD), empty fruit bunch, hydrothermal, nitrogen-doped, red-shifted CQD

1.0 INTRODUCTION

Carbon is one of the most abundant and environmentally friendly elements on earth. Carbon quantum dots (CQD) are a new class of carbon nanomaterials that have emerged recently due to their unique physical, chemical, optical and surface properties [1]. CQD are smaller in size (<10 nm), relatively strong fluorescence, fast and facile synthesis, and easily tunable optical properties [2]. These properties have allowed the use of CQD in various applications such as photocatalysis, solar cells, drug delivery, and agriculture [3].

Nowadays, the synthesis of CQD from natural sources has gained prominence due to the abundance of carbon precursors and the product's low toxicity for biological applications. Most attempts for green synthesis of CQD used hydrothermal method (simple, most cost-effective, and environmentally friendly) [9] or microwave-assisted method due to ease of fabrication and faster synthesis procedures [5].

Empty fruit bunches (EFB) from palm oil were used as the natural source of carbon to extract CQD. Biomass has attracted much interest in usage of CQD preparation because of its renewable, inexpensive, and readily doped benefits [6]. Nevertheless, the primary issue with biomass-based CQD is that their fluorescence features would severely limit their applications. Moreover, numerous strategies have been devised to raise the fluorescence of biomass-based CQD and nitrogen-doped modification shown to be a successful method for improving the fluorescence characteristics of CQD.

By doping the carbon dots with other elements, new functional groups could be introduced leading to the formation of surface defects which generate a new energy level, reducing the bandgap, and providing the ability to adjust the fluorescence properties of CQD. Consequently, reducing the energy gap and causing the wavelength emission to be longer [7].

In this work, we report the different methodological approach to synthesize R-CQD and the determination of chemical properties of R-CQD produced via selected method. EFB Biochar was used as a precursor carbon source to synthesize CQD, R-CQD and R-NCQD using a hydrothermal and microwave-assisted method. Additionally, 7.3 M of sulfuric acid as a solvent use for preparing R-CQD and R-NCQD. Urea was used as nitrogen sources for preparing R-NQCD in this study.

2.0 MATERIALS & EXPERIMENTAL

2.1 Chemicals

Empty fruit bunch (EFB) biochar from Pakar Go Green Sdn. Bhd. Urea, isoprophyl alcohol (IPA) (Chemiz) and 98% sulfuric acid (H_2SO_4) from R&M Chemicals. Distilled water was used throughout this study and all chemicals were used as received without further purification.

2.2 Synthesis of Carbon Quantum Dots (CQD)

2.2.1 Microwave-assisted

1g of biochar was taken and dissolved in a solvent mixture of IPA and distilled water; a mole fraction of 0.1 in 100 mL of total mixture. The biochar mixture was then microwaved for 5 minutes. The solution was cooled down to room temperature after the reaction. Then, the solution was centrifuged for 15 minutes at 5000 rpm to separate the precipitate from the liquid. Supernatant was collected and the residue was filtered using filter paper 601 (Filtres Fioroni, 125mm diameter) to remove any larger particles and impurities. The steps were repeated to synthesize nitrogen-doped CQD (N-CQD). 0.6 g of urea, was added during the first step.

The prepared CQD and N-CQD was then further modified by adding 4 mL of 50 mg/mL H_2SO_4 to 2 mL of the samples.

4.2.2 Hydrothermal

The sulfuric acid was diluted to 7.3 M prior to the experiment. Firstly, 0.11 g of the biochar was taken and dissolved in 25 mL of 7.3 M sulfuric acid. The solution was transferred into Teflon-lined stainless steel reaction chamber. The mixture was reacted at 200 °C for 10 hours. Then, the solution was cooled down to room temperature after the reaction. Then, the solution was filtered and

the supernatant was collected as R-CQD. The same procedure was repeated for R-NCQD with an additional step of adding 0.16 g urea to the reaction mixture.

4.3 Characterization

2.3.1 Optical properties using Photoluminescence (PL) Spectroscopy

The PL analysis was conducted using Perkin Elmer LS55 Photoluminescence Spectroscopy. Perkin Elmer LS55 is equipped with monochromators on both the excitation and emission sides capable of 200nm to 800nm excitation and 200nm to 900nm emission scans.

4.3.2 Structural study using FTIR

Fourier Transform Infrared spectroscopy was recorded to identify the functional groups or surface state present on the obtained R-CQD. The FTIR spectrum 100 was used in this research to characterize R-CQD.

3.0 RESULTS AND DISCUSSION

3.1 Optical properties

The synthesized untreated CQD emits blue-green luminescence under excitation with UV light similar to the observation reported by Jamaludin *et al* [3] in 2020. The color emitted by CQD when doped with nitrogen (N-CQD) using urea as a precursor showed no sign of having a much more intense luminescence emission than the CQD. This claim is further supported with the PL analysis depicted in Figure 1 (a). As observed, the maximum peak emission for both samples were identified at 378 nm consistent with the wavelength of carbon quantum dots in a study by Thambiraj *et al* [1] that synthesised CQD from organic precursor as well. The emission spectrum of these samples was determined to be excitation-dependent as the emission peaks lengthened towards the right as the excitation increased from 250 nm to 450 nm as illustrated in Figure 1 (b), and (c). Zhu *et al* [8] described that this behavior is found to be common in carbon-based fluorescent dots caused by the complex chemical groups on the surface of CQD, which affect the band structure of CQD. Each peak that can be seen in the emission spectra indicates the presence of new electron transitions due to the functional groups present on the surface creating a series of emissive traps [9].

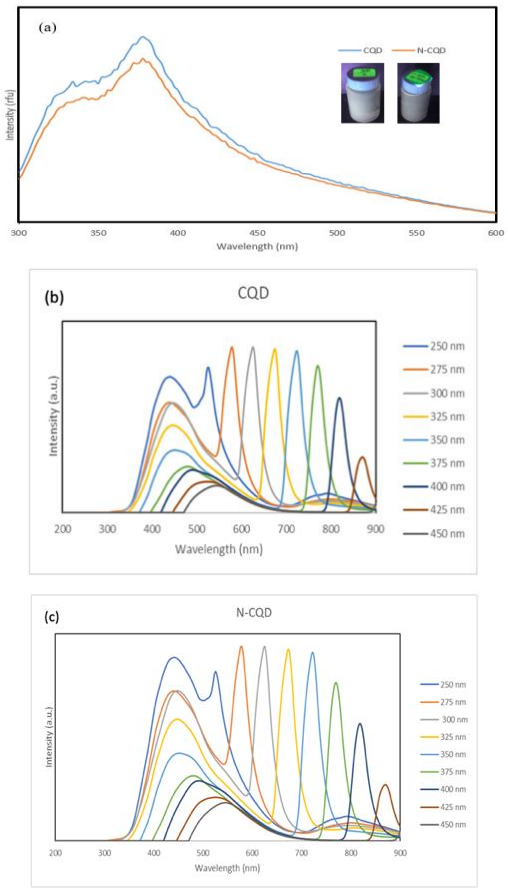

Fig. 1: (a) PL analysis of CQD and N-CQD excited at 255 nm, (b) PL analysis of CQD at different excitation wavelength and (c) PL analysis of N-CQD at different excitation wavelength.

As CQD doping with nitrogen did not shows any changes in emission, further modification by treating CQD and N-CQD with sulfuric acid, H_2SO_4 has been done. The emission spectrum was blue-shifted with a maximum peak located at 328 nm and 330 nm for H_2SO_4-CQD and H_2SO_4-NCQD depicted in Figure 2. This phenomenon occurs due to the addition of solvents in the CQD lead to the decreasing the concentration of carbon dots [10].

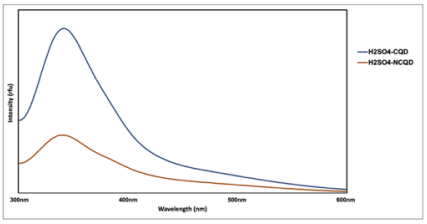

Fig. 2: PL spectra of H_2SO_4-CQD, and H_2SO_4-NCQD under 255 nm excitation.

This prove acid was successful in synthesizing red-shifted emission CQD. Thus, another method was carried out using the same materials but with different equipment known as the hydrothermal approach. This approach was able to overcome the issue of concentration reduction as the acid mixed with the starting materials and reacted in an autoclave reactor. The collected samples when irradiated with UV light appeared to emit blue to yellow luminescence for R-CQD and blue to orange luminescence for R-NCQD as depicted in Figure 3 (a) and (b), depending on the angles observed which is an indication of the emission being red-shifted.

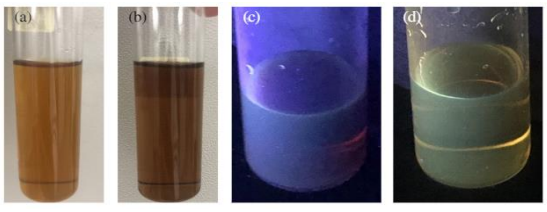

Fig. 3: (a) R-CQD under normal light, (b) R-NCQD under normal light, (c) R-CQD under UV light and (d) R-NCQD under UV light.

Under excitation at 255 nm as shown in Figure 4 (a), R-NCQD exhibits a broad range of red-shifted emission spectrum with the strongest peak located at 488 nm. Meanwhile, R-CQD also emits a similar spectrum but with lower intensity. The multiple peaks are due to the existence of new transition states on the surface of carbon dots. A detailed PL analysis was performed using excitation ranging from 200 nm to 900 nm for both samples as illustrated in Figures 4 (b), and (c). The maximum emission for R-CQD and R-NCQD shows at the excitation wavelength of 450 nm with maximum peak are 518 nm and 575 nm. The emission spectrum of R-CQD and R-NCQD are independent of the excitation spectrum as there is no significant peak change as the excitation increases. This behavior is strongly influenced by the surface states as claimed by several authors including [11].

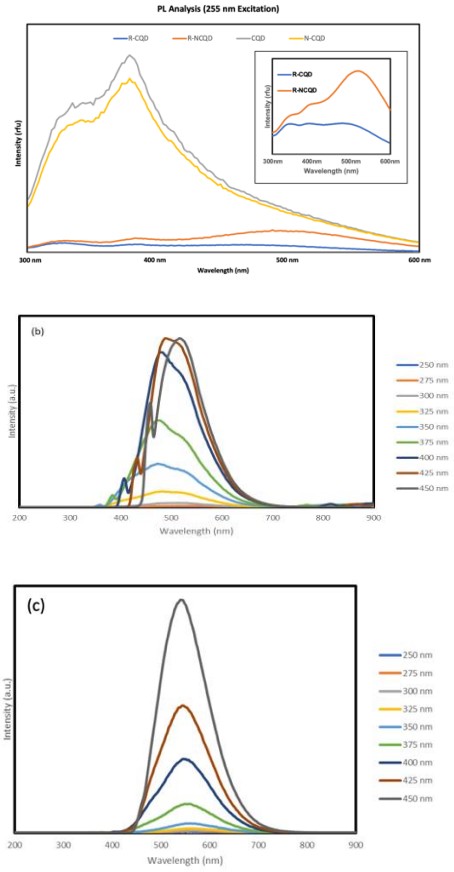

Fig. 4: (a) PL analysis of R-CQD and R-NCQD excited at 255 nm, (b) PL analysis of R-CQD at

different excitation wavelength, (c) PL analysis of R-NCQD at different excitation wavelength.

3.2 Spectroscopy study of CQD with red-shifted emission

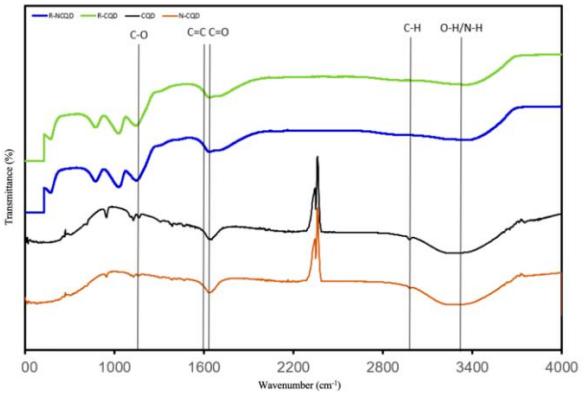

Fig. 5: FTIR spectra of CQD, N-CQD, R-CQD and R-NCQD.

The functional groups of the CQD, N-CQD, R-CQD and R-NCQD were investigated using FTIR spectroscopy. All of the samples contain carbonyl, hydroxyl, and carboxyl groups as shown in Figure 5.

Figure 5 illustrated a strong broad band stretching vibration at 3282 cm^{-1} of O-H group as referred to the CQD spectra by Jamaludin et al., 2020. In the same spectra, C-H peak at 2977 cm^{-1}, C=O peak 1631 cm^{-1}, and C=C peak at 1417 cm^{-1} were observed. The oxygen-rich groups present on the surface of the CQD and N-CQD explain the reason behind its good water-solubility properties. Comparing the spectra between the red-shifted and pure carbon dots, the O-H group appears to have a much broader peak at 3400 cm^{-1}, and 3409 cm^{-1} for R-CQD, and R-NCQD respectively. These peaks aligned with the finding from Ding et al., 2017 that showed the presence of O-H/N-H groups at 3444 cm^{-1}. The peak at 1590 cm^{-1} were attributed to the stretching vibrations of the C=C group and the peak displayed at 1145 cm^{-1} were due to the presence of the C-O group's stretching vibrations as well. Other peaks such as C=O at 1634 cm^{-1} were also observed. The intensity of C=C increases while C=O decreases compared to FTIR spectra of CQD and N-CQD indicating that the nitrogen content of the nitrogen-doped polyaromatic structures increases progressively during the dehydration process [12].

4.0 CONCLUSION

A method to synthesize R-CQD and R-NCQD using EFB biochar as the starting precursor and sulfuric acid (H_2SO_4) as solvent was established in this research. The R-CQD and R-NCQD prepared through the hydrothermal method showcased a blue to orange luminescence light upon irradiation with ultraviolet. Under normal daylight, R-CQD appears to be yellow while R-NCQD appears to be orange. The PL analysis conducted determined that both samples are independent of excitation wavelength. The strongest emission peak was identified to be at 518 nm for R-CQD and 575 nm for R-NCQD at excitation wavelength of 450 nm. The functional groups identified through FTIR was O-H/N-H groups at 3444 cm^{-1}, C=O at 1634 cm^{-1}, C-O at 1145 cm^{-1}, and C=C at 1590 cm^{-1}. The samples' hydrophilic properties are attributed to the broad stretching band of O-H/N-H groups of the FTIR spectra. The enhancement in red-shifted emission wavelength is due to the high intensity of C=C group.

ACKNOWLEDGEMENTS

The authors are thankful to Institute Nanoscience and Nanotechnology for providing the facilities to carry out this research work.

REFERENCES

[1] T. S. and R. S. D., "Green synthesis of highly fluorescent carbon quantum dots from sugarcane bagasse pulp," *Appl Surf Sci*, vol. 390, pp. 435–443, Dec 2016.

[2] P. Kumar, S. Dua, R. Kaur, M. Kumar, and G. Bhatt, “A review on advancements in carbon quantum dots and their application in photovoltaics,” *RSC Advances*, vol. 12, no. 8. Royal Society of Chemistry, pp. 4714–4759, Feb 2022

[3] N. Jamaludin, T. L. Tan, A. S. K. Zaman, A. R. Sadrolhosseini, and S. A. Rashid, “Acid-free hydrothermal-extraction and molecular structure of carbon quantum dots derived from empty fruit bunch biochar,” *Materials*, vol. 13, no. 15, Aug 2020.

[4] D. Qu *et al.*, “Highly luminescent S, N co-doped graphene quantum dots with broad visible absorption bands for visible light photocatalysts,” *Nanoscale*, vol. 5, no. 24, pp. 12272–12277, 2013.

[5] A. Tyagi, K. M. Tripathi, N. Singh, S. Choudhary, and R. K. Gupta, “Green synthesis of carbon quantum dots from lemon peel waste: Applications in sensing and photocatalysis,” *RSC Adv*, vol. 6, no. 76, pp. 72423–72432, 2016.

[6] C. Kang, Y. Huang, H. Yang, X. F. Yan, and Z. P. Chen, “A review of carbon dots produced from biomass wastes,” *Nanomaterials*, vol. 10, no. 11. MDPI AG, pp. 1–24, Nov. 01, 2020.

[7] Y. Liu, H. Gou, X. Huang, G. Zhang, K. Xi, and X. Jia, “Rational synthesis of highly efficient ultra-narrow red-emitting carbon quantum dots for NIR-II two-photon bioimaging,” *Nanoscale*, vol. 12, no. 3, pp. 1589–1601, Jan 2020.

[8] S. Zhu *et al.*, “Highly Photoluminescent Carbon Dots for Multicolor Patterning, Sensors, and Bioimaging,” *Angewandte Chemie*, vol. 125, no. 14, pp. 4045–4049, Apr 2013.

[9] S. Abdul Rashid, S. A. Mohd Zobir, S. Krishnan, M. M. Hassan, and H. N. Lim, “One-pot synthesis of graphene oxide sheets and graphene oxide quantum dots from graphite nanofibers,” *Journal of Nanoparticle Research*, vol. 17, no. 5, May 2015.

[10] S. Lin *et al.*, “Solvatochromism of bright carbon dots with tunable long-wavelength emission from green to red and their application as solid-state materials for warm WLEDs,” *RSC Adv*, vol. 7, no. 66, pp. 41552–41560, 2017.

[11] Y. Dong *et al.*, “Carbon-Based Dots Co-doped with Nitrogen and Sulfur for High Quantum Yield and Excitation-Independent Emission,” *Angewandte Chemie*, vol. 125, no. 30, pp. 7954–7958, Jul 2013.

[12] H. Ding, Y. Ji, J. S. Wei, Q. Y. Gao, Z. Y. Zhou, and H. M. Xiong, “Facile synthesis of red-emitting carbon dots from pulp-free lemon juice for bioimaging,” *J Mater Chem B*, vol. 5, no. 26, pp. 5272–5277, 2017.

Study of Optical Properties of the Agriculture Waste Based Carbon Quantum Dot (CQDs)

Mhammed Ali Khalifa Mhammed **Ali Alnigomi** [1], H. **Jaafar**,[1,2] S.**Shafie** [1,2], M.A. **Mustafa** [1] and M. A. **Kamarudin**[3]

[1]Department of Electrical and Electronic Engineering, Faculty of Engineering, Universiti Putra Malaysia, Serdang, Malaysia
[2]Institute of Nanoscience and Nanotechnology (ION2), Universiti Putra Malaysia, Serdang, Malaysia
[3]Department of Physics, Faculty of Science, Universiti Putra Malaysia, Serdang, Malaysia

*Corresponding author's phone:+60123005786
Email : jhaslina@upm.edu.my

ABSTRACT

In this study, Carbon Quantum Dots (CQDs) were successfully synthesized using watermelon peels as a carbon source. We investigated the optical properties of these CQDs through Photoluminescence (PL) and Zeta potentials, employing a carbonization technique with watermelon peels. The study used three distinct solvents: water (DI), Methanol (MtOH), and Ethanol (EtOH) for the carbonization process. The results of the study revealed that the density of CQDs increased with higher concentrations, leading to enhanced light dispersion. Specifically, concentrations of 6.9 mg/ml in both Ethanol and Methanol exhibited lower PL emission rates compared to Di water, but the concentration of 3 mg/ml showed emissions in a range between Ethanol and Methanol. The study also found that a concentration of 6 mg/ml resulted in the highest stability for CQDs in both Di water and Methanol. Additionally, a concentration of 3.9 mg/ml displayed the highest stability for CQDs in Ethanol. In summary, this research demonstrated that using watermelon peels as a carbon powder source for CQD synthesis in various solvents can yield interesting optical properties, with CQD density increasing with higher concentrations and leading to improved light dispersion. Different solvents showed variations in PL emission rates and stability of the CQDs, depending on the concentration used.

Keywords— CQDs, photoluminescence, zeta potential, dispersion, synthesis.

1.0 INTRODUCTION

CQDs have piqued the interest of many global researchers in recent years due to their unique properties such as small size (ideal for some bio-applications), biocompatibility, PL properties, high-temperature stability, chemically inert structure, and easy routes of functionalization [1]. The discovery of CQDs should be traced back to the 2004 publication [2] that fluorescent nanoparticles were generated from single-wall carbon nanotubes, and then in [3] synthesized the CQDs with surface passivation, which resulted in improved fluorescence emission.

Bottom-up and top-down methodologies can be used to synthesis CQDs. Top-down synthesis methods for CQD production

include mechanical milling [4], laser ablation [5], electrochemical oxidation [6] [7], chemical oxidation [8], and ultrasonic-assisted methods [9]. Bottom-up approaches include plasma treatment [10], hydrothermal synthesis [11][12], pyrolysis [13], and microwave-assisted carbonization [14].Nevertheless, these procedures typically entail complicated or post-treatment operations or need expensive raw materials and harsh synthetic conditions, which are unlikely to be expanded much soon. Most suggested uses have been hampered by the absence of an effective method for manufacturing processable fluorescent C-dots in large quantities. CQDs' size and particle surface chemical group must be precisely modified in order to make them fluorescent. Several attempts to surface-modify QD have been made to improve their luminescence performance and colloidal stability. The method of passivation employing organic ligands with anionic and cationic surface sites is intricate. As a result, dangling bonds are difficult to remove. Both cationic and anionic sites have been passivated using various organic and inorganic surface modification approaches. In this study, we demonstrate the synthesis of CQD from watermelon peels, with a focus on the effect of different solvents at varying concentrations. Carbon quantum dots were synthesized in this study utilizing watermelon peels as a corban powder source, and their optical properties were studied using Photoluminescence (PL) and Zeta potential.

2.0 METHODOLOGY

CQDs were created via a carbonization technique from watermelon peels. Watermelon peels were cleaned first before being sliced into smaller pieces. The diced peels were then dried in the sun for three days in order to eliminate moisture. The dried watermelon peels were carbonized in a furnace at 220 degrees Celsius for two hours. The carbonized peels were then ground and sieved to get smaller particles of carbon powder. The sieved were weighed appropriately, 3 mg, 6 mg, and 9 mg, and then employed in three distinct bass materials (solvents): water (Di), Methanol (MtOH), and Ethanol (EtOH). As followed (0.015)g of carbon powder in 5 ml of water .(0.03)g of carbon powder in 5 ml of water .(0.045)g of carbon powder in 5 ml of water .(0.015)g of carbon powder in 5 ml of Ethanol (0.03)g of carbon powder in 5 ml of Ethanol (0.045)g of carbon powder in 5 ml of Ethanol (0.015)g of carbon powder in 5 ml of Methanol (0.03)g of carbon powder in 5 ml of Methanol (0.045)g of carbon powder in 5 ml of Methanol.then theses solution were strir and then sonicated and lastly filter (0.45 µm). Figure 1 demonstrates the preparatory procedure for CQDs.

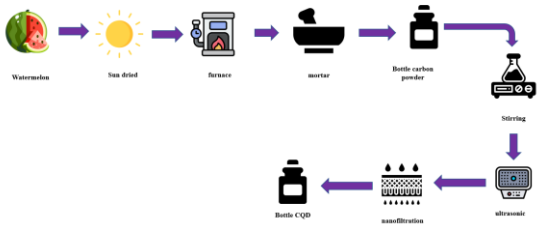

Fig 1 : step by step the process of preparing of carbon quantum dot from watermelon peels Watermelon peels were cleaned and cut then dried in the sun carbonized in a furnace at 220 degrees then sieved then sonicated filter (0.45 µm)

3.0 RESULTS AND DISCUSSION

The results demonstrate the photoluminescent (PL) properties and Zeta potentials. These properties arise from the carbon quantum confinement effect, surface state emissions, and other influencing factors. By altering the concentration of CQDs, the photoluminescence spectra reveal significant trends in the optical properties, including shifts in emission peak position, changes in intensity, and the full width half maximum (FWHM). This analysis also offers valuable

insights into how the photoluminescent behavior of CQDs changes with varying concentrations. Additionally, the comparison of PL spectral analysis of CQDs at different concentrations is shown in Fig 3 and Fig 4 respectively, non-destructive and sensitive approach to study their optical properties.

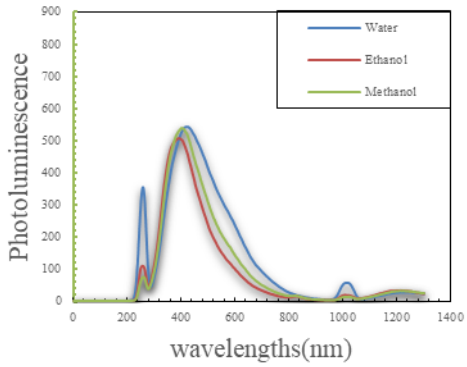

Fig 2 : PL spectra of CQDs DI water, CQDs Ethanol, CQDs Methanol Concentration 3 mg/ml with Excitation range of 375 nm

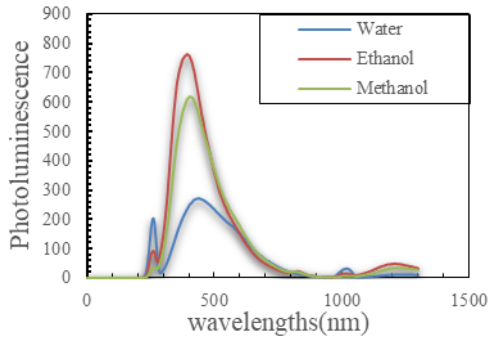

Fig 3 : PL spectra of CQDs DI water, CQDs Ethanol, CQDs Methanol Concentration 6 mg/ml with Excitation range of 375 nm

Fig 2 represents the PL spectra of CQDs/DI water/Ethanol/Methanol concentration 3 mg/ml, whereas Figure 3 illustrates the PL spectra of CQDs/DI water/Ethanol /Methanol concentration 6 mg/ml, and Figure 4 represents the PL spectra of CQDs/DI water/Ethanol /Methanol concentration 9 mg/ml. CQD PL spectra showed distinct emission peaks in the visible range, with the emission wavelength dependent on the base material and CQD concentration. An insignificant redshift in the emission peak location was observed as CQD concentration increased, indicating a reduction in the bandgap of CQDs as well as the contribution that comes from CQD size. This can be observed in the normalization graph of PL spectra in Fig 2, 3, and 4 as the energy shifts from greatest to lowest concentration. The redshift can be explained by the quantum confinement effect, which states that increasing the concentration of CQDs increases the probabilities of exciton confinement, resulting in a reduction in the bandgap and a redshift in the emission wavelength.

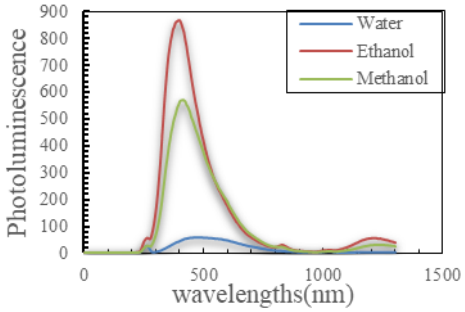

Fig 4 : PL spectra of CQDs DI water, CQDs Ethanol, CQDs Methanol Concentration 9 mg/ml with Excitation range of 375 nm

The FWHM analysis reveals CQD homogeneity and size dispersion. A smaller FWHM may indicate high purity and homogeneity if the size distribution is tighter. When compared to other samples, the concentration of 9 mg/ml has the smallest FWHM linewidth spectrum, as shown in Figure 4. This demonstrates that the CQDs' size and surface characteristics are more homogenous, which leads to more consistent emission behavior.

Additionally, the intensity of the PL spectra fluctuated with concentration. The PL intensity reduced at lower doses, increased at middle values and eventually reached saturation at higher concentrations

(6-9 mg/ml). When comparing the three base materials, as shown in Figures 2,3, and 4, Di water has the shortest PL emissions rate with concentration (6-9 mg/ml) in Ethanol and Methanol, whereas concentration 3 mg/ml is slightly higher than Ethanol and in the range of Methanol. Figs 5, 6, and 7 depict the zeta potential of CQDs in Di water, Ethanol, and Methanol at various carbon concentrations (3-6-9mg/ml).

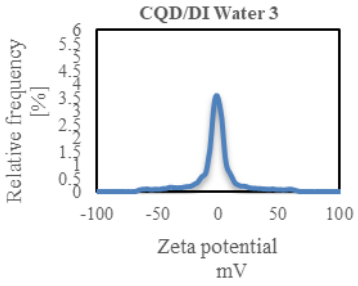

(a)

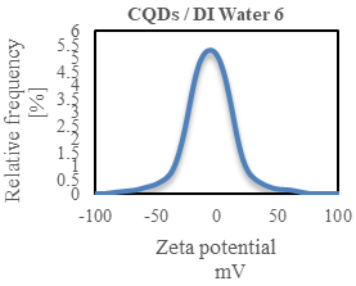

(b)

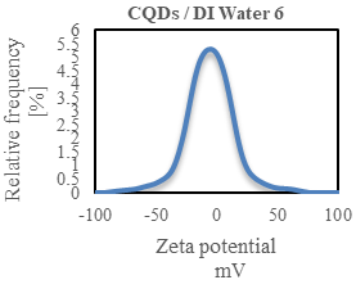

(c)

Fig 5 : Zeta potential of the Di water with concentration of(a) 3 mg/ml (b) 6 mg/ml (c) 9 mg/ml

Understanding the surface charge on CQDs is critical because it reveals the intensity of electrostatic attraction between like-charged particles in a dispersed system. The zeta potential of CQDs in three distinct solvents, Di water, Ethanol, and Methanol, was determined to be in the range of -25 mV to -67 mV, demonstrating the presence of negatively charged surface groups. The zeta potential

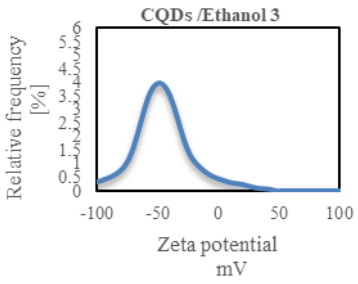

(a)

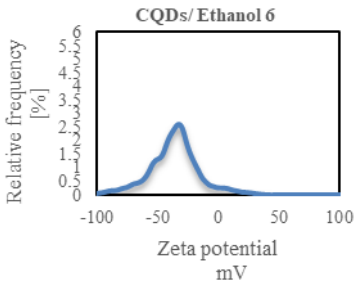

(b)

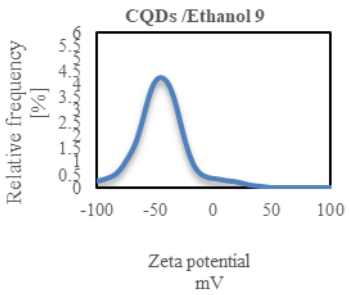

(c)

Fig 6 : Zeta potential of the Ethanol with concentration of (a)3 mg/ml (b) 6 mg/ml (c) 9 mg/ml

of CQDs collapses at high concentrations (6-9 mg/ml) and tends to aggregate in both solvents as the zeta potential values decrease below -30 mV.

The degree of amplitude and sign of a colloidal particle's zeta potential influences its stability. Colloidal particles experiencing a zeta potential higher than 30 mV are typically regarded as stable because repulsive relationships among the particles are strong enough that they prevent aggregation and precipitation. Particles having a zeta potential less than 30 mV, on the other hand, are considered unstable because attractive forces between the particles may overcome repulsive forces, resulting in particle aggregation and instability.

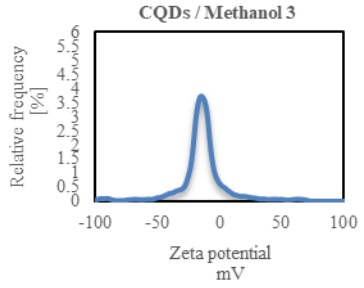

(a)

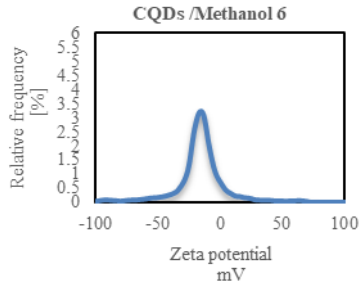

(b)

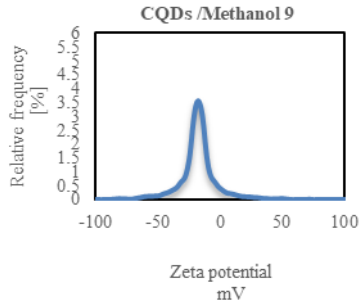

(c)

Fig 7 : Zeta potential of the Methanol with concentration of (a) 3 mg/ml (b) 6 mg/ml (c) 9 mg/ml

A higher zeta potential can lead to greater stability of CQD suspensions and reduced aggregation of CQDs. This is due to the stronger repulsive forces between CQDs that are present at higher zeta potentials in low concentrations (3-6-9) mg/ml Especially in this research, it had been found that the concentration of 6 mg/ml shows the highest degree of stability for both CQDs in the Di water and methanol as it has been illustrated in fig 7 and 5, and the concentration (3-9 mg/ml) for CQDs in Ethanol as presented in Fig 6.

4.0 CONCLUSION

In conclusion, CQD density increases with concentration, allowing for more dispersion of incoming light. When the three base materials are compared. Di water has the lowest PL emissions rate with concentrations (6-9 mg/ml) in Ethanol and Methanol, but concentration (3) mg/ml is somewhat higher than Ethanol and in the range of Methanol. The radiative decay processes take over at greater concentrations, resulting in a higher PL intensity. Furthermore, increased light scattering effects can result in greater PL intensity at larger concentrations. It was also discovered that the concentration of 6 mg/ml displays the maximum degree of stability for both CQDs in Di water and methanol and the concentration (3-9) mg/ml for CQDs in Ethanol.

ACKNOWLEDGEMENTS

This work funded by Putra-IPS Grant/2022/9735300 and Department of Physics, Faculty of Science, Universiti Putra Malaysia

REFERENCES

[1] M. J. Molaei, "A review on nanostructured carbon quantum dots and their applications in biotechnology, sensors, and chemiluminescence," *Talanta*, vol. 196, no. August 2018, pp. 456–478, 2019, doi: 10.1016/j.talanta.2018.12.042.

[2] X. Xu *et al.*, "Electrophoretic Analysis and Purification of Fluorescent Single-Walled Carbon Nanotube Fragments," *J. Am. Chem. Soc.*, vol. 126, no. 40, pp. 12736–12737, Oct. 2004, doi: 10.1021/ja040082h.

[3] Y.-P. Sun *et al.*, "Quantum-Sized Carbon Dots for Bright and Colorful Photoluminescence," *J. Am. Chem. Soc.*, vol. 128, no. 24, pp. 7756–7757, Jun. 2006, doi: 10.1021/ja062677d.

[4] W. Wu *et al.*, "Cu-N dopants boost electron transfer and photooxidation reactions of carbon dots," *Angew. Chemie - Int. Ed.*, vol. 54, no. 22, pp. 6540–6544, 2015, doi: 10.1002/anie.201501912.

[5] A. Singh, P. K. Mohapatra, D. Kalyanasundaram, and S. Kumar, "Self-functionalized ultrastable water suspension of luminescent carbon quantum dots," *Mater. Chem. Phys.*, vol. 225, no. October 2018, pp. 23–27, 2019, doi: 10.1016/j.matchemphys.2018.12.031.

[6] H. Li *et al.*, "Water-soluble fluorescent carbon quantum dots and photocatalyst design," *Angew. Chemie - Int. Ed.*, vol. 49, no. 26, pp. 4430–4434, 2010, doi: 10.1002/anie.200906154.

[7] L. Bao *et al.*, "Electrochemical tuning of luminescent carbon nanodots: From preparation to luminescence mechanism," *Adv. Mater.*, vol. 23, no. 48, pp. 5801–5806, 2011, doi: 10.1002/adma.201102866.

[8] M. Li, C. Hu, C. Yu, S. Wang, P. Zhang, and J. Qiu, "Organic amine-grafted carbon quantum dots with tailored surface and enhanced photoluminescence properties," *Carbon N. Y.*, vol. 91, pp. 291–297, 2015, doi: 10.1016/j.carbon.2015.04.083.

[9] H. Li *et al.*, "One-step ultrasonic synthesis of water-soluble carbon nanoparticles with excellent photoluminescent properties," *Carbon N. Y.*, vol. 49, no. 2, pp. 605–609, 2011, doi: 10.1016/j.carbon.2010.10.004.

[10] J. Wang, C. F. Wang, and S. Chen, "Amphiphilic egg-derived carbon dots: Rapid plasma fabrication, pyrolysis process, and multicolor printing patterns," *Angew. Chemie - Int. Ed.*, vol. 51, no. 37, pp. 9297–9301, 2012, doi: 10.1002/anie.201204381.

[11] M. F. Gomes, Y. F. Gomes, A. Lopes-Moriyama, E. L. de Barros Neto, and C. P. de Souza, "Design of carbon quantum dots via hydrothermal carbonization synthesis from renewable precursors. Biomass Convers. Biorefinery 9, 689–694 (2019)." 2019.

[12] Y. Liu *et al.*, "Hydrothermal synthesis of nitrogen and boron co-doped carbon quantum dots for application in acetone and dopamine sensors and multicolor cellular imaging," *Sensors Actuators, B Chem.*, vol. 281, no. October 2018, pp. 34–43, 2019, doi: 10.1016/j.snb.2018.10.075.

[13] H. Qi *et al.*, "Biomass-derived nitrogen-doped carbon quantum dots: highly selective fluorescent probe for detecting Fe 3+ ions and tetracyclines," *J. Colloid Interface Sci.*, vol. 539, pp. 332–341, 2019, doi: 10.1016/j.jcis.2018.12.047.

[14] J. Q. Zhang, M. H. Fan, W. Li, H. Xie, H. C. Wu, and S. P. Wang, "Fire safety of cables in power grid: Tracking combustion test standards of cables and new insights on test framework," *CIGRE Sess. 46*, vol. 2016-August, p. 3441, 2016.

The Optical Constant of Copper Sulfide Nanoparticles for Spectral Splitting PV/T System

Zhang **Jie**[1,2], Izyani **Mat Rusni**[1] and Salina **Muhamad**[1*]

[1]Faculty of Engineering and Life Sciences, Universiti Selangor, 45600 Bestari jaya, Selangor, Malaysia
[2]Jiangsu Shipping College, Nantong 226010, China

*Corresponding author's phone: 013-6690509
E-mail: msalina@unisel.edu.my

ABSTRACT

Spectral splitting medium is very important in the solar energy spectral splitting photovoltaic/thermal hybrid system. Due to good thermal conductivity and modulable spectral radiation characteristics, CuS is proposed as an alternative nanofluid in a PV/T hybrid system. The selective absorption characteristic of CuS nanofluid is closely related to the optical constant of nanoparticles. In this paper, the optical constant of CuS nanoparticles were studied. The results show that the refractive index *n* of CuS nanoparticles decreases with the increase of wavelength. The refractive index *n* characterizes the propagation speed of electromagnetic waves in the medium. The higher the refractive index *n*, the lower the propagation speed. The propagation speed of light in CuS nanoparticles increases with the increase of wavelength. For the extinction coefficient *k* of CuS nanoparticles, it is very small in the uv and visible light bands, and the order of magnitude is just 10^{-8}. In the near-infrared shortwave band, the extinction coefficient *k* gradually increases to the order of 10^{-5}. It shows a trend of first increasing and then decreasing in the wavelength range of 1300nm~1600nm, and reaches maximum at a wavelength of approximately 1500nm, with an order of magnitude of 10^{-4}. In the 1800nm-2000nm band, the extinction coefficient *k* shows a trend of first increasing, then decreasing, and then increasing. The maximum value appears at a wavelength of approximately 2000nm, with an order of magnitude of 10^{-3}. A minimum value appears at 2200nm, with an order of magnitude of 10^{-4}. In general, the extinction coefficient *k* of CuS nanoparticles is much higher in the near-infrared band than in the ultraviolet and visible light bands. It represents that CuS nanoparticles have better absorption characteristics in the near infrared band than in the ultraviolet and visible bands. These optical properties provide strong support for the wide application of CuS nanofluid in the spectral splitting photovoltaic/thermal hybrid technology.

Keywords- CuS, Nanoparticle, Optical Constant, Calculation

1.0 INTRODUCTION

The development of solar energy mainly includes photothermal conversion and photovoltaic conversion. In the latest research, spectral splitting photovoltaic/thermal system has attracted widespread attention due to its high

efficiency[1]. The spectral splitting photovoltaic/thermal system divides solar energy into two independent parts in the spectral range, photovoltaic spectrum and photothermal spectrum. However, the system has very high requirements for spectral splitting fluids. Compared with traditional fluids, nanofluids exhibit strong selective absorption characteristics in the ultraviolet, visible, and near-infrared bands, which makes them very suitable for the spectral splitting photovoltaic/thermal technology[2]. Due to the good thermal conductivity and modulable spectral radiation characteristics, CuS nanofluid is proposed as an alternative nanofluid to be applied into spectral splitting photovoltaic/thermal hybrid system[3]. Therefore, this study is carried out to calculate the optical constant of proposed CuS nanoparticles in order to ensure the suitability of such material in a PV/T hybrid system.

Many experiments have shown that the selective absorption characteristics of nanofluid are closely related to the characteristics of the nanoparticles themselves[4]. Different nanofluids exhibit different absorption characteristics. Gustav Mie proposed the Mie theory in 1869 [5], in which he believed that the radiation characteristics of particles are determined by their particle size and optical constants. The optical constant, also known as the complex refractive index, is a fundamental physical parameter that describes the propagation law of electromagnetic waves in a medium[6]. The optical constant is a complex number that can generally be expressed in the form of $m=n+ik$. It consist of two parts, which are respectively the refractive index n of the real part and the extinction coefficient k of the imaginary part. The real part represents the propagation speed of electromagnetic waves in the medium, while the imaginary part represents the attenuation law of electromagnetic waves in the medium. The optical constant, as an indispensable parameter for studying the photothermal efficiency of nanofluids, is related to factors such as medium temperature level, composition, and surface condition[7]. Generally, it cannot be directly measured through experiments, but can only be calculated by measuring physical quantities related to optical constants[8]. The inverse research method shown in Fig. 1 is used. The optical constant is the prerequisite and foundation for studying the radiation characteristics of media in various fields[9]. In the field of solar energy applications, the optical constant of a medium determines its absorption and transmission characteristics of solar radiation[10]. This has important application significance for studying the efficiency of solar energy. Therefore, the inversion of the optical constants of nanofluid is the foundation for studying the thermal radiation characteristics of nanofluids, which has great significance for the development of the spectral splitting photovoltaic/thermal system.

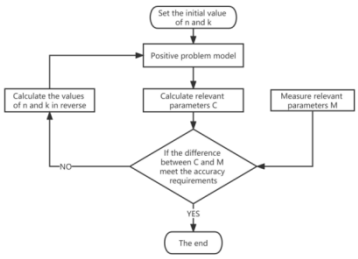

Fig. 1 Flow chart of inverse research method for optical constant

2.0 METHODOLOGY

Usually, it is necessary to solve the Maxwell equation and radiation transfer equation in the process of solving optical constant[11]. In this paper, the double thickness transmission method is used to solve the optical constants of the CuS nanofluid. This method skips the solution of differential and integral equation, simplifies

the calculation process, and improves the calculation speed. CuS nanofluid with optical thickness of 10 mm were studied in this paper. The model of the positive problem is the geometrical optical model. The inverse research model adopts a combination algorithm, which first uses particle swarm optimization to narrow the search range and improve the calculation speed, and then uses Conjugate gradient method to improve the calculation accuracy.

2.1 Positive research model

Positive research model is to find the result from the cause. The double thickness transmission method is used to solve the optical constants of CuS nanofluids, and its positive research model is the geometrical optical model. In this paper, 'cause' refers to the optical constant of CuS nanofluids. The 'result' refers to the collimated transmittance of a 10mm optical thickness CuS nanofluid.

2.1.1 Simplification of physical models

For the positive research model, the transmission process of light in the medium is discretized. As shown in Fig. 2, CuS nanofluid is contained in a cuvette. The transmission process of light in the cuvette containing CuS nanofluids is divided into three layers, which are respectively glass, nanofluid and glass. The transmittance of each layer, as well as the reflected luminous flux and incident luminous flux, need to be derived. Finally, the calculation formulas for total transmittance and total reflectance were derived.

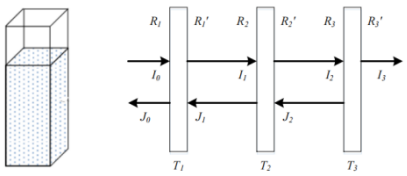

Fig. 2 Optical transmission dispersion diagram of the model

As shown in Fig. 2, R_i and R_i' are the reflectivity of the positive surface and negative surface. T_i is the transmittance of the corresponding element. I_0 is the incident luminous flux. I_i is the total luminous flux of the corresponding element. J_0 is the reflected luminous flux. J_i is the total luminous flux reflected back to the i element. The incident and reflected luminous flux of each surface can be expressed as follows.

$$J: J_0 = R_1 I_0 + T_1 J_1 \quad (1)$$

$$J_1 = R_2 I_1 + T_2 J_2 \quad (2)$$

$$J_2 = R_3 I_2 \quad (3)$$

$$I: I_1 = T_1 I_0 + R_1 J_1 \quad (4)$$

$$I_2 = T_2 I_1 + R_2 J_2 \quad (5)$$

$$I_3 = T_3 I_2 \quad (6)$$

Substitute formula (3) into formula (5) to obtain the following formula.

$$\frac{I_2}{I_1} = \frac{T_2}{1-R_2' R_3} \quad (7)$$

The following formula can be obtained by substituting formula (2) and formula (3) into formula (4).

$$\frac{I_1}{I_0} = \frac{T_1(1-R_2' R_3)}{(1-R_1' R_2)(1-R_2' R_3)-R_1' R_3 T_2^2} \quad (8)$$

$$\frac{I_2}{I_0} = \frac{T_1 T_2}{(1-R_1' R_2)(1-R_2' R_3)-R_1' R_3 T_2^2} \quad (9)$$

The total transmittance T_C is equal to the ratio of the luminous flux I_3 to the incident luminous flux I_0. The reflectivity R is equal to the ratio of the reflected luminous flux J_0 to the incident luminous flux I_0. Substitute formula (6) and formula (1) to get the following formula.

$$T_C = \frac{I_3}{I_0} = \frac{T_3 I_2}{I_0} \quad (10)$$

$$R = \frac{J_0}{I_0} = R_1 + R_2 T_1 \frac{I_1}{I_0} + T_1 T_2 R_2 \frac{I_2}{I_0} \quad (11)$$

Substitute formula (8) and formula (9) into formula (10) and formula (11) to get

the following formula.

$$T_C = \frac{T_1 T_2 T_3}{(1-R_1' R_2)(1-R_2' R_3)-R_1' R_3 T_2^2} \quad (12)$$

$$R = R_1 + \frac{R_2(1-R_2' R_3)+T_2^2 R_3}{(1-R_1' R_2)(1-R_2' R_3)-R_1' R_3 T_2^2} T_1^2 \quad (13)$$

2.1.2 Simplification of double-thickness transmission model

As shown in Fig. 3, the CuS nanofluid cuvette can be regarded as a glass-nanofluid-glass three-layer system. Where n_i is the refractive index of the i-layer medium. k_i is the extinction coefficient of the i-layer medium. l_2 is the optical thickness of the nanofluid.

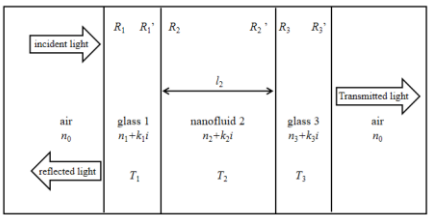

Fig. 3 Schematic diagram of the three-layer medium system

The propagation process of light in multi layer media follows Snell's refraction law and Fresnel's reflection law[12-13]. Based on the laws, a mathematical relationship can be established to associate the optical constant with the total transmittance. The specific process can be divided into three parts.

(1) Basis for derivation

Reflection satisfies Fresnel's law as shown in formula (14). Single-layer medium transmission meets single-layer medium transmission calculation method as shown in formula (15) .

$$R_{\mathrm{i}} = \frac{(n_j-n_i)^2+(k_j-k_i)^2}{(n_j+n_i)^2+(k_j+k_i)^2} \quad (14)$$

$$Ti = \frac{(1-R_i R_i')\exp\left(-\frac{4\pi k_i l_i}{\lambda}\right)}{1-R_i R_i' \exp\left(-\frac{8\pi k_i l_i}{\lambda}\right)} \quad (15)$$

In the formula, l_i is the sample thickness, j represent the medium on the left side of the interface, and i represent the medium on the right side of the interface.

(2)Simplification of the refractive index n_2 of CuS nanofluids

The extinction coefficientes of glasses, k_1 and k_3, are 0. Substitute k_1 and k_3 into the formulation (14) , the following formula can be obtained.

$$n_2 = \frac{(1+R_2)n_1 - \sqrt{n_1^2(1+R_2)^2-(1-R_2)^2(n_1^2+k_2^2)}}{1-R_2} \quad (16)$$

(3) Simplification of extinction coefficient k_2, reflectance R_2, and total transmittance of the model

Since the first layer and third layer are glasses, n_1=n_2, k_1=k_3=0. From the formula (14), we can obtain that R_1'=R_2=R_2'=R_3. In addition, since the extinction coefficient of most transparent media is small, it can be assumed that the extinction coefficient of CuS nanofluids is small. Ignoring the influence of the denominator index term and simplifying formula (15), the transmittance equations of CuS nanofluids with different optical thickness can be obtained as follows.

$$\begin{cases} T_{2,1} = (1-R_2^2)\exp\left(-\frac{4\pi k_2 l_{2,1}}{\lambda}\right) \\ T_{2,2} = (1-R_2^2)\exp\left(-\frac{4\pi k_2 l_{2,2}}{\lambda}\right) \end{cases} \quad (17)$$

Using the (17) equation set to solve k_2 and R_2, the following results can be obtained.

$$k_2 = \frac{\lambda \ln(T_{2,1}/T_{2,2})}{4\pi(l_{2,2}-l_{2,1})} \quad (18)$$

$$R_2 = \frac{\sqrt{1-T_{2,1}\exp\left(-\frac{4\pi k_2 l_{2,1}}{\lambda}\right)}+\sqrt{1-T_{2,2}\exp\left(-\frac{4\pi k_2 l_{2,2}}{\lambda}\right)}}{2} \quad (19)$$

The following formula can be obtained by substituting R_1'=R_2=R_2'=R_3 into formula (12).

$$T_{\mathrm{c}} = \frac{T_1 T_2 T_3}{(1-R_2{}^2)^2-R_2{}^2 T_2^2} \quad (20)$$

2.1.3 Calculation process of positive research model

The calculation process of the positive research model is shown in Fig. 4. On the basis of assuming that the optical constants of CuS nanofluids are known, the reflection R_1 of the glass and air contact side, the reflectivity R_2 of the glass and CuS nanofluids contact side, and the transmittance T_1 of the glass layer can be obtained. Then calculate the transmissivity $T_{2,1}$ and $T_{2,2}$ of CuS nanofluid layer. Finally, the collimation transmittance $T_{c,1}$ and $T_{c,2}$ are obtained.

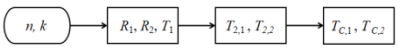

Figure 4 Calculation flow chart of positive research model

2.2 Inverse research model

The problem of finding the cause from the result is called the inverse research problem. In order to solve the optical constants, Particle Swarm Optimization (PSO) and Conjugate gradient method are combined. PSO is used to improve the calculation speed, and Conjugate gradient method is used to improve the calculation accuracy.

2.2.1 Particle Swarm Optimization

PSO is a random optimization technology based on population. Unlike other evolutionary algorithms, PSO avoids evolutionary operators and treats each individual as particles flying at a certain speed in the search space without volume or weight[14]. The PSO flow chart is shown in Fig. 5.

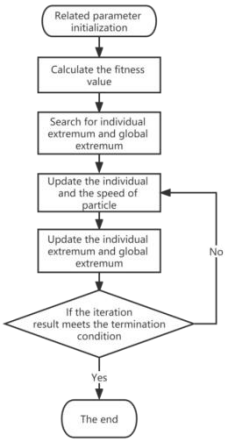

Fig. 5 PSO flow chart

2.2.2 Conjugate gradient method

The conjugate gradient method is an unconstrained optimization algorithm. It has a superlinear convergence rate. The algorithm uses the objective function and gradient value to avoid the calculation of the second derivative, which makes the structure of the algorithm simple and reduces the storage and calculation[15].

2.2.3 Combination of PSO algorithm and conjugate gradient method

In this paper, PSO algorithm and conjugate gradient method are combined to calculate the optical constants of CuS nanofluids. First, the PSO algorithm is used to calculate and narrow the range to obtain a value close to the true value. Then the conjugate gradient method is used for further calculation. The calculation process is shown in Fig. 6.

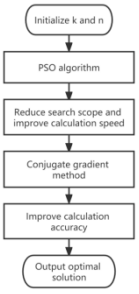

Fig. 6 Calculation flow diagram of combined algorithm

2.3 The calculation model of double-thickness transmission model

In this paper, the optical constants of CuS nanofluids are calculated by the double-thickness transmission model. The measurement method is double transmission method. The geometric optical model is selected for the forward problem model. The inverse research model is a combination of particle swarm optimization and conjugate gradient method. Firstly, the collimation transmittance of CuS nanofluids was measured by UV3600 spectrophotometer. The iterative initial values of refractive index *n* and extinction coefficient *k* were set. The geometric optical model and PSO algorithm are used firstly. Then, the value close to the true value is obtained. The geometric optical model and conjugate gradient method are used for further calculation, and the solution with high accuracy is obtained. The calculation process is shown in Fig. 7.

Fig. 7 Calculation flow of double-thickness transmission model

2.4 Maxwell-Garnett effective medium theory

For the medium system formed by spherical particles dispersed into continuous medium, Maxwell-Garnett effective medium theory can be adopted when the size of spherical particles is less than the wavelength of incident light[16]. The average particle size of CuS nanoparticles in this paper is 60.2 nm, and can be approximately regarded as spherical particles. Therefore, Maxwell-Garnett effective medium theory can be used for solution.

$$\varepsilon' = n^2 - k^2 \tag{21}$$

$$\varepsilon'' = 2nk \tag{22}$$

$$\varepsilon_{eff} = \varepsilon_f \left[1 + \frac{3f_v \frac{\varepsilon_p - \varepsilon_f}{\varepsilon_p + 2\varepsilon_f}}{1 - f_v \frac{\varepsilon_p - 2\varepsilon_f}{\varepsilon_p + 2\varepsilon_f}} \right] \tag{23}$$

In the formula, ε' is the real part of the dielectric constant. ε'' is the imaginary part of the dielectric constant. *eff*, *f* and *p* represent nanofluids, solution and nanoparticles, respectively. *Fv* is the volume fraction of nanoparticles. The volume fraction of copper sulfide nanoparticles in this paper is 6.35×10^{-5}.

3.0 RESULTs AND DISCUSSION

CuS nanofluids with an average particle size of 60.2 nm were studied. According to the collimated transmittance of CuS nanofluids at 10 mm optical thickness, the optical constants of CuS nanofluids are inversely calculated based on the double thickness transmission method. After that, the optical constants of CuS nanoparticles were calculated by Maxwell-Garnett effective medium theory. Fig. 8 shows the calculation results of refractive index *n* of CuS nanoparticles. In the ultraviolet band, the refractive index n rapidly decreases. In the visible light band, the reduction rate of refractive index n is the slowest. In the near-infrared band, the decrease rate of refractive index *n* gradually increases, but is lower than that in the ultraviolet band. The refractive index *n* of CuS nanoparticles decreases with the increase of wavelength. The refractive index *n* is the real part of the optical constant of the medium, which characterizes the propagation speed of electromagnetic waves in the medium. The

higher the refractive index *n*, the lower the propagation speed. The propagation speed of light in CuS nanoparticles increases with the increase of wavelength.

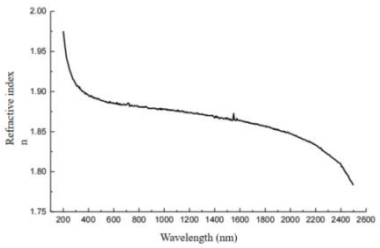

Fig. 8 Calculation results of refractive index n of CuS nanoparticles

Fig. 9 shows the calculation results of the extinction coefficient *k* of copper sulfide nanoparticles. In the uv and visible light bands, the extinction coefficient *k* of CuS nanoparticles is very small, the order of magnitude is 10^{-8}. In the near-infrared shortwave band, the extinction coefficient *k* gradually increases to the order of 10^{-5}. The extinction coefficient k shows a trend of first increasing and then decreasing in the wavelength range of 1300nm~1600nm. It reaches its maximum at a wavelength of approximately 1500nm, with an order of magnitude of 10^{-4}. In the 1800nm-2000nm band, the extinction coefficient *k* shows a trend of first increasing, then decreasing, and then increasing. The maximum value appears at a wavelength of approximately 2000nm, with an order of magnitude of 10^{-3}. A minimum value appears at 2200nm, with an order of magnitude of 10^{-4}. In general, the extinction coefficient *k* of CuS nanoparticles is much higher in the near-infrared band than in the ultraviolet and visible light bands.

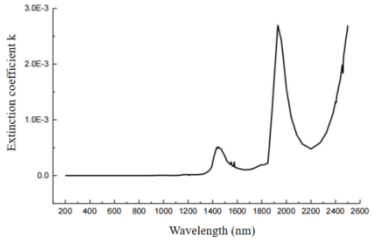

Fig. 9 Calculation results of extinction coefficient k of CuS nanoparticles

4.0 CONCLUSION

The optical constant of CuS nanoparticles for spectral splitting photovoltaic/thermal hybrid system have been successfully calculated. Firstly, the double-thickness transmission model is simplified. Then, the particle swarm optimization algorithm and the Conjugate gradient method is combined to inverse the optical constant model of CuS nanofluids. Finally, the optical constants of CuS nanoparticles are calculated by the effective medium theory. The results showed that the refractive index n of CuS nanoparticles decreased. The refractive index decreases at the highest rate in the ultraviolet band and the lowest rate in the visible light band. This also shows that the propagation speed of light in CuS nanoparticles gradually increases with the increase of wavelength. The extinction coefficient *k* of CuS nanoparticles is very small in the UV and visible light bands, which indicates that CuS nanofluids have good transmission performance in the UV and visible light bands. In the near-infrared band, there have been several significant fluctuations in the extinction coefficient *k*. In addition, the extinction coefficient in the infrared band is significantly higher than that in the ultraviolet and visible light bands. In other words, CuS nanoparticles have better absorption characteristics in the near-infrared band than in the ultraviolet and visible light bands. Therefore, CuS nanofluids are suitable for the application of spectral splitting photovoltaic/thermal hybrid system.

ACKNOWLEDGEMENT

This project received a funding from Basic Research and Development Project of Nantong City, No.JC22022066 and Science and Technology Project of Jiangsu Shipping College, No.HYKY/2022B01.

REFERENCES

[1] Lin J, Liu S, Ju X, et al. Investigation of two-stage concentrating splitting photovoltaic/thermal system with a flexible heat-electricity ratio based on nanofluid[J]. Energy Conversion and Management, 2022, 258: 115531.

[2] Alktranee M, Bencs P. Applications of nanotechnology with hybrid photovoltaic/thermal systems: a review[J]. Journal of Applied Engineering Science, 2021, 19(2): 292-306.

[3] Feng Qunfeng. Research on the regulation and application of near-infrared absorption performance of copper sulfide [D]. Shanghai Normal University, 2018.

[4] Dingler C, Walter R, Gompf B, et al. In situ monitoring of optical constants, conductivity, and swelling of PEDOT: PSS from doped to the fully neutral state[J]. Macromolecules, 2022, 55(5): 1600-1608.

[5] Ku J C, Felske J D. Determination of refractive indices of Mie Satters from Kramers-Kronig analysis of spectral extinction data [J]. Journal of the Optical Society of America A: Optics and Image Science, 1986, 3(5): 617-623.

[6] Herawati A, Khasanah R A N, Maulana L Z, et al. Simple and Low-Cost Rotating Analyzer Ellipsometer (RAE) for Wavelength Dependent Optical Constant Characterization of Novel Materials[J]. Key Engineering Materials, 2020, 840: 392-398.

[7] Shvets V A, Marin D V, Remesnik V G, et al. Parametric Model of the Optical Constant Spectra of Hg 1–x Cd x Te and Determination of the Compound Composition[J]. Optics and Spectroscopy, 2020, 128: 1948-1953.

[8] Pan Y, Liu H, Wang Z, et al. Optical constant and conformality analysis of SiO2 thin films deposited on linear array microstructure substrate by PECVD[J]. Coatings, 2021, 11(5): 510.

[9] Almaliky A , Qusay M A ,Hassan,et al.The optical constant and nonlinear properties of mixture of aluminum oxide-epoxy resin film[J]. 2021.

[10] Amoo O M, Fagbenle R O, Oyewola M O. Benchmark assessment of performance indices of a selection of hybrid nanofluids in a hybrid photovoltaic/thermal system[J]. Clean Energy, 2022, 6(2): 247-270.

[11] Moghtader M J, Lanteri S, Gobé A, et al. HDG Method for the 3d Frequency-Domain Maxwell's Equations With Application to Nanophotonics[C]//6th European Seminar on Computing. 2018.

[12] Shui L, Liu Y, Chen X. Snell's law of elastic waves propagation on moving property interface of time-varying materials[J]. International Journal of Solids and Structures, 2018, 143: 18-28.

[13] Mink A, Schediwy K, Haussmann M, et al. Fresnel reflection boundary for radiative transport lattice Boltzmann methods in highly scattering volume[J]. arXiv preprint arXiv:2107.09411, 2021.

[14] Shami T M, El-Saleh A A, Alswaitti M, et al. Particle swarm optimization: A comprehensive survey[J]. IEEE Access, 2022, 10: 10031-10061.

[15] He Q R, Chen C R, Li S J. Spectral conjugate gradient methods for vector optimization problems[J]. Computational Optimization and Applications, 2023: 1-33.

[16] Yao Y, Luo J, Duan X, et al. On the piezoresistive behavior of carbon fibers-Cantilever-based testing method and Maxwell-Garnett effective medium theory modeling[J]. Carbon, 2019, 141: 283-290.

Rice husk ash (RHA) Nano particles as new materials for Hydrogen Gas Sensor

Jamila Lamido **Sumaila**[1,2*], Dahiru **Sani** [1], Nuraddeen **Magaji**[1], Zainab **Yunusa**[1,3]
Mohd Nizar **Hamidon**[4], Azlinda **Abubakar**[4] Suleiman **Babani**[1,4], Farah Nabilah **Shafiee**[4]

[1]Department of Electrical Engineering, Bayero University Kano, BUK
Kano, Nigeria
[2] Department of Physics, Yusuf Maitama Sule University Kano, YUMSUK
Kano, Nigeria
[3] Department of Electrical Engineering, University of Hafr Al Batin Al Jamiah
Hafar Al Batin, Saudi Arabia
[4] Institute of Nanoscience and Nanotechnology, Universiti Putra Malaysia, UPM
Serdang, Malaysia

*Corresponding author's phone: +234 803 7571 636
E-mail: j.lamido@yahoo.com / sumailajamila@gmail.com

ABSTRACT

In this work, a hydrogen gas sensor was developed with carbon-based material from rice husk ash (RHA) mixed with an equal proportion of biochar obtained from the Prosopis Africana char (PAC) plant as a sensing material. The sensing material was mixed with a linseed organic binder to form a sensing film. Thermogravimetric analysis (TGA) was carried out on the thick film paste and the morphological and structural properties of the sensing film were characterized by field emission scanning electron microscopy (FESEM), energy-dispersive X-ray spectroscopy (EDX), and Raman Spectroscopy. The gas sensor was exposed to hydrogen with a concentration of 100–1000 ppm and was tested at room temperature.The gas sensor showed capability in sensing low concentrations of hydrogen to as low as 100 ppm at room temperature with appreciale sensitivity and the sensitivity inceases when the temperature was increased up to 250 ℃.

Keywords— Sensing film; linseed oil; organic binder; biochar; n-type

1.0 INTRODUCTION

As a result of the depletion of fossil resources, the field of hydrogen-powered fuel cells has rapidly developed. Hydrogen (H_2) provides various benefits, including a high energy density per unit area, renewability, and environmental friendliness [1]. In recent years, there has been considerable interest in the utilization of H_2 as a key energy source in the near future on account of its clean and abundant energy capability. However, it is extremely combustible, colorless, odorless, and air-borne with a flammability index ranging from 4 to 75% in the earth's atmosphere[2]. This consequently increases the likelihood of an explosion. In addition, it is commonly understood that H2 tends to leak rapidly and is difficult to store as the lightest known gas. Due to these features, any H_2 leak must be identified as fast as possible to ensure safety. Hence, H_2 sensors are required in different domains where it is used, including hydrogen fuel cells, H_2 storage systems, and infrastructure/industry containing or employing H_2 [3].

2.0 THEORY/LITERATURE REVIEW

H_2 sensors rely on H_2 reactions with sensing materials to function. Optical, electrochemical, mechanical, or electrical measurements are employed to convert these processes into a sensor signal. Electrochemical and chemiresistive H_2 sensors are both commercially available and considered state-of-the-art H_2 sensor technologies. Electrochemical H_2 sensors function by converting redox reactions of H_2 on the sensor into electrical signals[4]. Electrochemical sensors exhibit sensitive and selective H_2 detecting properties with low detection limits, but they are very sensitive to environmental variables (oxygen and humidity levels) and have rather complex systems that need expensive fabrication costs. [5]

On the other hand, chemiresistive sensors, which are powered by the conversion of chemical reactions into electrical signals (resistances or conductance), offer various advantages, including efficient sensing performance, inexpensive construction, and portability. Particularly, the detection of resistance (or conductance) changes in sensors can be interfaced with electronic readouts simply and with minimal signal processing, whereas other transduction methods need more complex signal processing[6][7].

Carbon is a unique element that, depending on its structure and chemical composition, possesses a vast range of distinctive qualities. The list of applications for carbon-based materials varies from building materials (carbon fiber composites) to electrical conductors (graphite) to ornaments (diamond) [8] Due to their huge sensing surface and chemical inertness, carbon-based sensors have drawn a significant deal of interest during the past few decades[9].

Concerns over the health, safety and environmental impact of nanomaterials and their manufacture have shifted focus to nanoparticles made from biomass [10]. Biomass is an acceptable carbon source, it is abundant and of good quality, and it is regarded as an environmentally benign renewable resource. In recent years, biochar applications have expanded into other fields, while pyrolysis of agricultural waste remains its primary source. In addition, various biochars (residues of biomass pyrolysis) are becoming available from biogas and energy-producing pilot plants. Biochar is a carbonaceous material derived from the thermochemical decomposition (pyrolysis) of naturally available raw materials (biomass) that has garnered a great deal of interest due to its distinctive physicochemical features, sustainability, and low cost[11]. In addition, biochar has been investigated intensively in recent years as an alternative to more expensive carbon compounds such as carbon nanotubes, graphene, and others[12]. Emerging trends in green technology have recently emphasized the use of environmentally friendly, biodegradable, and cost-effective sensing materials that are highly functional in ambient conditions. This study describes the use of rice husk ash and Prosopis Africana char to develop gas sensors for the detection of hydrogen gas at varying temperatures. To the best of our knowledge this is the first time these two materials are used for hydrogen gas sensing.

3.0 MATERIALS

Rice husk obtained from local farmers in Kano Nigeria, prosopis Africana char obtained from local market in Nigeria, Dalar Rowney Linseed stand oil, α-Terpineol from Sigma Aldrich, and m-Xylene sigma Aldrich. Silver conductive paste from Serdang paste tech. was used for electrode printing on Kepton substrate.

.

4.0 EXPERIMENTAL

M-xylene, linseed oil, and α-terpineol were combined to create an organic binder. Thick film paste was developed by mixing 40:60 weight RHA-PAC with an organic binder using a magnetic stirrer for 24hrs. silver-conductive substance was used as the conductive IDE. IDE and the sensing film were deposited using screen printing on a Kepton substrate. Initial deposition of IDE as the first layer on the Kepton substrate was followed by 30 minutes of annealing at 120 C on a hot plate. Then, RHA-PAC paste material was deposited on top of IDE, and it was annealed at 400 C for 1hour:30 minutes in a furnace.

5.0 RESULTS AND DISCUSSION

Characterizations of the sensing film using TGA, FESEM, EDX and Raman Spectroscopy.

The thermal behavior of the RHA-PAC paste and the determination of an optimal calcination temperature were investigated through TGA analysis. The results depicted in Figure 4 illustrate the overall mass loss of the paste within a temperature range of 25 to 1000 ◦C. Notably, at 400 ◦C, the mass loss was approximately 49.61%, indicating incomplete evaporation of the organic binder at this temperature. However, the mass loss decreased again to around 25.12% when the temperature reached 500 ◦C. The composition ratio of RHA-PAC powder to organic binder in this study was 40:60. Consequently, it can be observed that the organic binder was fully evaporated at a temperature of 500 ◦C.

.

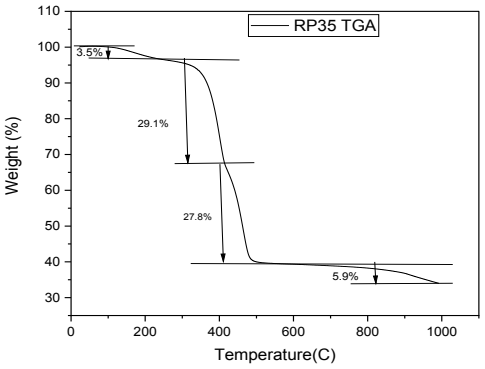

Fig. 1 TGA Analysis of the Thick film paste

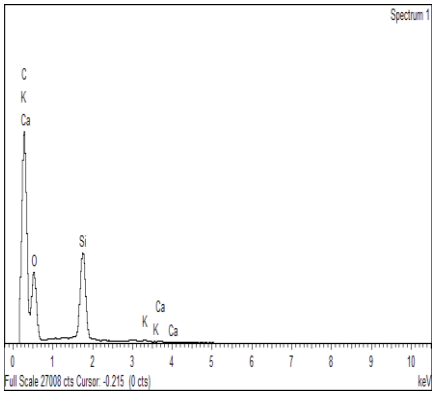

Fig.2 EDX Spectra of the sensing film

Table 1 Elemental analysis

Elements	Atomic%
C	65.15
O	30.12
Si	4.17
K	0.30
Ca	0.26
Total	100

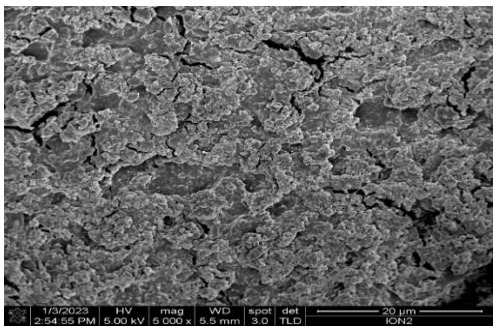

Fig.3 FESEM Micrograph of the sensing film

The EDX spectra of the plotted result of the elemental analysis are shown above. Carbon and Silicon are all found in the sensing material, indicating semi-conductivity. The FESEM micrographs of the sensing film as shown in the fig. 3 above also indicates the sensimg material cemented all the particles together with some cracks which is likely due to the annealing process.

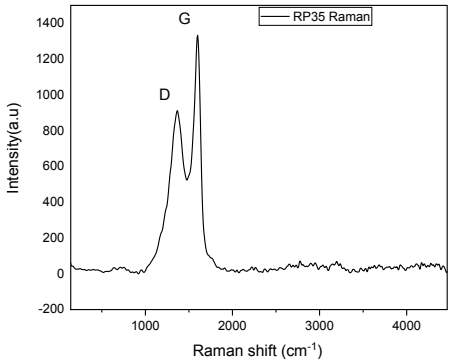

Fig.4 Raman Specstroscopy of the sensing film

The Raman spectroscopy result indicates disorderliness with graphitization. The disorder was due to milling of the biochar powders for six hours.

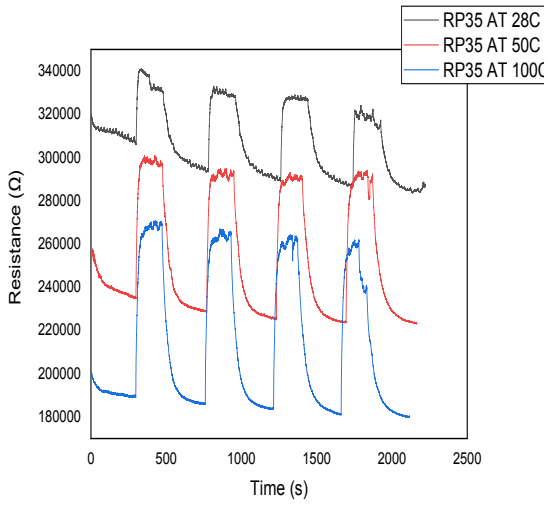

Fig. 5 Gas sensor Measurment

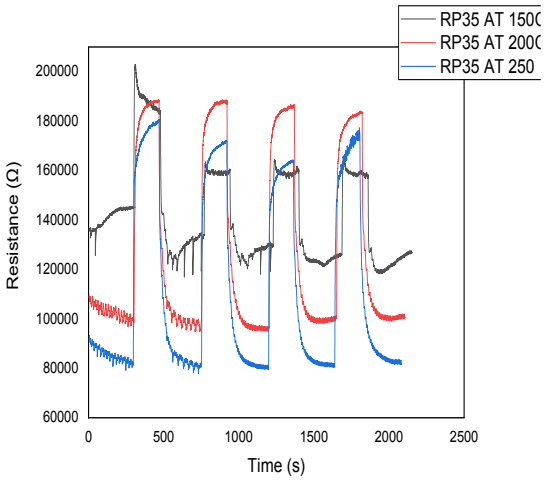

Fig. 6 Gas sensor measurement

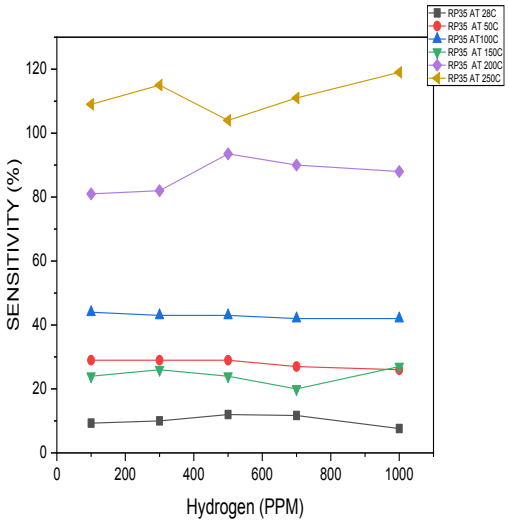

Fig. 7 Gas sensor sensitivity measurement

The gas sensor measurement was shown in figure 5 above. The sensing measurement was carried out in a gas sensing chamber. Air was first allowed to flow for 3 minutes then followed by Hydrogen gas, which was observed for 5 minutes. The input voltage used was 10 volts, it could be observed that the resistance value increases during gas flow and decreases when air flows, this behavior indicates a P-type material. Fig. 7 shows the sensitivity graph which indicates the highest sensitivity at 250˚C and the lowest sensitivity occurred at 28˚C.

6.0 CONCLUSION

The sensor was fabricated and was tested with hydrogen gas at room temperature and the temperature was varied up to 250℃. The sensor exhibits good sensitivity with the highest sensitivity obtained at 250˚ C. The response and recovery time was very fast with a value of less than 60s.

ACKNOWLEDGEMENT

The work was sponsored by Yusuf Maitama Sule University, Kano.

REFERENCES

1. A. M. Al-Diabat, N. A. Algadri, N. M. Ahmed, A. Abuelsamen, and S. A. Bidier, "A high-sensitivity hydrogen gas sensor based on carbon nanotubes fabricated on SiO2 substrate," *Nanocomposites*, vol. 7, no. 1, pp. 172–183, 2021, doi: 10.1080/20550324.2021.1977063.
2. D. Zilli, P. R. Bonelli, and A. L. Cukierman, "Room temperature hydrogen gas sensor nanocomposite based on Pd-decorated multi-walled carbon nanotubes thin films," *Sensors Actuators, B Chem.*, vol. 157, no. 1, pp. 169–176, 2011, doi: 10.1016/j.snb.2011.03.045.
3. D. Jung, M. Han, and G. S. Lee, "Room-temperature gas sensor using carbon nanotube with cobalt oxides," *Sensors Actuators, B Chem.*, vol. 204, pp. 596–601, 2014, doi: 10.1016/j.snb.2014.08.020.
4. S. Dhall, N. Jaggi, and R. Nathawat, "Functionalized multiwalled carbon nanotubes based hydrogen gas sensor," *Sensors Actuators, A Phys.*, vol. 201, pp. 321–327, 2013, doi: 10.1016/j.sna.2013.07.018.
5. J. Wang, Y. Kwak, I. Y. Lee, S. Maeng, and G. H. Kim, "Highly responsive hydrogen gas sensing by partially reduced graphite oxide thin films at room temperature," *Carbon N. Y.*, vol. 50, no. 11, pp. 4061–4067, 2012, doi: 10.1016/j.carbon.2012.04.053.
6. W. T. Koo *et al.*, "Chemiresistive hydrogen sensors: Fundamentals, recent advances, and challenges," *ACS Nano*, vol. 14, no. 11, pp. 14284–14322, 2020, doi: 10.1021/acsnano.0c05307.
7. Z. Li *et al.*, "Resistive-type hydrogen gas sensor based on TiO2: A review," *Int. J. Hydrogen Energy*, vol. 43, no. 45, pp. 21114–21132, 2018, doi: 10.1016/j.ijhydene.2018.09.051.
8. A. Ilnicka and J. P. Lukaszewicz, "Graphene-based hydrogen gas sensors: A review," *Processes*, vol. 8, no. 5, 2020, doi: 10.3390/PR8050633.
9. E. Llobet, "Gas sensors using carbon nanomaterials: A review," *Sensors Actuators, B Chem.*, vol. 179, pp. 32–45, 2013, doi: 10.1016/j.snb.2012.11.014.
10. C. D. S. Wong, J. X. Yeoh, T. Wu, S. Manickam, and C. H. Pang, "Biomass to nanoparticles: Recent advances in the process and processing towards sustainability," *Chem. Eng. Process. - Process Intensif.*, vol. 175, no. January, p. 108908, 2022, doi: 10.1016/j.cep.2022.108908.
11. D. Spanu, G. Binda, C. Dossi, and D. Monticelli, "Biochar as an alternative sustainable platform for sensing applications: A review," *Microchem. J.*, vol. 159, no. September, p. 105506, 2020, doi: 10.1016/j.microc.2020.105506.
12. N. Jafri, W. Y. Wong, V. Doshi, L. W. Yoon, and K. H. Cheah, "A review on production and characterization of biochars for application in direct carbon fuel cells," *Process Saf. Environ. Prot.*, vol. 118, pp. 152–166, 2018, doi: 10.1016/j.psep.2018.06.036.

Organised by:
Institute of Nanoscience and Nanotechnology (ION2)
Universiti Putra Malaysia

https://ion2.upm.edu.my

iSAMN 2023

eISSN 2811-4655

AGRICULTURE • INNOVATION • LIFE

BERILMU BERBAKTI
WITH KNOWLEDGE WE SERVE

www.upm.edu.my